

MULTIVARIABLE CONTROL OF A SUBMARINE
USING THE LQG/LTR METHOD

by
JAMES ALLEN NETTE, JR.

BSME, Purdue University (1978)

SUBMITTED TO THE DEPARTMENTS OF OCEAN ENGINEERING
AND MECHANICAL ENGINEERING IN PARTIAL FULFILLMENT
OF THE REQUIREMENTS FOR THE DEGREES OF

OCEAN ENGINEER
AND
MASTER OF SCIENCE IN MECHANICAL ENGINEERING

at the

MASSACHUSETTS INSTITUTE OF TECHNOLOGY

10 MAY 1985

© James Allen Nette, Jr., 1985

Permission is hereby granted to the Charles Stark Draper Laboratory,
to the Massachusetts Institute of Technology and to the United States
Government and its agencies to reproduce and to distribute copies of
this thesis document in whole or in part.

Signature of Author: _____
Department of Ocean Engineering, May 10, 1985

Certified by: _____
Professor Michael Athans
Thesis Co-Supervisor

Certified by: _____
Professor Lena Valavani
Thesis Co-Supervisor

Certified by: _____
Professor Michael Triantafyllou
Thesis Reader

Accepted by: _____
Professor A.D. Carrichael
Chairman, Ocean Engineering Departmental Committee

Accepted by: _____
Professor Ain A. Sonin
Chairman, Mechanical Engineering Departmental Committee

MULTIVARIABLE CONTROL OF A SUBMARINE
USING THE LQG/LTR METHOD

by

James Allen Mette, Jr.

Submitted to the Departments of Ocean Engineering and Mechanical Engineering in Partial Fulfillment of the Requirements for the Degrees of Ocean Engineer and Master of Science in Mechanical Engineering.

ABSTRACT

A multivariable control system for a deeply submerged submarine with active roll control is designed using the Linear Quadratic Gaussian with Loop Transfer Recovery (LQG/LTR) method. A linear model of the submarine is developed for a 1 degree rudder deflection at a speed of 15 knots. The linear model is then scaled for units and input/output weightings and augmented with integral control in all four input channels. Using the properties of the linear model, a Model Based Compensator (MBC) is designed by shaping the singular values of a Kalman Filter to meet desired performance criteria and then recovering the singular value shapes using the Kwakernaak recovery process. During extensive testing at speeds from 15 to 30 knots, the compensator performed well enough so that gain scheduling was not employed. Next, the compensator is compared to one designed for a 30 knot model. Finally, an Anti-Reset Windup (ARW) strategy is employed to counter the effects of control surface saturation.

THESIS SUPERVISORS: Dr. Michael Athans, Professor of Systems Science
and Engineering
Dr. Lena Valavani, Assistant Professor of
Aeronautics and Astronautics

ACKNOWLEDGEMENTS

I would like express my thanks to my thesis supervisors, Michael Athans and Lena Valavani, for their support, guidance and patience. I would also like to thank Mr. Petros Kapsouris for his ideas and the interaction that helped in many ways.

The Charles S. Draper Laboratory deserves special recognition for providing the submarine simulation facilities. A special thanks to Mr. William Bonnice for his continual programming and technical support.

Last, but not least, I want to express my thanks to Sue, Lizzie and Jimmy for the support they have given not only during my stay at MIT but throughout my naval career. A man could not ask for a more loving or supportive family.

This research was performed at the MIT Laboratory for Information and Decision Systems with partial support provided by the Office of Naval Research under contract ONR/N00014-82-K-0582(NR606-003).

TABLE OF CONTENTS

ABSTRACT	2
ACKNOWLEDGEMENTS	3
TABLE OF CONTENTS	4
LIST OF FIGURES	6
LIST OF TABLES	7
CHAPTER 1: INTRODUCTION AND SUMMARY	
1.1 Background and Discussion of Prior Work	8
1.2 Contributions of the Thesis	10
1.3 Outline of the Thesis	10
CHAPTER 2: MODELING OF THE SUBMARINE	
2.1 Introduction	12
2.2 Description of the Nonlinear Submarine Model	12
2.3 Description of the Linear Submarine Model.....	16
2.4 Selection of the Output Variables	19
2.5 Summary	27
CHAPTER 3: LINEAR MODEL ANALYSIS	
3.1 Introduction	28
3.2 Reduction of the Model	28
3.3 Scaling	29
3.4 Eigenstructure	31
3.5 Performance Specifications	41
3.6 Summary	47
CHAPTER 4: LINEAR COMPENSATOR DESIGN	
4.1 Introduction	48
4.2 The LQG/LTR Design Methodology	48
4.3 Design of the LQG/LTR Compensator	55
4.4 Preliminary Testing of the Compensator.....	65
4.5 Summary	81
CHAPTER 5: ADDITIONAL ANALYSIS OF THE COMPENSATOR	
5.1 Introduction	82
5.2 Additional Analysis of the S15R1 Compensator	82
5.3 Comparison of the 15 and 30 Knot Compensators	91
5.4 Summary	118

CHAPTER 6: IMPLEMENTATION OF ANTI-RESET WINDUP FEEDBACK

6.1	Introduction.....	119
6.2	ARW Feedback Loop.....	119
6.3	Simulations for a System With ARW Feedback.....	123
6.4	Summary.....	136

CHAPTER 7: SUMMARY AND DIRECTIONS FOR FURTHER RESEARCH

7.1	Summary	137
7.2	Conclusions and Directions for Further Research	138

REFERENCES.....	141
-----------------	-----

APPENDIX A: MATRICES OF THE S15R1 LINEAR MODEL

A1	Original Plant Matrices Prior to Reduction and Scaling..	144
A2	Matrices Scaled for Units.....	145
A3	Matrices Scaled for Units and Weights.....	149

APPENDIX B: PROPERTIES OF THE 15 KNOT PLANT AND COMPENSATOR

B1	Poles, Zeros and Eigenvectors of S15R1.....	152
B2	Observability and Controllability Matrices.....	153
B3	Model Based Compensator Matrices.....	154
B4	Poles and Zeros of the Open and Closed Loop Systems.....	156

APPENDIX C: MATRICES OF THE 30 KNOT PLANT AND COMPENSATOR

C1	State Space Matrices of the S30R1 Linear Model.....	159
C2	Matrices of the 30 Knot Compensator.....	162

LIST OF FIGURES

2.1	Body-Fixed Coordinate System for a Submarine.....	13
2.2	Comparison of Nonlinear and Linear Dynamics for Model S15R1.....	20
2.3	Comparison of Nonlinear and Linear Response for 20% Perturbation Above Nominal Point.....	23
3.1	Block Diagram Representation After Scaling.....	31
3.2	Breakdown of S15R1 Modes by State.....	33
3.3	Effect of Control Surfaces by Mode.....	36
3.4	Singular Value Decomposition of S15R1.....	39
3.5	Feedback Loop Structure.....	42
3.6	Singular Value Requirements for $\underline{G}(s)\underline{K}(s)$	42
3.7	Plant with Integrators in Input Channels.....	43
3.8	Singular Values of Original Plant $\underline{G}_p(s)$	44
3.9	Singular Values of Augmented Plant $\underline{G}(s)$	44
3.10	MIMO Feedback Loop with Multiplicative Error.....	45
4.1	Feedback Loop Structure with $\underline{G}(s)$	49
4.2	Structure of the Model Based Compensator in a Feedback Configuration.....	50
4.3a	Singular Values of $\underline{G}_{f01}(s)$	58
4.3b	Singular Values of $\underline{G}_{kf}(s)$	58
4.3c	Singular Values of $\underline{G}(s)\underline{K}(s)$	58
4.4	Block Diagram Representation of the Closed Loop System.....	59
4.5a	Singular Values of $\underline{K}(s)$	61
4.5b	Singular Values of $\underline{K}_a(s)$	61
4.6	Singular Values of the Closed Loop.....	62
4.7	Singular Values of $\underline{K}_r(s)$	62
4.8	Singular Value Decomposition of $\underline{K}_r(s)$	63
4.9	Symmetry Comparison for +/- 1 Degree/Second Yawrate.....	66
4.10	Symmetry Comparison for +/- 5 Degree Roll Angle.....	72
4.11	Simulation for 1 Foot/Second Depthrate.....	77
4.12	Simulation for 4.5 Feet/Second and -10 Degree Pitch Angle.....	79
5.1	Comparison of Singular Values of S15R1 and S30R1 Linear Models..	84
5.2	Robustness Comparison of $\underline{G}(s)\underline{K}(s)$ and the Error $\underline{E}(s)$	85
5.3	Comparison of 15 Knot Compensator Performance for Simultaneous Turn and Dive During Speed Change.....	87
5.4	Comparison of 15 Knot Compensator Performance for Simultaneous Roll and Dive During Speed Change.....	92
5.5	Comparison of 15 Knot and 30 Knot Compensators for -1 Degree/Second Yawrate at 15 Knots.....	97
5.6	Comparison of 15 Knot and 30 Knot Compensators for -1 Degree/Second Yawrate at 30 Knots.....	102
5.7	Comparison of 15 Knot and 30 Knot Compensators for Simultaneous Turn and Dive (30 to 15 Knots).....	107
5.8	Comparison of 15 Knot and 30 Knot Compensators for Simultaneous Turn and Dive (15 to 30 Knots).....	113

6.1	Structure of the Closed Loop System with ARW.....	120
6.2	Bode Plot of Simple Lag for Varying α	121
6.3a	Singular Values of $\underline{G}(s)\underline{K}(s)$ for $\alpha = 0.1$	122
6.3b	Singular Values of $\underline{G}(s)\underline{K}(s)$ for $\alpha = 0.05$	122
6.4	Singular Values of the Closed Loop for $\alpha = 0.05$	124
6.5	Comparison of Systems Without and With ARW ($\alpha = 0.05$) for 2 Feet/Second Depthrate.....	126
6.6	Comparison of Systems Without and With ARW ($\alpha = 0.05$) for 4 Feet/Second Depthrate.....	131

LIST OF TABLES

2.1	State and Control Variables.....	15
2.2	20% Perturbations Applied to Model S15R1.....	19
3.1	Control Surface Rate and Deflection Limits.....	30

CHAPTER 1

INTRODUCTION AND SUMMARY

1.1 Background and Discussion of Prior Work

The introduction of nuclear propulsion and hydrodynamically efficient hullforms on submarines have resulted in platforms capable of very high submerged speed for prolonged periods of time. At these high speeds, ship control is a complex problem due to the dynamic forces and moments acting on the submarine. During a maneuvering situation, the cross-flow and nonsymmetric flow over the hull may create a situation in which the submarine can not be safely operated using our present method of ship control. This requires that speed and depth restrictions be imposed on the employment of the submarine.

Presently, submarine control systems are designed by decoupling the vertical and horizontal planes of motion, looking at the individual input/output transfer functions and "shaping" the response as desired. This requires the use of an oversimplified model of a very complex dynamic system. The recent development of the Linear-Quadratic-Gaussian with Loop Transfer Recovery (LQG/LTR) methodology has provided a powerful tool for the design of multivariable control systems. However, as LQG/LTR is relatively new, research is required to investigate the inherent limitations of the methodology and develop practical applications for its use.

Within the last few years, several examples of the practical use of LQG/LTR have been researched. Multiple Input Multiple Output (MIMO)

controllers for gas turbine engines have been developed [1] [2] [3]. Several examples of submarine control systems have also been developed. The submarine controller design by Harris [4] dealt with use of an inverted-Y sternplane configuration. Of particular interest though are the designs of Milliken [5], Dreher [6] and Lively [7]. These designs all used the standard cruciform stern configuration presently in use on U.S. submarines. Milliken's controller was sufficient for depth and course keeping. Acceptable performance during depth and/or heading changes was obtained only for small changes over long periods of time (i.e. small depth and heading rates). Dreher designed two rate controllers. One controlled depthrate and heading rate directly and the other attempted to control these rates by using pitch angle and yawrate. In both cases, acceptable performance was obtained only for small rates.

The design by Lively provided the best example of using the Linear-Quadratic-Gaussian with Loop Transfer Recovery (LQG/LTR) design methodology for submarine control. In an attempt to capture the maneuvering dynamics of the submarine, the linear model for this design used a diving turn for a nominal point. By using linear compensators designed at speeds of 5, 10, 15, 20 and 25 knots, a nonlinear compensator was employed using gain scheduling. This provided for control of the submarine over the speed range of 5 to 25 knots during speed changes as well as at discrete intermediate speeds.

Additionally, Martin [8] has recently shown the merits of active roll control over the conventional cruciform configuration for a submarine at 30 knots. By comparing LQG/LTR controllers with and without differential sternplane deflection capability, better maneuvering characteristics were realized especially in the area of depthkeeping during turns.

1.2 Contributions of the Thesis

The purpose of this thesis is twofold; to develop a practical example of the use of LQG/LTR and to help open an avenue for advancement in the area of submarine ship control systems. It is intended that this thesis be considered a feasibility design showing the promise of using active roll control through differential deflection of the sternplanes and not a final detailed design ready for implementation aboard a submarine. A project of that magnitude is obviously beyond the scope of this thesis due to financial and time considerations.

In comparison to the work of Lively, this thesis shows that using active roll control through differential deflection of the sternplanes eliminates the need for a gain scheduled nonlinear compensator to provide adequate control for speeds of 15 to 30 knots. Further research may even permit this speed range to be expanded.

To show the effects of crossover frequency on the response and stability of the closed loop system, a comparison is made to the compensator designed by Martin [8]. Following this comparison, an Anti-Reset Windup (ARW) feedback loop is employed to counter the effects of integrator windup during control surface saturation.

1.3 Outline of the Thesis

The nonlinear and linear models of the submarine are discussed in Chapter 2. A brief description of the nonlinear equations of motion used for submarine simulation at the Charles S. Draper Laboratory (CSDL) is presented. This is followed by a discussion of the linearized model employed in the design of the LQG/LTR compensator.

Chapter 3 contains an analysis of the linear model. The analysis begins with a reduction in the order of the linear model. Scaling is then applied to provide the designer with a more understandable system of units and to weight the inputs and outputs. Next, the pole/zero structure and eigenvectors of the open loop submarine model are presented. The chapter ends with a discussion of performance requirements and specifications. In this section, the concept of singular values is introduced.

Chapter 4 begins with a discussion of the Model Based Compensator (MBC) concept and the LQG/LTR methodology. The design of the compensator for the linear model is then presented. The chapter ends with a description of the compensator and results of some of the maneuvering simulations.

Chapter 5 begins with a discussion of additional maneuvering simulations for the 15 knot compensator, concentrating on more complex maneuvers. A direct comparison between the compensator designed in this thesis and that designed by Martin [8] is also presented in Chapter 5.

A brief discussion on the use of Anti-Reset Windup feedback to reduce the effects of integrator windup in the presence of saturating actuators is contained in Chapter 6. This is followed by implementation of an Anti-Reset Windup feedback loop in the 15 knot compensator and presentation of some results which demonstrate its effectiveness.

Chapter 7 contains a summary of results, conclusions and some recommendations for future research.

CHAPTER 2

MODELING AND ANALYSIS OF THE SUBMARINE

2.1 Introduction

The design of any control system begins with a mathematical representation of the real world nonlinear system which we want to control. The model used for this thesis was the analytic version of the SUBMODEL submarine simulation computer programs resident on the computer systems at the Charles Stark Draper Laboratory (CSDL).

The chapter begins with a brief description of the nonlinear model and relevant computer programs. This is followed by a description of the 15 knot linear model using differential deflection of the sternplanes to provide the necessary degree of freedom to actively control the roll angle of the submarine.

2.2 Description of the Nonlinear Submarine Model

Motion of the submarine is described in six degrees of freedom, three translational and three rotational. Three force equations (X, Y and Z) define the translational motions of surge (axial), sway (lateral) and heave (normal). The rotational motions of roll, pitch and yaw are described by three moment equations (K, M and N).

The complex hydrodynamic forces and moments which act on a submerged submarine are best defined in a right-hand orthogonal coordinate system fixed in the body. Figure 2.1 shows this coordinate system (and sign

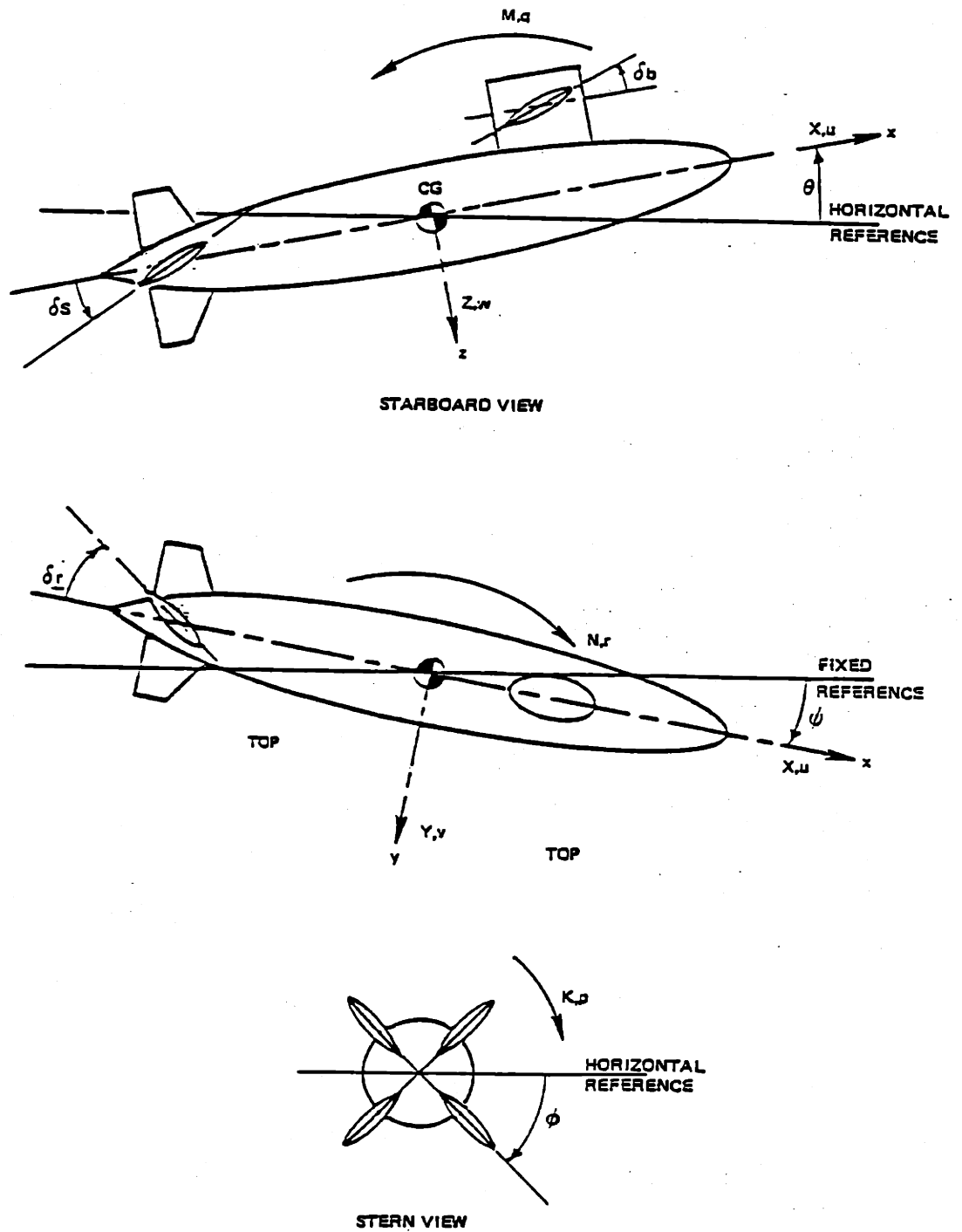


Figure 2.1 Body-Fixed Coordinate System for a Submarine

convention) with the origin at the center of gravity (CG). The equations of motion are more easily derived in and control of the submarine requires knowledge of the submarine's motion (i.e. course, speed, depth and orientation) with respect to an inertial or earth-fixed coordinate system. The earth-fixed system is also a right-handed orthogonal system, but is fixed at some geographic point on the surface of the water. The orientation and motion of the submarine in these two reference frames are related by Euler angles [9], each representing a rotation about a body-fixed axis. By convention, the rotations are applied in the following order.

1. Ψ (rotation about the z-axis)
2. θ (rotation about the y-axis)
3. ϕ (rotation about the x-axis)

From the discussion above, it is evident that we are talking about nine state variables, six representing the translational and rotational velocities in the body-fixed reference frame and three representing the orientation of the body-fixed axes with respect to earth reference. The submarine's depth represents a tenth state variable. Control of the submarine is accomplished by deflecting the rudder, stern planes, fairwater planes and/or changing propeller speed.

The SUBMODEL simulation facilities at CSDL are based on the "2510 Equations" [10], updated with the cross-flow terms of the "Revised Equations" [11]. Several additional features have been added to provide a constant RPS constraint on the propeller and a differential deflection option for the sternplanes. The constant RPS constraint reflects the current operating policy used on submarines. The use of differential

sternplane deflection provides an avenue for active roll control that is not otherwise possible. Table 2.1 contains a summary of state and control variables.

State Variables

$u = X_1$, axial velocity (along x axis) - ft/sec

$v = X_2$, lateral velocity (along y axis) - ft/sec

$w = X_3$, heave velocity (along z axis) - ft/sec

$p = X_4$, roll rate (angular velocity about x axis) - rad/sec

$q = X_5$, pitch rate (angular velocity about y axis) - rad/sec

$r = X_6$, yaw rate (angular velocity about z axis) - rad/sec

$\phi = X_7$, roll (rotation about x axis) - radians

$\theta = X_8$, pitch (rotation about y axis) - radians

$\psi = X_9$, yaw (rotation about z axis) - radians

$z = X_{10}$, depth - feet

Control Variables

$db = u_1$, fairwater plane deflection - radians

$dr = u_2$, rudder deflection - radians

$ds_1 = u_3$, port stern plane deflection - radians

$ds_2 = u_4$, starboard stern plane deflection - radians

Table 2.1 State and Control Variables

It should be noted that these equations of motion do not account for actuator dynamics. This will be addressed further in the discussion of performance requirements in Section 3.5. Intuitively, one would expect the dynamics of the submarine to be independent of the depth (z) and the

heading angle (ψ). This will prove true as we will see in the next section.

The SUBMODEL program provides the following analytic capabilities:

1. Integration of the nonlinear equations of motion
2. Determination of a local equilibrium point in the nonlinear equations
3. Calculation of the linearized dynamics about the equilibrium point
4. Integration of the linearized equations of motion

During integration of the equations of motion, the control surface deflections may be set to initial values, varied as a function of time or calculated using full state feedback or the dynamic compensation derived using the LQG/LTR method. The analytical results of the integration may be output graphically, in tabular form or both. A full description of the submarine model may be found in [12] through [15].

2.3 Description of the Linear Submarine Model

The compensator design procedure is based on a Linear Time Invariant (LTI) model of the nonlinear system. The nonlinear equations described in Section 2.2 can be generally put in the form

$$\dot{\underline{x}}(t) = \underline{f}[\underline{x}(t), \underline{u}(t)] \quad (2.1)$$

$$\underline{y}(t) = \underline{g}[\underline{x}(t)] \quad (2.2)$$

where

$\underline{x}(t)$ is the state vector

$\underline{u}(t)$ is the control input vector

$y(t)$ is the output vector

These equations can then be linearized about some nominal point (x_0, u_0) by using a Taylor Series expansion. Neglecting the higher order terms of the expansion, the linear dynamics may be expressed in the state space form

$$\dot{x}(t) = A x(t) + B u(t) \quad (2.3)$$

$$y(t) = C x(t) \quad (2.4)$$

where

$$A = \left(\frac{\partial f}{\partial x} \right) \Big|_{x_0, u_0}$$

$$B = \left(\frac{\partial f}{\partial u} \right) \Big|_{x_0, u_0}$$

$$C = \left(\frac{\partial g}{\partial x} \right) \Big|_{x_0}$$

The nominal point used here corresponds to a local equilibrium point. This point is found by integrating the nonlinear equations of motion for a specific set of initial conditions. At their steady-state value, each state variable is then perturbed so that its local minimum is found.

Since the linear dynamics change with different nominal points, the question arises as to what is the "correct" nominal or operating point about which to linearize. Selection of a "benign" nominal point such as that by Milliken [5] is probably satisfactory for an "autopilot" type of controller. This controller however, will be used for maneuvering as well as course and depth keeping. For this reason, a nominal point which "captures" the maneuvering dynamics of the submarine is required. To achieve this, the submarine must be oriented such that it experiences crossflow over the hull such like it would encounter while simultaneously turning and diving.

The nominal point used in this thesis was determined using an initial forward velocity (surge) of 15 knots with a rudder deflection of 1 degree. This model is named S15R1 to reflect the speed and rudder deflection. This nominal point was selected so the linear model would have dynamics similar to that used by Martin [8] and provide a basis for comparison. The nominal point provides sufficient cross-coupling between the horizontal and vertical planes of motion to capture the desired maneuvering characteristics but is not too "radical". As a result, acceptable performance was obtained for straight and level as well as maneuvering trajectories. Figure 2.2 shows the excellent agreement between the time response of the linear and nonlinear models. The A and B matrices and values of the nominal states may be found in Appendix A1. Inspection of the last two rows of these matrices indicate that our intuition about the effect of z and ψ on the other states was correct. This will be of value when we consider reducing the order of the system.

To determine the range of accuracy of the linear model, it can be perturbed from its nominal point by a set of initial conditions, integrated and then compared to the nonlinear system for the same set of initial conditions. Figure 2.3 shows the results of the initial condition perturbation of 20% above the nominal point. The perturbations are summarized in Table 2.2.

u = 5.08 ft/sec
v = 0.150 ft/sec
w = 0.395E-02 ft/sec
p = -.115E-04 rad/sec
q = 0.352E-04 rad/sec
r = -.125E-02 rad/sec
 ϕ = -.325 deg
 θ = -.105 deg

Table 2.2 20% Perturbations Applied to S15R1

2.4 Selection of the Output Variables

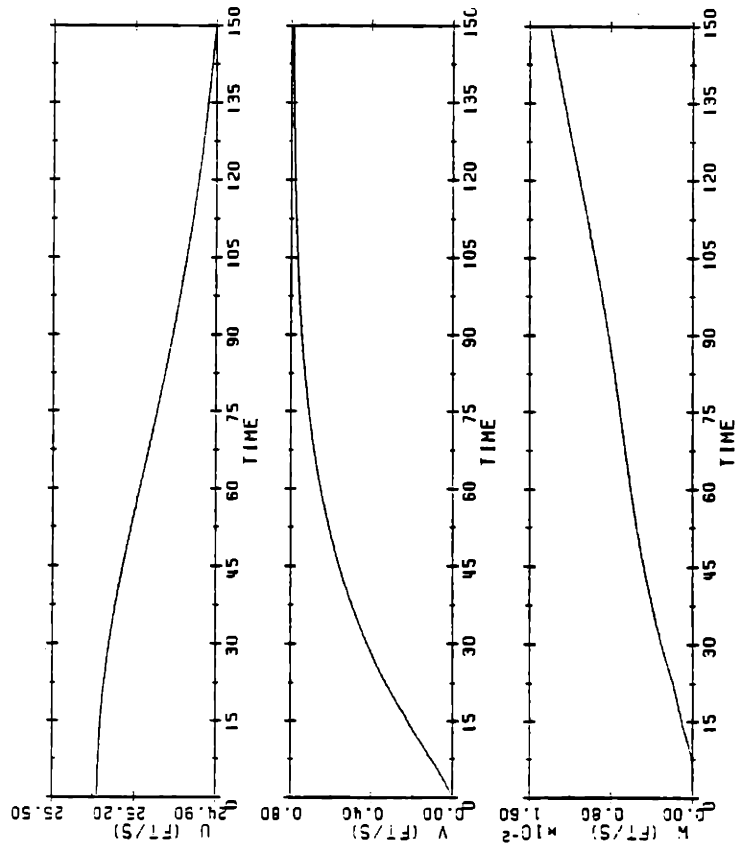
Several factors must be considered in the selection of the output variables. First and foremost is the intent of the controller and the inherent capabilities of the system to be controlled. For example, an attempt to control roll angle without using differential sternplane deflection cannot possibly succeed.

Next, a constraint of the methodology is that the dimension of the output vector must equal the dimension of the control input vector [16]. Since there are four control inputs (db, dr, ds1, ds2), there must be four system outputs.

Finally, the effect of each control input "felt" at the output must be considered. Two states may have influence on the results the designer is trying to affect. The state which requires the least control surface deflection to achieve the desired results is the better one to use since it will require less energy, result in lower compensator gains and reduce the chance of saturating the inputs.

VELOCITIES

NONLINEAR INTEGRATION USING 1 DEG RUDDER AT 15 KNOTS



VELOCITIES

LINEAR INTEGRATION USING 1 DEG RUDDER

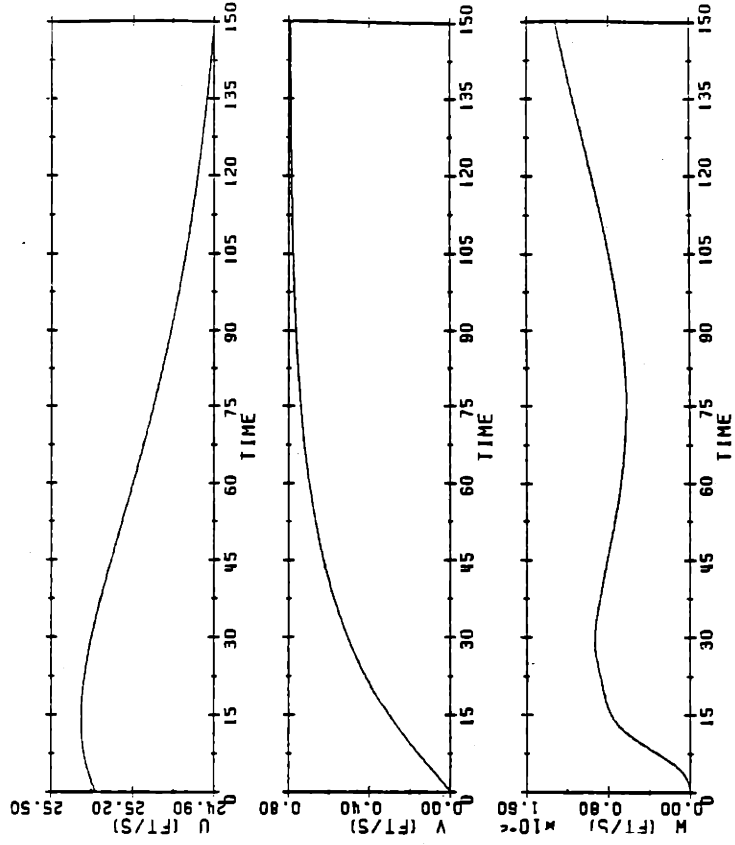
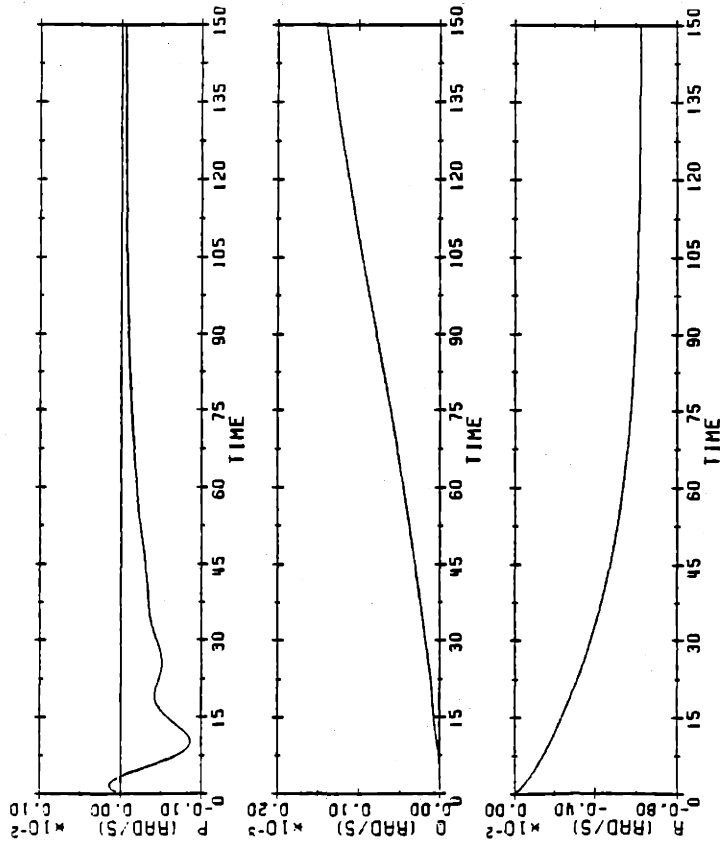


Figure 2.2 Comparison of Nonlinear and Linear Dynamics for Model S15R1

ANGULAR VELOCITIES

NONLINEAR INTEGRATION USING 1 DEG RUDDER AT 15 KNOTS



ANGULAR VELOCITIES

LINEAR INTEGRATION USING 1 DEG RUDDER

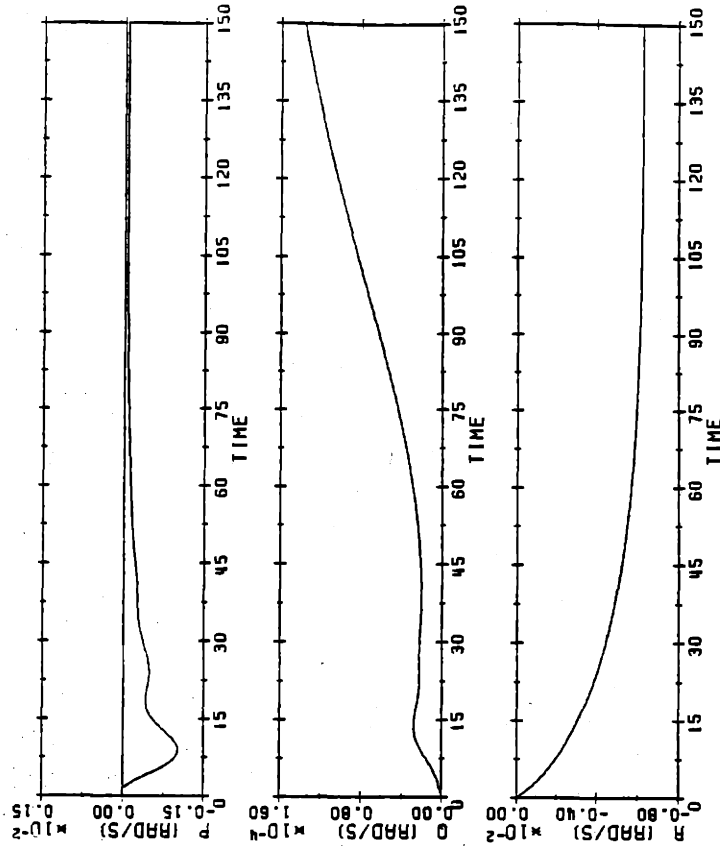
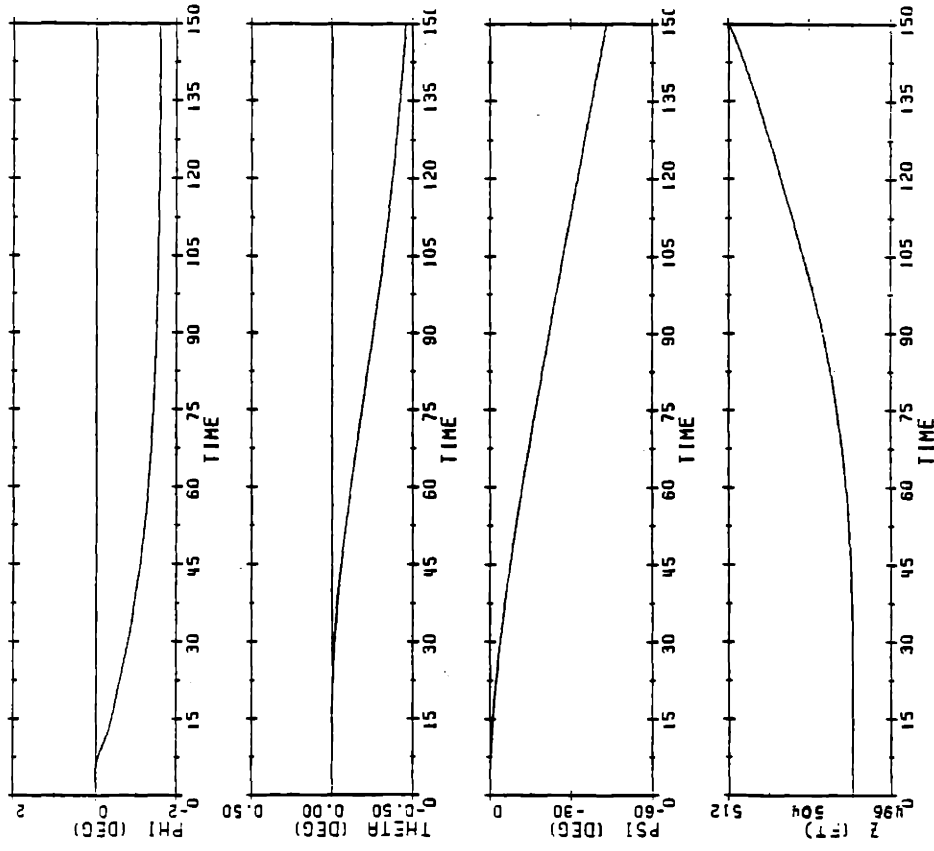


Figure 2.2 Comparison of Nonlinear and Linear Dynamics for Model S15R1

ATTITUDE AND DEPTH

NONLINEAR INTEGRATION USING 1 DEG RUDDER AT 15 KNOTS



ATTITUDE AND DEPTH

LINEAR INTEGRATION USING 1 DEG RUDDER

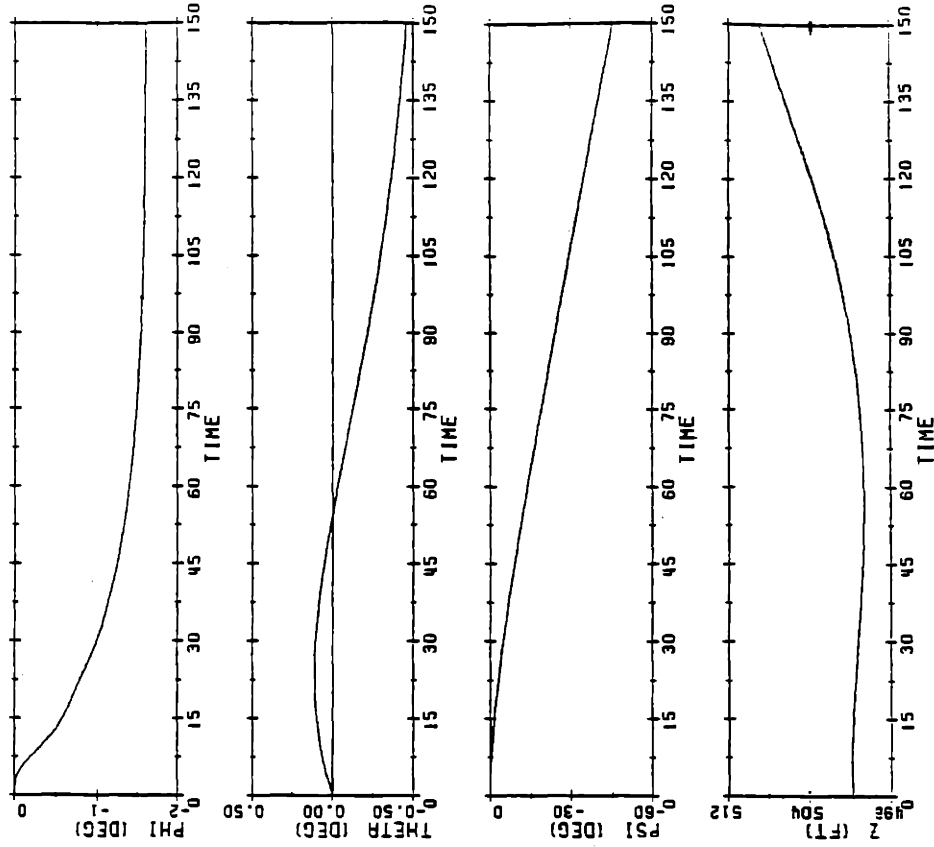
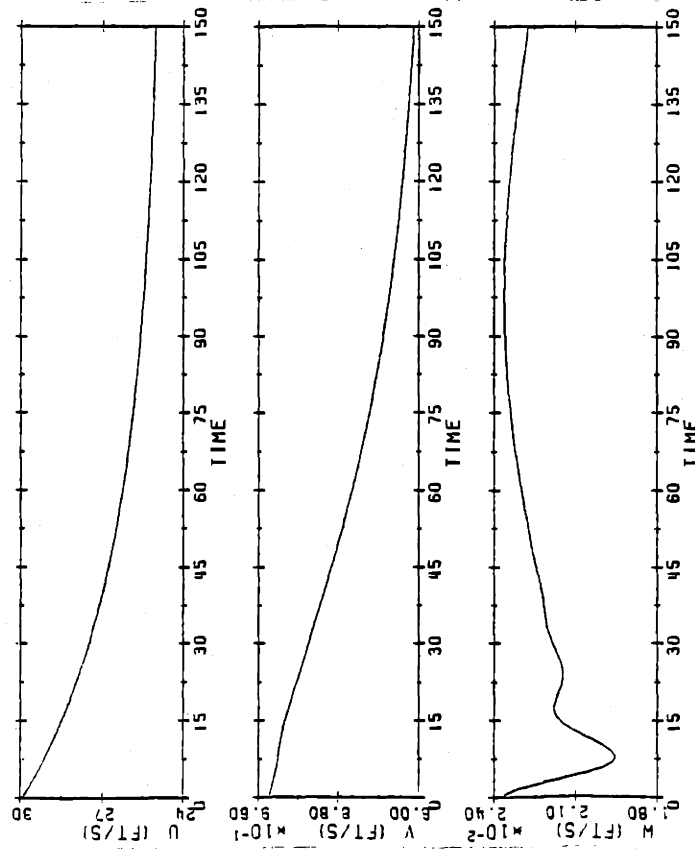


Figure 2.2 Comparison of Nonlinear and Linear Dynamics for Model S15R1

VELOCITIES

NONLINEAR INTEGRATION USING 20% PERTURBATION ABOVE NOMINAL



VELOCITIES

LINEAR INTEGRATION WITH 20% PERTURBATION ABOVE NOMINAL

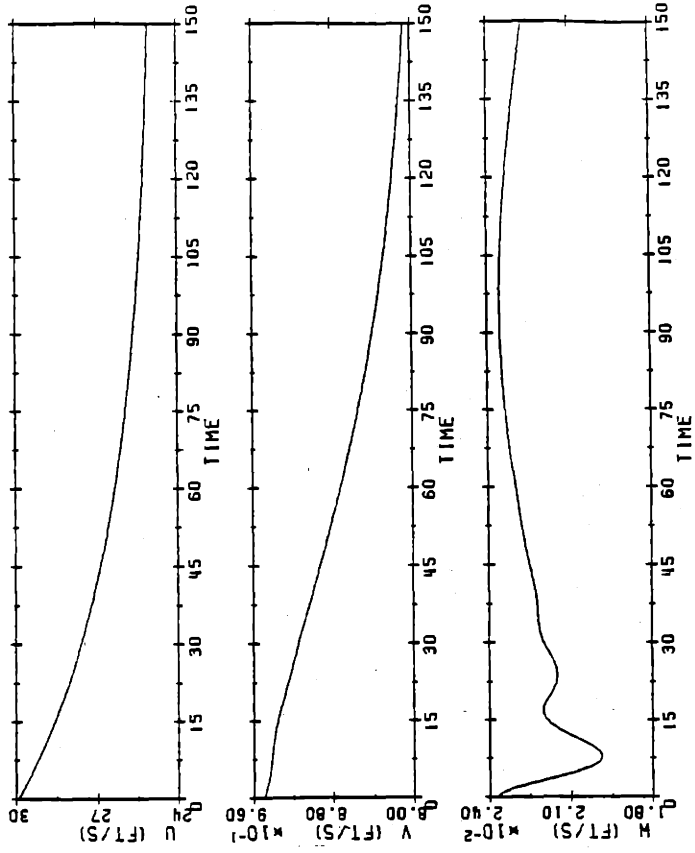


Figure 2.3 Comparison of Nonlinear and Linear Response 20% Perturbation Above Nominal Point

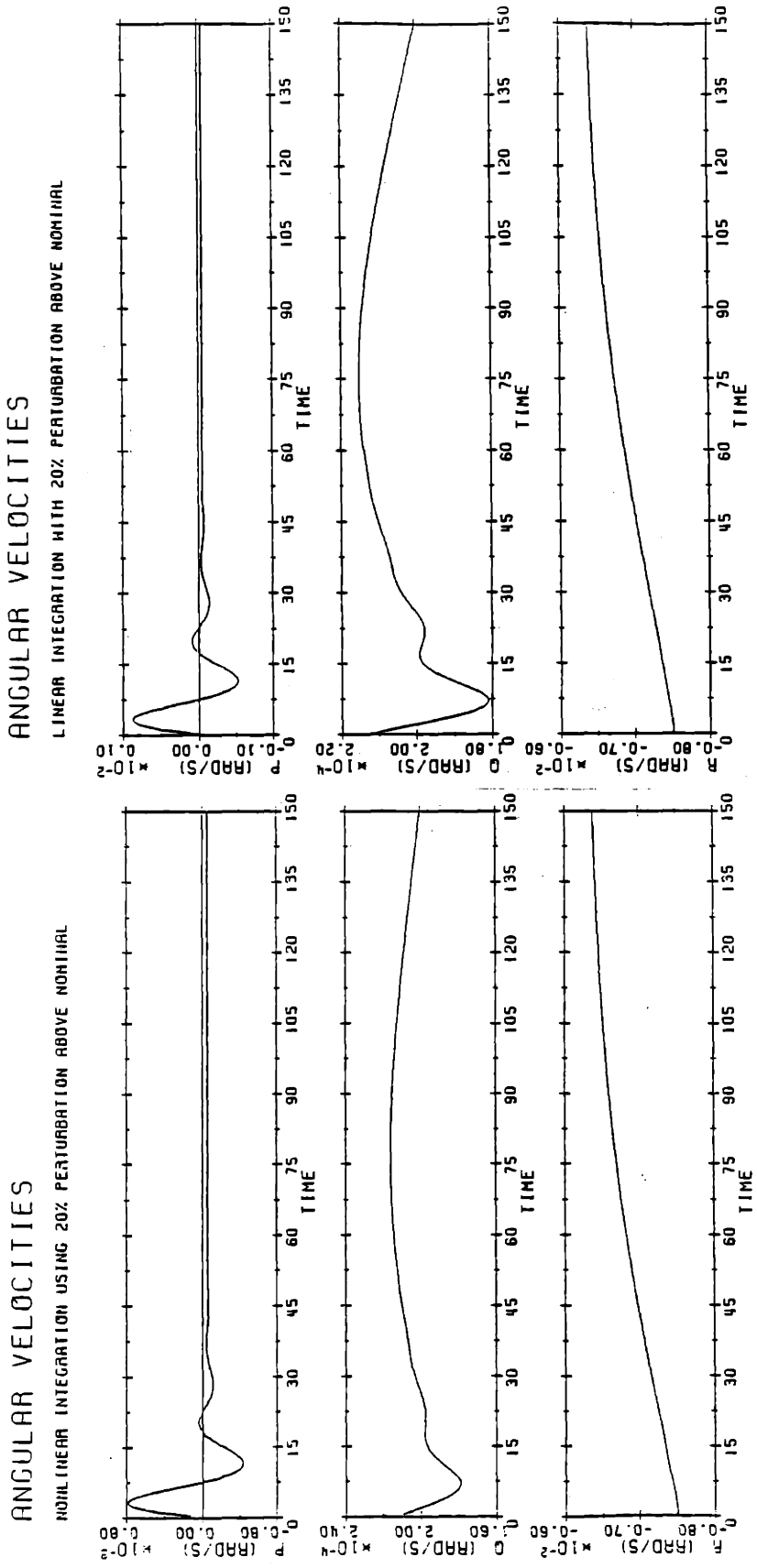
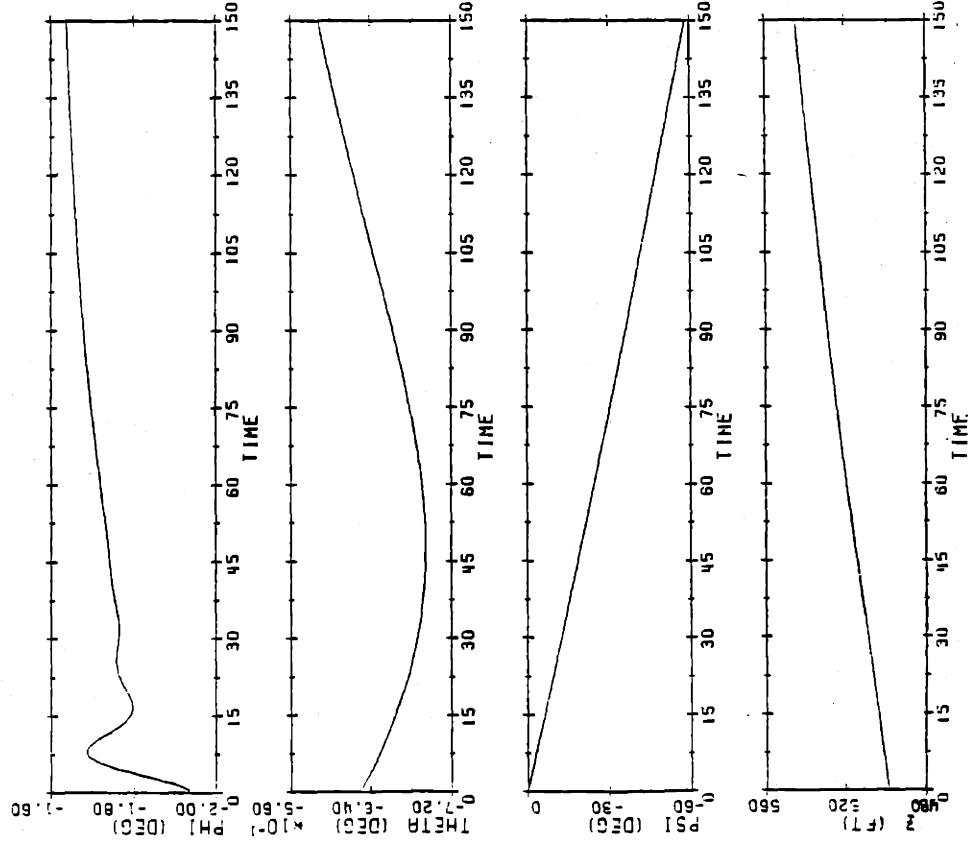


Figure 2.3 Comparison of Nonlinear and Linear Response 20% Perturbation Above Nominal Point

ATTITUDE AND DEPTH

NONLINEAR INTEGRATION USING 20% PERTURBATION ABOVE NOMINAL



ATTITUDE AND DEPTH

LINEAR INTEGRATION WITH 20% PERTURBATION ABOVE NOMINAL

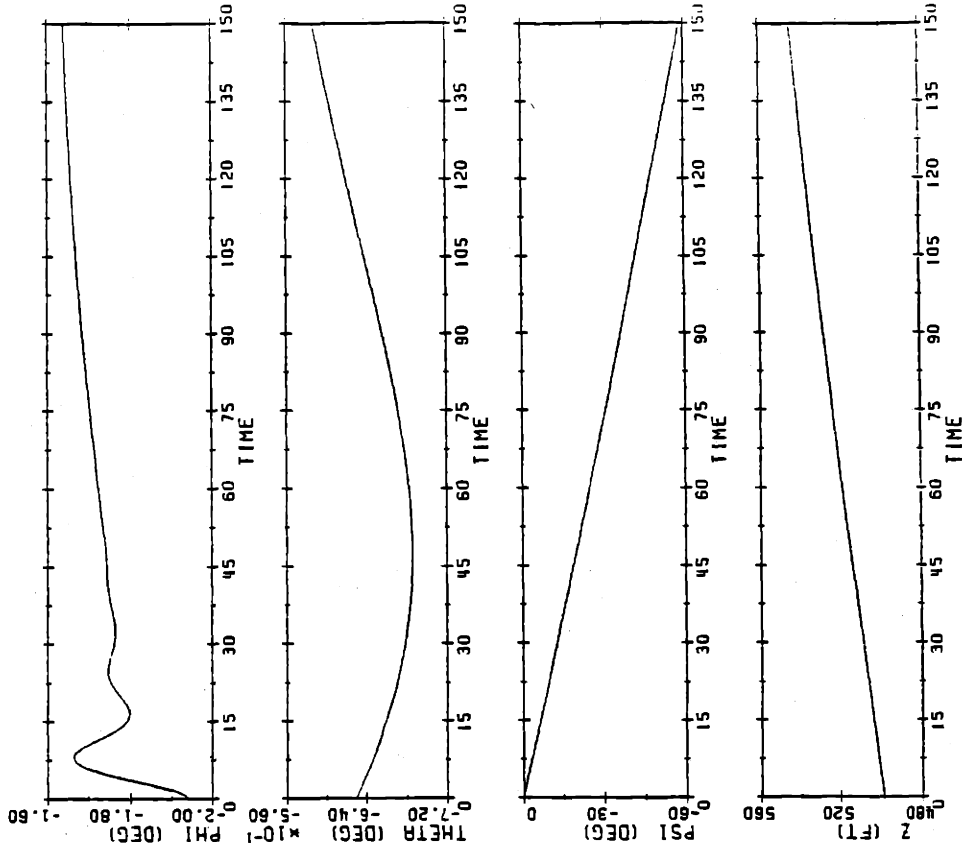


Figure 2.3 Comparison of Nonlinear and Linear Response 20% Perturbation Above Nominal Point

A submarine is presently maneuvered by deflecting the control surfaces until a particular turning rate, depth rate or attitude is achieved. Knowing the handling characteristics of the submarine, the operators maintain the rates until a predetermined point when the surfaces are deflected to counteract the rates which have developed. If done correctly, the submarine will "meet" the desired course and/or depth with little or no overshoot. For this reason, the yaw rate $\dot{\psi}$ and depth rate \dot{z} will be used as output variables.

The attitude of the submarine in pitch and roll strongly affects its performance. As the pitch angle becomes excessive, it becomes increasingly difficult to maintain depth or control depth rate because the fairwater planes saturate. As roll angle increases, the forces generated by the control surfaces act out of the plane they were meant to. To visualize this problem imagine the submarine rolling 90°. At this point, the rudder will act as a sternplane and the sternplanes as rudders. Additionally, the force and moment generated by crossflow over the sail is quite significant and contributes to roll and pitch. These illustrations show the importance of roll ϕ and pitch θ .

For this thesis then, the output vector $y(t)$ is given by

$$y(t) = [\phi(t) \quad \theta(t) \quad \dot{\psi}(t) \quad \dot{z}(t)]^T \quad (2.5)$$

where

$$\dot{\psi}(t) = -u \sin \theta + v \cos \theta \sin \phi + w \cos \theta \cos \phi \quad (2.6)$$

$$\dot{z}(t) = (r \cos \phi + q \sin \theta) / \cos \theta \quad (2.7)$$

The linearized equations for $\dot{\psi}$ and \dot{z} are easily derived from the state space equation (2.3). The elements of the \underline{C} matrix which represent $\dot{\psi}$ and \dot{z} are simply the last 2 rows of the \underline{A} matrix.

2.5 Summary

This chapter has briefly described the origin of the nonlinear model and the linearization process. The state space form of the linear model and the reasoning behind selection of the output variables were also presented. Chapter 3 will cover model reduction, scaling, the eigenstructure of the linear model and performance specifications.

CHAPTER 3

LINEAR MODEL ANALYSIS

3.1 Introduction

This chapter begins with a reduction of the tenth-order model and discussion of the scaling. Next, the eigenstructure and pole/zero structure of the reduced model will be presented. Finally, system performance in the area of steady state error and crossover frequency will be discussed. In the section on performance, the concept of singular values and their use will be introduced. The reader already familiar with the concept and its application to MIMO control system design may wish to skip to the last paragraph of that section for a summary of the performance specifications applicable to this design.

3.2 Reduction of the Model

As noted in Section 2.3, the depth and heading angle (yaw) have no effect on the dynamic response of the other eight states. This may be verified by inspection of the last two columns of the A matrix in Appendix A1. Had the assumption of a deeply submerged submarine not been made, one would expect depth and heading to have a significant effect on the states due to near-surface suction forces and direction of the seas. Additionally, inspection of the last four rows of the B matrix reveals that the control surfaces have no direct effect on ψ , θ , ϕ or z .

Since this controller does not use ψ or z as outputs and the other states are not functions of these variables, they may be deleted from the model. This is accomplished by deleting the last two columns of the A matrix and the last two rows of the A and B matrices. As we will see in Chapter 4, this will also reduce the order of the compensator state vector.

3.3 Scaling

The use of scaling has been employed to change the state and control variables of the linear system into units which are more easily understood and to provide weighting on the inputs and outputs of the system. Kappos [2] and Boettcher [17] have addressed scaling and its effects. Obviously, the singular values of the system will be changed but the effect on system robustness is not fully understood.

To provide the designer with a more easily understood system of units, rotational or angular variables are expressed in units of degrees and degrees per second vice radians and radians per second. Translational variables remain in units of feet and feet per second.

The unscaled state space system as expressed in equations (2.3) and (2.4) is scaled by defining new state, control and output vectors where

$$\begin{aligned} \underline{x}' &= \underline{S}_x \underline{x} \\ \underline{u}' &= \underline{S}_u \underline{u} \\ \underline{y}' &= \underline{S}_y \underline{y} \end{aligned} \tag{3.1}$$

The scaling matrices \underline{S}_x , \underline{S}_u and \underline{S}_y are diagonal matrices whose elements provide the desired transformation of units. Consequently, the system matrices (scaled for units) become

$$\begin{aligned}
\mathbf{A}' &= \mathbf{S}_x \mathbf{A} \mathbf{S}_x^{-1} \\
\mathbf{B}' &= \mathbf{S}_x \mathbf{B} \mathbf{S}_u^{-1} \\
\mathbf{C}' &= \mathbf{S}_y \mathbf{C} \mathbf{S}_x^{-1}
\end{aligned}
\tag{3.2}$$

Details of the unit transformation scaling matrices and scaled system matrices may be found in Appendix A2.

Now that the system has been scaled for units, we must consider scaling the outputs and inputs to reflect their relative importance. These weights were selected to coincide with those for a compensator being concurrently developed by Martin [8]. Weights were selected for the outputs such that yaw rate and depth rate were more important than roll and pitch and are given by

$$\tilde{\mathbf{S}}_y = \begin{bmatrix} .1 & & & \\ & .1 & & \\ & & 1 & \\ & & & 1 \end{bmatrix}$$

Input weights were selected by comparing the maximum deflection of each control surface. Rate and deflection limits are listed in Table 3.1.

<u>Control</u>	<u>Rate Limit</u>	<u>Deflection Limit</u>
d_b	7 deg/sec	± 20 degrees
d_r	4 deg/sec	± 30 degrees
d_{s1}, d_{s2}	7 deg/sec	± 25 degrees

Table 3.1 Control Surface Rate and Deflection Limits

For this thesis, the control surface dynamics (deflection rates) will be treated as high frequency modeling error. Considering the deflection limits above, the selected input scaling is given by

$$\tilde{S}_{11} = \begin{bmatrix} 1 & & & \\ & 0.567 & & \\ & & 0.8 & \\ & & & 0.8 \end{bmatrix}$$

Figure 3.1 shows the block diagram representation of the system after applying the scaling for units and input/output weights.

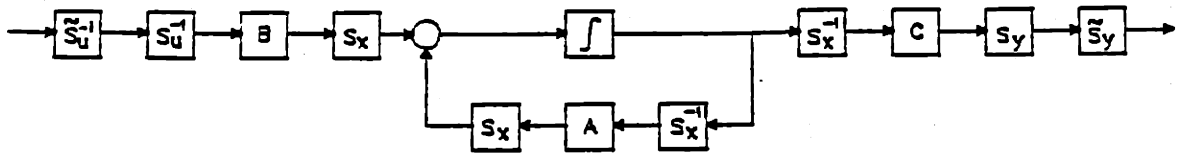


Figure 3.1 Block Diagram Representation After Scaling

The effect of scaling on the plant transfer function matrix is given by

$$\underline{G}'(s) = \tilde{S}_y \underline{S}_y \underline{G}(s) \underline{S}_{11}^{-1} \tilde{S}_{11}^{-1} \quad (3.3)$$

where $\underline{G}(s)$ is the plant transfer function matrix prior to any scaling. The input and output scaling as well as the unit transformation is identical to that used by Martin [8] so that a better comparison of the two compensators may be made (presented in Chapter 5). A summary of the plant matrices after scaling can be found in Appendix A3.

3.4 Eigenstructure

To examine the modes of the state space system defined by (2.3) and (2.4), the linear transformation (3.4) is applied to the state vector where

$$\underline{x}(t) = \underline{p} \underline{z}(t) \quad (3.4)$$

the matrix \underline{P} is the constant and nonsingular matrix of eigenvectors \underline{P}_{1i} through \underline{P}_{ni} as defined in (3.5). The new state space (3.6) representation

$$\underline{P} = \left[\begin{array}{c|c|c|c|c} \underline{P}_{1i} & \underline{P}_{2i} & \underline{P}_{3i} & \dots & \underline{P}_{ni} \end{array} \right] \quad (3.5)$$

$$\dot{\underline{z}}(t) = \underline{P}^{-1} \underline{A} \underline{P} \underline{z}(t) + \underline{P}^{-1} \underline{B} \underline{u}(t)$$

$$\underline{y}(t) = \underline{C} \underline{I} \underline{z}(t) \quad (3.6)$$

consists of n decoupled equations describing the modal response of the system. The matrix $\underline{P}^{-1} \underline{A} \underline{P}$ is a diagonal matrix whose elements are the eigenvalues of the state space. Each eigenvector describes the motion of its associated submarine mode along the coordinate axes of the 8-dimensional \underline{A} matrix. Since the dynamic response of the submarine is a linear combination of these modal responses, useful information may be obtained by analyzing the contribution of each state to a particular mode.

Figure 3.2 shows the state breakdown of each normalized eigenvector and its associated eigenvalue in bar chart form. The vertical scale of 0.0 to 1.0 has been selected to reflect the percent contribution of each state to the overall magnitude of the eigenvector. Due to the difference in variables and units (translational and rotational), cross-coupling between terms and the complex nature of the dynamics involved, a clear cut physical explanation of all the modes is not always possible. Several modes do however exhibit clear physical meaning leading to the following interpretation.

- (1) Modes 1 and 2 are a complex conjugate pair representing the oscillatory nature of pitch.

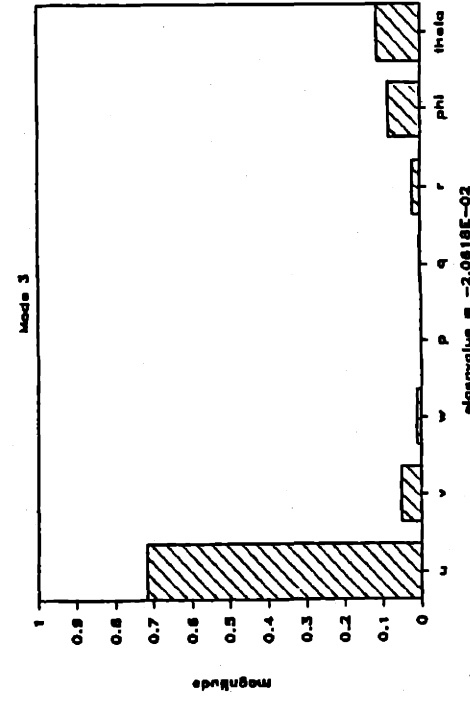
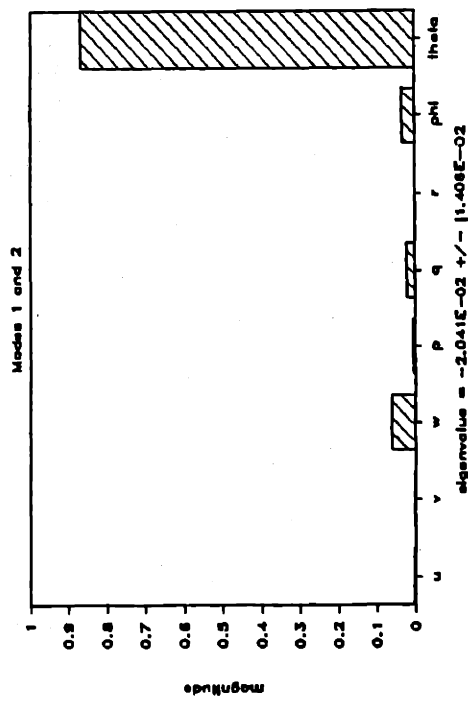
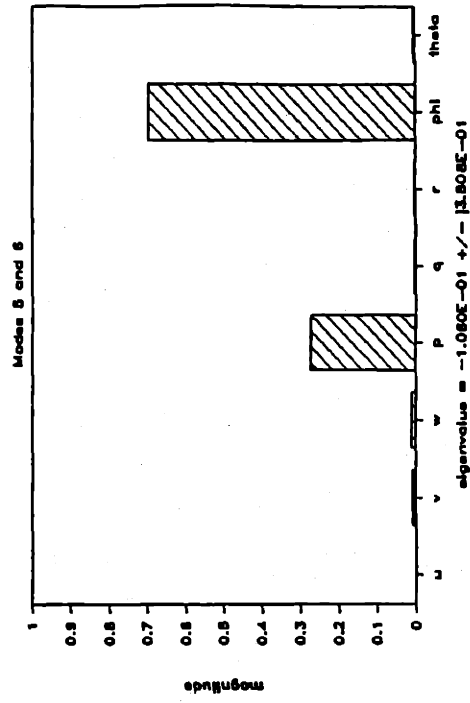
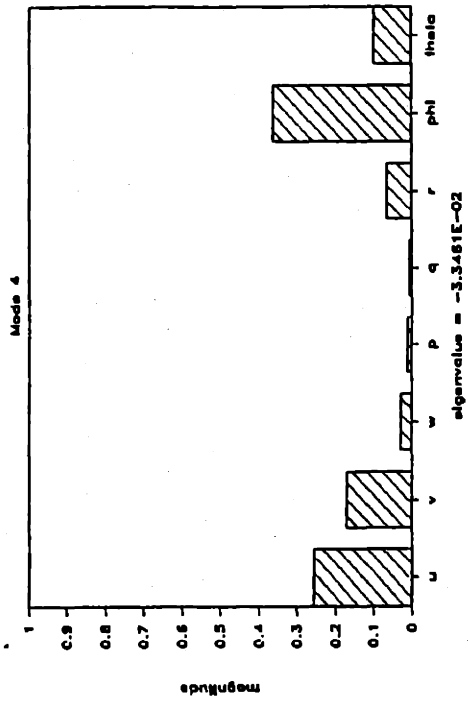


Figure 3.2 Breakdown of S15R1 Modes by State

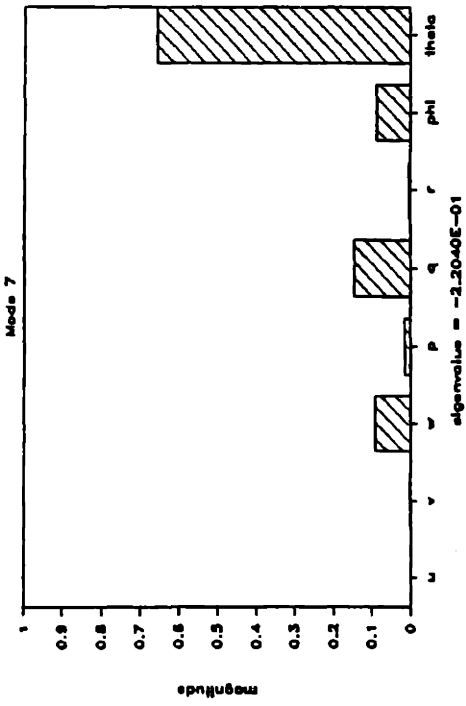
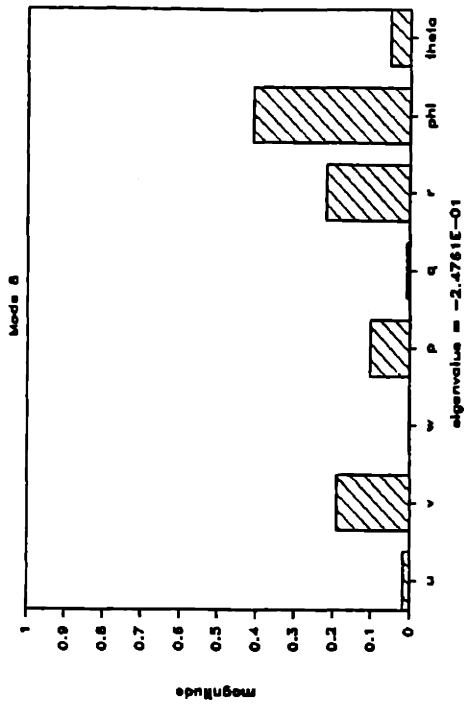


Figure 3.2 Breakdown of S15R1 Modes by State

- (2) Mode 3 is heavily dependent on forward speed and is therefore most likely related to drag.
- (3) Modes 5 and 6 are a complex conjugate pair representing the oscillatory nature of roll.
- (4) The submarine is open loop stable since all poles are in the left half plane (LHP).

The eigenvalues, eigenvectors (modal matrix) and transmission zeros for the linear model are presented in Appendix B1.

System stabilizability (unstable modes are controllable) and detectability (unstable modes are observable) can also be addressed by simple inspection of the $\underline{T}^{-1} \underline{B}$ and $\underline{C} \underline{T}$ matrices in Appendix B2. The elements of these matrices represent the link between the original state space system and the decoupled system and a zero element in one of these matrices would indicate that the link is not present. The breakdown of the controllability matrix in Figure 3.3 shows the relative impact of the control inputs on each mode. Similarly, the observability matrix represents the relative contribution of each mode to the system output variables. When used in conjunction with the eigenvector breakdown, additional physical information can be gained about the system dynamics.

Inspection of Figure 3.3 reveals that Modes 1 and 2 which represent pitch of the submarine are mostly affected by the fairwater planes and sternplanes. The dominance of Mode 3 by rudder deflections explains the reason for the large dependence of Mode 3 on forward velocity. All control surface deflections cause a loss in forward speed due to added drag. The rudder, being the largest control surface, has significant effect even for small deflections. Mode 4 which has no real dominant state is also most

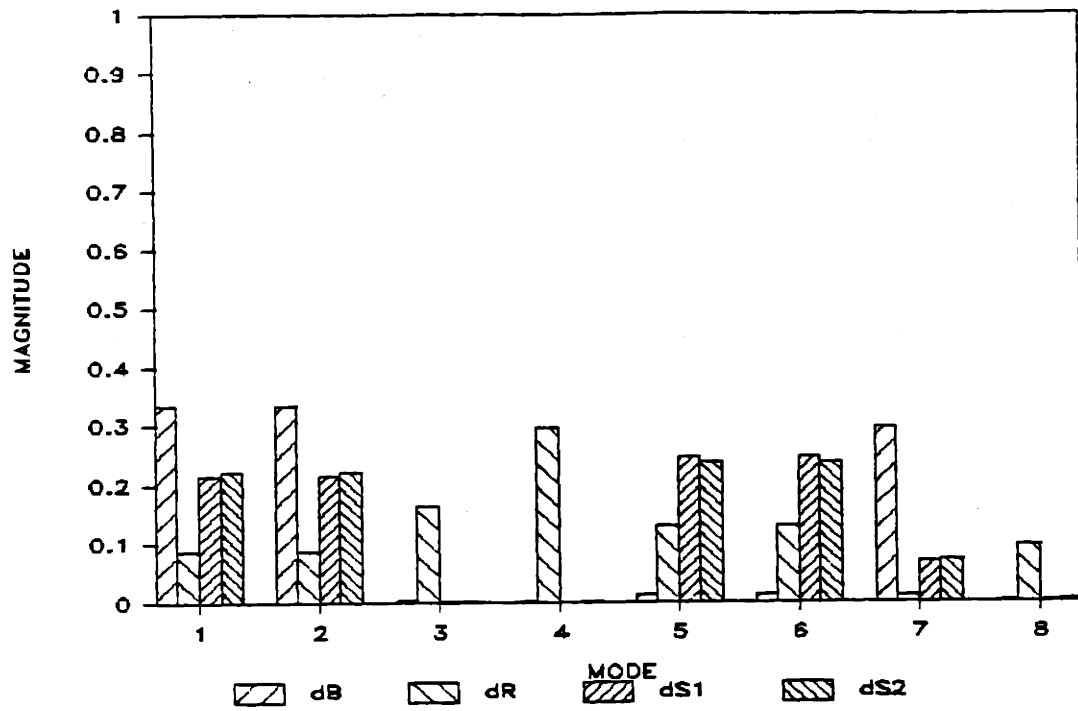


Figure 3.3 Effect of Control Surfaces by Mode

affected by rudder deflection. Since roll angle is a major contributor to this mode followed closely by forward speed, this probably represents the speed loss and roll angle induced by the crossflow over the sail of a turning submarine. Modes 5 and 6 which represent the roll characteristics of the submarine are dominated by the sternplanes with a smaller contribution from the rudder. Obviously, the differential deflection of the sternplanes will affect roll. The effect of the rudder on roll has already been mentioned. Mode 7 which is dominated by pitch with lesser contributions from pitch-related states is mostly controlled by the fairwater planes. No clear interpretation of the rudder deflections which control Mode 8 is possible.

To provide an indication of the coupling between control inputs and output variables, a singular value decomposition of the plant transfer function $\underline{G}(s)$ is presented. Details of the theory behind singular value decomposition may be found in Athans [16] and Lehtomaki [18]. The plant transfer function matrix is given by

$$\underline{G}(s) = \underline{C} (s\underline{I} - \underline{A})^{-1} \underline{B} = \underline{U} \underline{E} \underline{V}^H$$

where

\underline{U} is the matrix of left singular vectors

\underline{E} is a diagonal matrix of the singular values

\underline{V}^H is the matrix of right singular vectors

and at $s = 0$ by

$$\underline{G}(0) = \underline{C} (-\underline{A})^{-1} \underline{B}$$

Therefore, since

$$\underline{y}(t) = \underline{G}(0) \underline{u}(t) = \underline{U} \underline{E} \underline{V}^H \underline{u}(t)$$

we can define

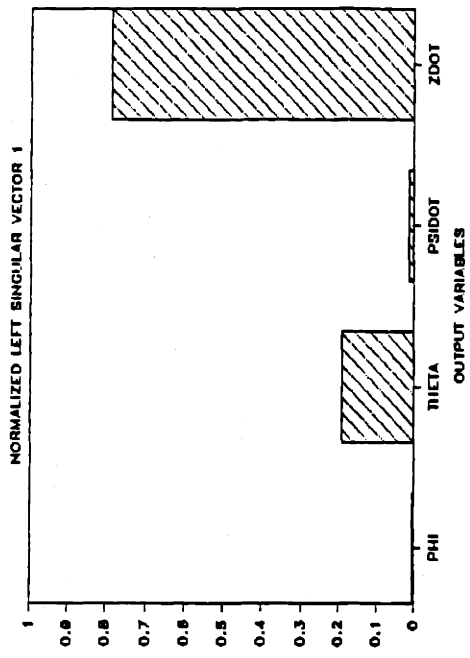
$$\underline{y}'(t) = \underline{E} \underline{u}'(t)$$

where

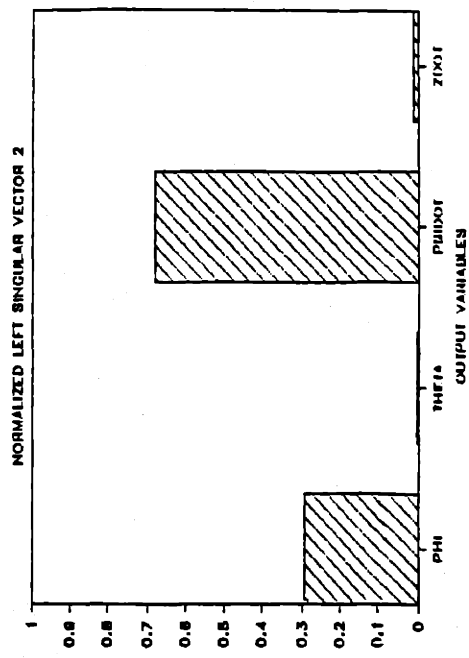
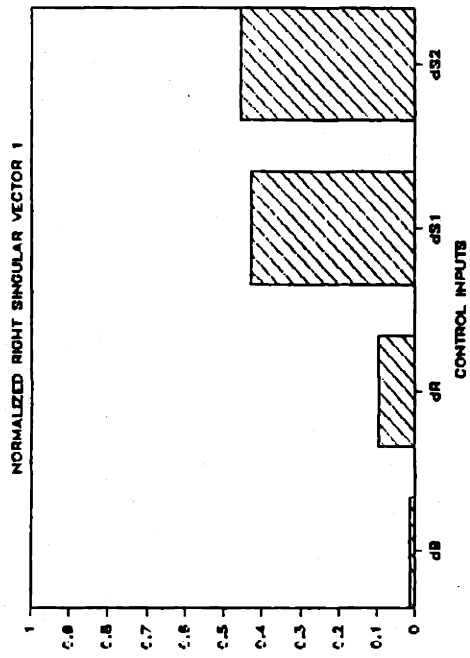
$$\underline{y}'(t) = \underline{U}^{-1} \underline{y}(t)$$

$$\underline{u}'(t) = \underline{V}^H \underline{u}(t)$$

Since \underline{E} is a diagonal matrix, a direct comparison of the left and right singular vectors for each singular value will yield the desired information about input/output coupling. The left and right singular vectors for each singular value are presented in Figure 3.4. For σ_{11} , we see that deflection of the sternplanes results in the coupled response in pitch angle and depthrate. Intuitively, one would think that sternplanes would affect pitch more than depthrate. One explanation is that these variables are strongly coupled but have different units. As is obvious from σ_{22} , deflection of the rudder affects primarily \dot{z} but does exhibit some effect on roll angle. This is a reflection of the effect of rudder movement and should not be interpreted as a feasible way to control roll angle. The effect of differential deflection of the sternplanes is exhibited by σ_{33} . As shown by σ_{44} , deflection of the fairwater planes affects primarily pitch and depthrate to a somewhat lesser extent. Again, the difference in variables and coupling between pitch and depthrate is the probable reason for this behavior.



$$\sigma_1 \rightarrow 2.79E+00$$



$$\sigma_2 \rightarrow 3.55E-01$$

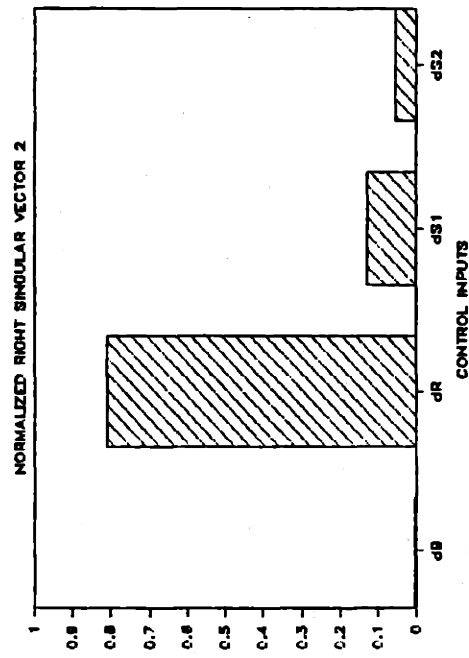


Figure 3.4 Singular Value Decomposition of S1SR1

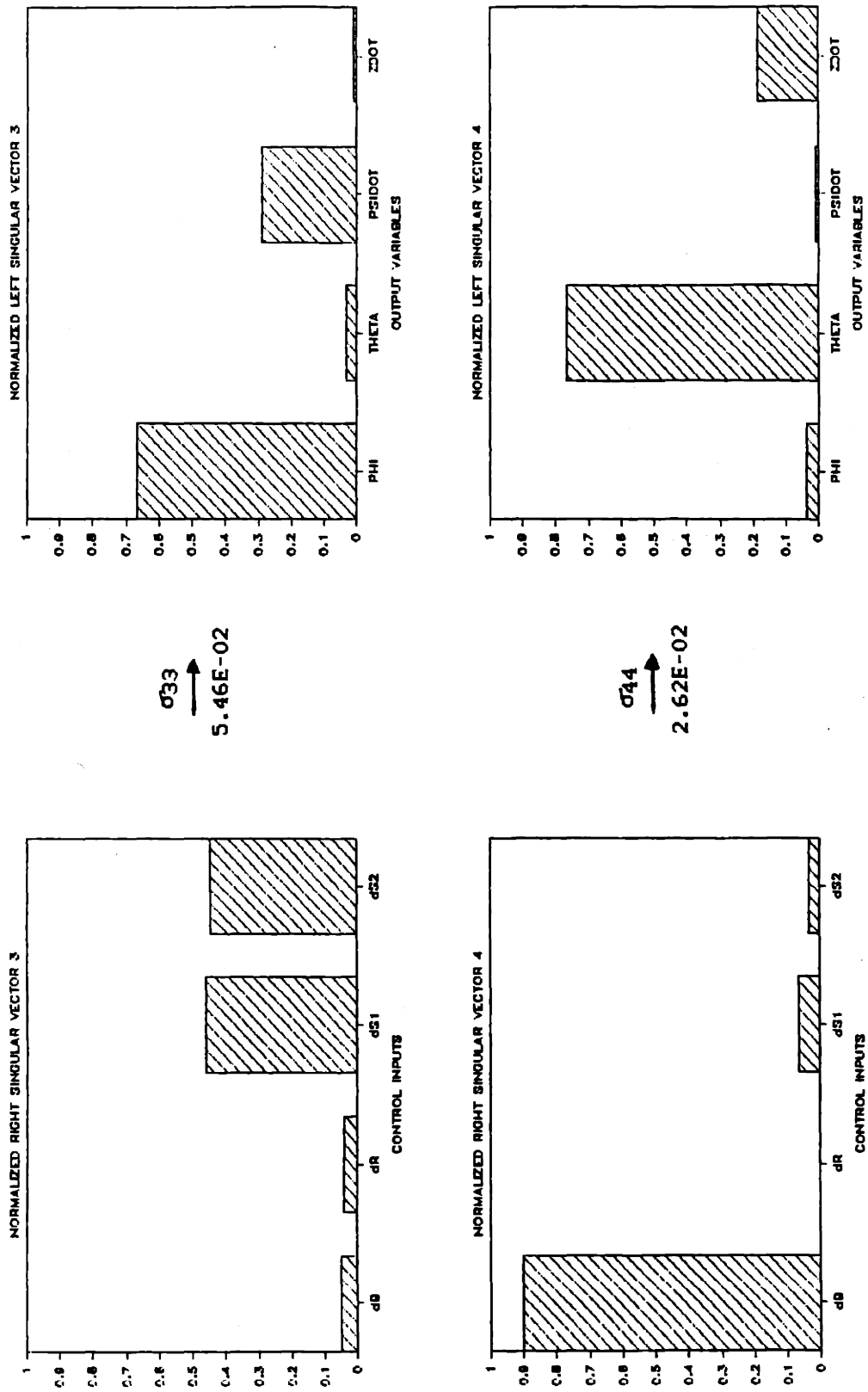


Figure 3.4 Singular Value Decomposition of SISR1

3.5 Performance Specifications

The performance requirements used in this thesis represent the choices of the designer and may not necessarily meet any established criteria set by legal authority. The specifications here will deal with steady-state error, disturbance rejection and stability robustness. First, the concept of singular values will be briefly discussed.

A logical extension of the Bode plot can be made from the SISO case to the MIMO system by consideration of the singular values of the system. The singular values of a complex matrix \underline{M} are defined by

$$\sigma_i(\underline{M}) = \sqrt{\lambda_i[\underline{M}^H \underline{M}]} \quad (3.4)$$

where

σ_i is the i th singular value of \underline{M}

\underline{M}^H is the complex conjugate transpose of \underline{M}

λ_i is the i th eigenvalue of $[\underline{M}^H \underline{M}]$

Referring to (3.4), a matrix \underline{M} is considered "large" when its minimum singular value is large and "small" when its maximum singular value is small. Using these definitions, we can now address command following, disturbance rejection, reduction in sensitivity to modeling errors and response to sensor noise.

Our ultimate goal is to design a robust, dynamic compensator, $\underline{K}(s)$ to control the Linear Time Invariant (LTI) plant, $\underline{G}_p(s)$. Figure 3.5 shows the feedback loop structure with unity negative feedback, command input $\underline{r}(s)$, plant input $\underline{u}(s)$, system output $\underline{y}(s)$, output disturbance vector $\underline{d}(s)$ and measurement noise $\underline{n}(s)$. From Figure 3.5, the following frequency domain

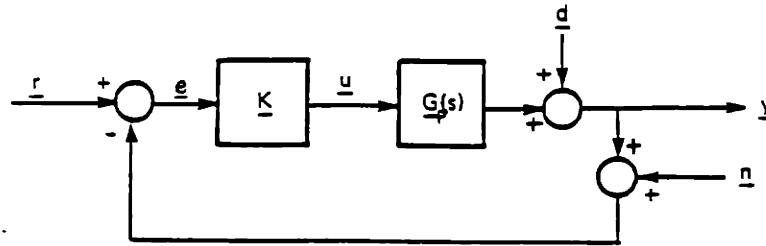


Figure 3.5 Feedback Loop Structure

relation can be easily derived

$$\begin{aligned}
 y(s) = & [\underline{I} + \underline{G}(s)\underline{K}(s)]^{-1}\underline{G}(s)\underline{K}(s) \underline{r}(s) \\
 & + [\underline{I} + \underline{G}(s)\underline{K}(s)]^{-1} \underline{d}(s) \\
 & + [\underline{I} + \underline{G}(s)\underline{K}(s)]^{-1} \underline{n}(s)
 \end{aligned} \tag{3.5}$$

From (3.5), we see that to have "good" command following and disturbance rejection, the Loop Transfer Matrix $\underline{G}(s)\underline{K}(s)$ and therefore $\sigma_{\min}[\underline{G}(s)\underline{K}(s)]$ must be "large" in the frequency range of the reference commands. To reduce the sensitivity to modeling errors, $\sigma_{\max}[\underline{G}(s)\underline{K}(s)]$ must be "small" in the frequency range of the modeling errors. Similarly, for "good" noise rejection, $\sigma_{\max}[\underline{G}(s)\underline{K}(s)]$ must be "small" in the frequency range of the noise. Figure 3.6 shows the Bode-like plot interpretation of

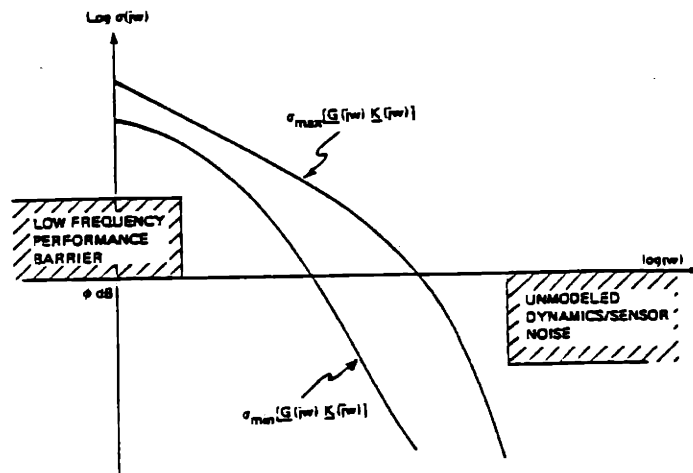


Figure 3.6 Singular Value Requirements for $G(s)K(s)$

these singular value requirements. More detail on this subject may be found in Athans [16].

With respect to command following, it is desired to have zero steady state error to step inputs. This coincides with the singular value requirement discussed above. As such, integrators were placed in all four input channels. Figure 3.7 shows the new plant configuration where the

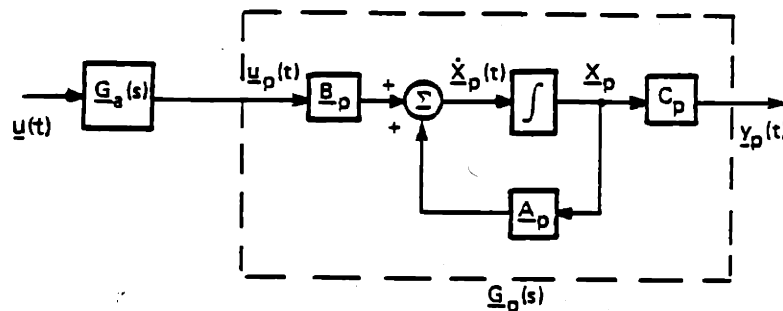


Figure 3.7 Plant With Integrators in Input Channels

state space representation of the augmentation is defined by

$$\underline{G}_A(s) = (\underline{I}/s) \quad (3.6)$$

and the resultant plant transfer function matrix is

$$\underline{G}(s) = \underline{G}_p(s)\underline{G}_A(s) \quad (3.7)$$

The augmented plant is now a 12-dimensional system, however the 4 integrator states are included as part of the plant only during the LQG/LTR compensator design. During implementation, the integrators become part of the compensator. The singular values of the original plant $\underline{G}_p(s)$ and the augmented plant $\underline{G}(s)$ are shown in Figures 3.8 and 3.9 respectively. Note that augmenting the plant has increased the singular values at .001 radians/second by approximately 60 db. The matrices of the augmented plant may be found in Appendix A3.

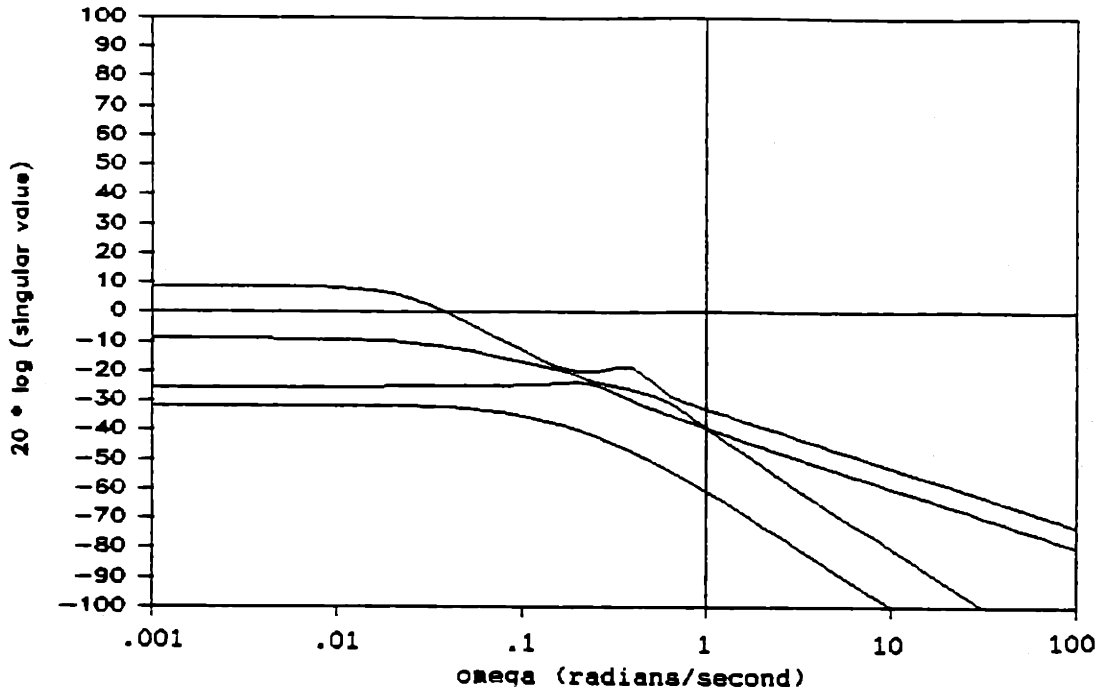


Figure 3.8 Singular Values of Original Plant $G_p(s)$

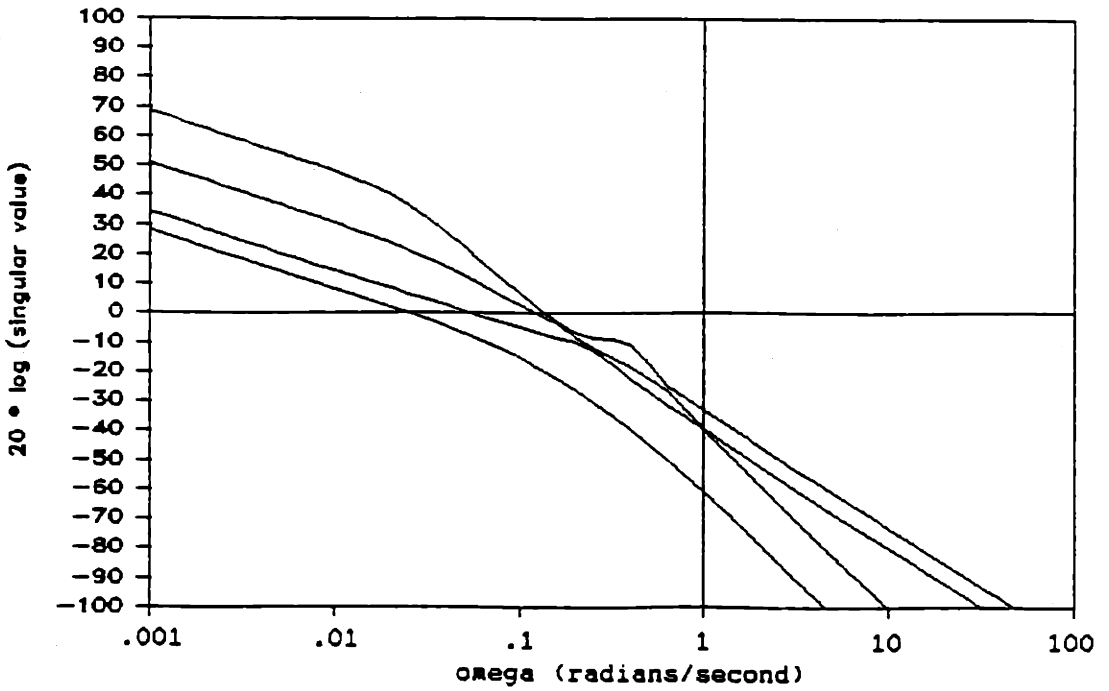


Figure 3.9 Singular Values of Augmented Plant $G(s)$

The next area which needs to be addressed is crossover frequency. As crossover frequency is increased, the system responds faster and one would expect better performance. At slower speeds however, the control surfaces have less effect for a given deflection since the forces and moments generated are proportional to speed squared. Since this compensator will be compared to the one being concurrently developed by Martin [8], a comparable crossover frequency is desired. To avoid frequent control surface saturation and in some cases limit cycling due to the decrease in effectiveness, a compromise must be reached. Additionally, actuator dynamics which exist at approximately 2 to 3 radians/second [5] [6], have not been included in this model and must be treated as modeling error. For this thesis, a crossover frequency of 0.1 radian per second was found to be suitable.

Finally, a brief discussion of robustness is in order. According to Lehtomaki [18], the error $\underline{E}(s)$ between the real system $\underline{\tilde{G}}(s)$ and the linear model $\underline{G}(s)$ can provide a measure of stability robustness. These errors are characterized as additive, subtractive, multiplicative or division in nature. In particular, the multiplicative and additive errors can be used to provide a measure of the relative and absolute errors, respectively. A block diagram representation of multiplicative error as defined by (3.8) is shown in Figure 3.10. Additive error is defined by (3.9). Using these

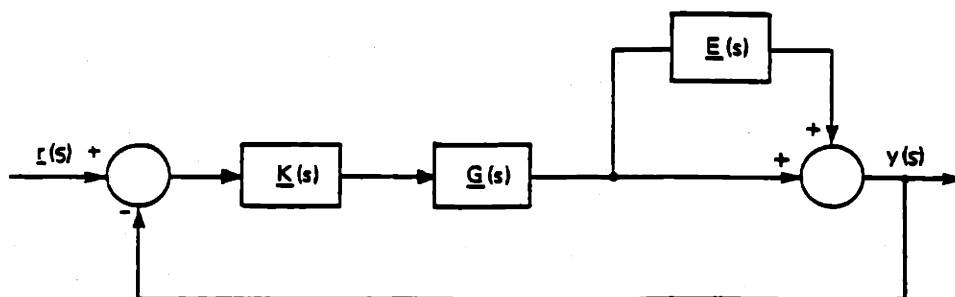


Figure 3.10 MIMO Feedback Loop With Multiplicative Error

$$\begin{aligned}\tilde{\underline{G}}(s) &= [\underline{I} + \underline{E}(s)] \underline{G}(s) = \underline{L}(s)\underline{G}(s) \\ \underline{E}(s) &= [\tilde{\underline{G}}(s) - \underline{G}(s)] \underline{G}(s)^{-1}\end{aligned}\quad (3.8)$$

$$\begin{aligned}\tilde{\underline{G}}(s) &= \underline{E}(s) + \underline{G}(s) \\ \underline{E}(s) &= \tilde{\underline{G}}(s) - \underline{G}(s)\end{aligned}\quad (3.9)$$

relationships, it can be shown that if the singular value inequalities (3.10) and (3.11) hold, we are guaranteed a closed loop stable system.

$$\sigma_{\max}(\underline{L}(s) - \underline{I}) < \sigma_{\min}(\underline{I} + [\underline{G}(s)\underline{K}(s)]^{-1}) \quad (3.10)$$

$$\sigma_{\max}(\underline{L}^{-1}(s) - \underline{I}) < \sigma_{\min}(\underline{I} + \underline{G}(s)\underline{K}(s)) \quad (3.11)$$

The modeling errors may be difficult to quantify but looking at it from another aspect, if we calculate the right hand side of the inequalities, then the maximum tolerable error is known. These relationships provide conservative stability bounds so that a closed loop system may still be stable if the bounds are crossed. System stability would then have to be determined through extensive testing and evaluation. Additional information on stability robustness may be found in [19] through [22].

Performance specifications may therefore be quickly summarized as

- (1) The singular value requirements in Figure 3.6 must be met
- (2) Integrators in all input channels will insure zero steady-state error to step inputs
- (3) Maximum crossover frequency is 0.1 radian/second

3.6 Summary

In Chapter 3, the order of the linear model has been reduced by 2 states and scaled for units and input/output weightings. The pole/zero structure and eigenvectors have been presented. In the section on modal analysis, the relative contribution of the states to each mode was considered and the issues of stabilizability and detectability were addressed. The coupling between inputs and outputs was also presented. Finally, the performance specifications in terms of singular value requirements and crossover frequency were detailed. In Chapter 4, the LQG/LTR methodology and a summary of the compensator design are presented.

CHAPTER 4

LINEAR COMPENSATOR DESIGN

4.1 Introduction

This chapter covers the design of linear compensator for the S15R1 model discussed in Chapters 2 and 3. It begins with a general discussion of the Model Based Compensator (MBC) concept and the Linear Quadratic Gaussian with Loop Transfer Recovery (LQG/LTR) methodology tailored for performance and robustness at the plant output. This is followed by a summary of the linear compensator design for the S15R1 model. Finally, the results of several simulations with the compensator integrated in the nonlinear analytic model at CSDL are presented. The compensator is further analyzed and critiqued in Chapter 5 where it is compared to the S30R1 compensator designed by Martin [8].

4.2 The LQG/LTR Design Methodology

Figure 4.1 again shows the feedback loop structure with unity negative feedback. Note that the original plant $G_p(s)$ has been replaced with the augmented plant $\underline{G}(s)$ as defined by (3.7). The compensator $\underline{K}(s)$ must provide closed loop performance commensurate with the criteria noted in Chapter 3. This will be accomplished through the design of a Model Based Compensator (MBC) [16] using the Linear Quadratic Gaussian with Loop Transfer Recovery (LQG/LTR) methodology [23] through [25].

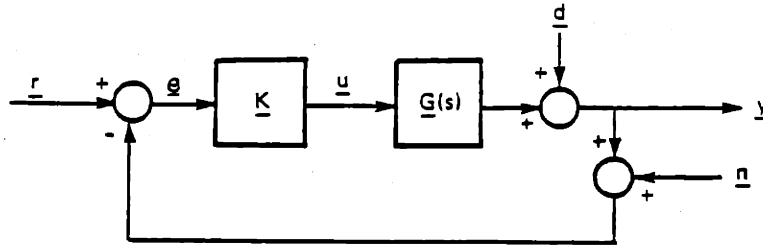


Figure 4.1 Feedback Loop Structure with $G(s)$

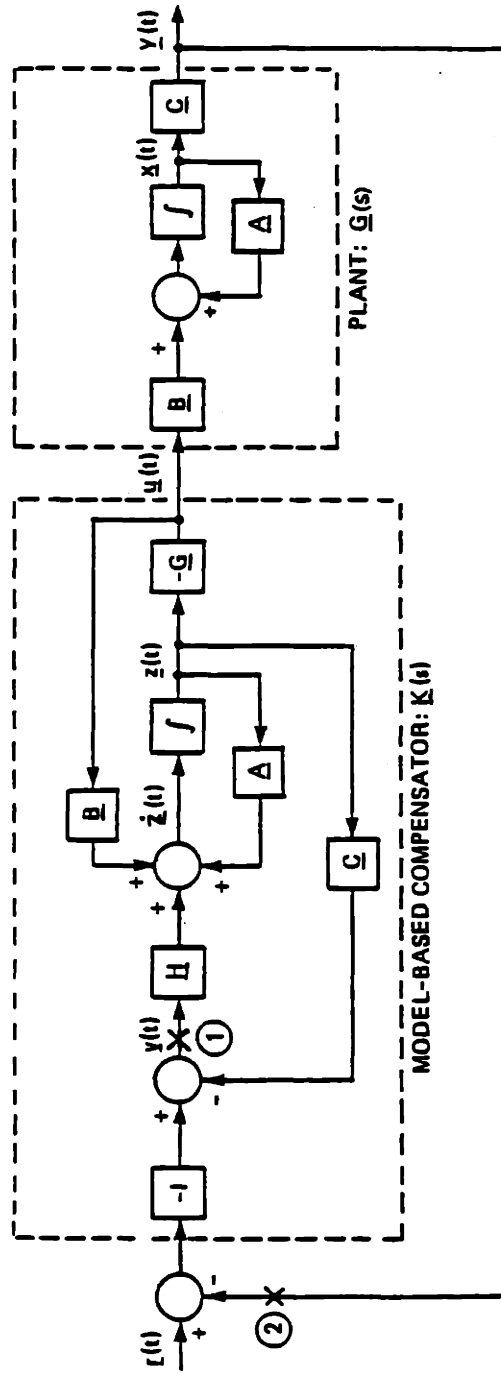
The LQG/LTR methodology guarantees the designer a MIMO compensator $\underline{K}(s)$ that is closed loop stable while providing the necessary degrees of freedom for "loop shaping" (shaping of the singular values of $\underline{G}(s)\underline{K}(s)$) to achieve desired performance while maintaining stability robustness. Figure 4.2 shows the structure of the feedback loop using the MBC. The state vector of the MBC is $\underline{z}(t) \in \mathbb{R}^n$ (i.e. the same dimension as $\underline{x}(t)$, the plant state vector), hence we ultimately wind up with an open loop system $\underline{G}(s)\underline{K}(s)$ which is $2n$ -dimensional. The reduction of the model described in Section 3.2 has therefore reduced the resultant closed loop system by a total of 4 states.

The MBC derives its name from the fact that the \underline{A} , \underline{B} and \underline{C} matrices defined in the state-space representation of the plant appear in the dynamics of the compensator. The open-loop plant dynamics are

$$\dot{\underline{x}}(t) = \underline{A} \underline{x}(t) + \underline{B} \underline{u}(t) \quad (4.1)$$

$$\underline{y}(t) = \underline{C} \underline{x}(t) \quad (4.2)$$

where $\underline{x}(t) \in \mathbb{R}^n$, $\underline{u}(t) \in \mathbb{R}^m$ and $\underline{y}(t) \in \mathbb{R}^m$. Note that $\underline{u}(t)$ and $\underline{y}(t)$ are the same dimension as constrained by the methodology. The frequency domain representation for the plant transfer function $\underline{G}(s)$ is given by



OPEN LOOP PLANT

$$\begin{aligned} \dot{\bar{x}}(t) &= \Delta \dot{x}(t) + B \bar{u}(t) \\ \bar{y}(t) &= C \bar{x}(t) \\ \bar{Y}(s) &= G(s) \bar{u}(s) \\ G(s) &= C(sI - \Delta)^{-1} B \end{aligned}$$

MODEL BASED COMPENSATOR

$$\begin{aligned} \dot{\bar{z}}(t) &= \Delta \dot{z}(t) + B \bar{u}(t) + H \bar{y}(t) \\ \bar{y}(t) &= \bar{y}(t) - C \bar{z}(t) - f(t) = -g(t) - C \bar{z}(t) \\ \bar{u}(t) &= -G \bar{z}(t) \\ \bar{u}(s) &= K(s) \bar{e}(s) \\ K(s) &= G(sI - A + B G + H C)^{-1} H \end{aligned}$$

Figure 4.2 Structure of the Model Based Compensator in a Feedback Configuration

$$\underline{G}(s) = \underline{C} (s\underline{I} - \underline{A})^{-1} \underline{B} \quad (4.3)$$

Dynamics of the MBC in the time domain are

$$\dot{\underline{z}}(t) = [\underline{A} - \underline{B} \underline{G} - \underline{H} \underline{C}] \underline{z}(t) - \underline{H} \underline{e}(t) \quad (4.4)$$

$$\underline{u}(t) = -\underline{G} \underline{z}(t) \quad (4.5)$$

and the compensator transfer function $\underline{K}(s)$ is

$$\underline{K}(s) = \underline{G} (s\underline{I} - \underline{A} + \underline{B} \underline{G} + \underline{H} \underline{C})^{-1} \underline{H} \quad (4.6)$$

where the Filter Gain Matrix \underline{H} and Control Gain Matrix \underline{G} are design parameters for the compensator.

As derived in [16], by defining a state estimation vector (4.7), the dynamics of the closed loop system can be represented by (4.8).

$$\underline{w}(t) = \underline{x}(t) - \underline{z}(t) \quad (4.7)$$

$$\begin{bmatrix} \dot{\underline{x}}(t) \\ \dot{\underline{w}}(t) \end{bmatrix} = \begin{bmatrix} (\underline{A} - \underline{B} \underline{G}) & -\underline{B} \underline{G} \\ \underline{0} & (\underline{A} - \underline{H} \underline{C}) \end{bmatrix} \begin{bmatrix} \underline{x}(t) \\ \underline{w}(t) \end{bmatrix} + \begin{bmatrix} \underline{0} \\ -\underline{H} \end{bmatrix} \underline{z}(t) \quad (4.8)$$

By examining the closed loop \underline{A} matrix above, it is evident that the roots of (4.9) yield the $2n$ eigenvalues of the closed loop system and for closed loop stability, (4.10) and (4.11) must hold.

$$\det[s\underline{I} - \underline{A} + \underline{B} \underline{G}] \cdot \det[s\underline{I} - \underline{A} + \underline{H} \underline{C}] = 0 \quad (4.9)$$

$$\operatorname{Re}(\lambda_i [\underline{A} - \underline{B} \underline{G}]) < 0 ; i=1,2,\dots,n \quad (4.10)$$

$$\operatorname{Re}(\lambda_i [\underline{A} - \underline{H} \underline{C}]) < 0 ; i=1,2,\dots,n \quad (4.11)$$

It now becomes clear that the compensator design decomposes into finding \underline{G} and \underline{H} such that (4.10) and (4.11) hold. The Linear Quadratic Gaussian (LQG) methodology provides the necessary tools to make

"intelligent" choices for the compensator gain matrices thus the LQG controller is a special type of Model Based Compensator. A review of equations (4.4) and (4.5) reveal the LQG controller to be a cascaded combination of a Kalman-Bucy Filter and a full-state feedback Linear Quadratic Regulator.

Selection of the Filter Gain Matrix \underline{H} is made through the solution of a Kalman-Bucy Filter (KBF) problem based on equation (4.4). The Filter Gain Matrix is defined by

$$\underline{H} = (1/\mu) \underline{E} \underline{C}^T \quad (4.12)$$

where $\underline{E} = \underline{E}^T \geq \underline{Q}$ is the unique solution of the Filter Algebraic Riccati Equation (FARE)

$$\underline{Q} = \underline{A} \underline{E} + \underline{E} \underline{A}^T + \underline{L} \underline{L}^T - (1/\mu) \underline{E} \underline{C}^T \underline{C} \underline{E} \quad (4.13)$$

subject to the constraints

- $[\underline{A}, \underline{C}]$ detectable
- $[\underline{A}, \underline{L}]$ stabilizable
- $\mu > 0$

The Control Gain Matrix \underline{G} is defined by (4.14) as determined through the solution of the "cheap" LQR (Linear Quadratic Regulator) control problem

$$\underline{u}(t) = -\underline{G} \underline{z}(t) = -\underline{R}^{-1} \underline{B}^T \underline{K} \quad (4.14)$$

where $\underline{K} = \underline{K}^T \geq \underline{Q}$ is the unique solution of the Control Algebraic Riccati Equation (CARE)

$$\underline{Q} = -\underline{K} \underline{A} - \underline{A}^T \underline{K} - \rho \underline{C}^T \underline{C} + \underline{K} \underline{B} \underline{R}^{-1} \underline{B}^T \underline{K} \quad (4.15)$$

subject to the constraints

- * $[A, B]$ stabilizable
- * $[A, C]$ detectable
- * $R = I$
- * $q > 0$

The compensator gains could now be determined if the design parameters q , u and L were known. To determine the "correct" values for these design parameters, we now turn our attention to Loop Transfer Recovery (LTR).

Referring to Figure 4.2, performance and stability robustness can be measured at the plant input or plant output by breaking the loop at the corresponding point. For the design of the submarine controller, physical significance at the plant output has been retained (point ② on Figure 4.2) and therefore the latter approach will be used. The reader is referred to [23] and [24] for an explanation of the methodology with respect to performance and robustness at the plant input.

The design of the controller can now be performed in the following fashion.

- (1) Design a Kalman Filter with appropriate singular values using the KBF equations (4.12) and (4.13)
- (2) Recover the singular value shapes using the LQR equations (4.14) and (4.15)

The following definitions of the filter open loop and Kalman Filter transfer functions are useful in the development of the design procedure

$$G_{fol}(s) = C (sI - A)^{-1} L \quad (4.16)$$

$$G_{kf}(s) = C (sI - A)^{-1} H \quad (4.17)$$

Note that (4.17) represents the loop transfer function when the LQG loop in Figure 4.2 is broken at point ①. The relationship between these transfer functions is given by the following Return Difference Identity (4.18) also known as the Kalman Frequency Domain Equality (FDE) for the filter.

$$[\underline{I} + \underline{G}_{kf}(s)][\underline{I} + \underline{G}_{kf}(s)]^H = \underline{I} + (1/\mu)\underline{G}_{fol}(s)\underline{G}_{fol}^H(s) \quad (4.18)$$

By looking at the singular values of both sides of the FDE (4.19), the approximation (4.20) holds for $\sigma_1(\underline{G}_{kf}(s)) \gg 1$, i.e. at low frequency.

$$\sigma_1(\underline{I} + \underline{G}_{kf}(s)) = \sqrt{1 + (1/\mu)\sigma_1^2(\underline{G}_{fol}(s))} \quad (4.19)$$

$$\sigma_1(\underline{G}_{kf}(s)) = \sigma_1((1/\sqrt{\mu})\underline{G}_{fol}(s)) \quad (4.20)$$

This means the singular values of the KBF can be "shaped" to meet the desired performance, crossover and robustness requirements by selecting

1. \underline{L} for the desired loop shape
2. μ for the desired crossover frequency

Using the value of μ and the matrix \underline{L} from above, \underline{H} is calculated using the KBF equations and the following properties are guaranteed.

- Closed-loop stability (for the filter)
- $-6\text{db} < \text{Gain Margin} < \infty$
- $-60^\circ < \text{Phase Margin} < 60^\circ$

Now that the Filter Gain Matrix has been determined, the zeros of the plant transfer function $\underline{G}(s)$ are checked. If the plant is minimum phase, we are guaranteed recovery of the "nice" shape and properties of the Kalman Filter using the Kwakernaak "sensitivity recovery" [26] via the LQR

equations. At this time, the effects of non-minimum phase (NMP) zeros are not clearly understood, but suffice it to say that some degradation in the recovery process and resulting closed loop performance is certain if one or more NMP zeros are within the bandwidth of the controller. If the plant is non-minimum phase, all that can presently be done is to proceed and use extensive testing and evaluation to detect instabilities or other problems.

The LQR equations are now solved (as $q \rightarrow \infty$) to determine the Control Gain Matrix \underline{G} . Using the \underline{G} and \underline{H} matrices, the LQG compensator matrix $K(s)$ is determined using (4.6). The singular values of $\underline{G}(s)\underline{K}(s)$ are then compared to the singular values of $\underline{G}_{kf}(s)$. If the $\sigma_i(\underline{G}(s)\underline{K}(s))$ are sufficiently different from $\sigma_i(\underline{G}_{kf}(s))$, q must be increased and the LQR equations solved for a new Control Gain Matrix. Recovery of the Kalman Filter loop shape is considered satisfactory when there is good agreement for at least 1 decade past crossover. At that point, the rolloff of the singular values is at least -40 db/decade (two pole rolloff). The Loop Transfer Matrix $\underline{G}(s)\underline{K}(s)$ is then checked for robustness as discussed in Section 3.5.

4.3 Design of the LQG/LTR Compensator for the S15R1 Model

As discussed in the previous section, the design of the compensator is performed as follows.

- (1) Design a Kalman Filter loop with appropriate singular value shapes
- (2) Attempt to recover these singular value shapes using the Kwakernaak recovery method

The reader is once again reminded that during the LQG/LTR design process, the plant matrices which are used are that for the augmented scaled plant $\underline{G}(s)$. Any augmentation is separated from the plant model and included in the compensator prior to implementation for testing.

Design of the Kalman Filter loop hinges on selection of the parameter μ (magnitude of the measurement noise intensity) and the matrix \underline{L} so that the singular values of $\underline{G}_{fol}(s)$ as defined by (4.16), have a "nice" shape like that shown in Figure 3.5 and meet the performance specifications set in Section 3.5. To enhance chances of a good recovery of these shapes in the LQR loop, it is desired to have the minimum and maximum singular values match. This is accomplished by selecting \underline{L} such that the singular values match at high and low frequencies.

The augmented plant transfer function $\underline{G}(s) = \underline{G}_A(s)\underline{G}_P(s)$ is defined by

$$\underline{G}(s) = \underline{C} (s\underline{I} - \underline{A})^{-1} \underline{B} \quad (4.21)$$

where

$$\underline{A} = \begin{bmatrix} \underline{0} & \underline{0} \\ \underline{B}_p & \underline{C}_p \end{bmatrix} \quad \underline{C} = \begin{bmatrix} \underline{0} & \underline{C}_p \end{bmatrix}$$

and therefore

$$\begin{bmatrix} s\underline{I} - \underline{A} \end{bmatrix} = \begin{bmatrix} s\underline{I} & \underline{0} \\ -\underline{B}_p & (s\underline{I} - \underline{A}_p) \end{bmatrix} \quad (4.22)$$

Looking at (4.22) at low frequency, $(s\underline{I} - \underline{A}_p) \rightarrow -\underline{A}_p$ and a good approximation for $(s\underline{I} - \underline{A})^{-1}$ is

$$(s\underline{I} - \underline{A})^{-1} \approx \begin{bmatrix} (1/s)\underline{I} & \underline{0} \\ -(1/s)\underline{A}_p^{-1}\underline{B}_p & -\underline{A}_p^{-1} \end{bmatrix} \quad (4.23)$$

provided \underline{A}_p^{-1} exists. Therefore by (4.16), $\underline{G}_{fol}(s)$ is approximately

$$\begin{aligned} \underline{G}_{fol}(s) &\approx \begin{bmatrix} \underline{0} & \underline{C}_p \end{bmatrix} \begin{bmatrix} (1/s)\underline{I} & \underline{0} \\ -(1/s)\underline{A}_p^{-1}\underline{B}_p & -\underline{A}_p^{-1} \end{bmatrix} \begin{bmatrix} \underline{L}_1 \\ \underline{L}_2 \end{bmatrix} \\ &= -(1/s)\underline{C}_p\underline{A}_p^{-1}\underline{B}_p\underline{L}_1 - \underline{C}_p\underline{A}_p^{-1}\underline{L}_2 \end{aligned} \quad (4.24)$$

Note that the matrix \underline{L} has been partitioned into \underline{L}_1 and \underline{L}_2 associated with the low frequency and high frequency behavior respectively. From (4.24), low frequency matching of singular values occurs if

$$\underline{L}_1 = -[\underline{C}_p\underline{A}_p^{-1}\underline{B}_p]^{-1} \quad (4.25)$$

Similarly, at high frequency, $(s\underline{I} - \underline{A}_p) \rightarrow s\underline{I}$ and

$$\begin{aligned} (s\underline{I} - \underline{A})^{-1} &\approx \begin{bmatrix} (1/s)\underline{I} & \underline{0} \\ (1/s^2)\underline{B}_p & (1/s)\underline{I} \end{bmatrix} \\ \underline{G}_{fol}(s) &\approx \begin{bmatrix} \underline{0} & \underline{C}_p \end{bmatrix} \begin{bmatrix} (1/s)\underline{I} & \underline{0} \\ -(1/s^2)\underline{B}_p & (1/s)\underline{I} \end{bmatrix} \begin{bmatrix} \underline{L}_1 \\ \underline{L}_2 \end{bmatrix} \\ &= (1/s^2)\underline{C}_p\underline{B}_p\underline{L}_1 + (1/s)\underline{C}_p\underline{L}_2 \end{aligned} \quad (4.27)$$

As $s \rightarrow \infty$, the second term in (4.27) dominates and the singular values are matched if

$$\underline{L}_2 = \underline{C}_p^T(\underline{C}_p\underline{C}_p^T)^{-1} \quad (4.28)$$

The \underline{L} matrix (listed in Appendix B3) has now been selected for low and high frequency matching, however the behavior of the singular values at middle frequencies has not been considered. Unacceptable differences at these frequencies are dealt with by appropriate scaling of the plant inputs and outputs such as that described in Section 3.3.

Once an appropriate \underline{L} matrix has been determined, the singular values are shifted up or down by varying the scalar parameter μ until the desired crossover frequency is obtained. The value of $\mu = 132$ produced the desired

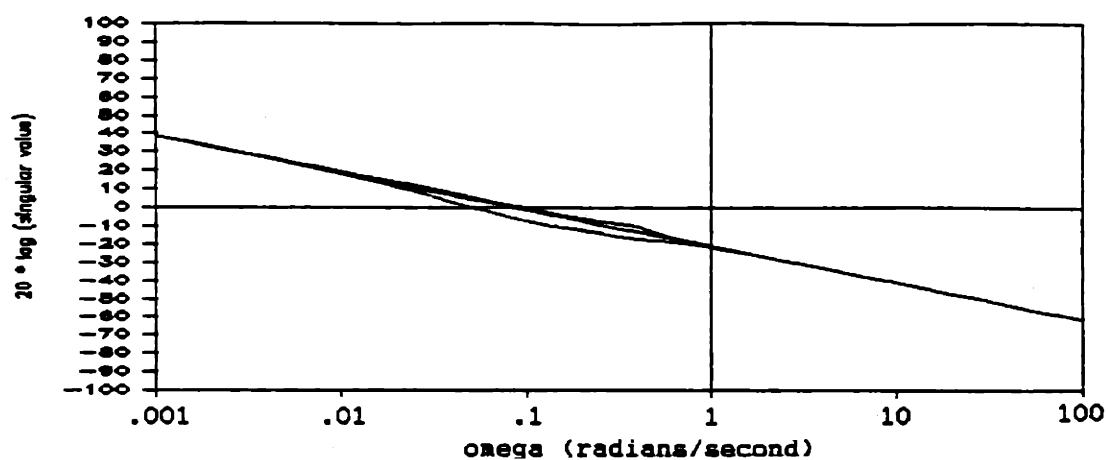


Figure 4.3a Singular Values of $G_{f1}(s)$

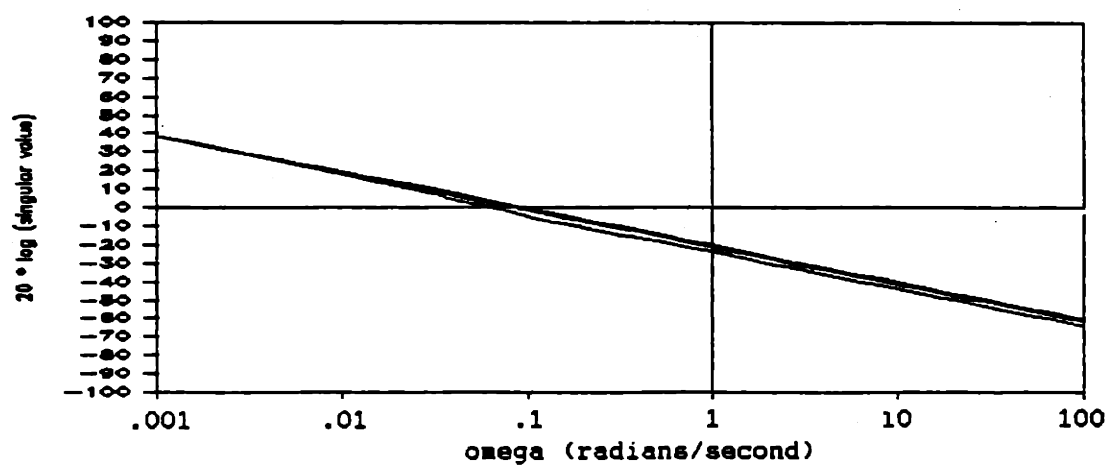


Figure 4.3b Singular Values of $G_{kf}(s)$

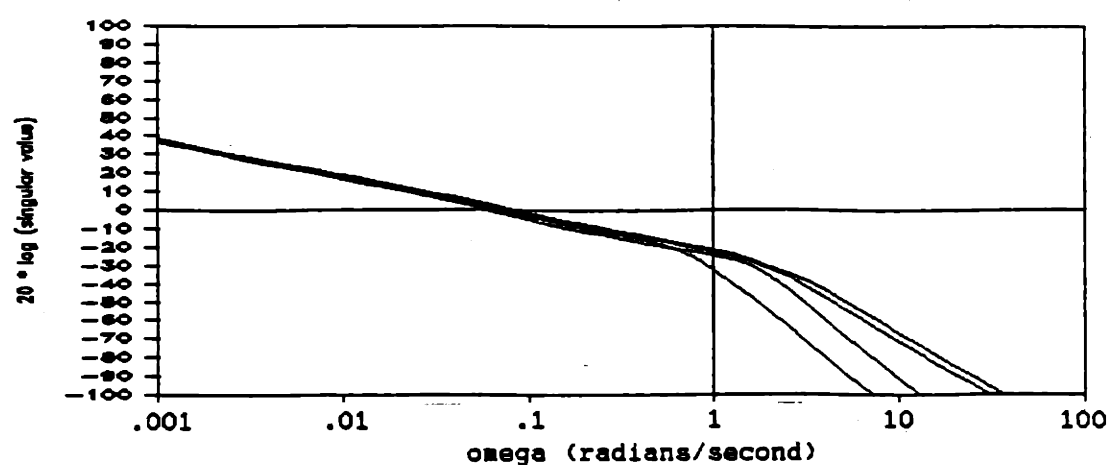


Figure 4.3c Singular Values of $G(s)K(s)$

maximum crossover frequency of 0.1 radians/second. Figure 4.3a shows the plot of $\sigma_1\{(1/\sqrt{\mu})\underline{G}_{f01}(s)\}$ for these parameters.

Now, using the μ and \underline{l} such that meet the desired specifications, the FARE is solved and the Filter Gain Matrix \underline{H} determined from (4.12). Next, the singular values of the Kalman Filter $\sigma_1\{\underline{G}_{kf}(s)\}$ are calculated as shown in Figure 4.3b and compared to the performance specifications. This is the "loop shape" of $\underline{G}(s)\underline{K}(s)$ which results from the Kwakernaak recovery.

The next step in the LQG/LTR process is solution of the CARE (the MIMO transmission zeros have already been checked in Section 3.4) and calculation of the Control Gain Matrix using (4.14). Using the \underline{H} and \underline{G} matrices, the compensator $\underline{K}(s)$ is calculated using (4.6) and the singular values of the Loop Transfer Matrix $\underline{G}(s)\underline{K}(s)$ are compared to the singular values of the Kalman Filter loop. As stated in Section 4.2, satisfactory recovery is said to occur when $\sigma_1\{\underline{G}(s)\underline{K}(s)\}$ match $\sigma_1\{\underline{G}_{kf}(s)\}$ for at least one decade past crossover. Figure 4.3c shows the recovered singular value loop shape for $q = 105$. The crossover bandwidth for this design was from approximately 0.05 to 0.1 radians/second. The \underline{G} and \underline{H} matrices are listed in Appendix B3.

As stated in Section 3.5, the integrators are actually part of the final compensator matrix $\underline{K}_a(s)$. The final compensator must also include the effects of scaling on the inputs and outputs. Figure 4.4 shows the block diagram representation of the resultant closed loop system. The

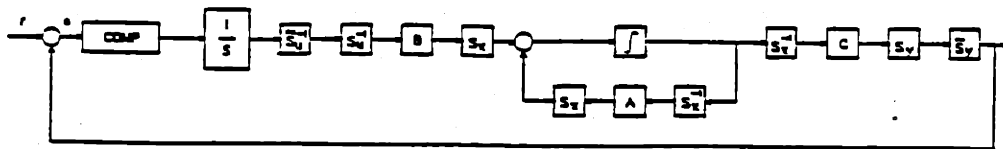


Figure 4.4 Block Diagram Representation of Closed Loop System

singular values for the LQG compensator $\underline{K}(s)$ and the augmented and scaled compensator $\underline{K}_a(s)$ are shown in Figures 4.5a and 4.5b respectively. From these singular value plots, the lead-lag characteristics, particularly the effects of the integrators at low frequency, are evident. The spread in singular values at frequencies below crossover reflects the different amplification requirements for certain directions so that the singular values of the recovered Loop Transfer Matrix $\underline{G}(s)\underline{K}(s)$ match.

The singular values of the closed loop plant as defined by (4.8) are shown in Figure 4.6. They reflect the desired characteristic of 0 db gain until crossover or break frequency and at least 2 pole rolloff (-40 db/decade) after crossover. The poles and zeros of the open loop and closed loop systems are found in Appendix B4.

By examining the transfer function matrix for the loop broken at the plant input, information can be obtained on how the control inputs vary with respect to reference commands. The transfer function relating $\underline{r}(s)$ to $\underline{u}(s)$ is given by

$$\underline{u}(s) = (\underline{I} + \underline{K}(s)\underline{G}(s))^{-1} \underline{K}(s) \underline{r}(s) = \underline{K}_r(s) \underline{r}(s) \quad (4.29)$$

Figure 4.7 shows the singular values for the frequency range of interest. The spread in singular values indicates that certain directions have higher gains than others. The singular value decomposition of (4.29) shown in Figure 4.8 allows us to examine the coupling of reference commands to control inputs. The singular value decomposition was accomplished in the manner discussed in Section 3.4 on plant eigenstructure. From Figure 4.8, we see that for σ_{11} , the controller responds to a depthrate command with deflection of the fairwater planes which makes physical sense. For σ_{22} , it is evident that if a yawrate command causes deflection of the rudder and

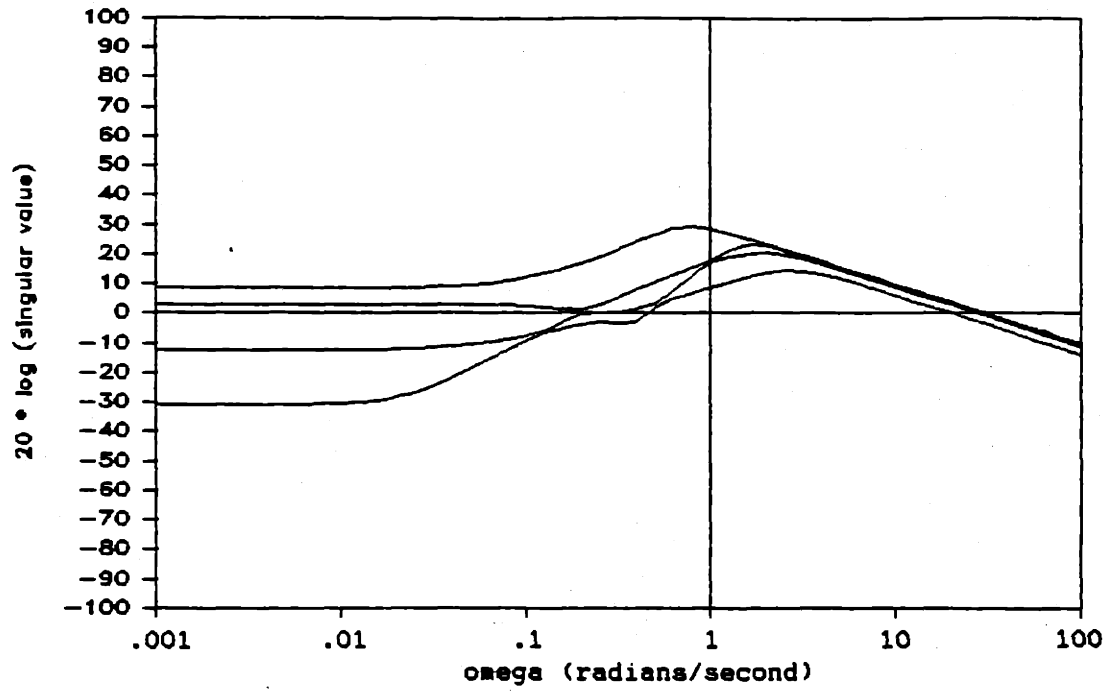


Figure 4.5a Singular Values of $K(s)$

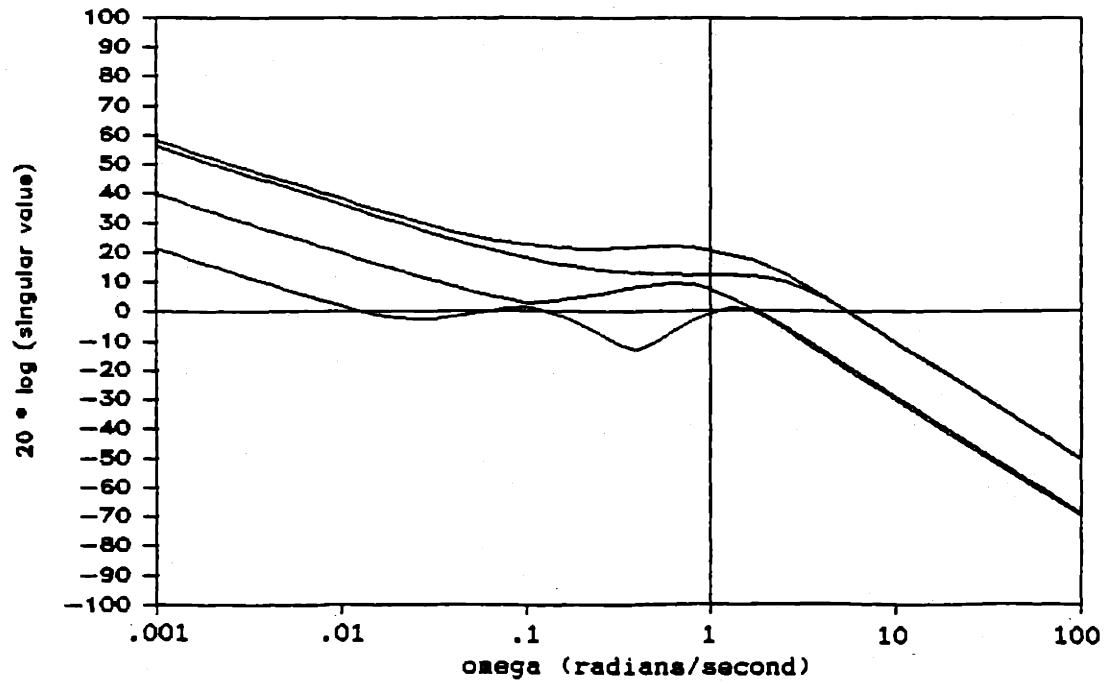


Figure 4.5b Singular Values of $K_A(s)$

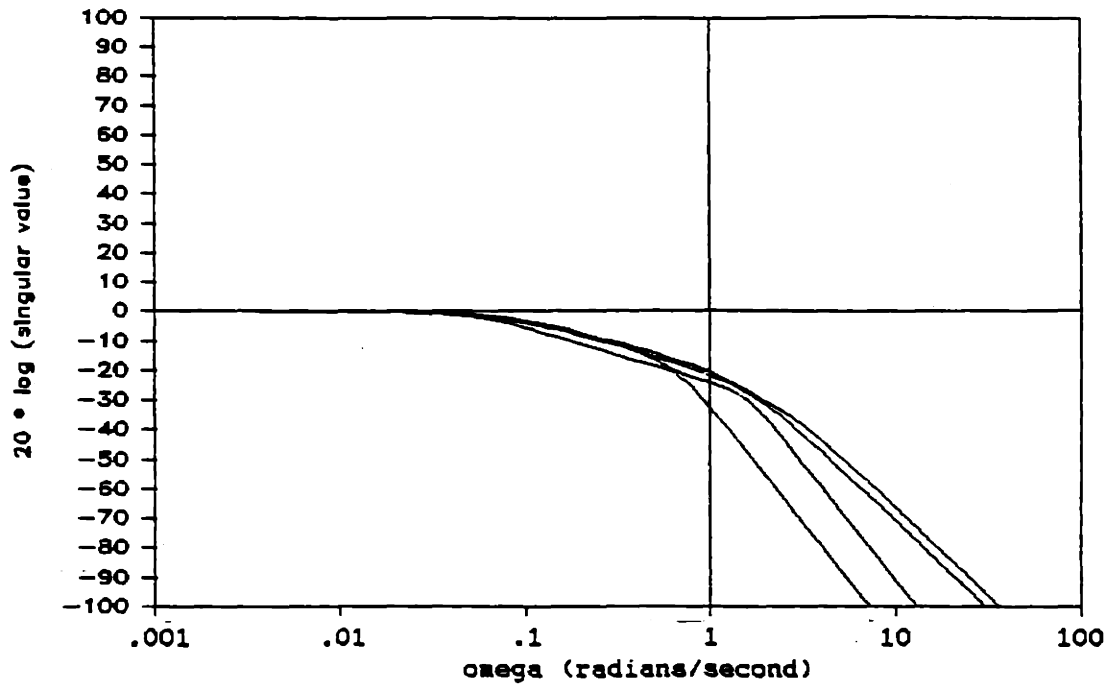


Figure 4.6 Singular Values of the Closed Loop

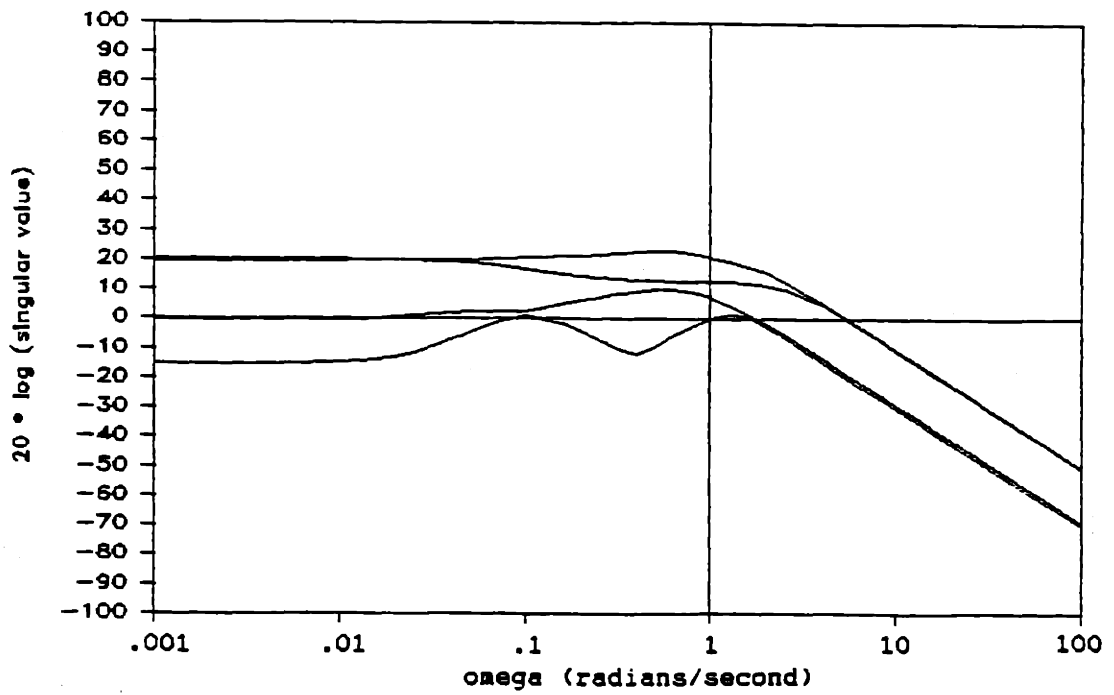


Figure 4.7 Singular Values of $K_r(s)$

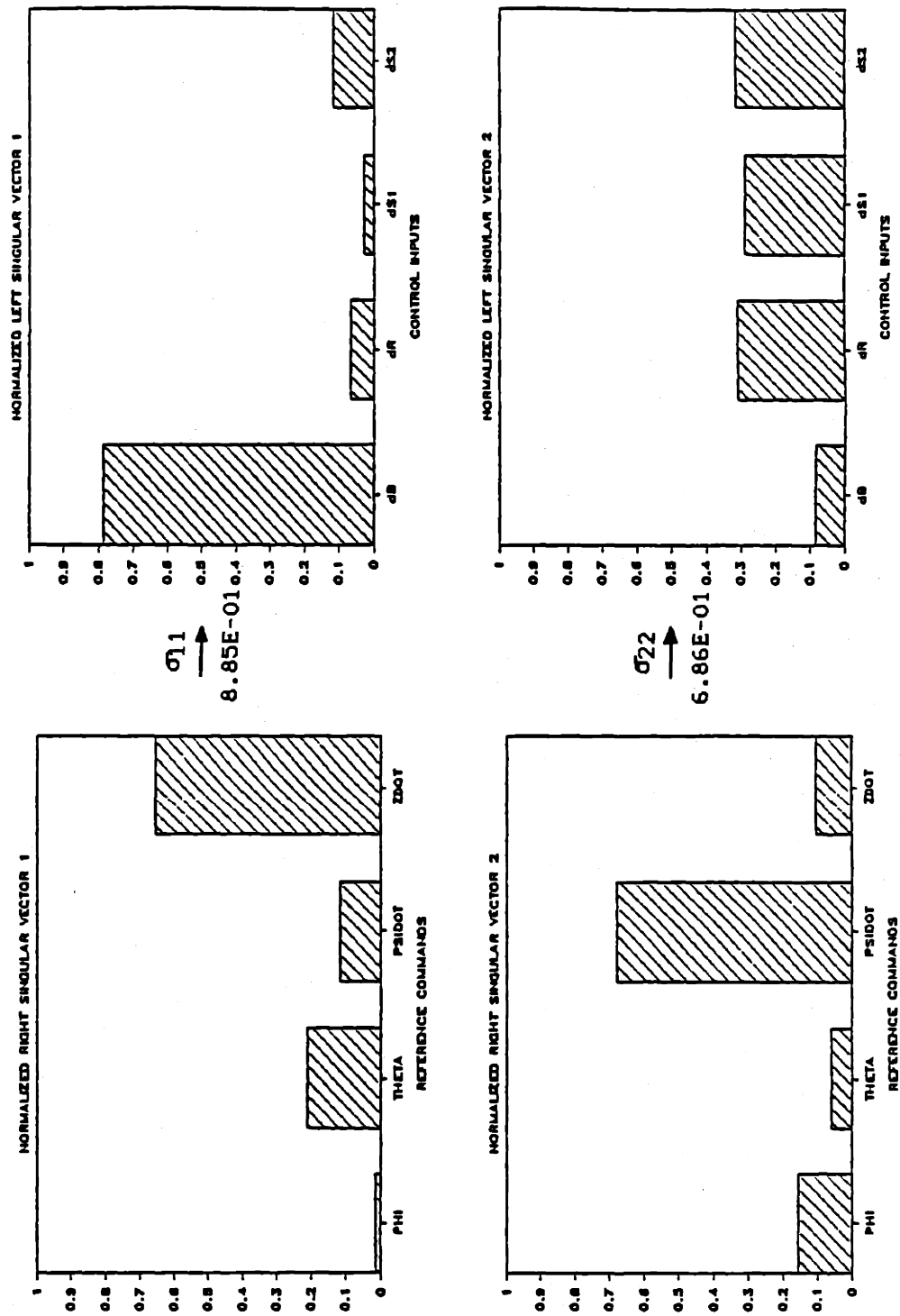


Figure 4.8 Singular Value Decomposition of $K_r(s)$

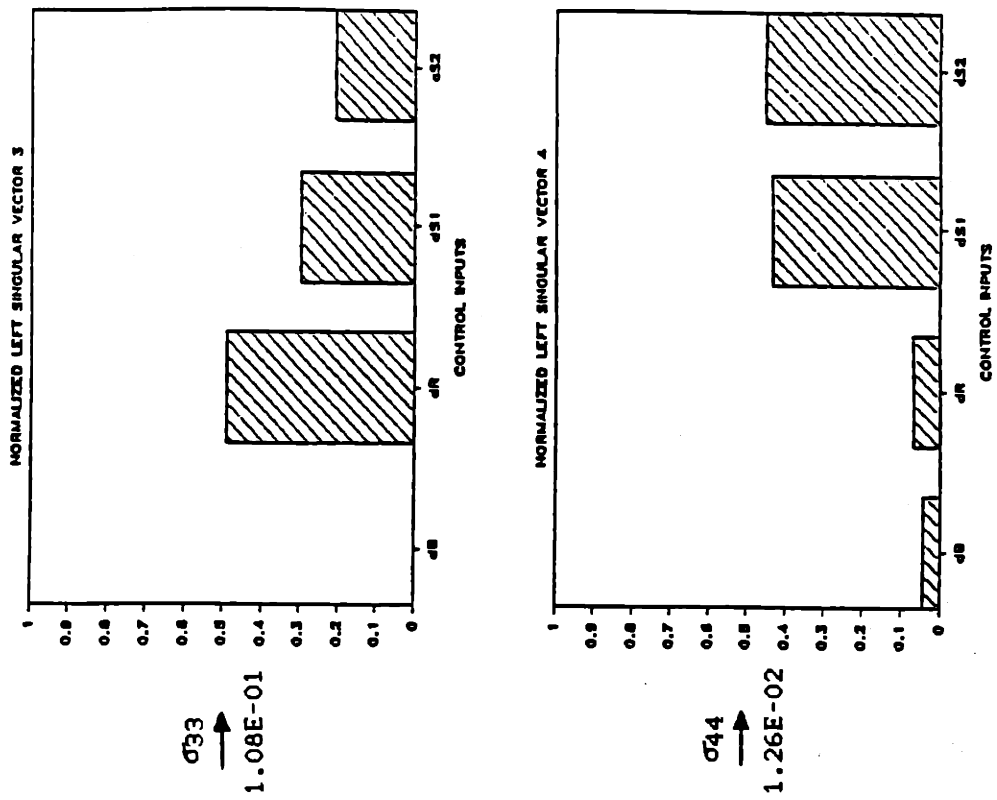


Figure 4.8 Singular Value Decomposition of $K_r(s)$

the sternplanes. The rudder obviously deflects to induce the yawrate. Movement of the sternplanes can be attributed to differential deflection to counter the initial roll angle caused by the rudder deflection and the steady state roll angle induced by crossflow over the sail. Furthermore, the σ_{33} information indicates that roll commands will cause the rudder and sternplanes to respond. Differential sternplane deflection is obviously the only feasible way to control roll so the question arises as to why the rudder deflects so much. This is most likely due to the coupling between the rudder and sternplanes. Finally, σ_{44} shows that a pitch command results in deflection of the sternplanes. In this case we would expect deflection in the same general direction with possible slight differences due to induced roll angles.

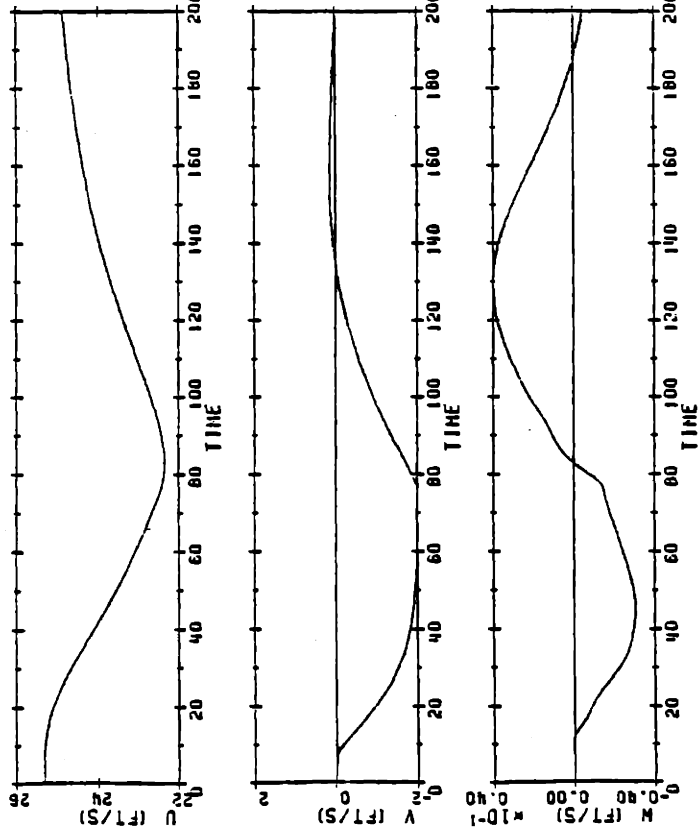
4.4 Preliminary Testing of the Compensator

As a prelude to further analysis, preliminary testing of the compensator was performed to gain some insight on possible limitations of the design. Simulations were performed for single command inputs and multiple command inputs using step and square commands.

First, a series of simulations were made to examine the effects of symmetry on the response of the submarine. Figure 4.9 shows the results of the 15 knot nonlinear simulations for ± 1 degree/second yawrate step inputs applied at $t = 5$ seconds and removed at $t = 75$ seconds. As the submarine enters into the turn, it initially rolls slightly outward and then due to the large force generated by crossflow over the sail, snap rolls inward. To counter this effect, the sternplanes deflect differentially to generate a righting moment which drives the roll angle to zero. To counter the effect of the initial rudder deflection on pitch and depthrate, there is

VELOCITIES

NONLINEAR INTEGRATION FOR 1 DEG/SEC COMMANDED YAWRATE



VELOCITIES

NONLINEAR INTEGRATION FOR -1 DEG/SEC COMMANDED YAWRATE

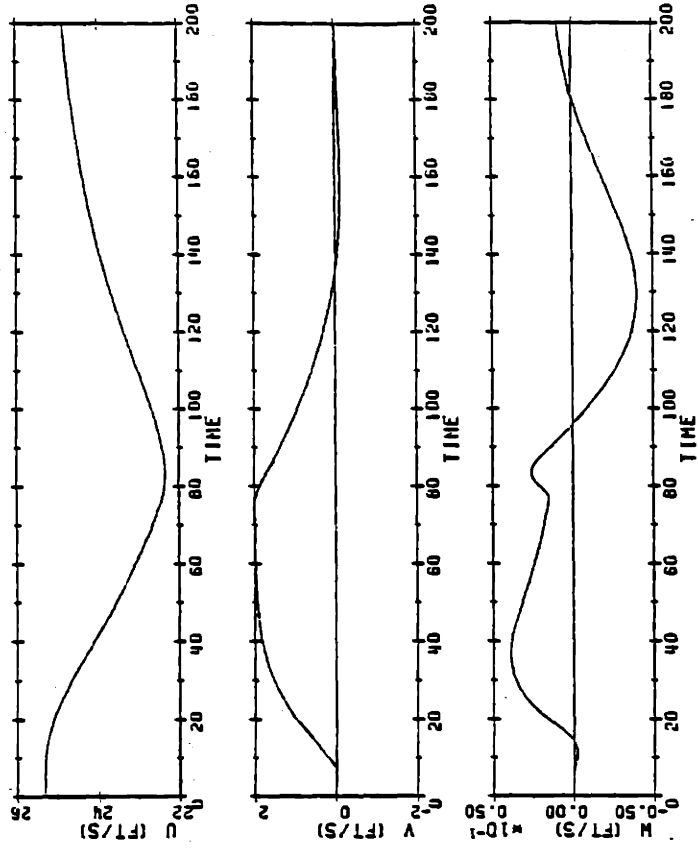
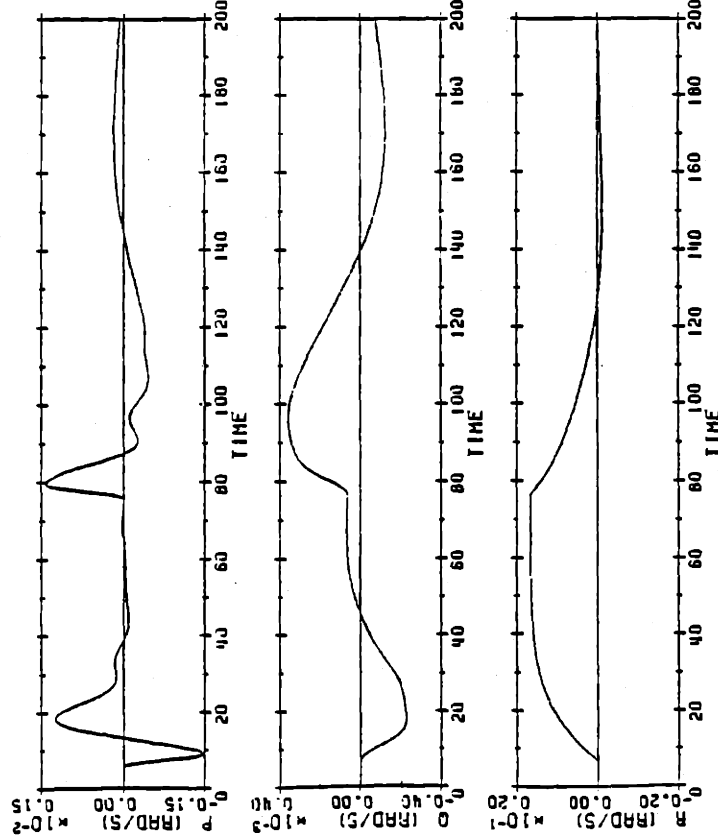


Figure 4.9 Symmetry Comparison for +/- 1 Degree/Second Yawrate

ANGULAR VELOCITIES

NONLINEAR INTEGRATION FOR 1 DEG/SEC COMMANDED YAWRATE



ANGULAR VELOCITIES

NONLINEAR INTEGRATION FOR -1 DEG/SEC COMMANDED YAWRATE

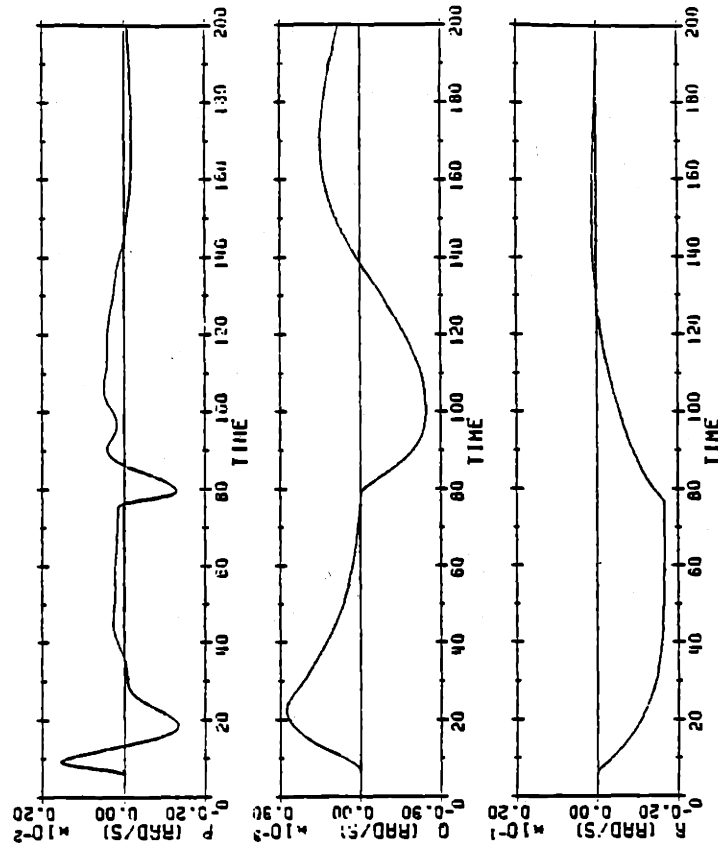
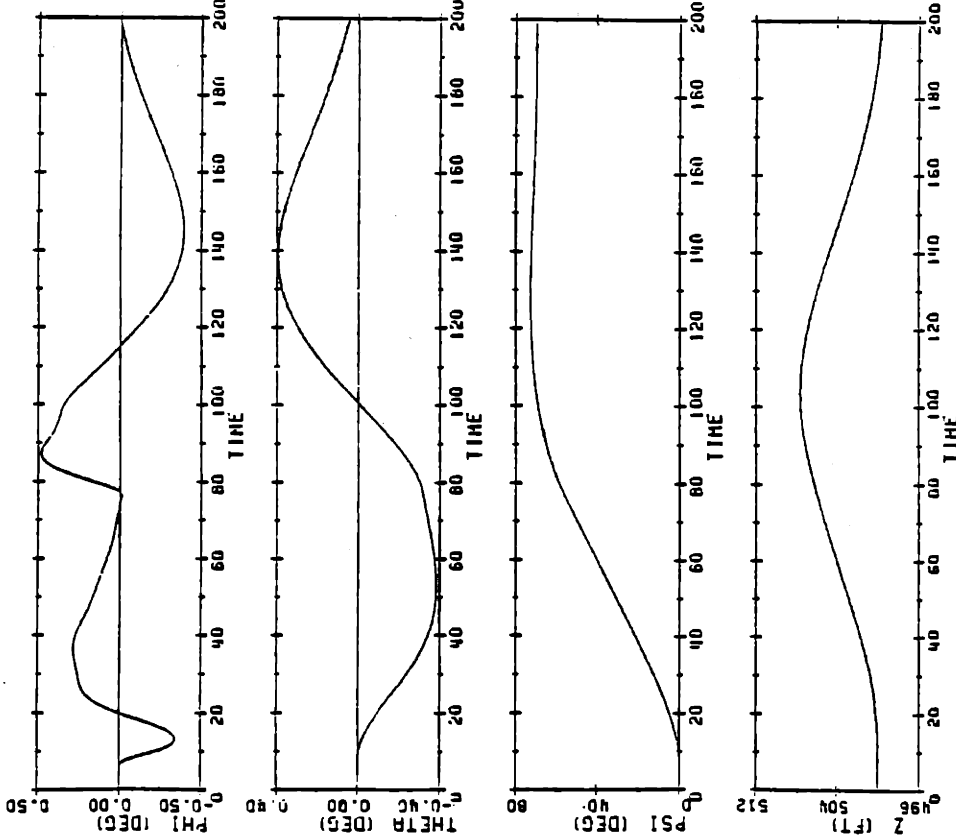


Figure 4.9 Symmetry Comparison for +/- 1 Degree/Second Yawrate

ATTITUDE AND DEPTH

NONLINEAR INTEGRATION FOR 1 DEG/SEC COMMANDED YAWRATE



ATTITUDE AND DEPTH

NONLINEAR INTEGRATION FOR -1 DEG/SEC COMMANDED YAWRATE

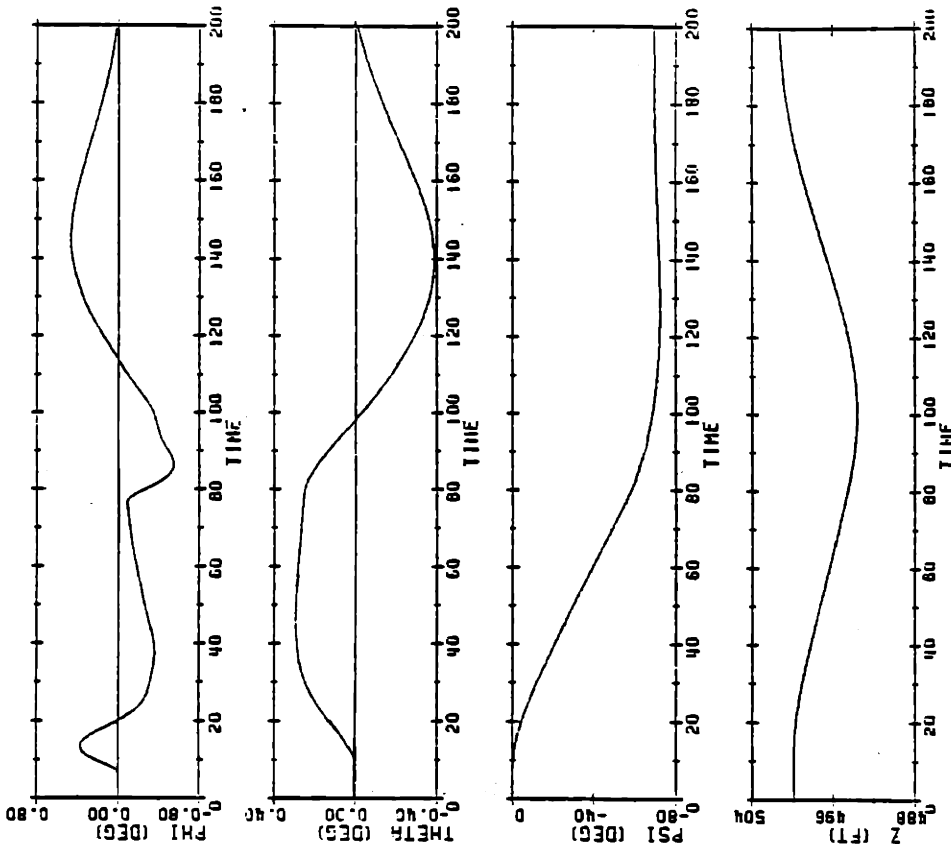
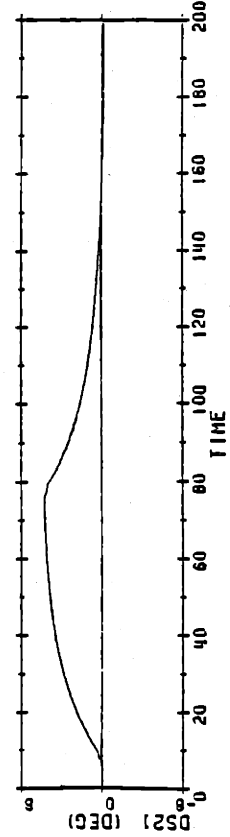
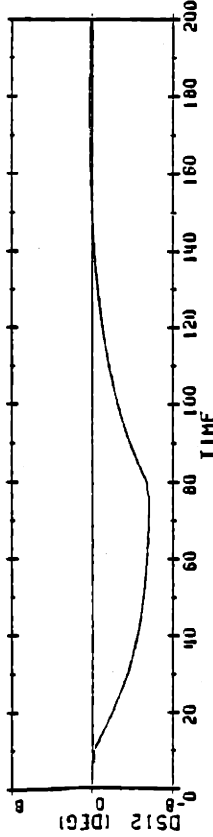
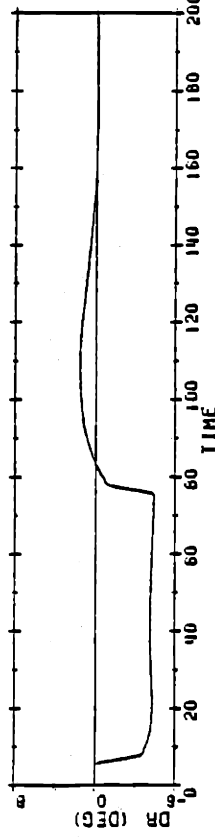
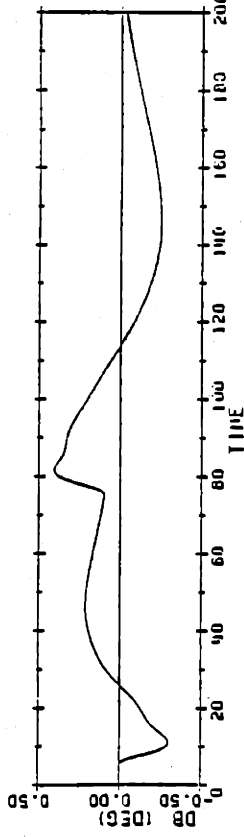


Figure 4.9 Symmetry Comparison for +/- 1 Degree/Second Yawrate

CONTROL INPUTS

NONLINEAR INTEGRATION FOR 1 DEG/SEC COMMANDED YAWRATE



CONTROL INPUTS

NONLINEAR INTEGRATION FOR -1 DEG/SEC COMMANDED YAWRATE

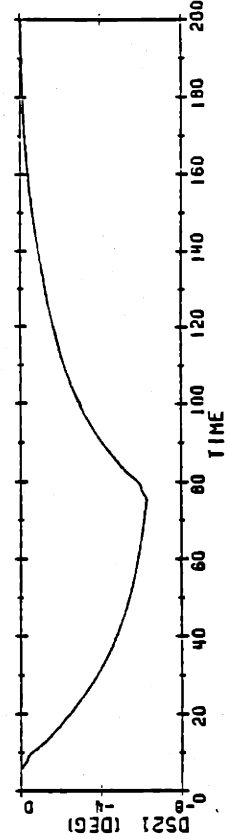
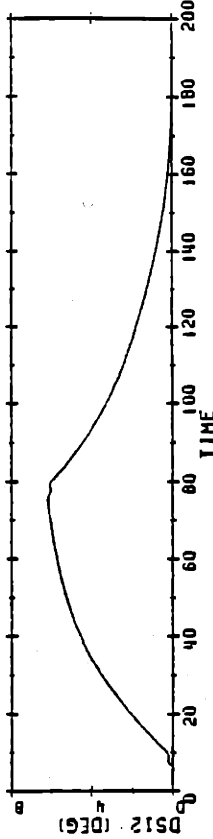
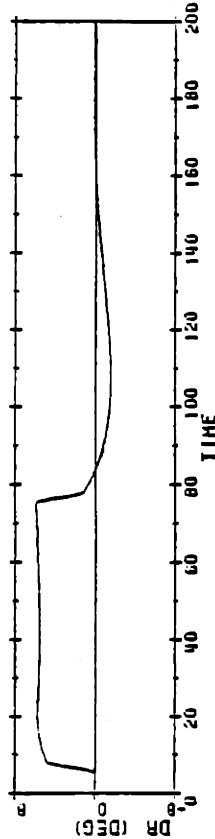
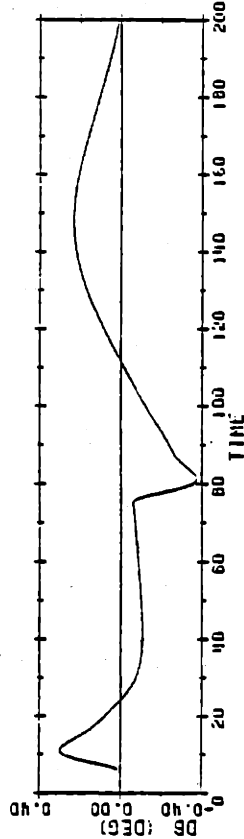
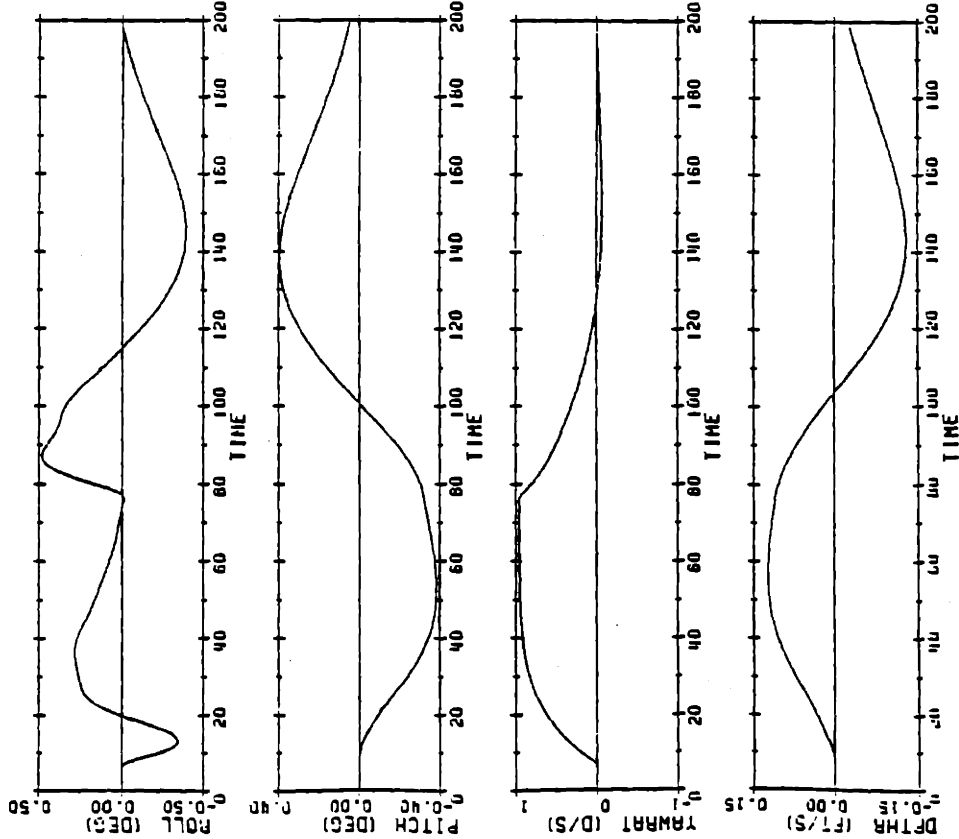


Figure 4.9 Symmetry Comparison for +/- 1 Degree/Second Yawrate

OUTPUTS

NONLINEAR INTEGRATION FOR 1 DEG/SEC COMMANDED YAWRATE



OUTPUTS

NONLINEAR INTEGRATION FOR -1 DEG/SEC COMMANDED YAWRATE

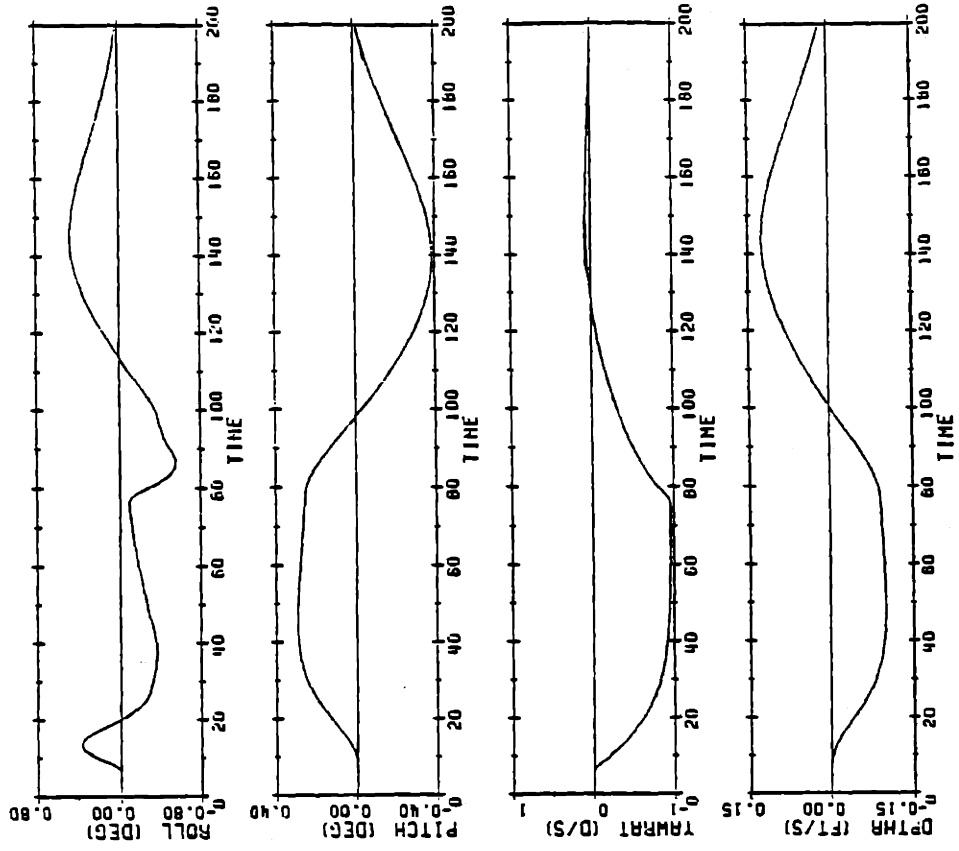


Figure 4.9 Symmetry Comparison for +/- 1 Degree/Second Yawrate

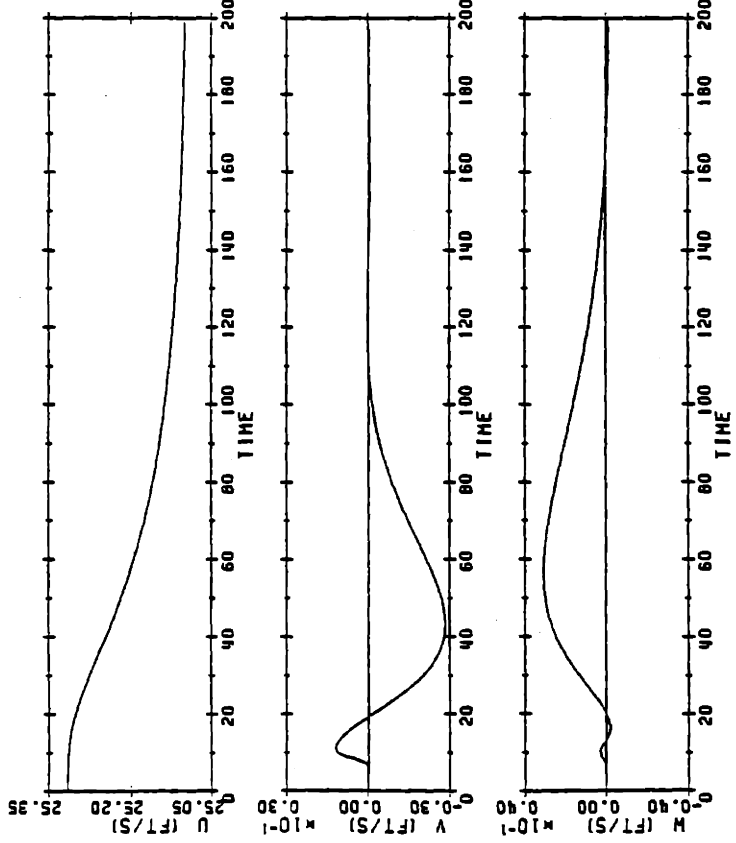
slight movement of the fairwater planes. The slight differences which do exist are most likely due to propeller torque with a smaller contribution probably due to the -1 degree/second command (turn to port) being in the direction of the nominal point whereas the +1 degree/second (turn to starboard) is in the opposite direction.

Another maneuver which demonstrates motion about a plane of symmetry is displayed in Figure 4.10. At $t = 5$ seconds, a ± 5 roll angle step input is applied. The sternplanes deflect differentially to a steady-state value of approximately ± 7.5 degrees to achieve the desired roll angle. The rudder and fairwater planes deflect only slightly in reaction to the initial transients and then go to zero.

Various other maneuvers were simulated for depthrate with and without pitch to ensure control surface deflections for motion in the vertical plane were practical. The results of the simulation for a 1 foot/second depthrate are presented in Figure 4.11. The singular value decomposition in Figure 4.8 predicts that the fairwater planes should deflect in response to this reference command. This does indeed occur as shown in Figure 4.11 and is accompanied by a small deflection of the sternplanes which produce a moment to counter the slight trimming moment induced by the fairwater planes.

Figure 4.12 shows the results of the simulation for a 4.5 feet/second at -10 degree pitch. The initial decrease is attributed to the additional drag generated by movement of the control surfaces. As the control surface movements decrease, forward speed is regained. The small transient disturbances in the states are a result of of control surface deflection and to a lesser degree, mild cross-coupling. Referring again to the singular value decomposition in Figure 4.8 (σ_{11} and σ_{44}), one would predict

VELOCITIES



VELOCITIES

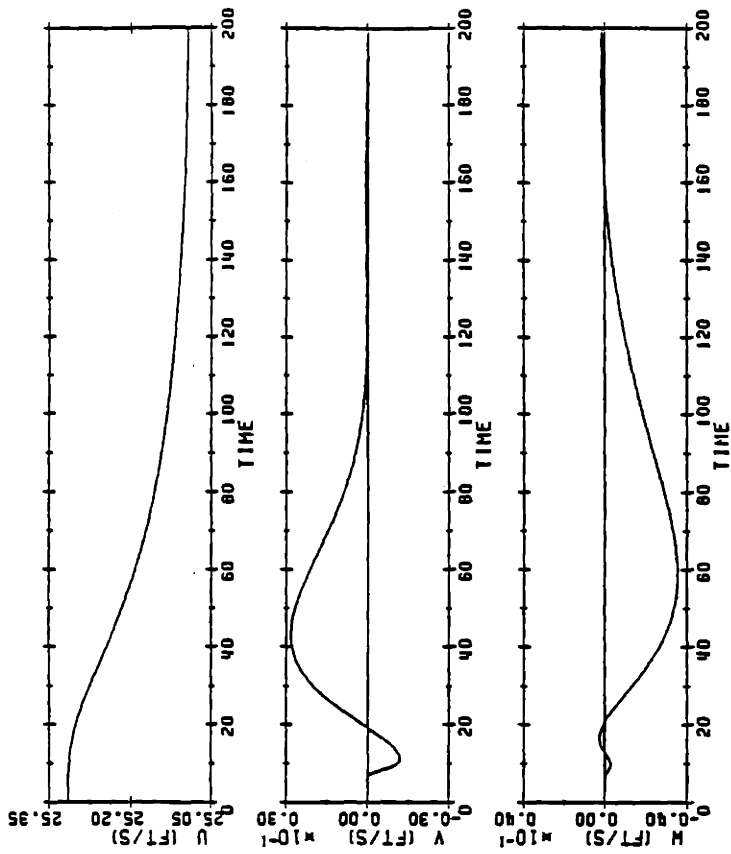


Figure 4.10 Symmetry Comparison for +/- 5 Degree Roll Angle

ANGULAR VELOCITIES

ANGULAR VELOCITIES

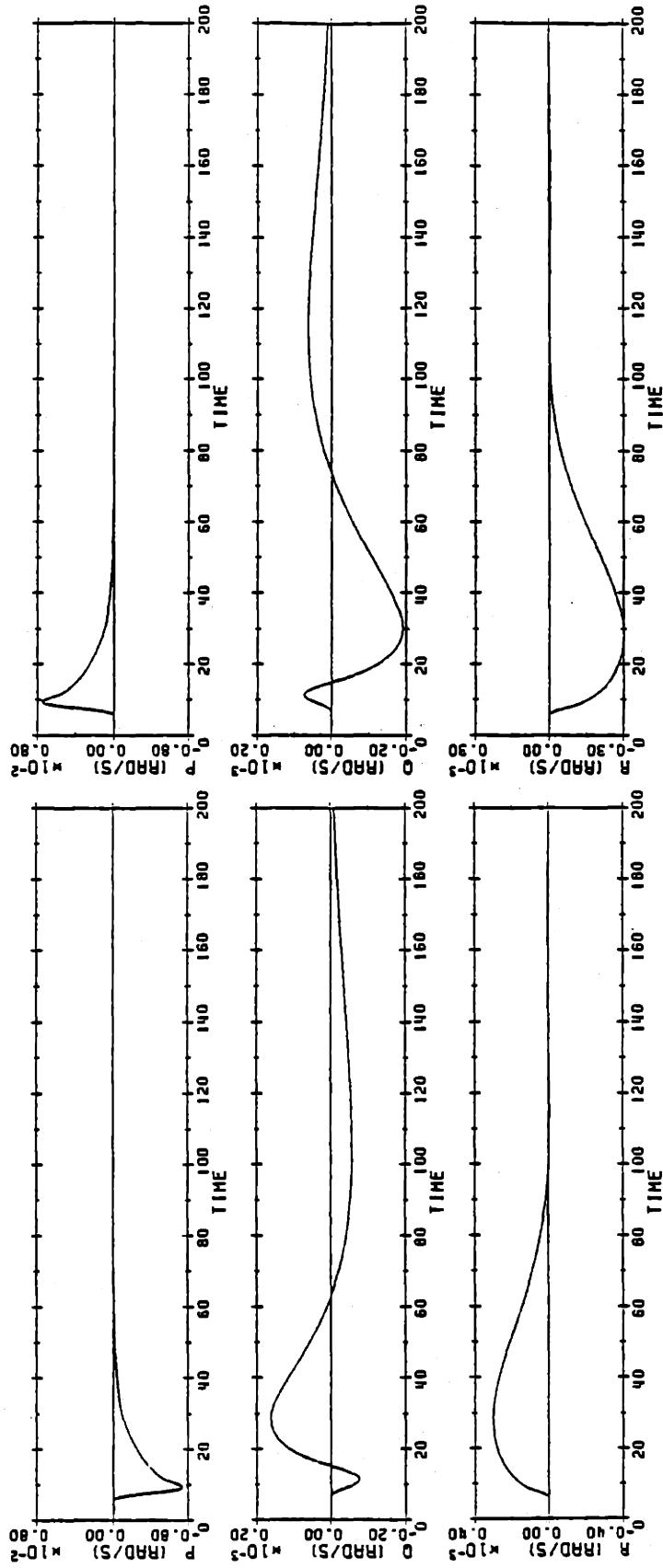
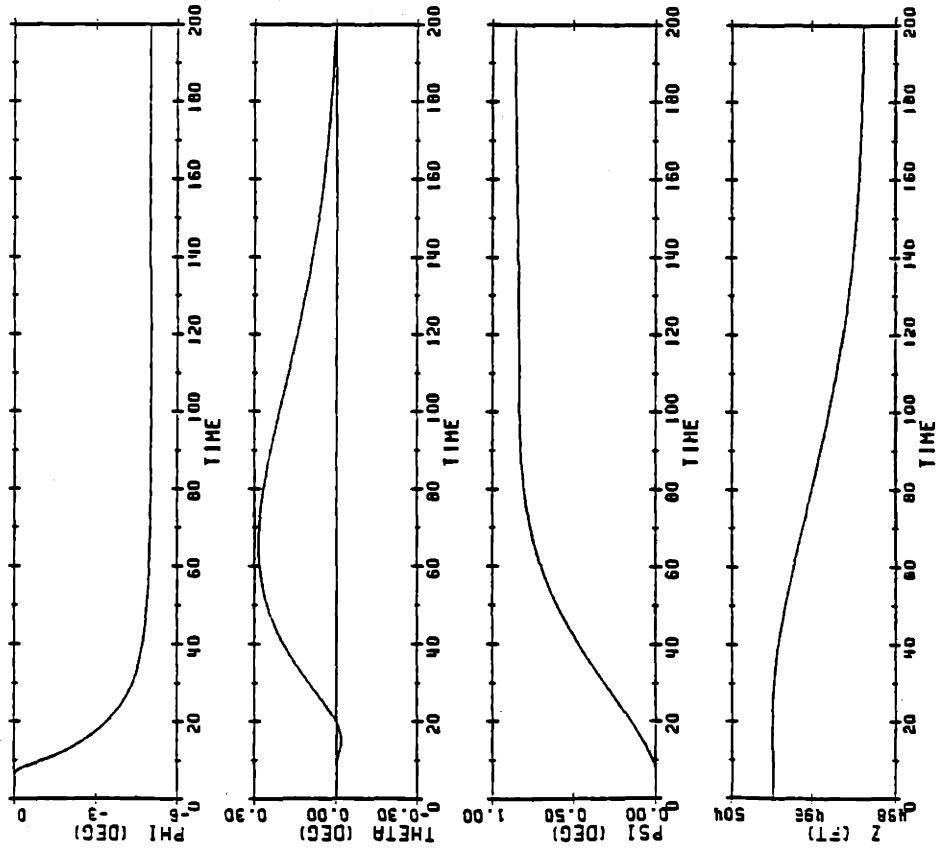


Figure 4.10 Symmetry Comparison for +/- 5 Degree Roll Angle

ATTITUDE AND DEPTH



ATTITUDE AND DEPTH

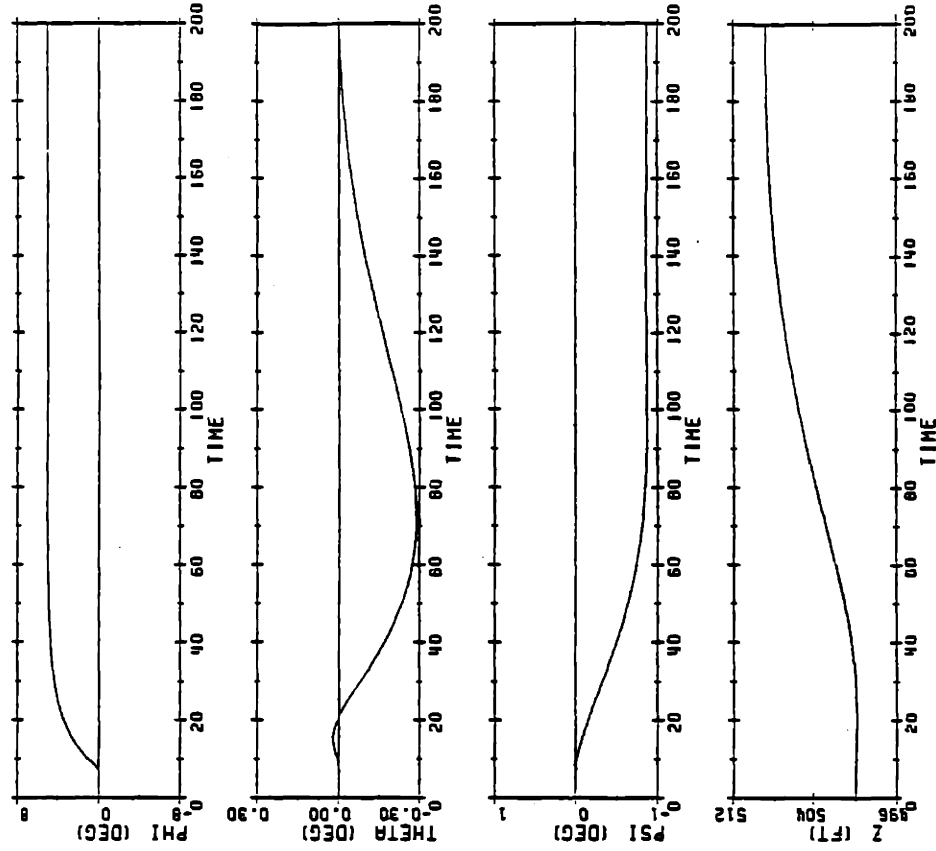
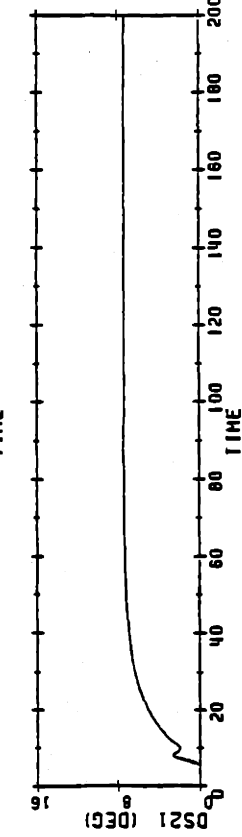
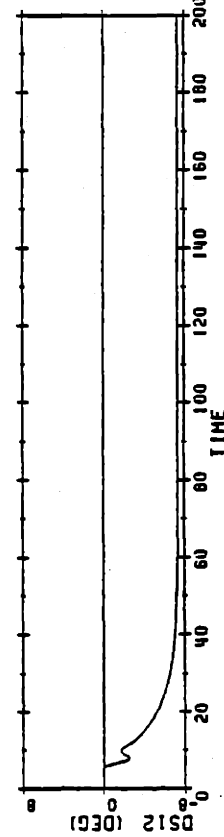
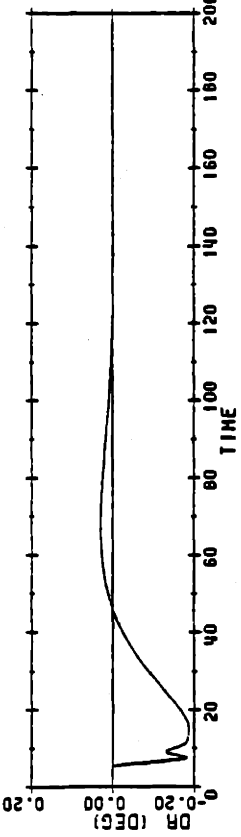
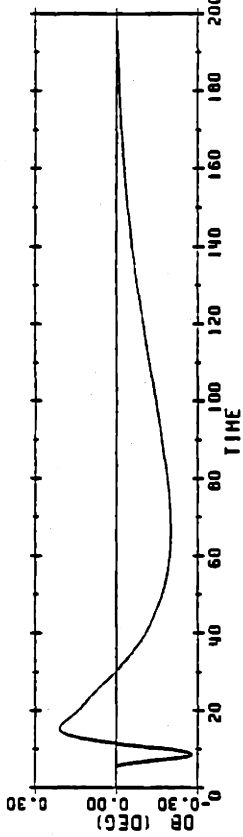


Figure 4.10 Symmetry Comparison for +/- 5 Degree Roll Angle

CONTROL INPUTS



CONTROL INPUTS

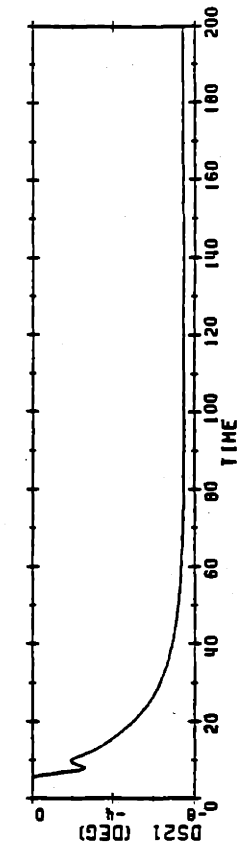
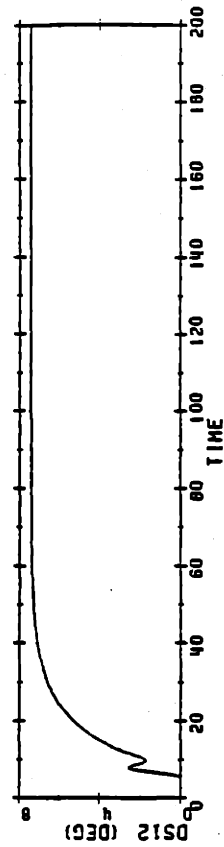
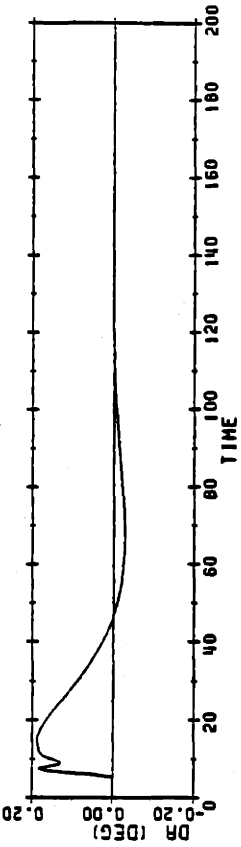
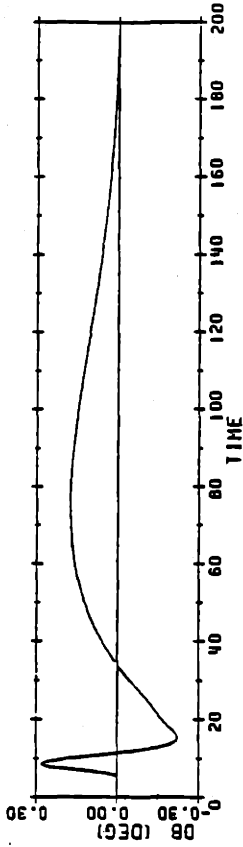
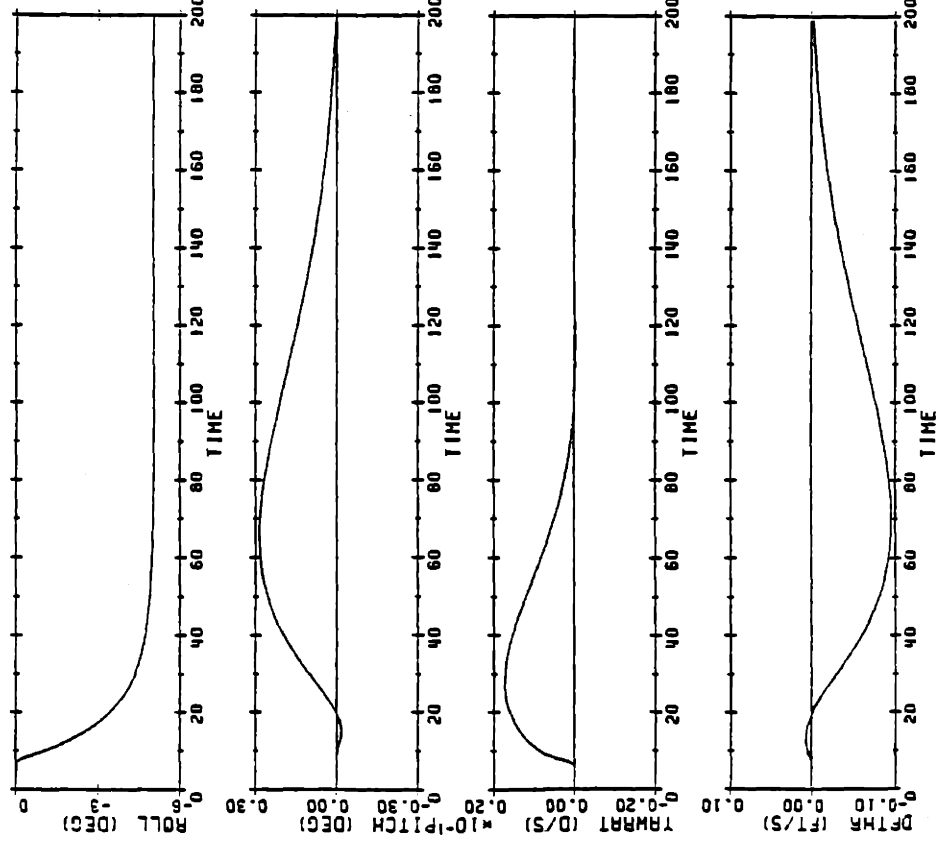


Figure 4.10 Symmetry Comparison for +/- 5 Degree Roll Angle

OUTPUTS



OUTPUTS

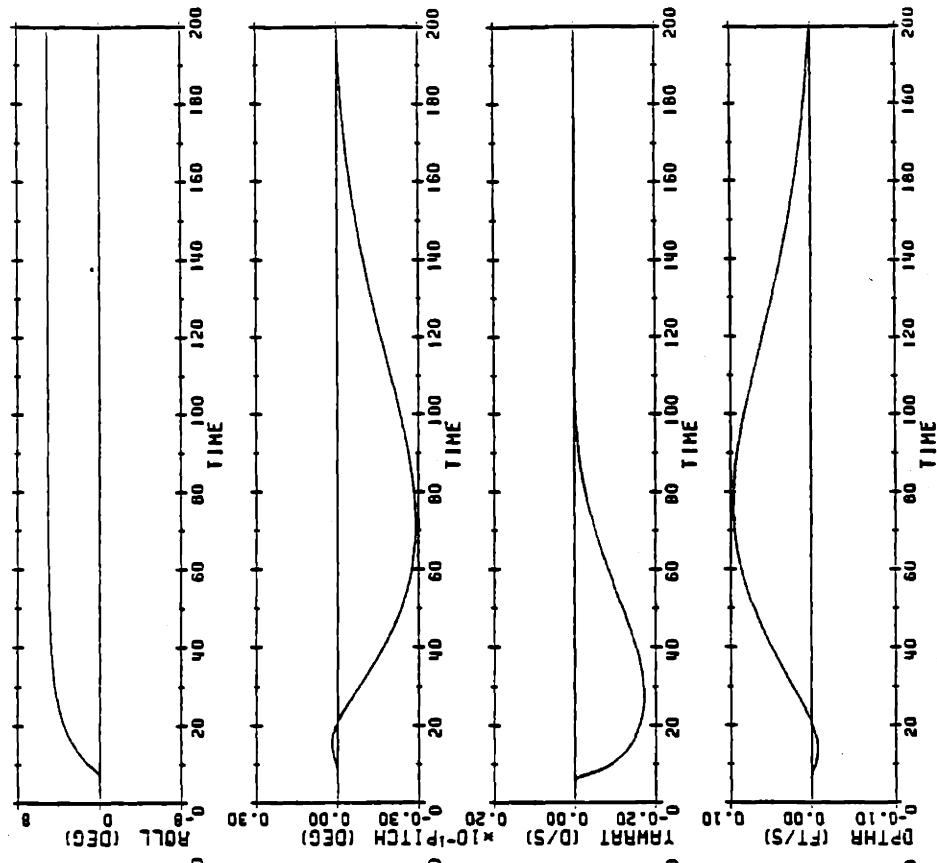
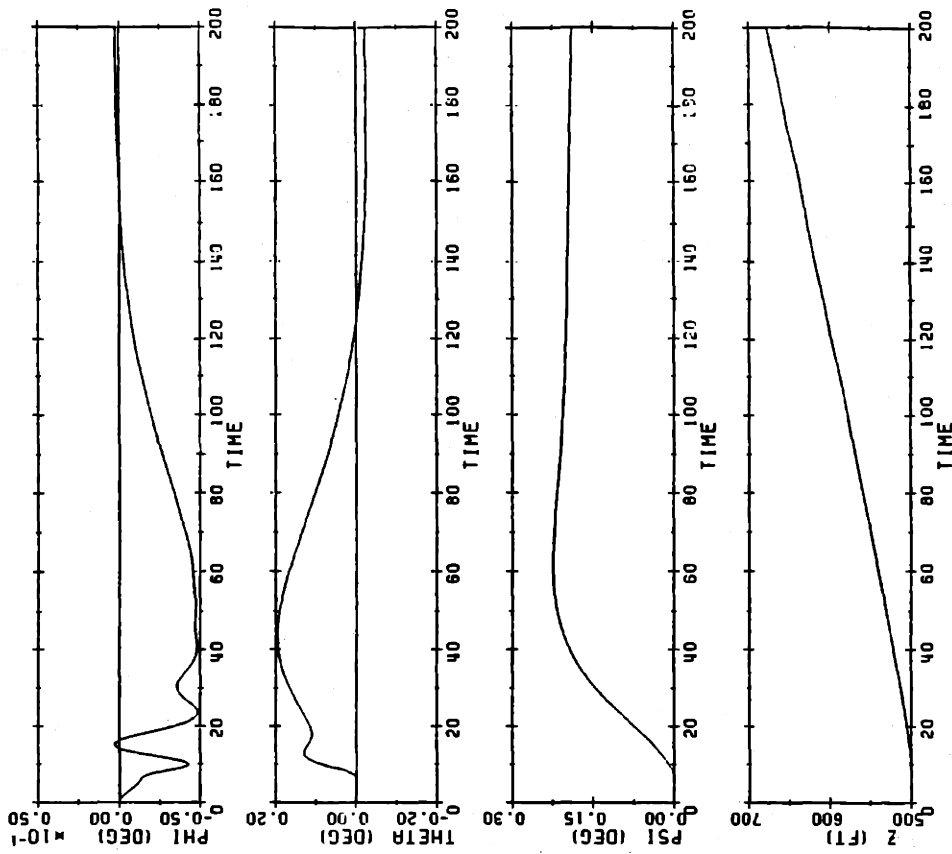


Figure 4.10 Symmetry Comparison for +/- 5 Degree Roll Angle

ATTITUDE AND DEPTH

NONLINEAR INTEGRATION FOR 1 FT/SEC DEPTH RATE, 15 KNOT COMPENSATOR



VELOCITIES

NONLINEAR INTEGRATION FOR 1 FT/SEC DEPTH RATE, 15 KNOT COMPENSATOR

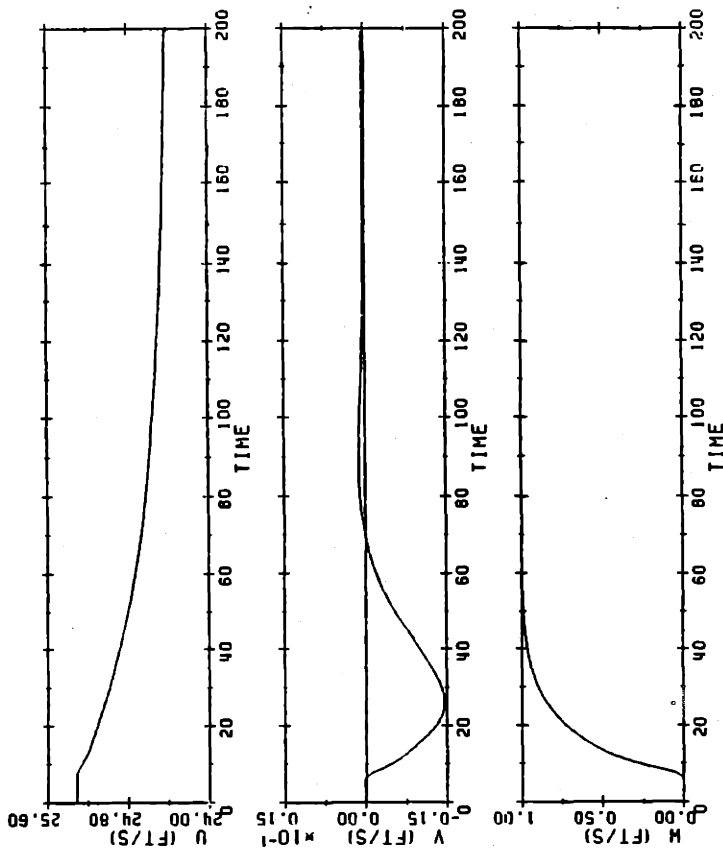
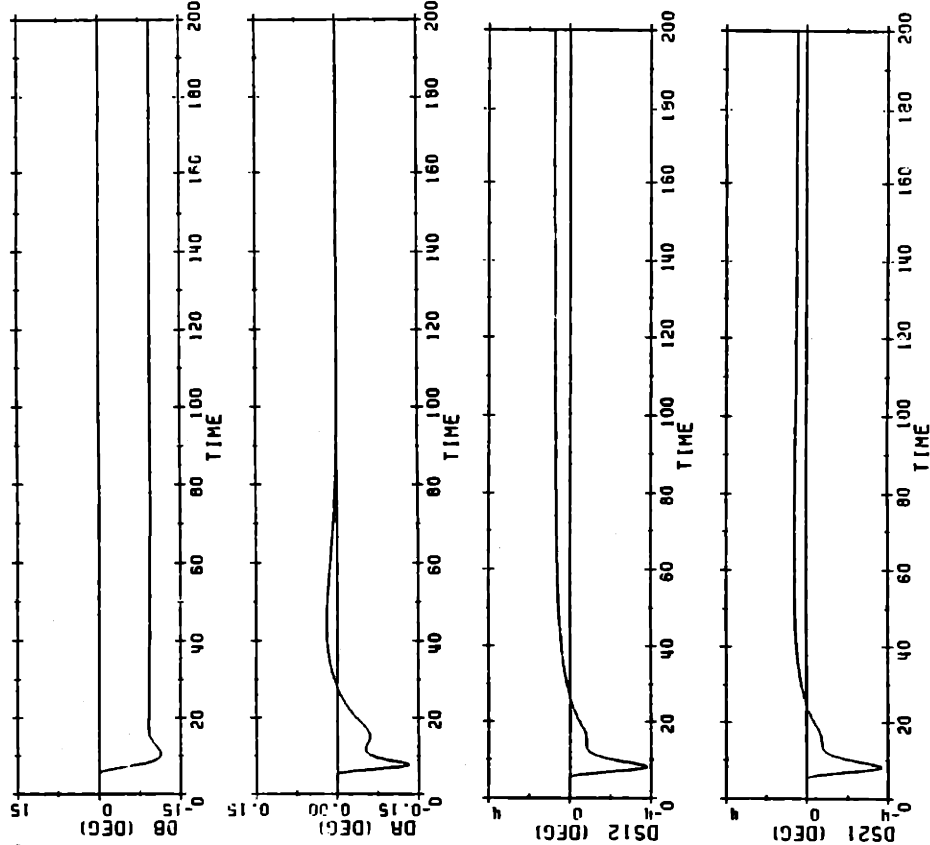


Figure 4.11 Simulation for 1 Foot/Second Depthrate

CONTROL INPUTS

NONLINEAR INTEGRATION FOR 1 FT/SEC DEPTH RATE, 15 KNOT COMPENSATOR



OUTPUTS

NONLINEAR INTEGRATION FOR 1 FT/SEC DEPTH RATE, 15 KNOT COMPENSATOR

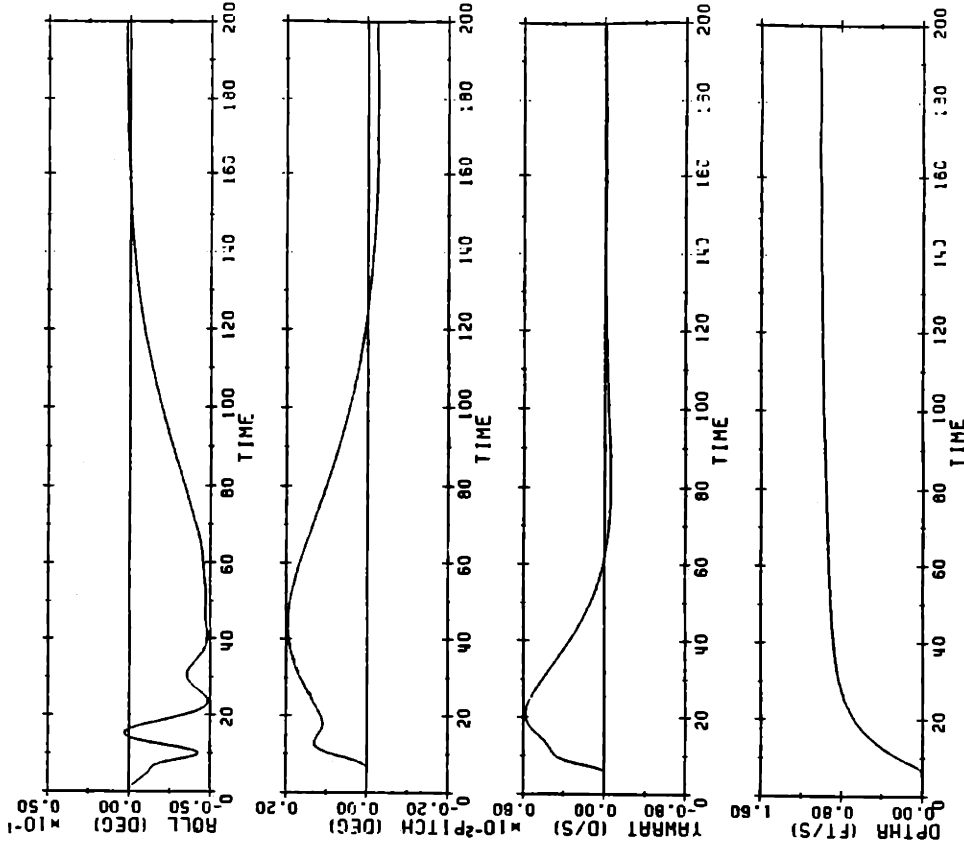
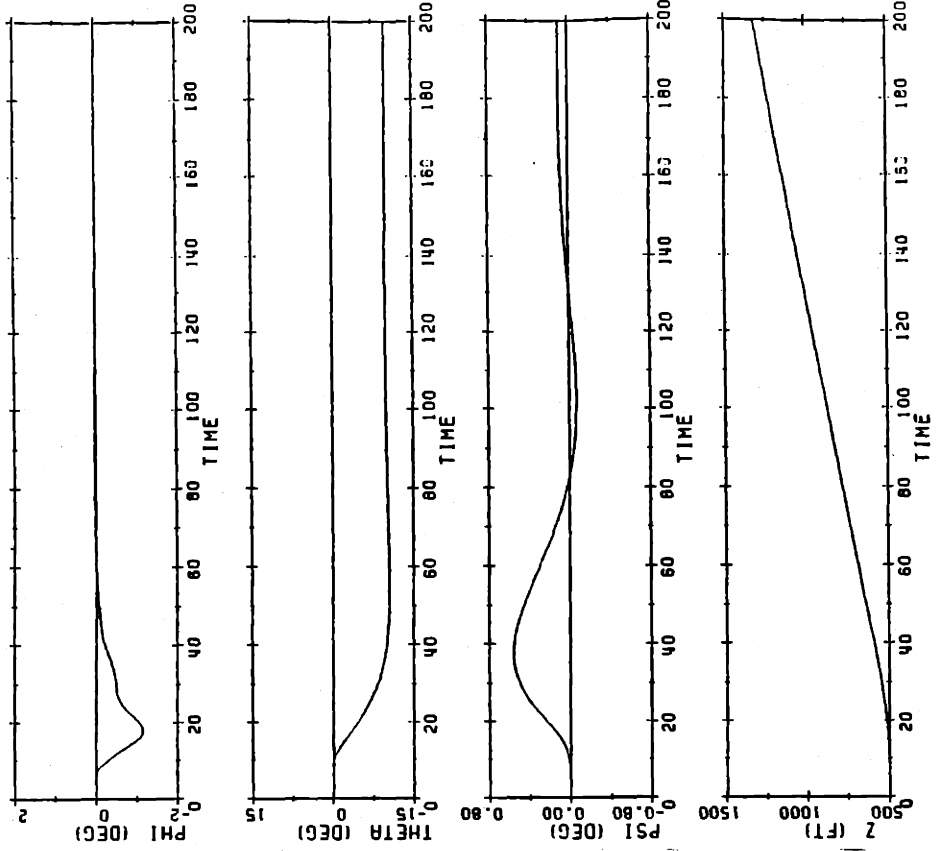


Figure 4.11 Simulation for 1 Foot/Second Depthrate

ATTITUDE AND DEPTH

NONLINEAR INTEGRATION FOR 4.5 FT/SEC AND -10 DEG



VELOCITIES

NONLINEAR INTEGRATION FOR 4.5 FT/SEC AND -10 DEG

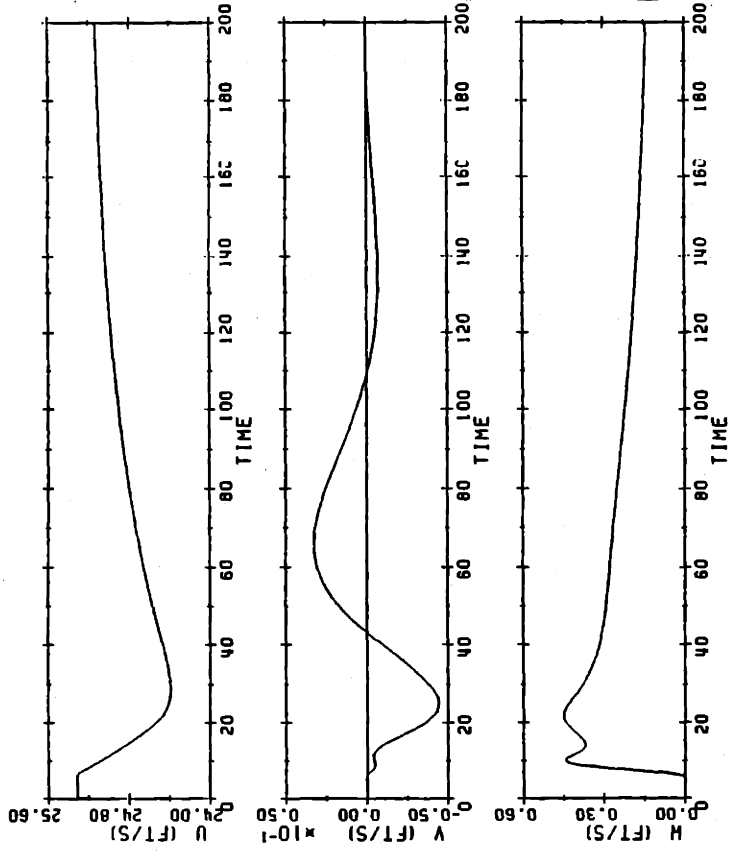
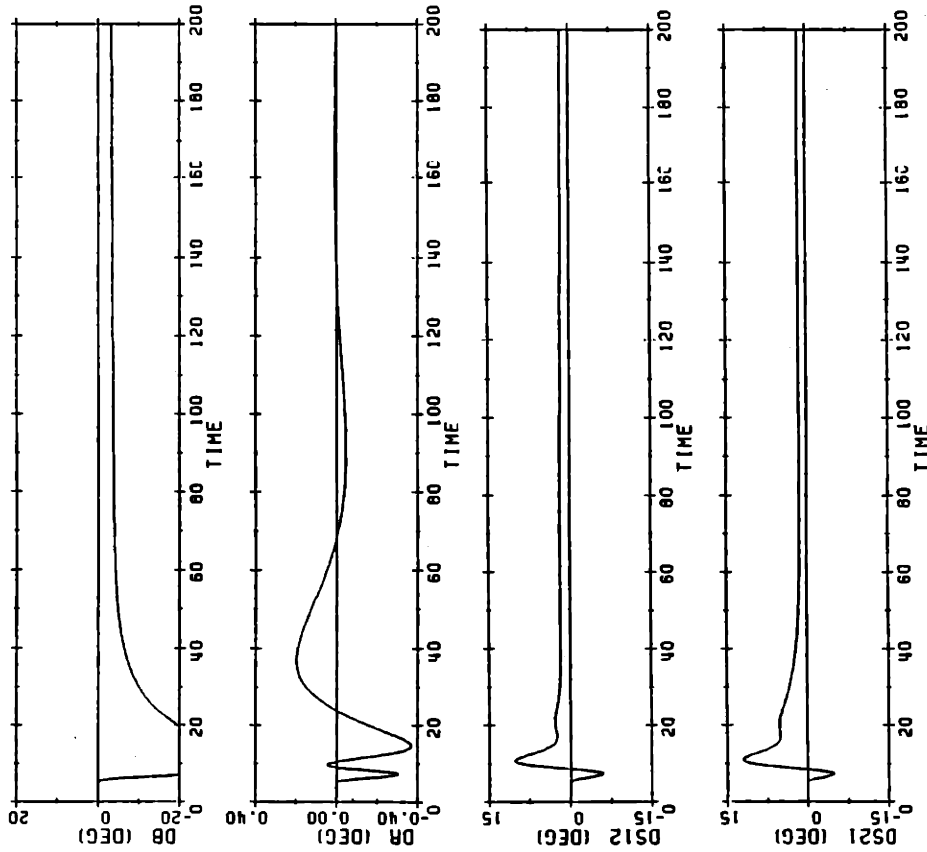


Figure 4.12 Simulation for 4.5 Feet/Second and -10 Degree Pitch Angle

CONTROL INPUTS

NONLINEAR INTEGRATION FOR 4.5 FT/SEC AND -10 DEG



OUTPUTS

NONLINEAR INTEGRATION FOR 4.5 FT/SEC AND -10 DEG

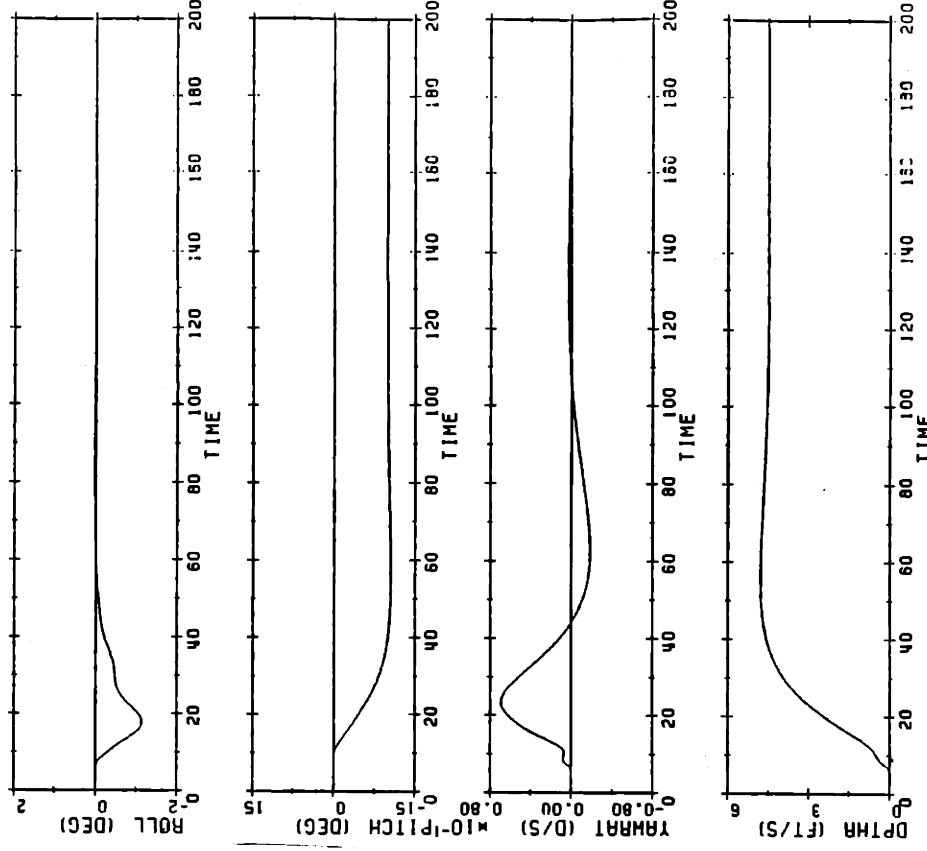


Figure 4.12 Simulation for 4.5 Feet/Second and -10 Degree Pitch Angle

deflection of the fairwater planes in response to the depthrate command, sternplanes in response to the ordered pitch angle and minor deflection of the rudder. Figure 4.12 confirms this to be the case.

Subsequently, simulations which flexed the compensated system in the vertical and horizontal planes of motion simultaneously were made at speeds from 15 to 30 knots as a prelude to gain scheduling. These simulations and justification for not employing gain scheduling are discussed in Chapter 5.

4.5 Summary

The first section of this chapter covered the LQG/LTR methodology for robustness and performance at the plant output. Next, the design and analysis of the linear compensator for the S15R1 model were presented. Finally, results of some simulations at 15 knots were presented. These simulations demonstrated the symmetry of yawrate and roll angle and confirmed the predictions of the singular value decomposition for the transfer function relating the control inputs to the reference commands. Chapter 5 will cover some additional simulations which were performed for speeds from 15 to 30 knots. A comparison to the compensator designed by Martin [8] is also presented.

CHAPTER 5

ADDITIONAL ANALYSIS OF THE COMPENSATOR

5.1 Introduction

This chapter covers additional analysis performed on the compensator designed for the S15R1 linear model at speeds from 15 to 30 knots. This is followed by a comparison to the S30R1 compensator designed by Martin [8]. As a result of this analysis, it was determined that while gain scheduling would offer improved performance, it was not required to assure a closed loop stable system and therefore would not be implemented.

5.2 Additional Analysis of S15R1 Compensator

It has been shown that using active roll control through differential deflection of the sternplanes reduces the depth excursion problem experienced by a high speed submarine in a turn. In this section, it becomes obvious that active roll control also provides improved performance for depth changing and coordinated maneuvers over a wide speed range.

To implement a gain scheduling scheme, linear compensators must be designed for various discrete speeds in the speed range of interest. A question arises as to how to select those discrete speeds. In this case, quantifying the modelling error between the linear model and the actual plant is difficult. We can use the robustness singular value inequalities (3.10) and (3.11) in a similar manner by assuming the linear model at one speed is the real system $\tilde{G}(s)$, the linear model at another speed is the

model $\underline{G}(s)$ and using the relationships (3.8) and (3.9) as a gauge of the errors between the models. This is not strictly accurate representation of the errors and the following comments should be kept in mind. Due to this assumption, the error between the S15R1 model and the actual 30 knot system is probably larger in some directions and smaller in others. The inequalities provide a conservative estimate of stability robustness so that the system may be stable even if the relations (3.10) and (3.11) do not hold. These two conditions tend to offset one another and determination of system stability must be confirmed through extensive simulation.

A comparison of the singular values of the S15R1 and S30R1 linear models is shown in Figure 5.1. At low frequency, the singular values of S15R1 are generally lower than those of S30R1 with the exception of the minimum singular values which are identical up to approximately 0.05 radians/second. We see that use of integral augmentation has increased the gain of all singular values by approximately 60 dB at 0.001 radians/second and has shifted the maximum crossover frequency somewhat higher. The state space matrices for S30R1 can be found in Appendix C1.

Preliminary simulations showed that the compensator designed for the 15 knot model adequately controlled the nonlinear model even at 30 knots. Assuming the S30R1 model as representative of the real or nominal system $\tilde{\underline{G}}(s)$ and the S15R1 model as the system model $\underline{G}(s)$, we can get a feel for the error of the S15R1 model at 30 knots. Figure 5.2 shows the comparison of the singular values of $[\underline{I} + (\underline{G}(s)\underline{K}(s))^{-1}]$ and $[\underline{I} + \underline{G}(s)\underline{K}(s)]$ with the singular values of $[\underline{L}(s) - \underline{I}]$ and $[\underline{L}^{-1}(s) - \underline{I}]$ and reveals that the singular value inequalities (3.10) and (3.11) do not hold. As previously stated, the relations provide a conservative estimate of stability and the

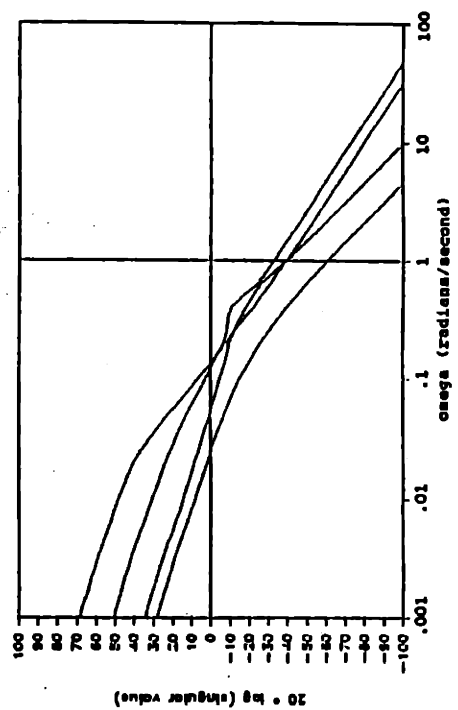
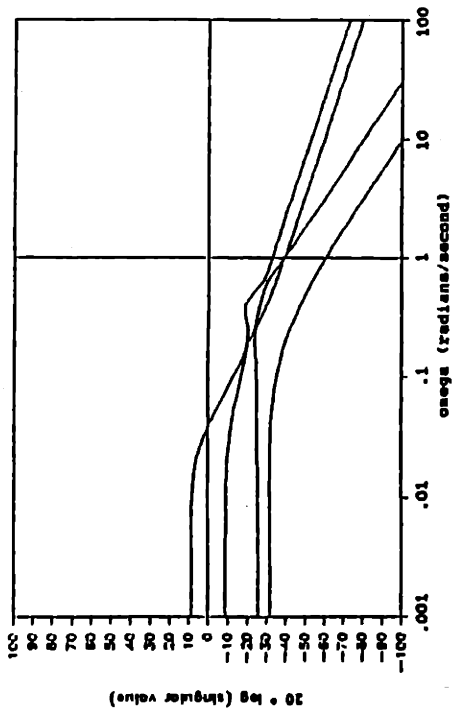
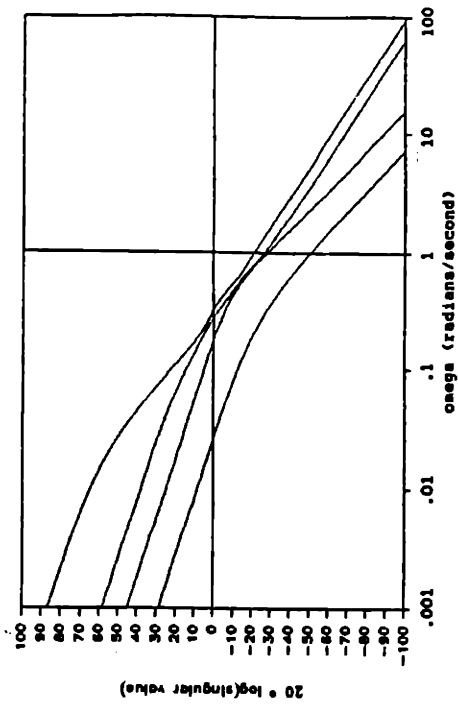
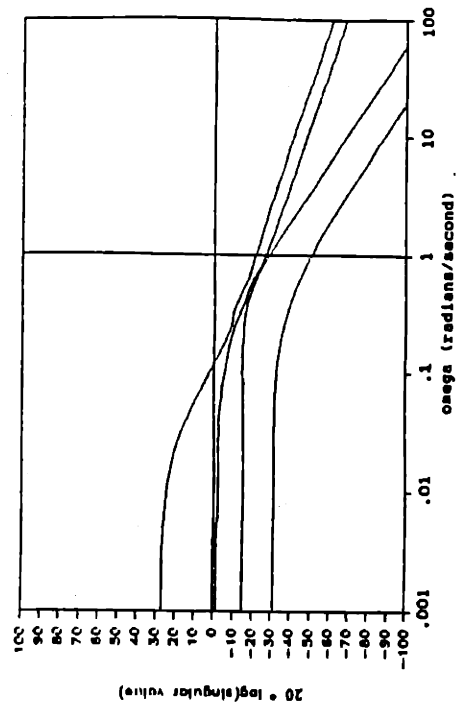


Figure 5.1 Comparison of Singular Values of S1SR1 and S3OR1 Linear Models

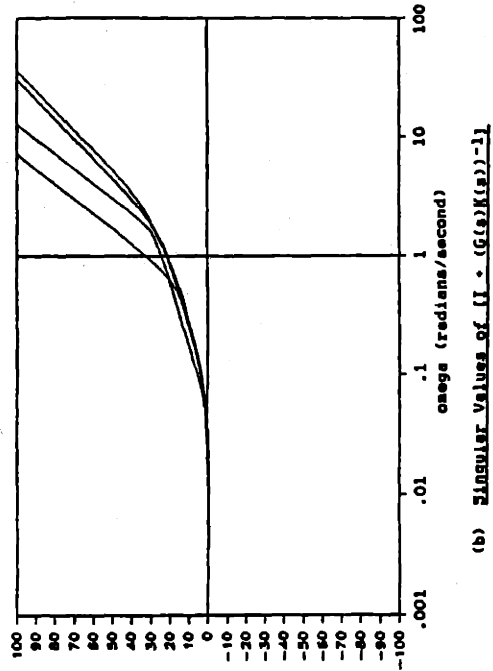
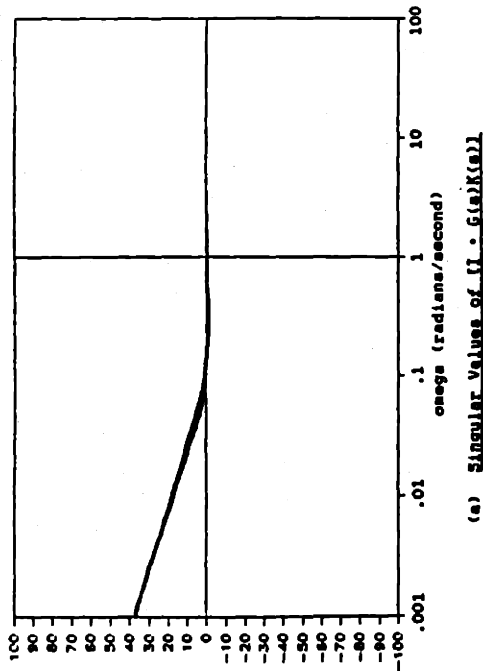
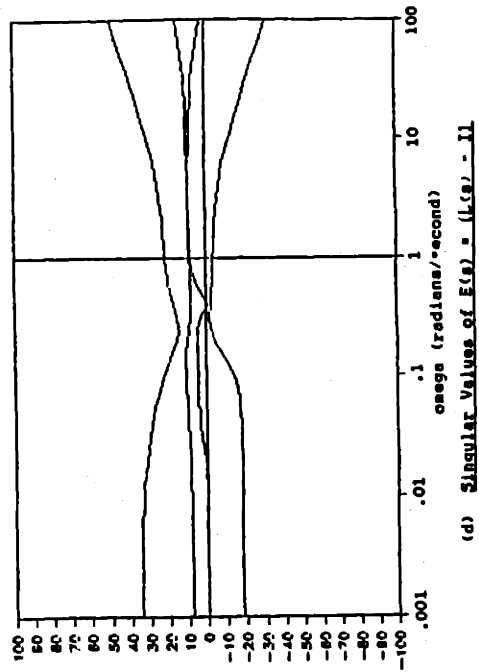
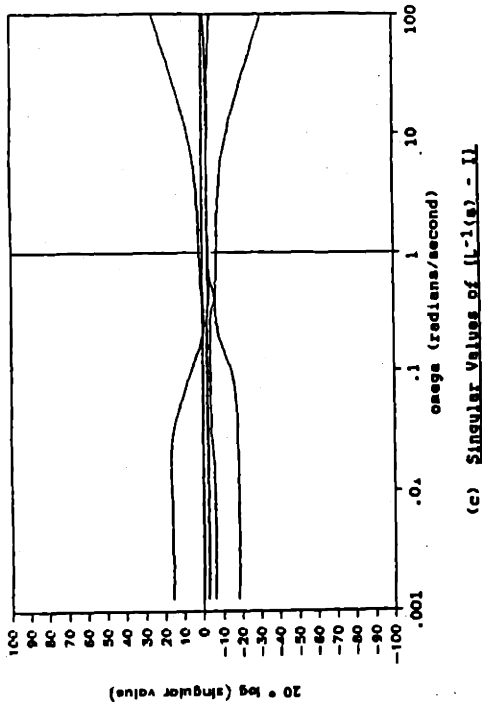


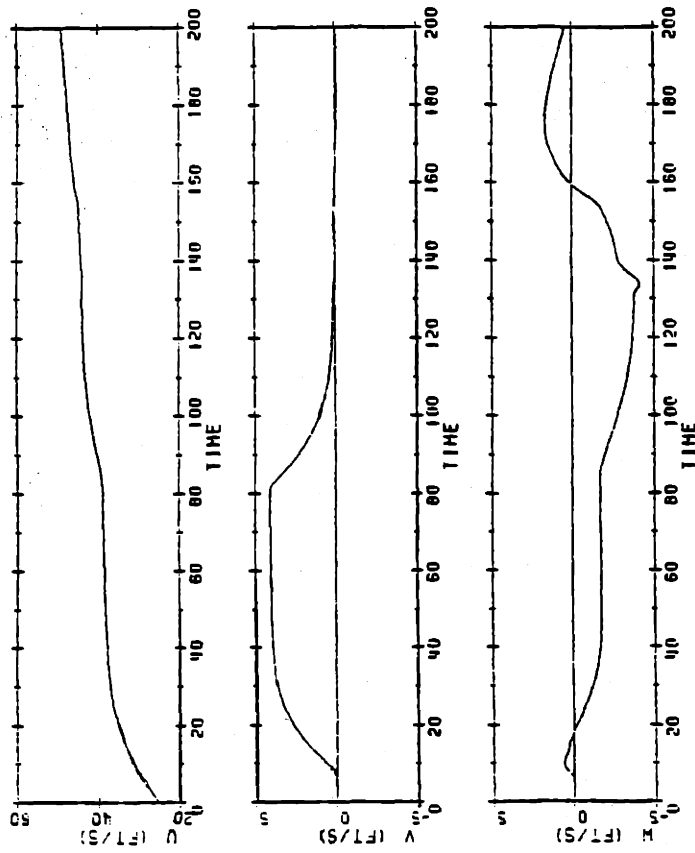
Figure 5.2 Robustness Comparison of $G(s)K(s)$ and the Error $E(s)$

direction of the instability (if it does exist) must be determined through testing. The results of some nonlinear simulations for the 15 knot compensator are now presented to support this claim.

The maneuvers presented in Chapter 4 were rerun for various speed between 15 and 30 knots with favorable results. Since these maneuvers were not very stressful, two maneuvers which flexed the system were simulated. The first maneuver consisted of a combined dive and turn performed at 15 knots, at 30 knots, as speed increased from 15 to 30 knots and finally as speed decreased from 30 to 15 knots. The maneuver begins with a 4.5 feet/second depthrate, -10 degree pitch angle and -2 degree/second yawrate initially applied at $t = 5$ seconds. At $t = 80$ seconds, the yawrate command is zeroed, followed at $t = 130$ by the depthrate and pitch commands. Results of these simulations were satisfactory. For the sake of brevity, only the speed change maneuvers are presented. Figure 5.3 shows the results with the 15 to 30 knot run on the left. Both simulations were completed without encountering instability however, there were notable differences in the yawrate command following and minor differences in depth change. The roll angle for both simulations was adequately controlled after the initial transients due to control surface movement died out. Maximum pitch errors of approximately 3 degrees and 2 degrees respectively were experienced. The bottom line of this maneuver though was to effect a course and depth change through appropriate rate commands during a speed change to stress the system. Considering the time the rate commands were in effect, the depth should have increased to approximately 1060 feet and the course change have been 150 degrees. The 15 to 30 knot simulation displayed some overshoot in depth but both converged to within a few percent of the intended depth as did the 30 to 15 knot simulation. Even

VELOCITIES

NONLINEAR INTEGRATION FOR 4.5 FT/SEC, -10 DEG & -2 DEG/SEC



VELOCITIES

NONLINEAR INTEGRATION FOR 4.5 FT/SEC, -10 DEG & -2 DEG/SEC

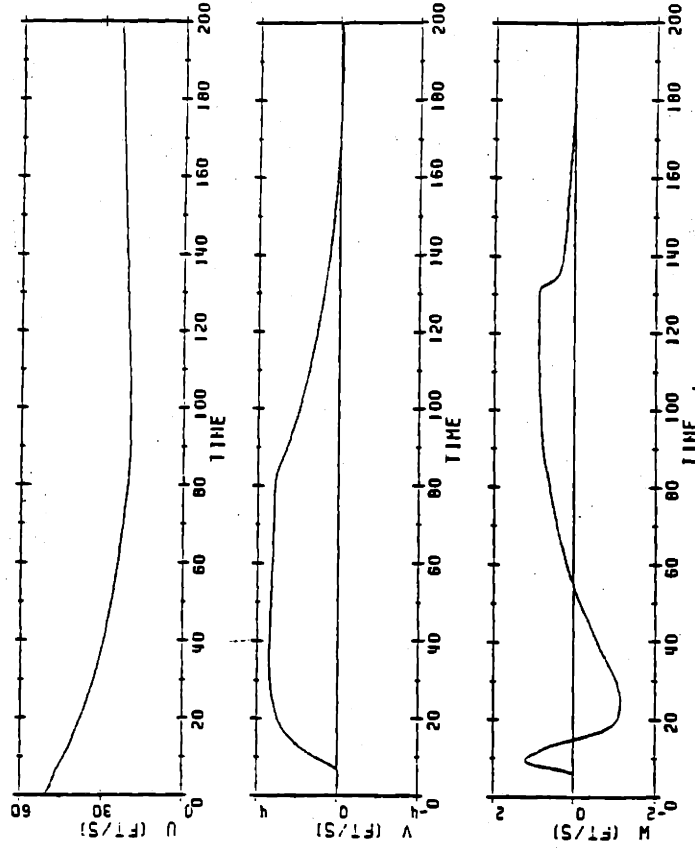
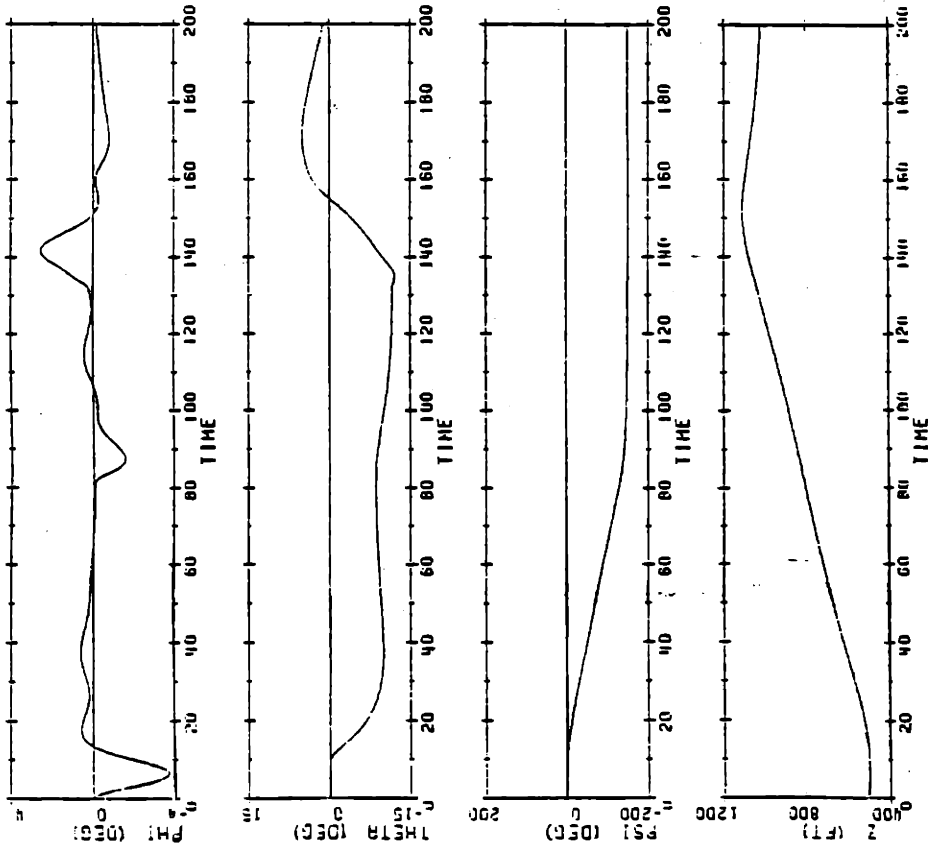


Figure 5.3 Comparison of 15 Knot Compensator Performance for Simultaneous Turn and Dive During Speed Change

ATTITUDE AND DEPTH

NONLINEAR INTEGRATION FOR 4.5 FT/SEC, -10 DEG A, -2 DEG/SEC



ATTITUDE AND DEPTH

NONLINEAR INTEGRATION FOR 4.5 FT/SEC, -10 DEG A, -2 DEG/SEC

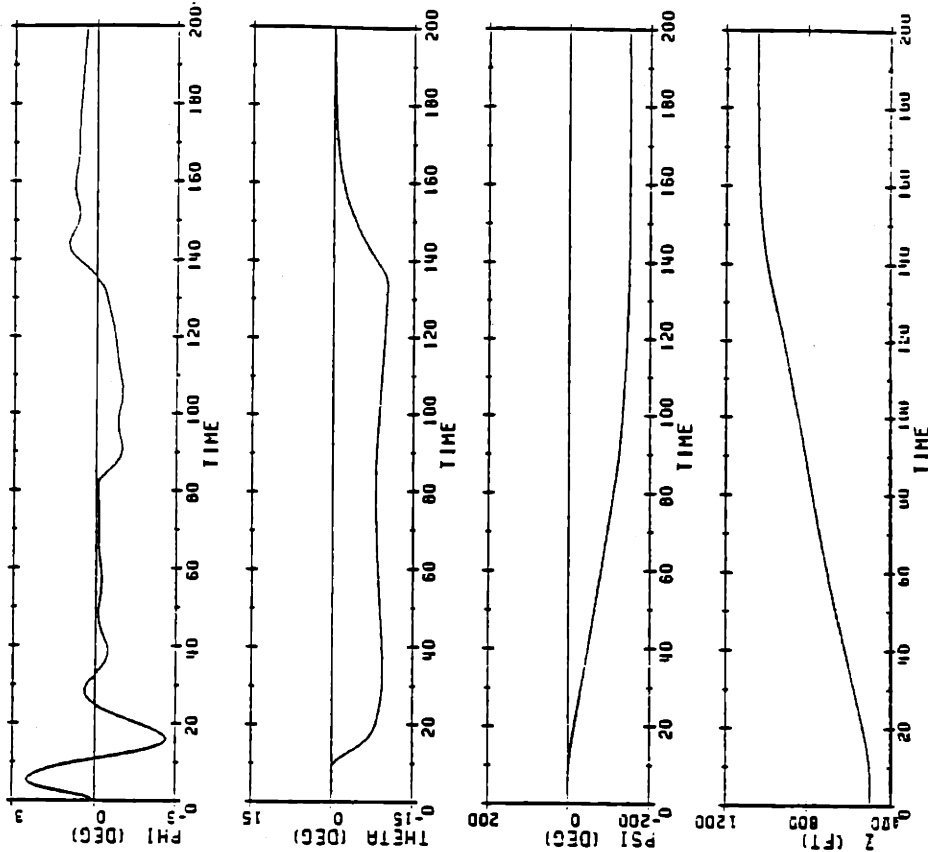
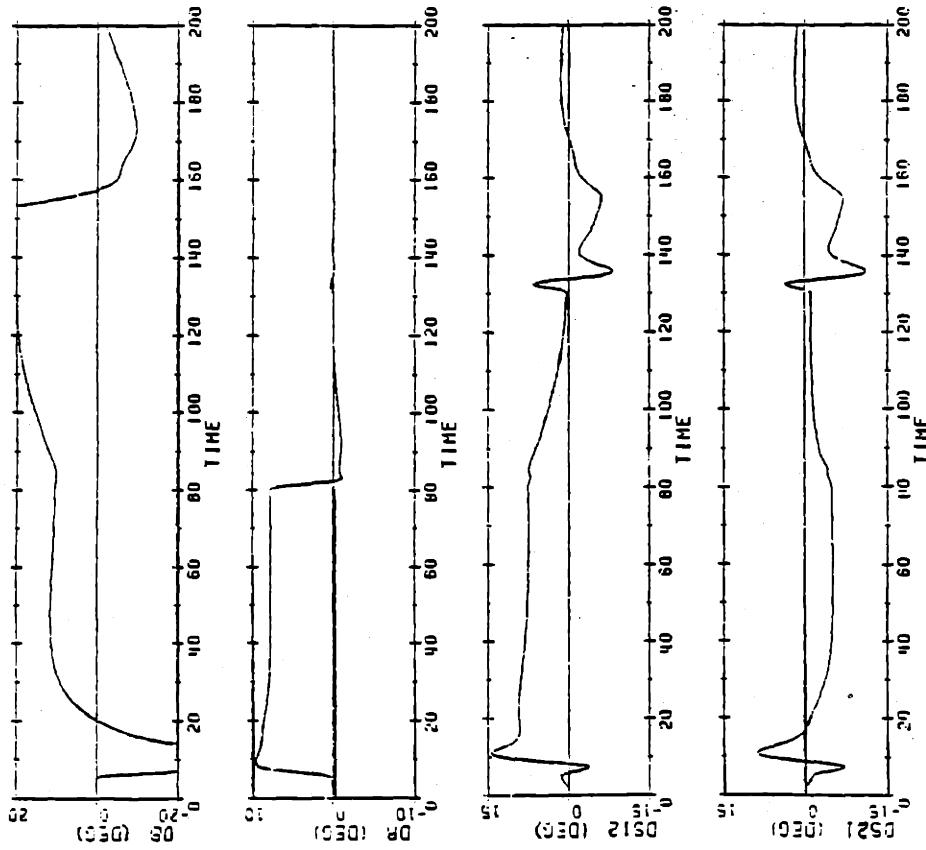


Figure 5.3 Comparison of 15 Knot Compensator Performance for Simultaneous Turn and Dive During Speed Change

CONTROL INPUTS

NONLINEAR INTEGRATION FOR 4.5 FT/SEC, -10 DEG & -2 DEG/SEC



CONTROL INPUTS

NONLINEAR INTEGRATION FOR 4.5 FT/SEC, -10 DEG & -2 DEG/SEC

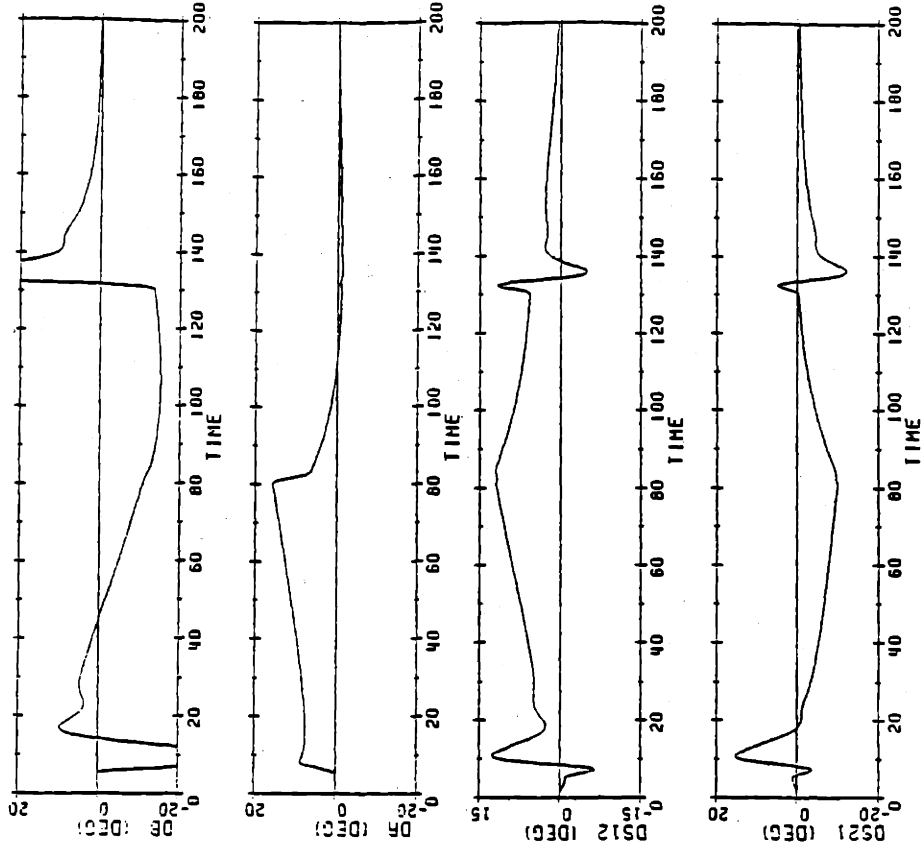
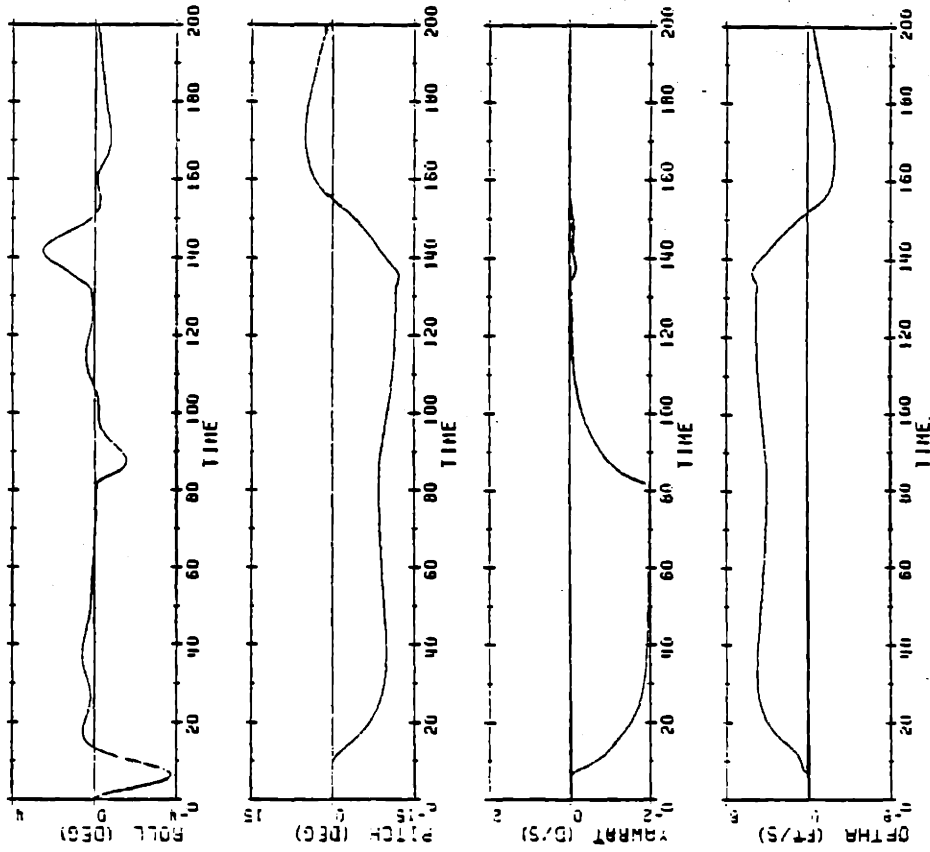


Figure 5.3 Comparison of 15 Knot Compensator Performance for Simultaneous Turn and Dive During Speed Change

OUTPUTS

NONLINEAR INTEGRATION FOR 4.5 FT/SEC. -10 DEG 4 -2 DEG/SEC



OUTPUTS

NONLINEAR INTEGRATION FOR 4.5 FT/SEC. -10 DEG 4 -2 DEG/SEC

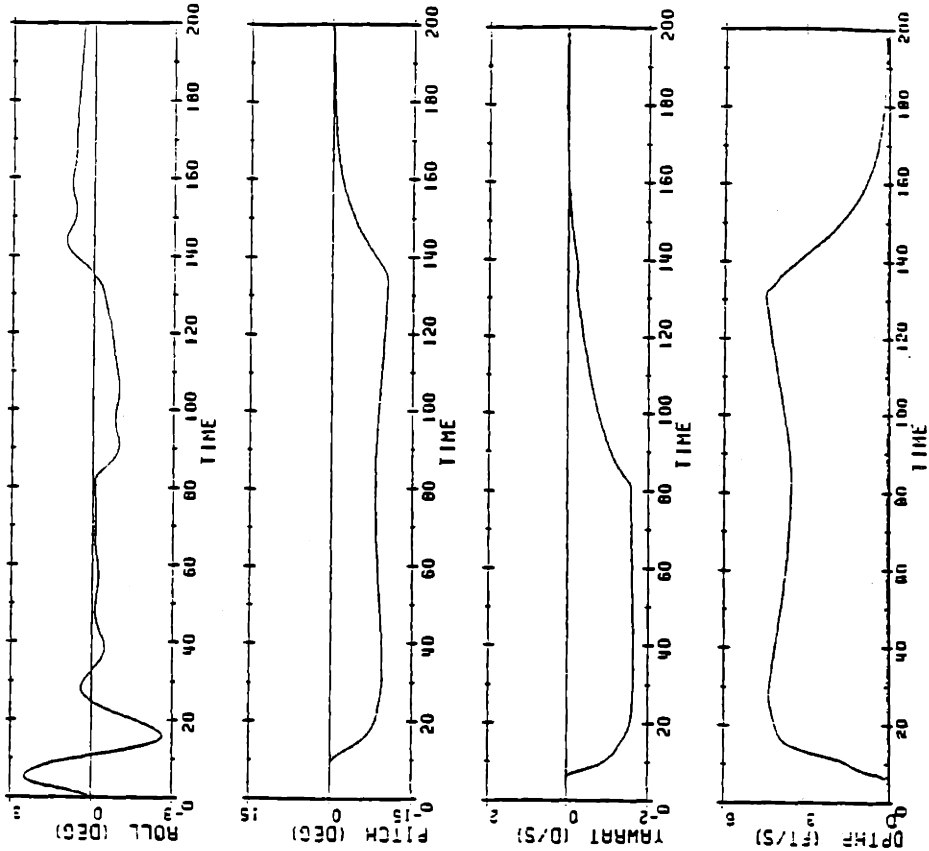


Figure 5.3 Comparison of 15 Knot Compensator Performance for Simultaneous Turn and Dive During Speed Change

though the yawrate command following for the 30 to 15 knot was not felt to be adequate, both simulations converged on a 150 degree course change.

The second maneuver consisted of a dive with an ordered roll angle during speed changes such as that in the previous maneuver. At $t = 5$ seconds, a 20 degree roll angle, 4.5 feet/second depthrate and -10 degree pitch angle were ordered. The 20 degree roll angle remains for the entire simulation however, the depthrate and pitch angle orders are removed at $t = 130$ seconds. Figure 5.4 shows the results with the 15 to 30 knot simulation on the left again. The simulation for 15 to 30 knots showed favorable results by maintaining the ordered 20 degree roll angle. The depthrate and pitch angle responses exhibited some overshoot but were converging on the commanded values as the fairwater planes came out of saturation. Throughout the maneuver only slight disturbances to the yawrate were present. The 30 to 15 knot simulation showed that the system was stable, but due to the speed decrease, the roll angle could not be maintained as is evident by sternplane saturation at $t = 95$ seconds.

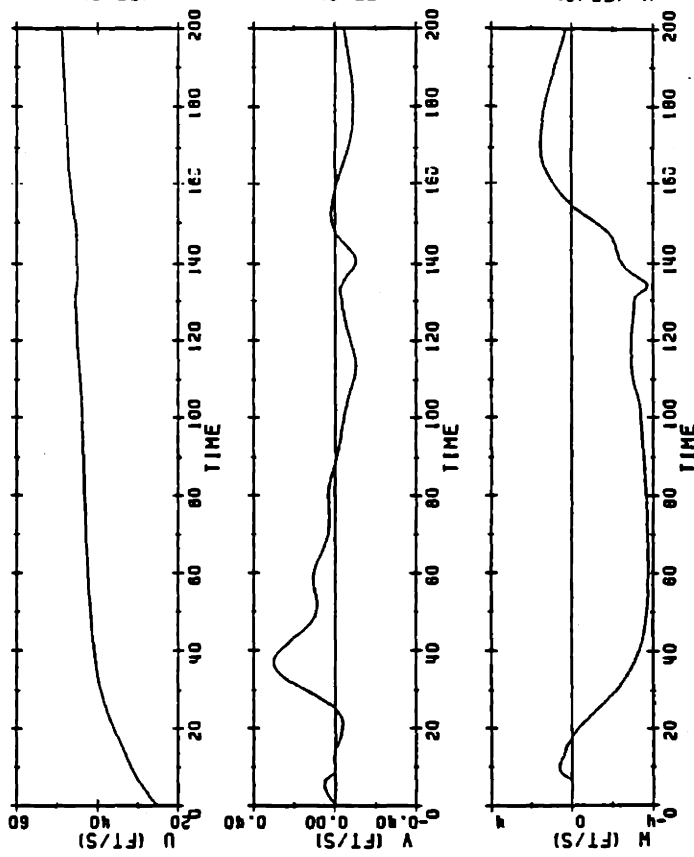
5.3 Comparison of 15 and 30 Knot Compensators

Since the 15 knot compensator performed adequately, the next logical step was to determine how it's performance at various speeds compared to the compensator designed by Martin for the 30 knot model. For details of the design as well as a comparison to a system without active roll control the reader is referred to [8]. The matrices for the 30 knot compensator are found in Appendix C2.

First, several benign maneuvers were performed to observe how the control inputs and outputs of the two systems responded. The first set of

VELOCITIES

NONLINEAR INTEGRATION FOR 4.5 FT/SEC, -10 DEG & 20 DEG ROLL



VELOCITIES

NONLINEAR INTEGRATION FOR 4.5 FT/SEC, -10 DEG & 20 DEG ROLL

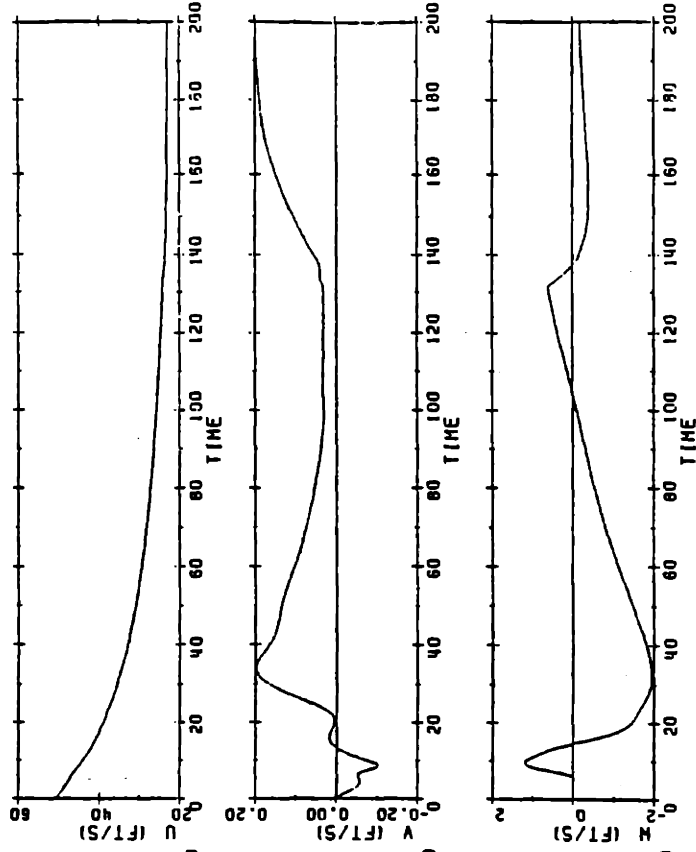
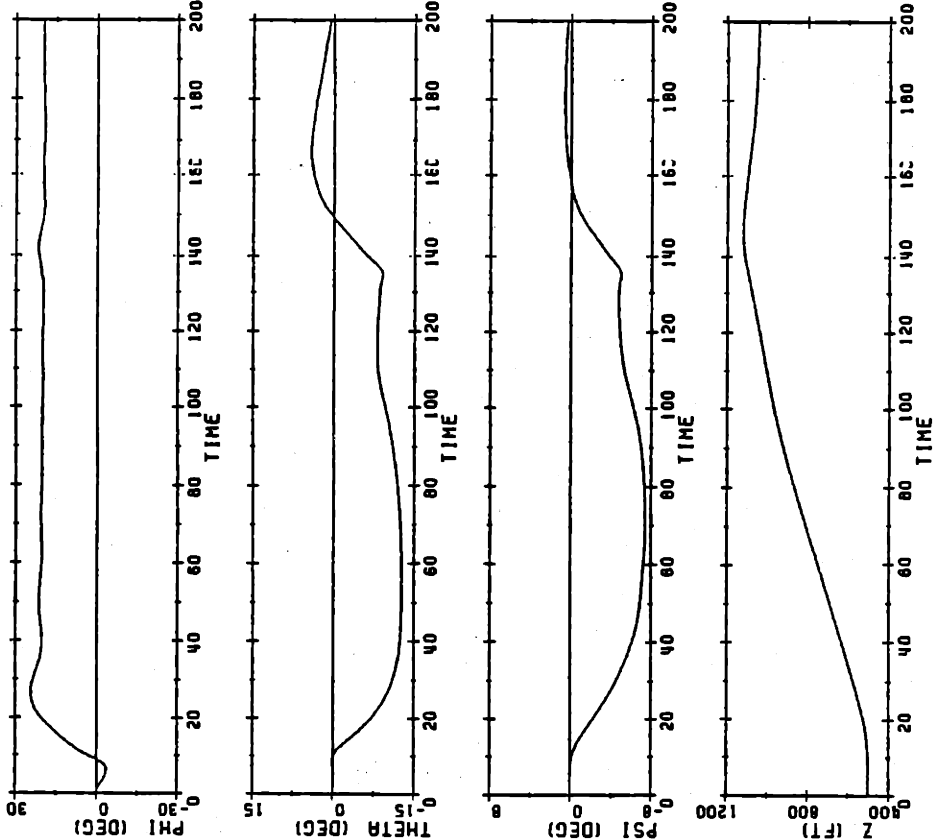


Figure 5.4 Comparison of 15 Knot Compensator Performance for Simultaneous Roll and Dive During Speed Change

ATTITUDE AND DEPTH

NONLINEAR INTEGRATION FOR 4.5 FT/SEC. -10 DEG & 20 DEG ROLL



ATTITUDE AND DEPTH

NONLINEAR INTEGRATION FOR 4.5 FT/SEC. -10 DEG & 20 DEG ROLL

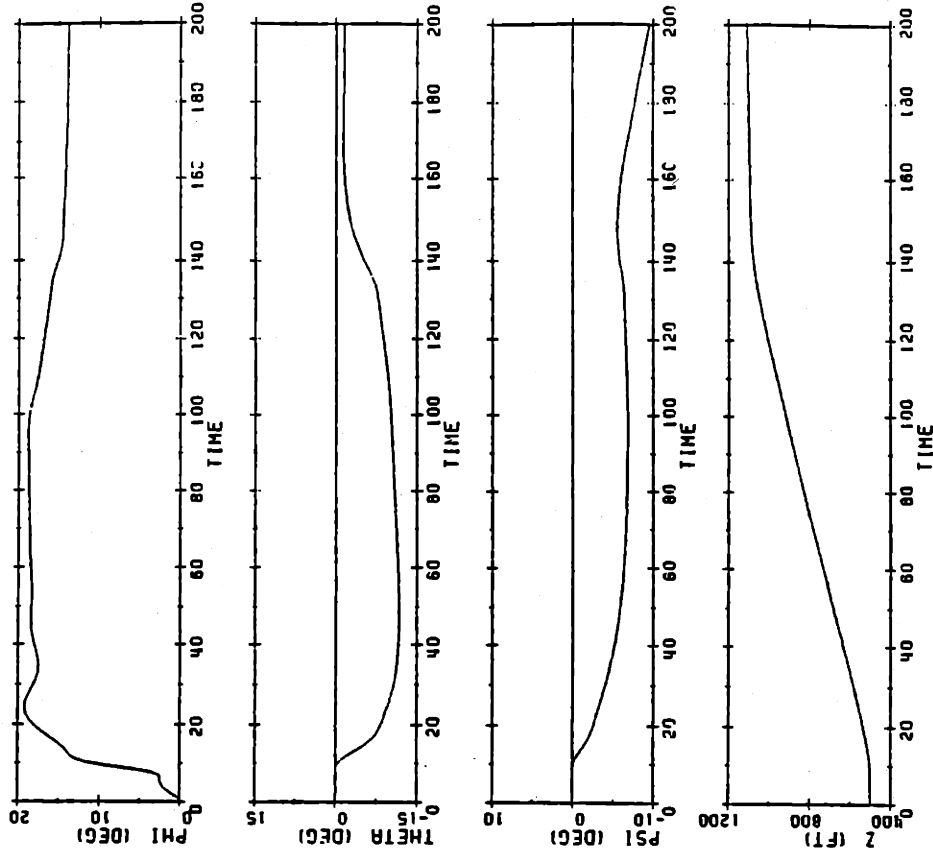
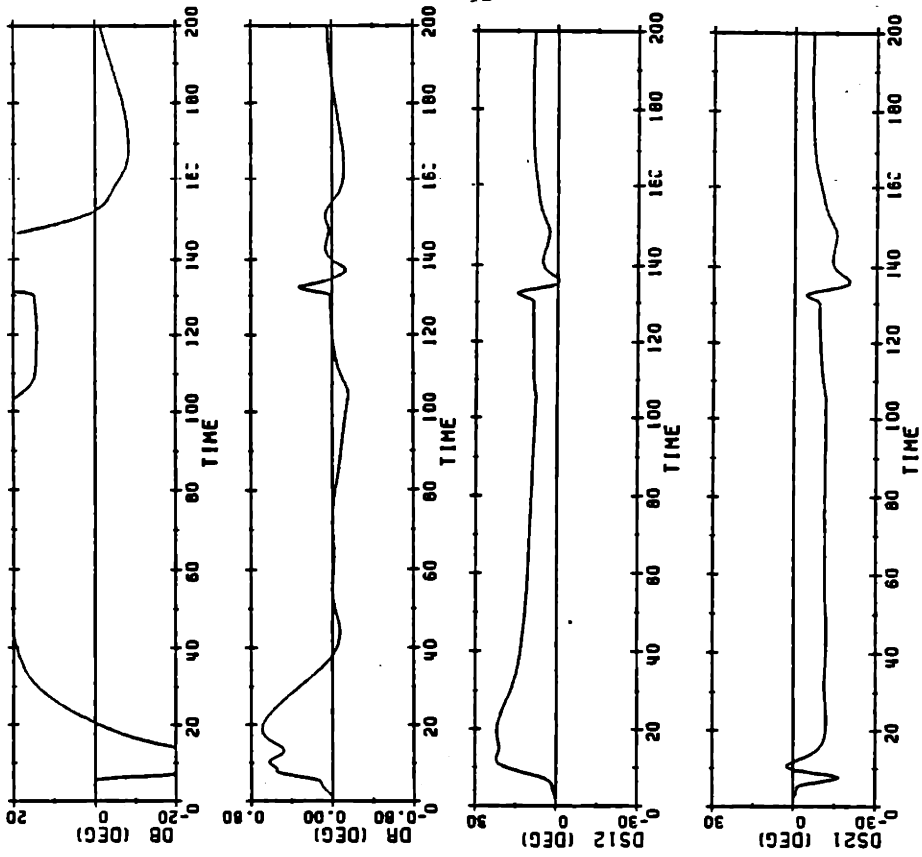


Figure 5.4 Comparison of 15 Knot Compensator Performance for Simultaneous Roll and Dive During Speed Change

CONTROL INPUTS

NONLINEAR INTEGRATION FOR 4.5 FT/SEC. -10 DEG & 20 DEG FALL



CONTROL INPUTS

NONLINEAR INTEGRATION FOR 4.5 FT/SEC. -10 DEG & 20 DEG RISE

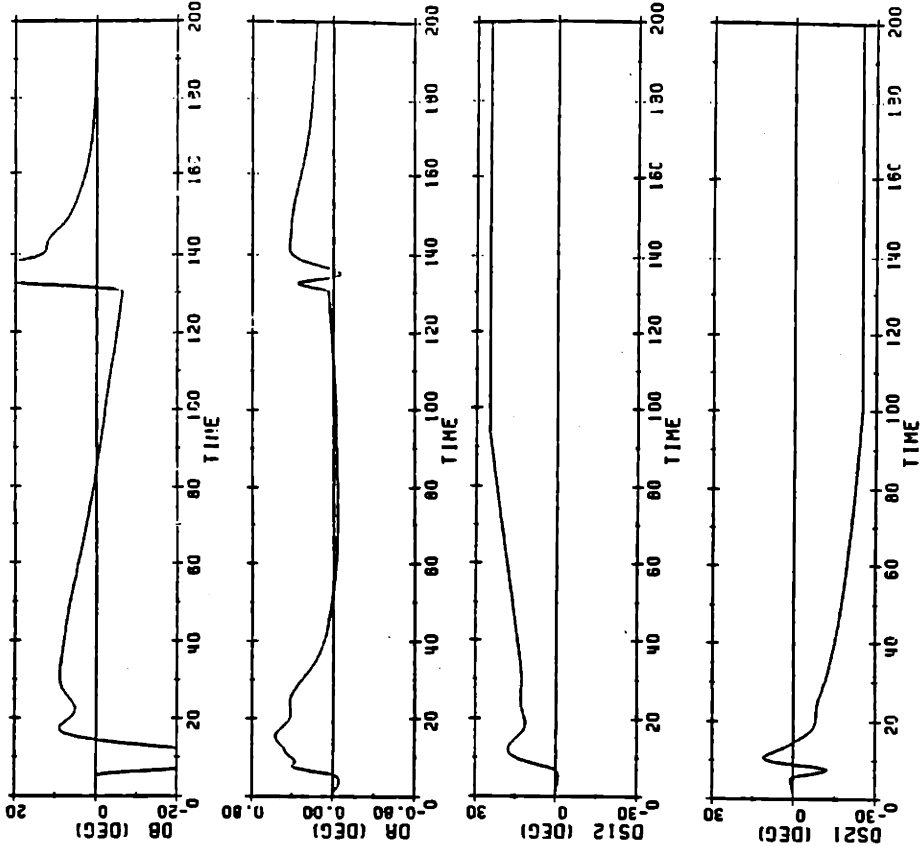
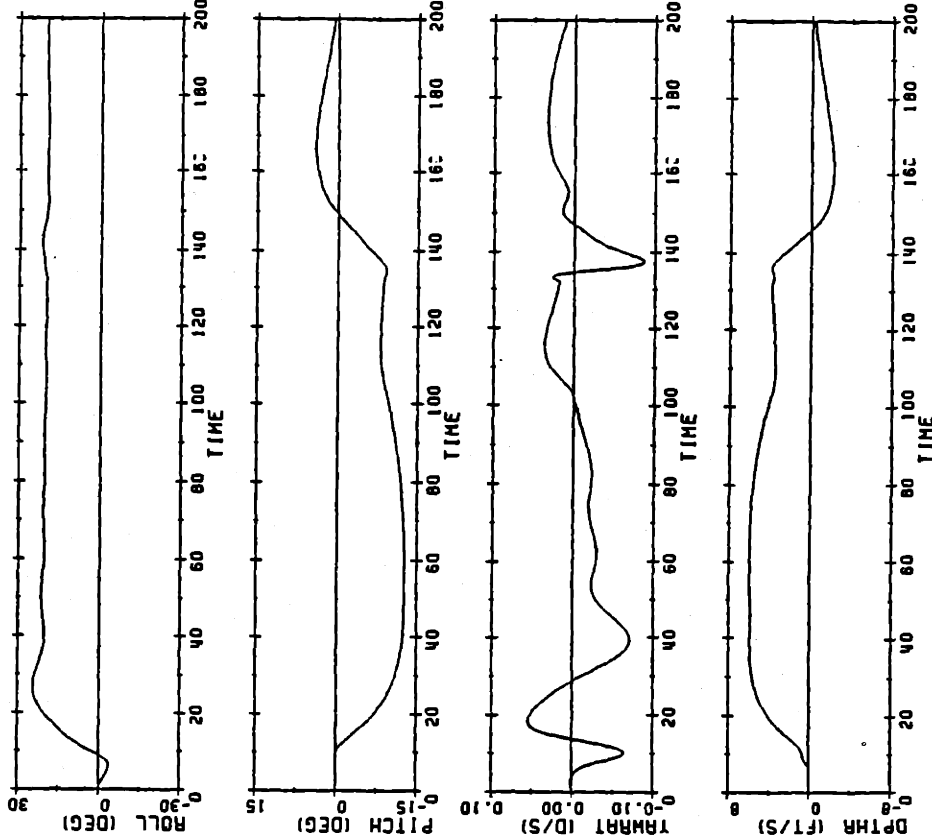


Figure 5.4 Comparison of 15 Knot Compensator Performance for Simultaneous Roll and Dive During Speed Change

OUTPUTS

NONLINEAR INTEGRATION FOR 4.5 FT/SEC. -10 DEG & 20 DEG ROLL



OUTPUTS

NONLINEAR INTEGRATION FOR 4.5 FT/SEC. -10 DEG & 20 DEG ROLL

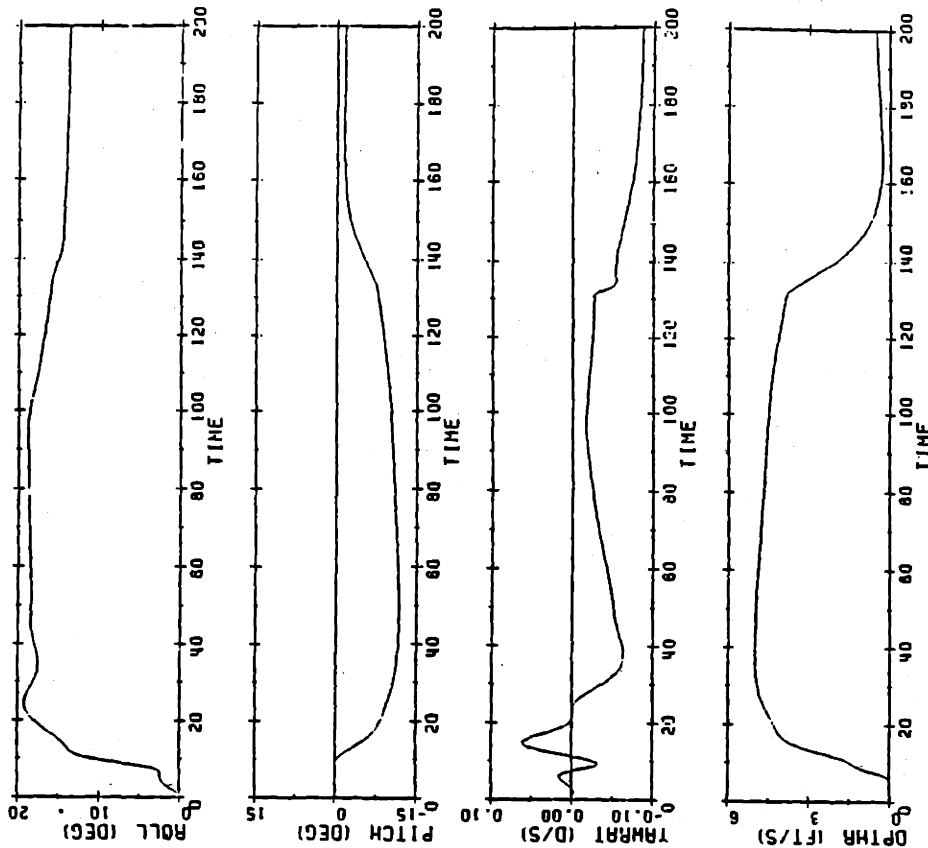


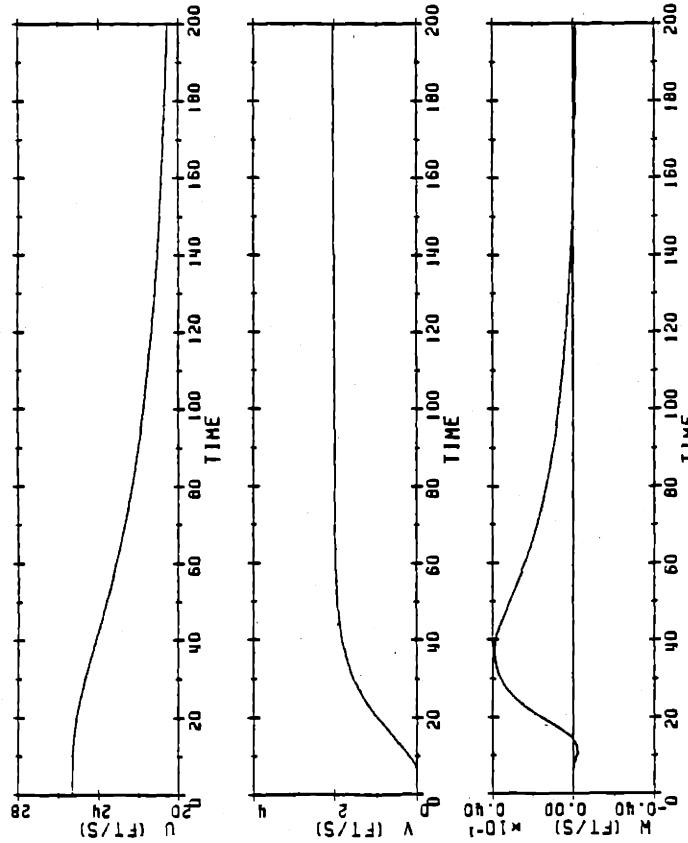
Figure 5.4 Comparison of 15 Knot Compensator Performance for Simultaneous Roll and Dive During Speed Change

simulations shown in Figures 5.5 and 5.6 were for a -1 degree/second yawrate step input applied at $t = 5$ seconds at speeds of 15 and 30 knots respectively. The response for the 15 knot compensator is on the left and the 30 knot on the right. In general, both exhibited good command following with the 30 knot compensator reaching the commanded yawrate quicker. It is evident that this occurs because the control surfaces move much faster than the 15 knot compensator. It should also be noted that this causes major disturbances to the states and other outputs as compared to the 15 knot compensator. Of particular interest is that the 15 knot compensator showed more oscillation at 30 knots and the 30 knot compensator showed more oscillation at 15 knots. This is due to the particular simulation being far from the nominal point. The oscillations for the system using the 30 knot compensator were generally of larger amplitude than those of the system with the 15 knot compensator. This set of simulations was followed by a similar set for a 1 foot/second depthrate with similar results.

The two maneuvers presented in Section 5.2 above were then repeated for the 30 knot compensator. The results of the simulations are again shown with the 15 knot compensator on the left and the 30 knot compensator on the right. The 30 to 15 knot simulation for the turn and dive is presented in Figures 5.7. The results are generally the same as previously stated. The 30 knot compensator responds quicker, is more oscillatory and exhibits more overshoot. Of particular interest though is the saturation of the fairwater planes at $t = 80$ seconds due to the sternplanes deflecting quicker than those of the 15 knot compensator as the yawrate command is removed. This results in growing errors in pitch and depthrate until these

VELOCITIES

NONLINEAR INTEGRATION FOR -1 DEG/SEC. 15 KNOT COMPENSATOR



VELOCITIES

NONLINEAR INTEGRATION FOR -1 DEG/SEC. 30 KNOT COMPENSATOR

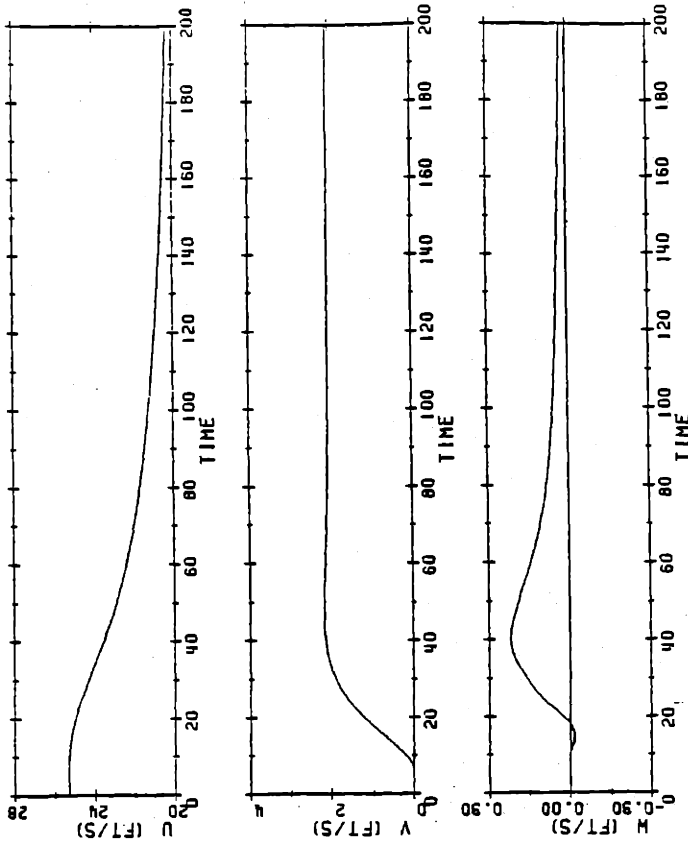
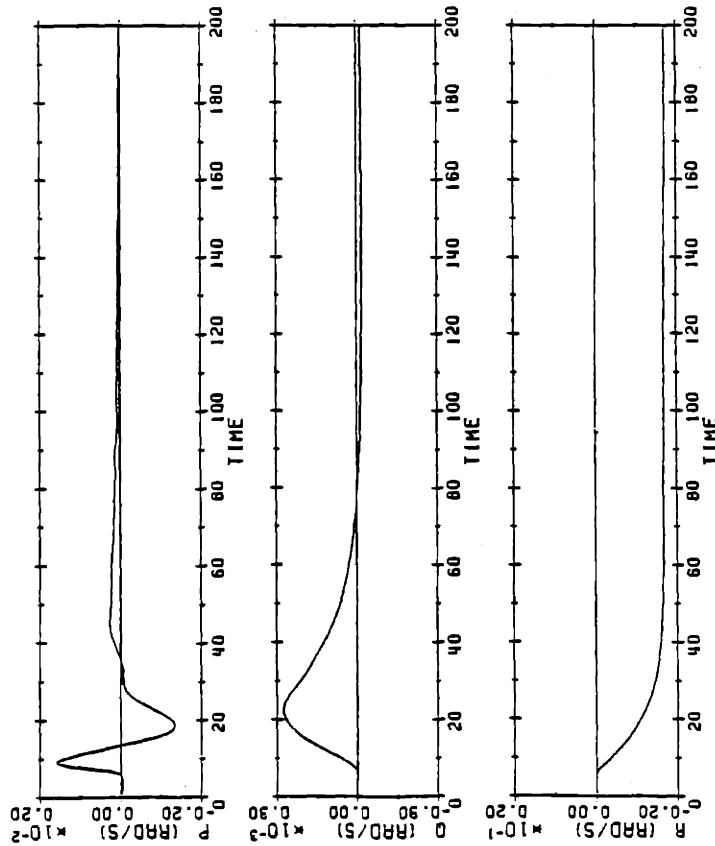


Figure 5.5 Comparison of 15 Knot and 30 Knot Compensators for -1 Degree/Second Yawrate at 15 Knots

ANGULAR VELOCITIES

NONLINEAR INTEGRATION FOR -1 DEG/SEC, 15 KNOT COMPENSATOR



ANGULAR VELOCITIES

NONLINEAR INTEGRATION FOR -1 DEG/SEC, 30 KNOT COMPENSATOR

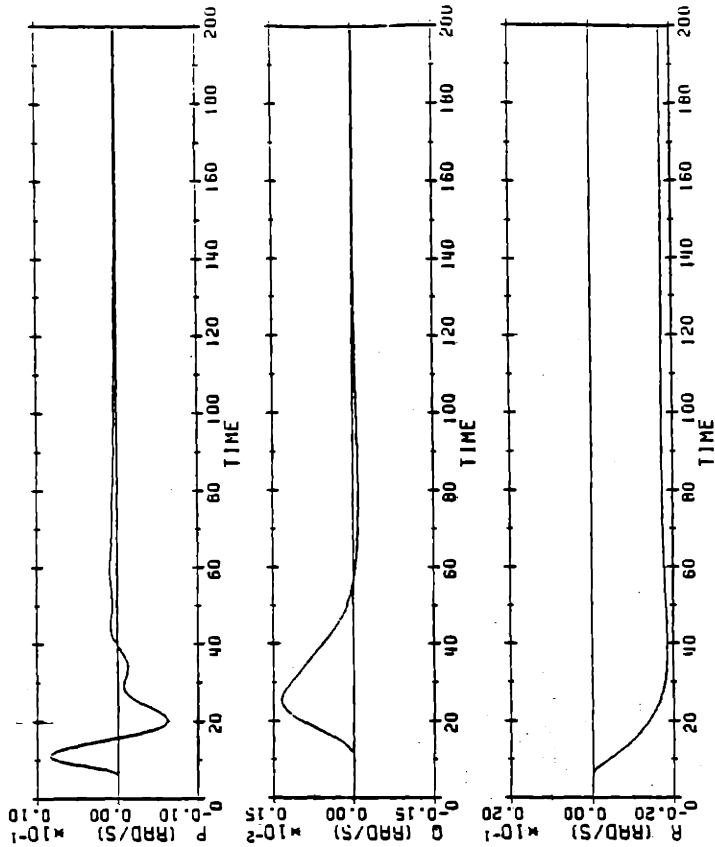
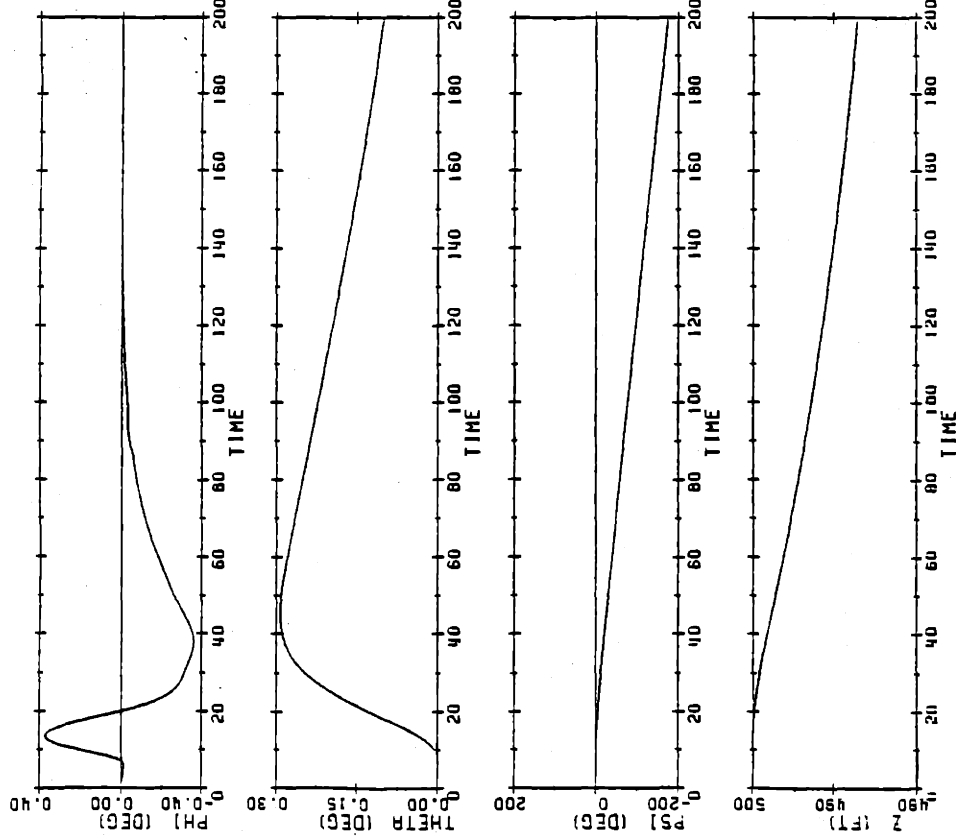


Figure 5.5 Comparison of 15 Knot and 30 Knot Compensators for -1 Degree/Second Yawrate at 15 Knots

ATTITUDE AND DEPTH

NONLINEAR INTEGRATION FOR -1 DEG/SEC. 15 KNOT COMPENSATOR



ATTITUDE AND DEPTH

NONLINEAR INTEGRATION FOR -1 DEG/SEC. 30 KNOT COMPENSATOR

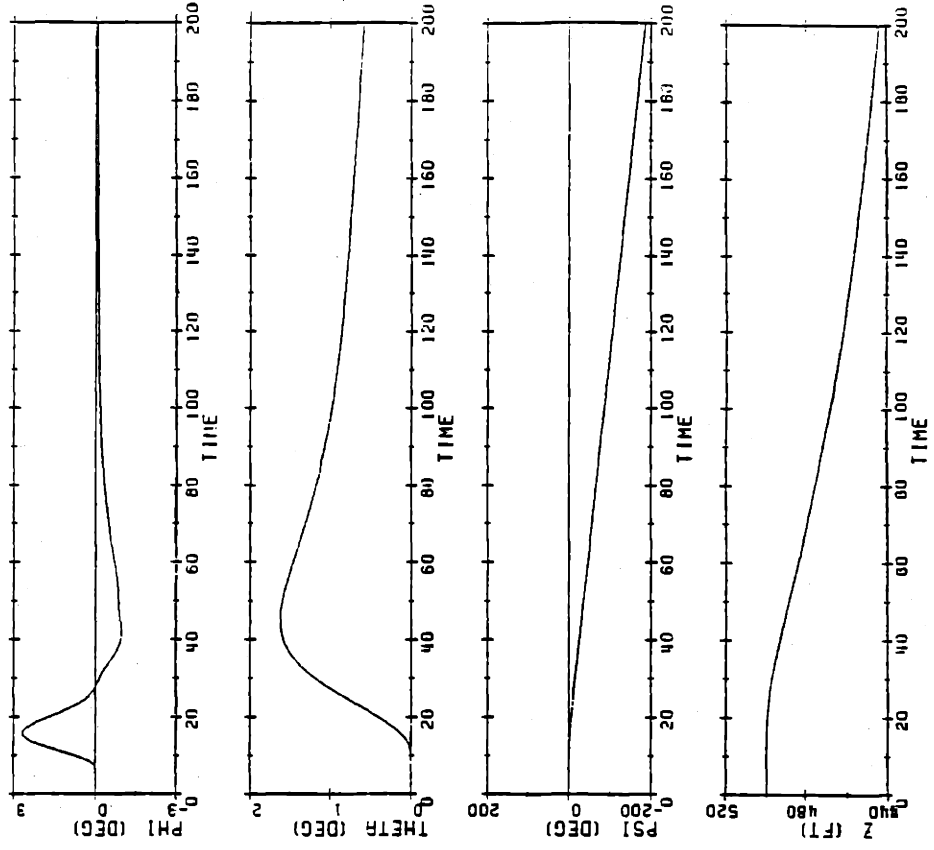
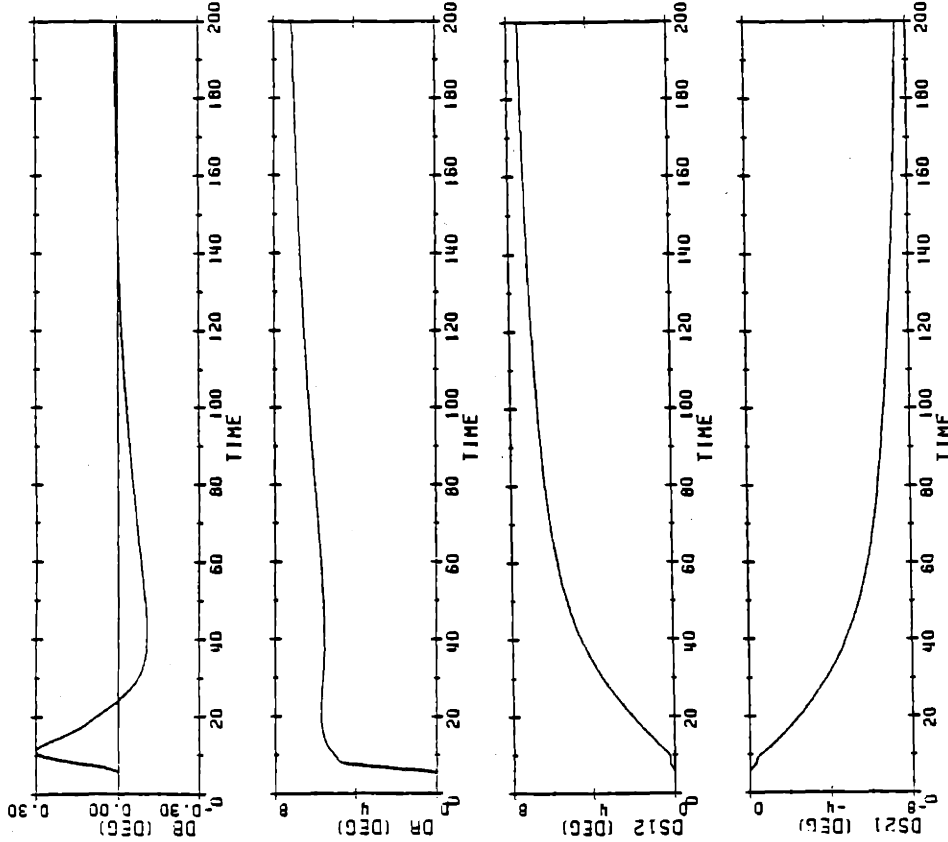


Figure 5.5 Comparison of 15 Knot and 30 Knot Compensators for -1 Degree/Second Yawrate at 15 Knots

CONTROL INPUTS

NONLINEAR INTEGRATION FOR -1 DEG/SEC. 15 KNOT COMPENSATOR



CONTROL INPUTS

NONLINEAR INTEGRATION FOR -1 DEG/SEC. 30 KNOT COMPENSATOR

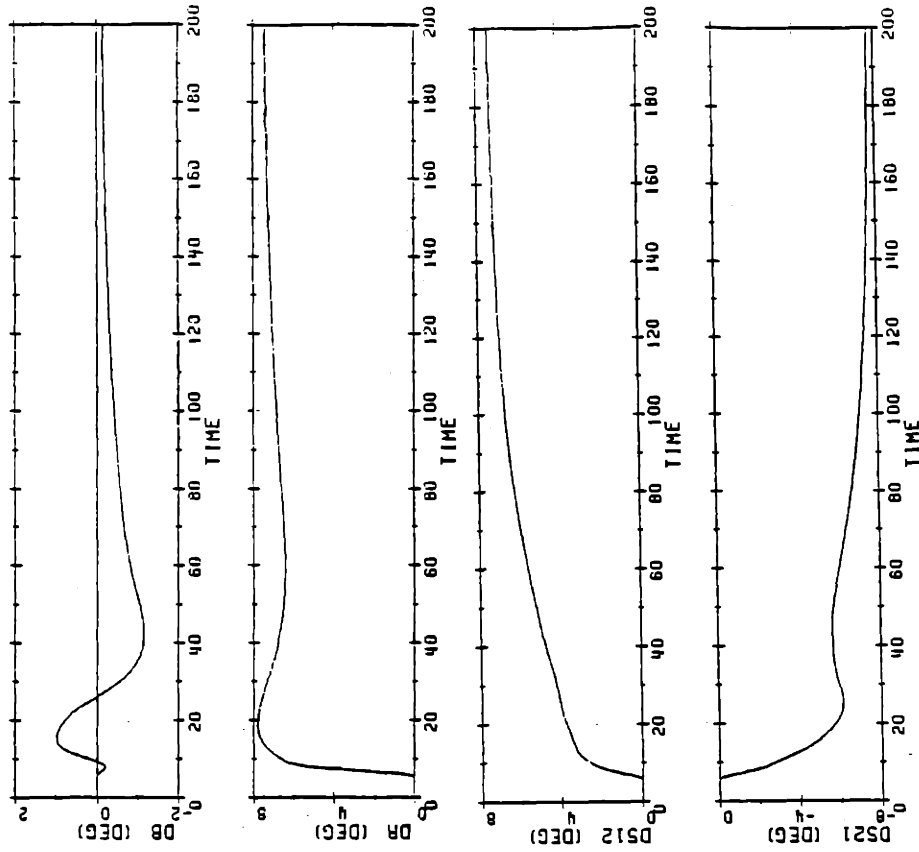
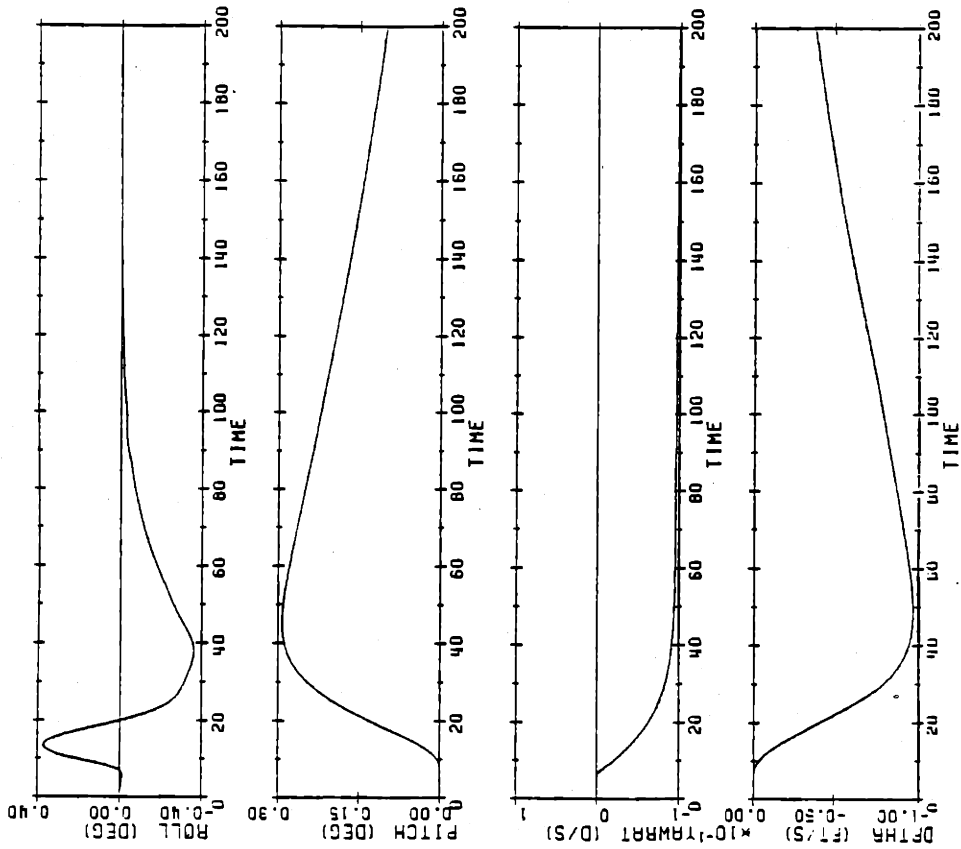


Figure 5.5 Comparison of 15 Knot and 30 Knot Compensators for -1 Degree/Second Yawrate at 15 Knots

OUTPUTS

NONLINEAR INTEGRATION FOR -1 DEG/SEC. 15 KNOT COMPENSATOR



OUTPUTS

NONLINEAR INTEGRATION FOR -1 DEG/SEC. 30 KNOT COMPENSATOR

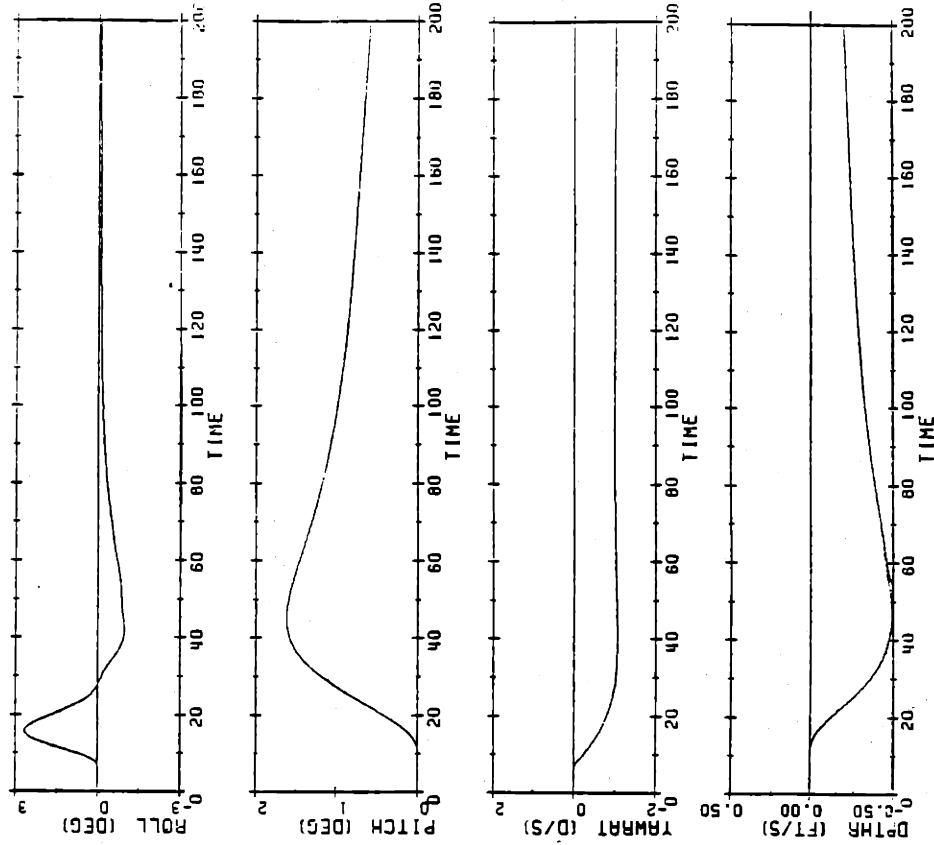
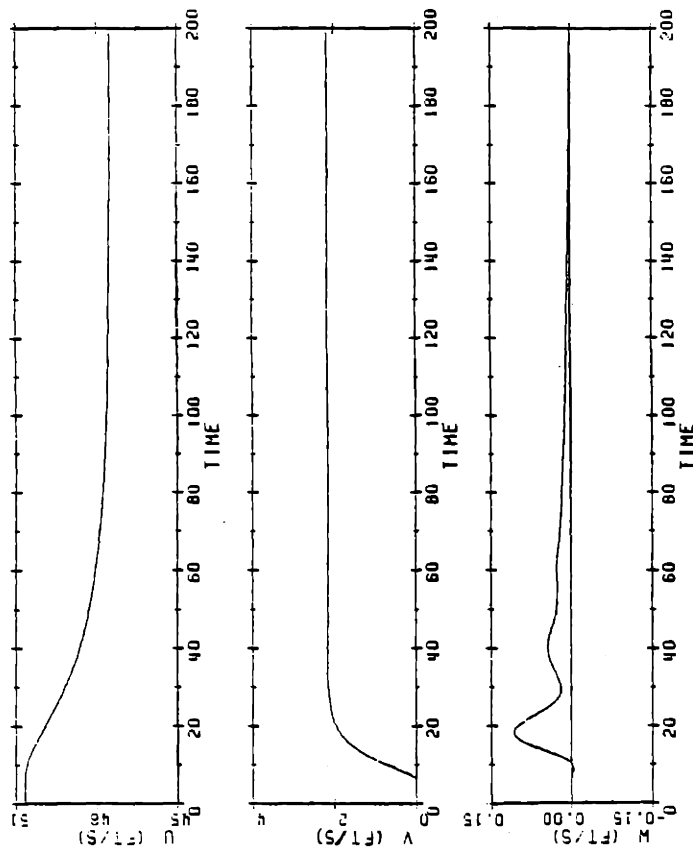


Figure 5.5 Comparison of 15 Knot and 30 Knot Compensators for -1 Degree/Second Yawrate at 15 Knots

VELOCITIES

NONLINEAR INTEGRATION FOR -1 DEG/SEC, 15 KNOT COMPENSATOR



VELOCITIES

NONLINEAR INTEGRATION FOR -1 DEG/SEC COMMANDED YAWRATE

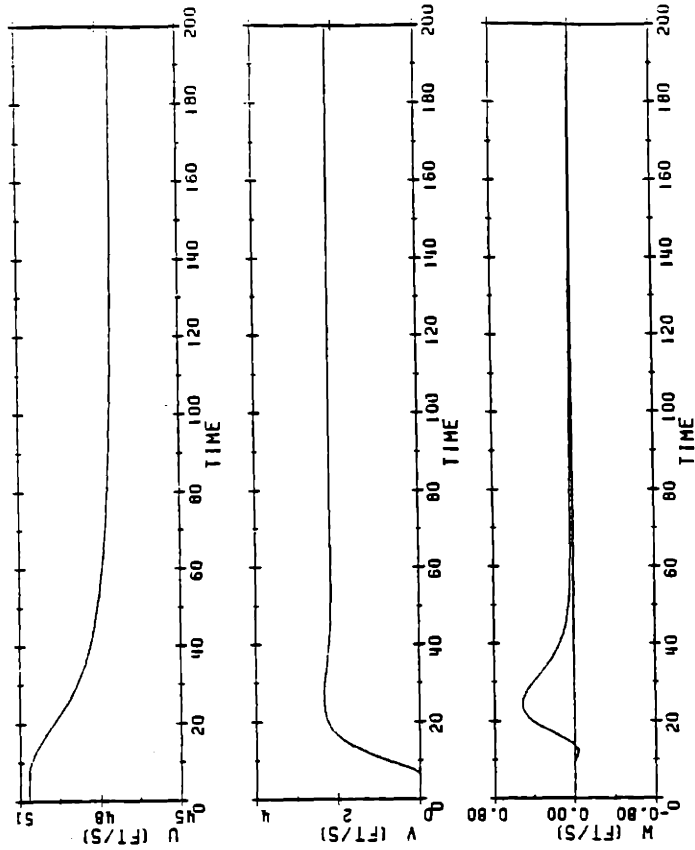
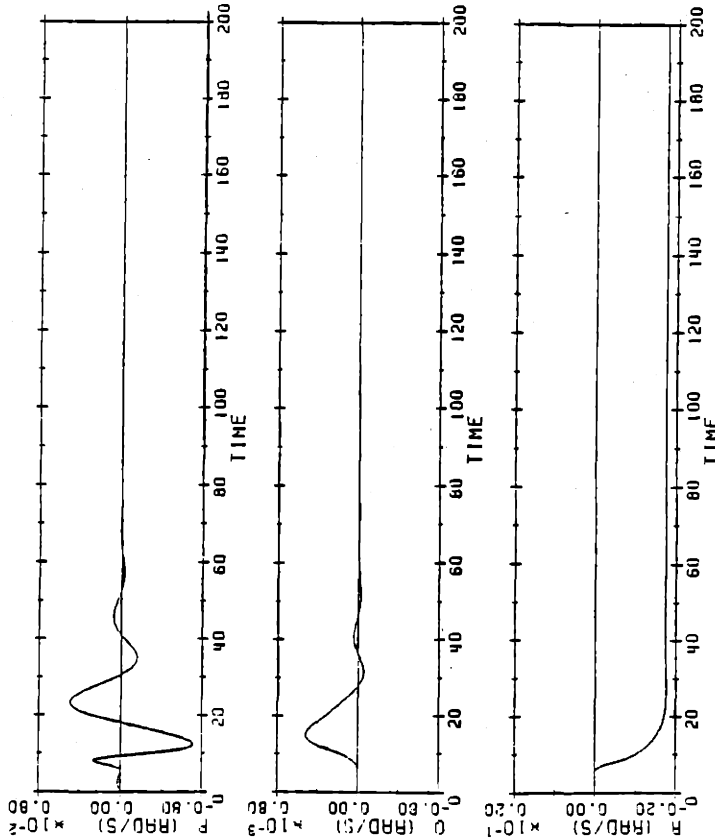


Figure 5.6 Comparison of 15 Knot and 30 Knot Compensators for -1 Degree/Second Yawrate at 30 Knots

ANGULAR VELOCITIES

NONLINEAR INTEGRATION FOR -1 DEG/SEC. 15 KNOT COMPENSATOR



ANGULAR VELOCITIES

NONLINEAR INTEGRATION FOR -1 DEG/SEC COMMANDED YAWRATE

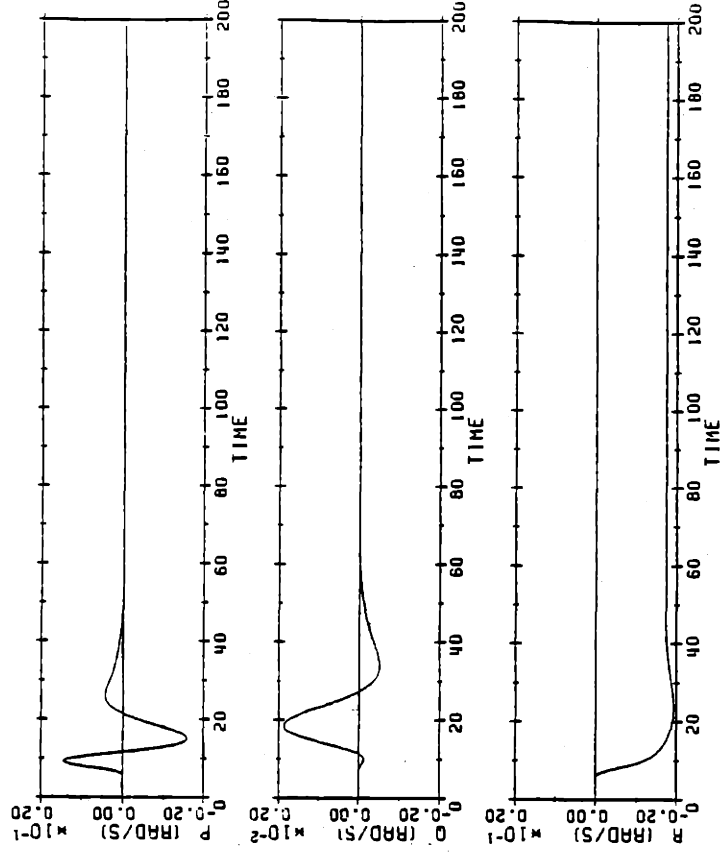
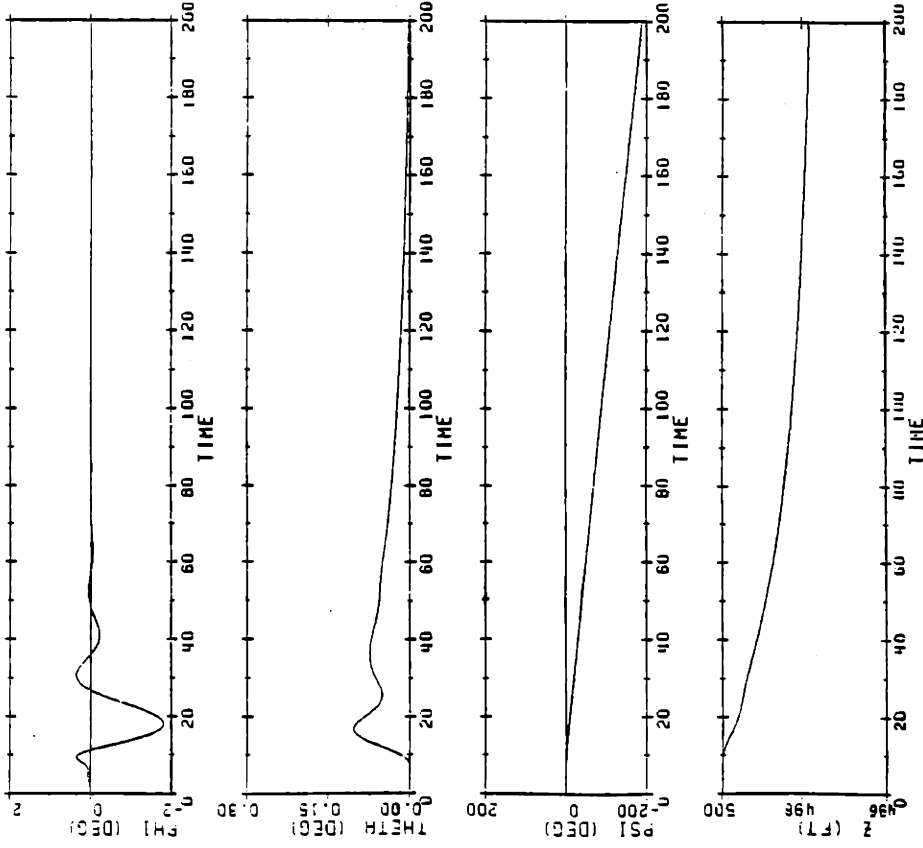


Figure 5.6 Comparison of 15 Knot and 30 Knot Compensators for -1 Degree/Second Yawrate at 30 Knots

ATTITUDE AND DEPTH

NONLINEAR INTEGRATION FOR -1 DEG/SEC, 15 KNOT COMPENSATOR



ATTITUDE AND DEPTH

NONLINEAR INTEGRATION FOR -1 DEG/SEC COMMANDED YAWRATE

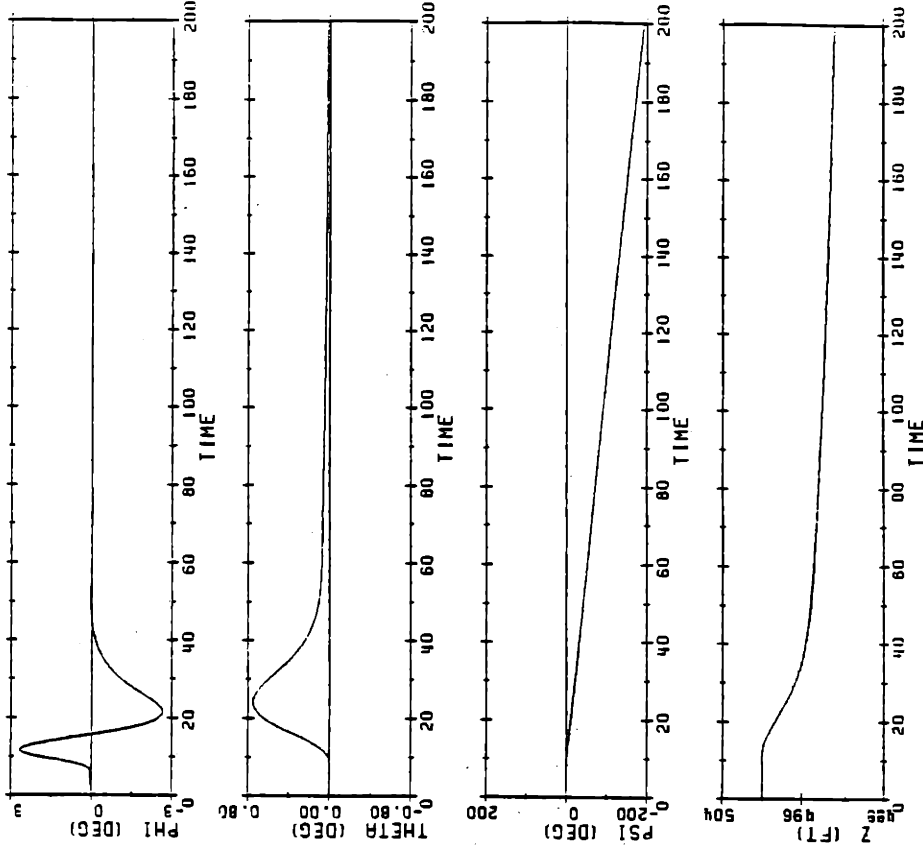
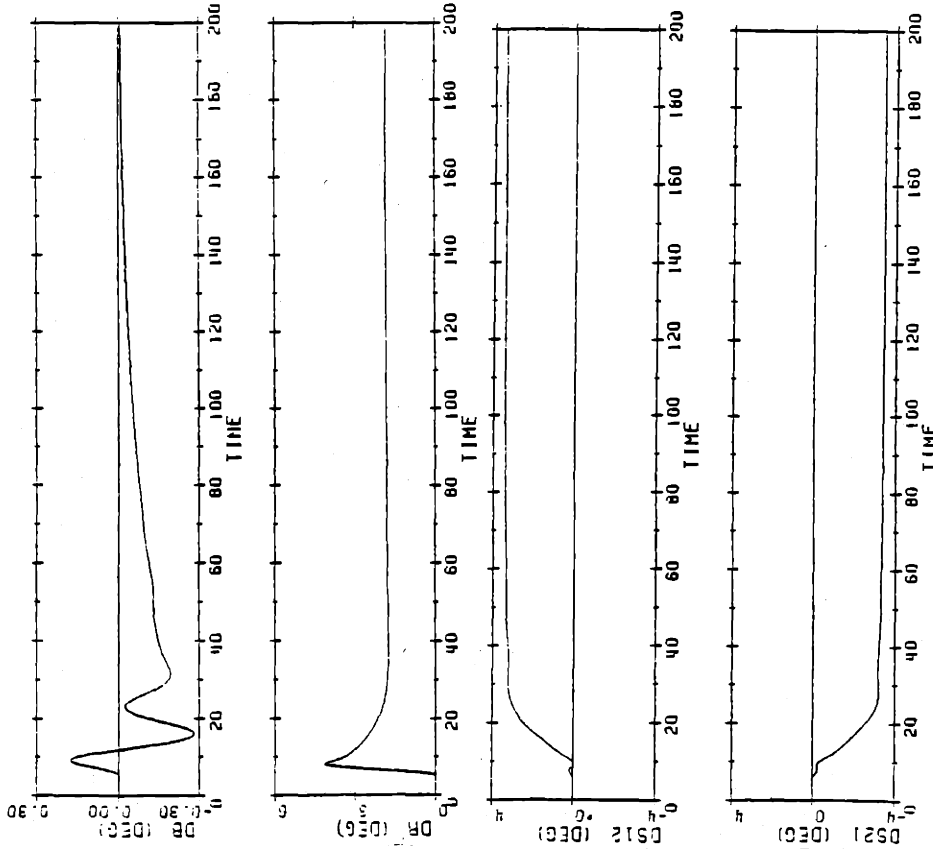


Figure 5.6 Comparison of 15 Knot and 30 Knot Compensators for -1 Degree/Second Yawrate at 30 Knots

CONTROL INPUTS

NONLINEAR INTEGRATION FOR -1 DEG/SEC. 15 KNOT COMPENSATOR



CONTROL INPUTS

NONLINEAR INTEGRATION FOR -1 DEG/SEC COMMANDED YAWRATE

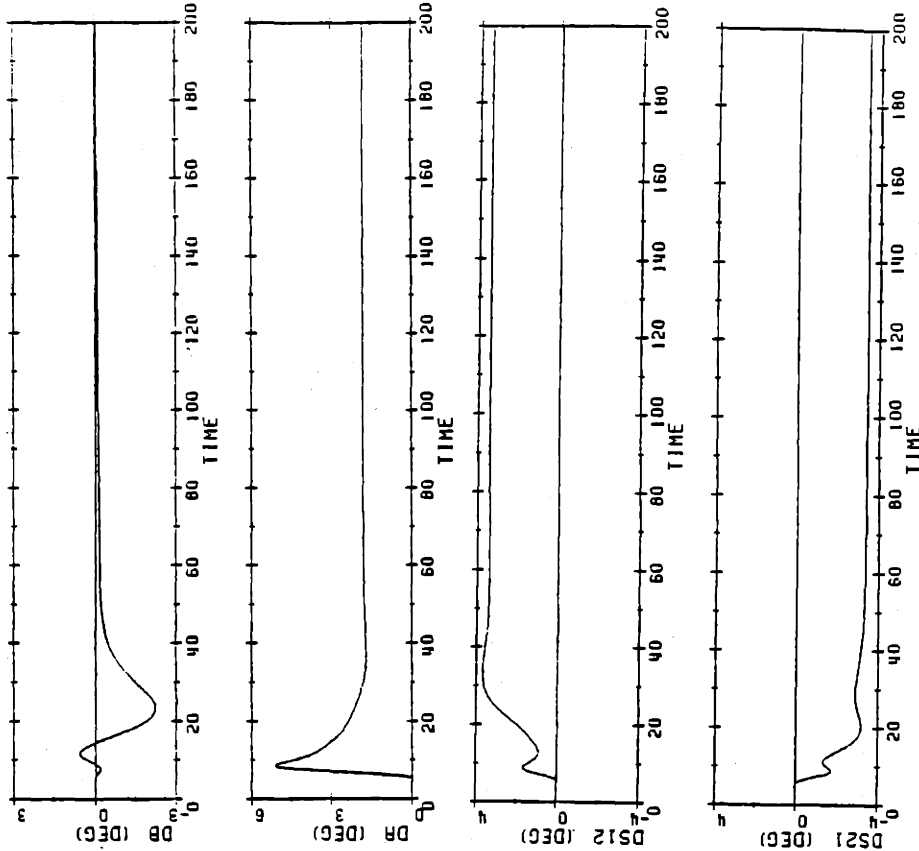
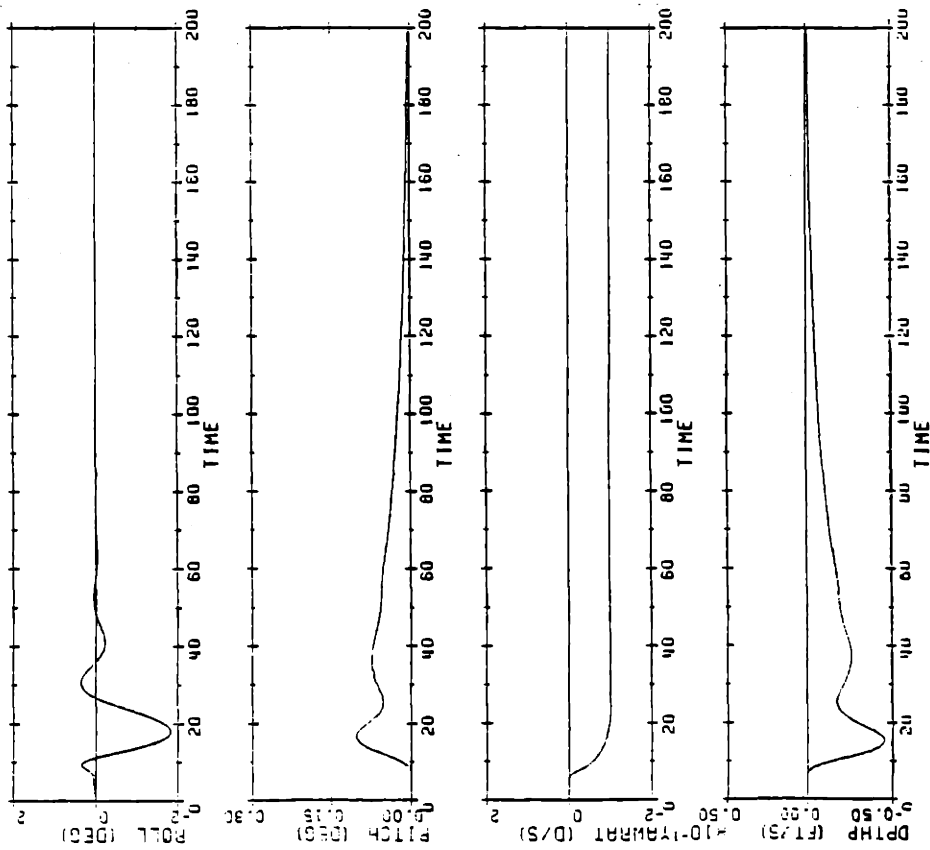


Figure 5.6 Comparison of 15 Knot and 30 Knot Compensators for -1 Degree/Second Yawrate at 30 Knots

OUTPUTS

NONLINEAR INTEGRATION FOR -1 DEG/SEC, 15 KNOT COMPENSATOR



OUTPUTS

NONLINEAR INTEGRATION FOR -1 DEG/SEC COMMANDED YAWRATE

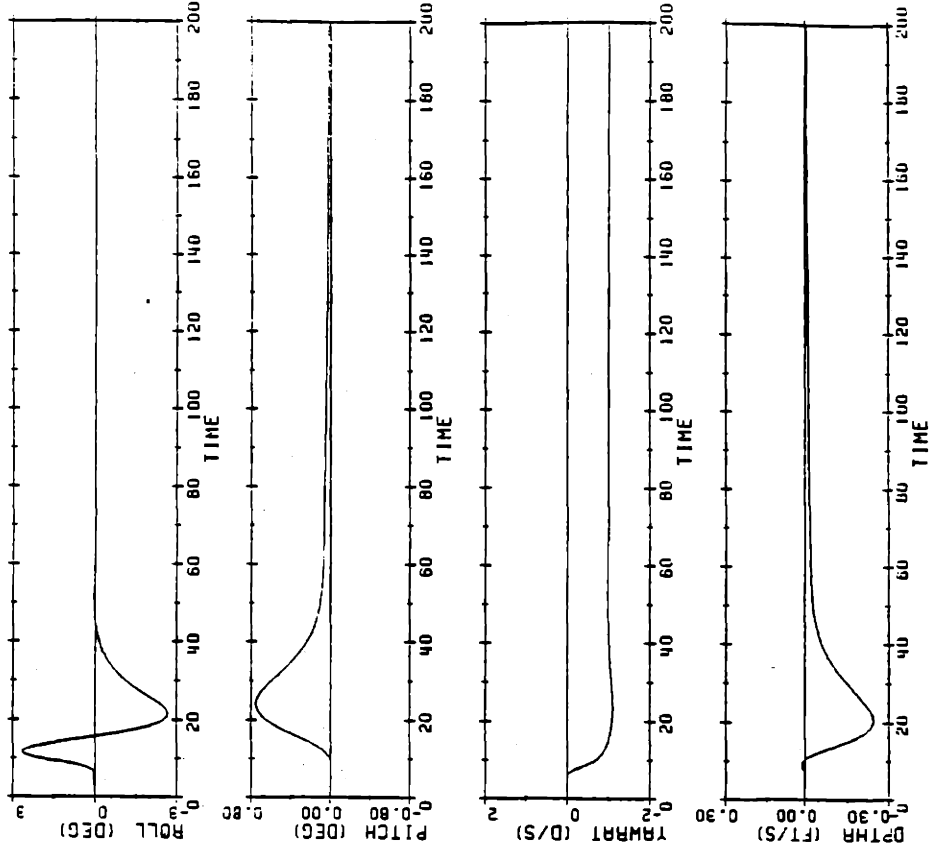
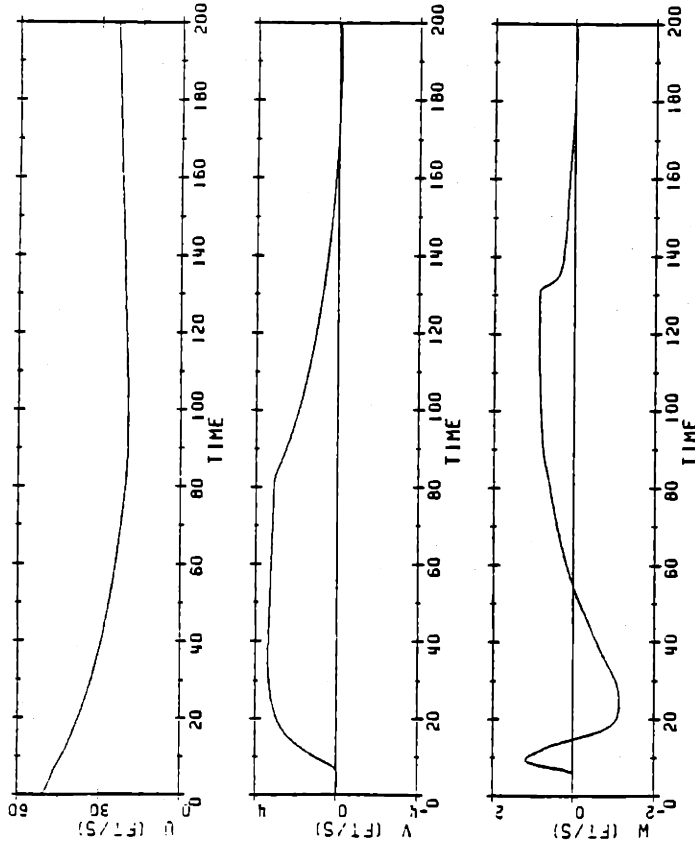


Figure 5.6 Comparison of 15 Knot and 30 Knot Compensators for -1 Degree/Second Yawrate at 30 Knots

VELOCITIES

NONLINEAR INTEGRATION FOR 4.5 FT/SEC. -10 DEG λ -2 DEG/SEC



VELOCITIES

NONLINEAR INTEGRATION FOR 4.5 FT/SEC. -10 DEG λ -2 DEG/SEC YAMARITE

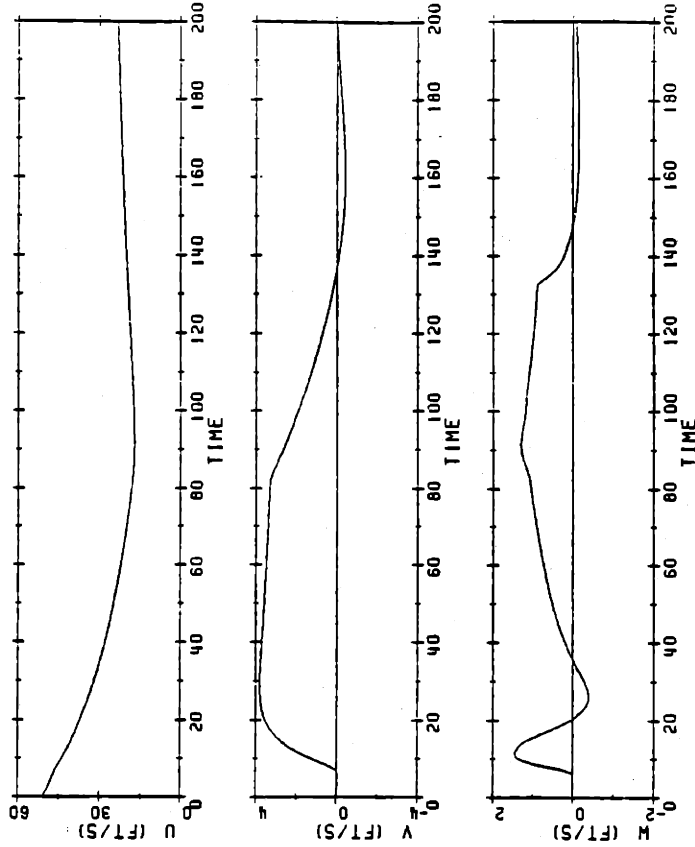


Figure 5.7 Comparison of 15 Knot and 30 Knot Compensators for Simultaneous Turn and Dive (30 to 15 Knots)

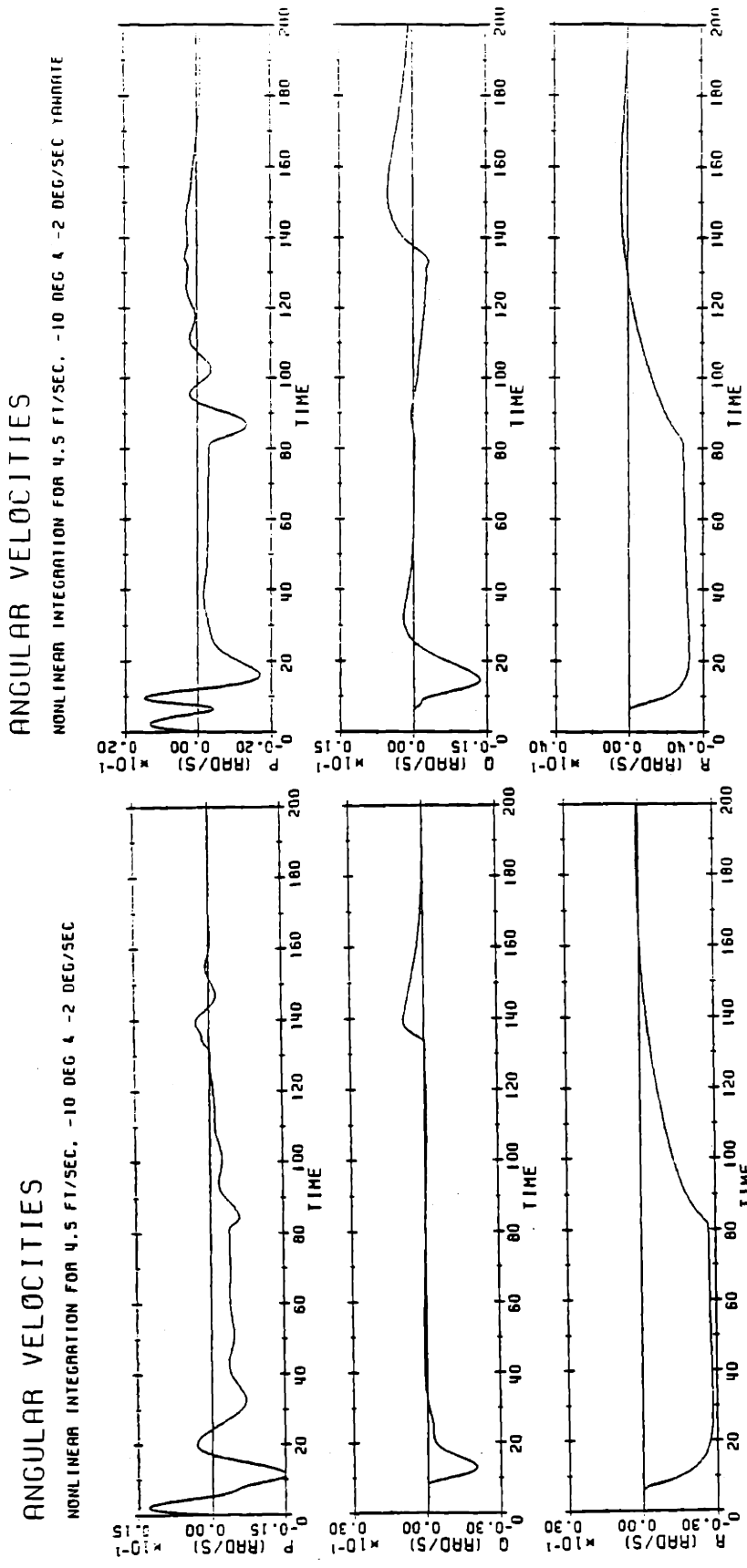
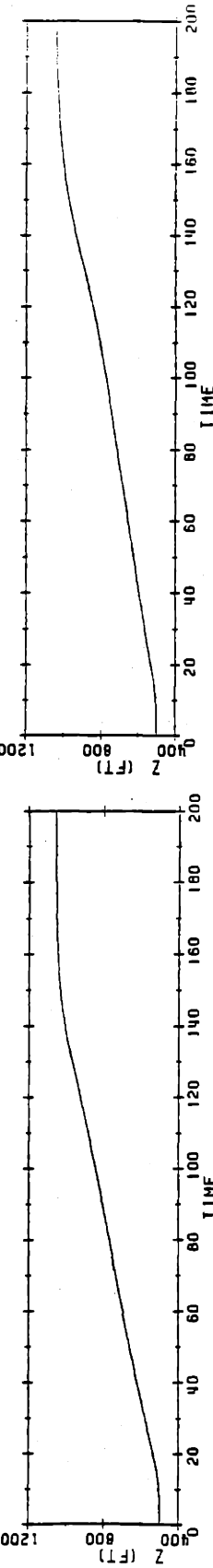
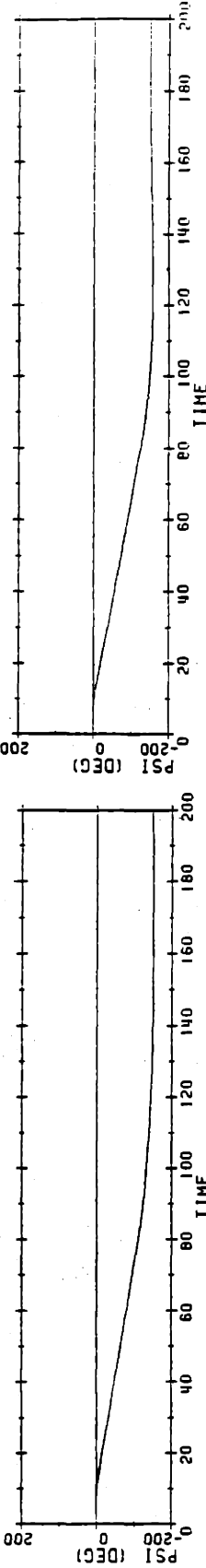
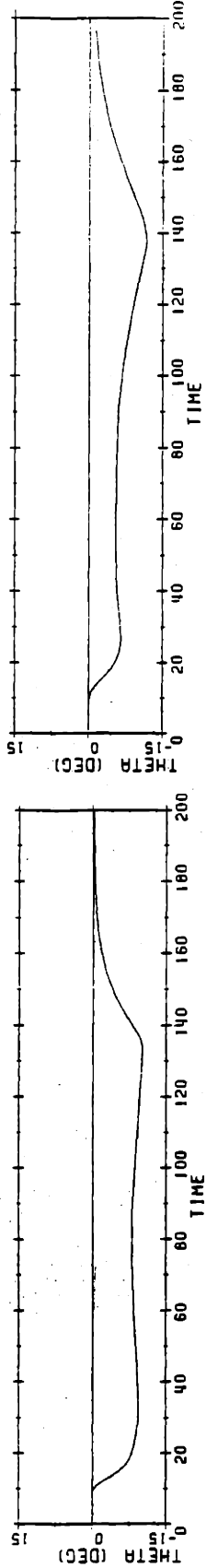
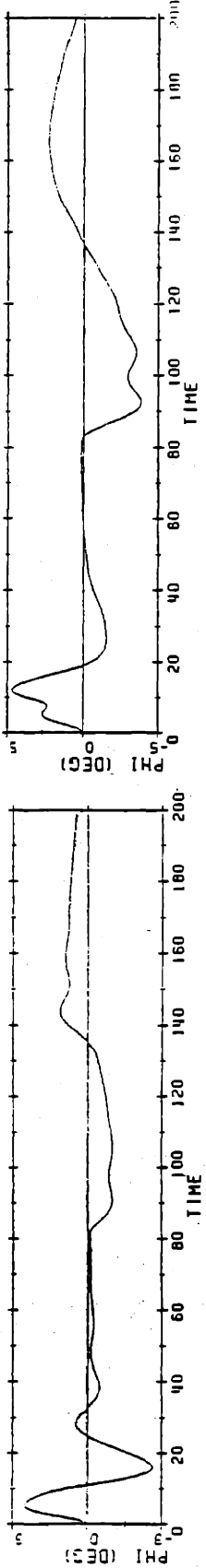


Figure 5.7 Comparison of 15 Knot and 30 Knot Compensators for Simultaneous Turn and Dive (30 to 15 Knots)

ATTITUDE AND DEPTH

NONLINEAR INTEGRATION FOR 4.5 FT/SEC. -10 DEG 4 -2 DEG/SEC



ATTITUDE AND DEPTH

NONLINEAR INTEGRATION FOR 4.5 FT/SEC. -10 DEG 4 -2 DEG/SEC YAWRATE

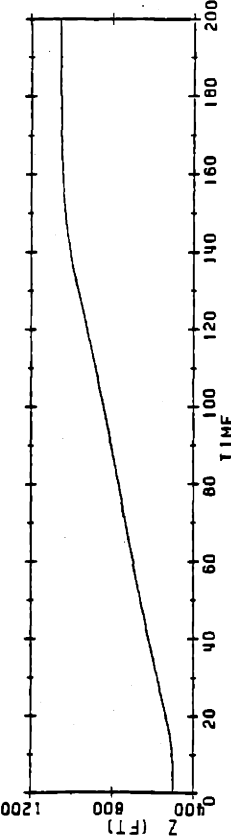
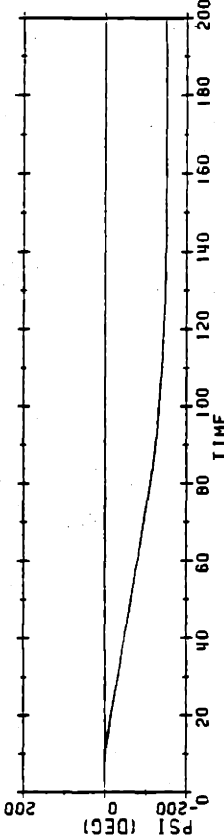
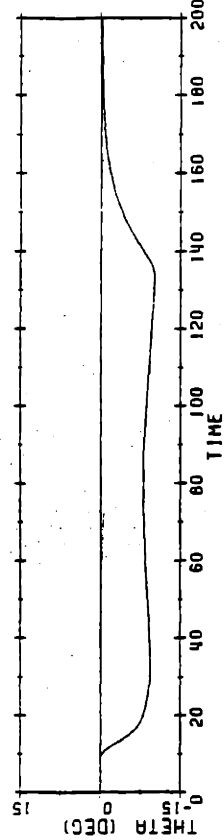
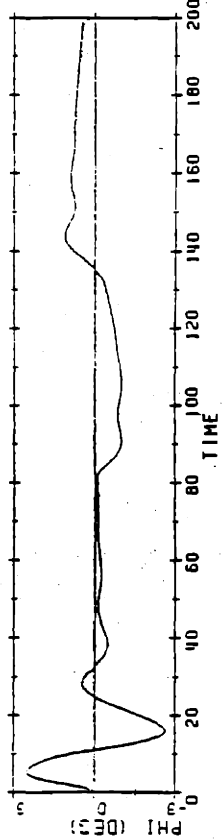
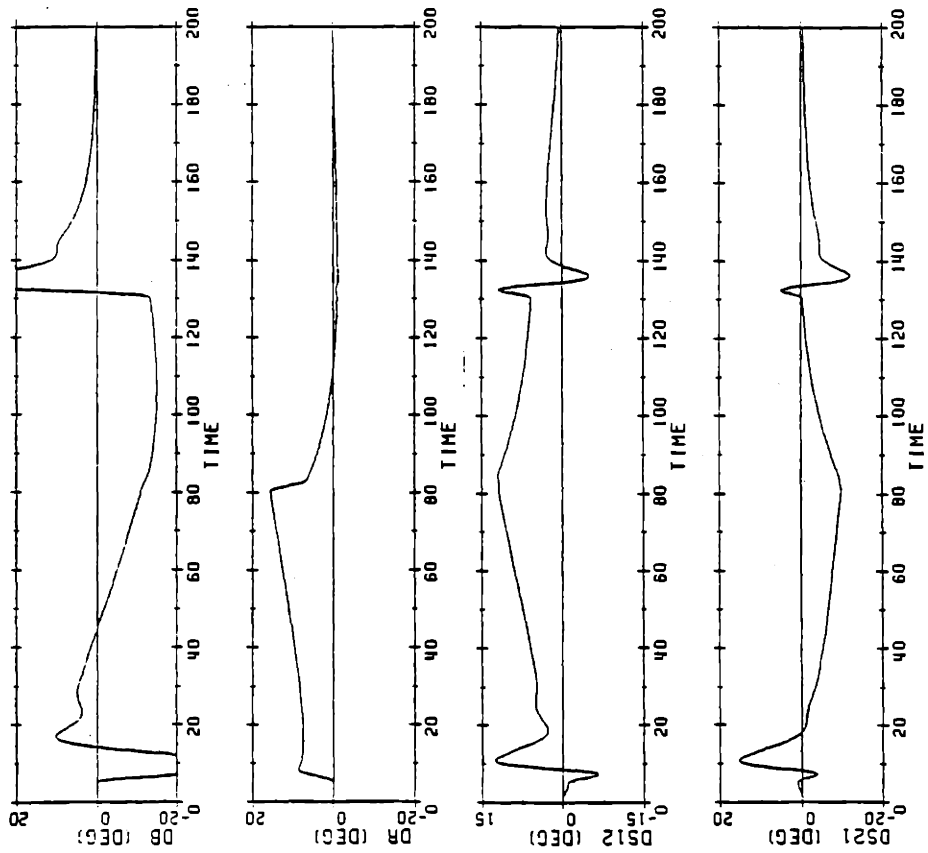


Figure 5.7 Comparison of 15 Knot and 30 Knot Compensators for Simultaneous Turn and Dive (30 to 15 Knots)

CONTROL INPUTS

NONLINEAR INTEGRATION FOR 4.5 FT/SEC. -10 DEG 4 -2 DEG/SEC



CONTROL INPUTS

NONLINEAR INTEGRATION FOR 4.5 FT/SEC. -10 DEG 4 -2 DEG/SEC INMINUTE

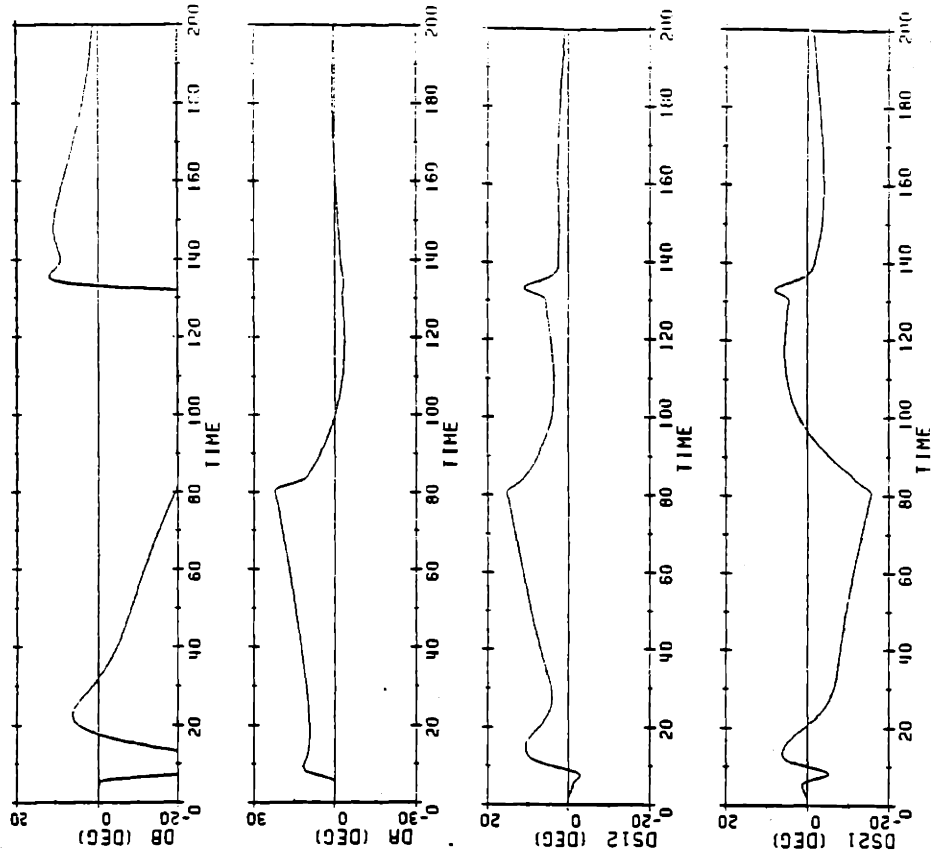
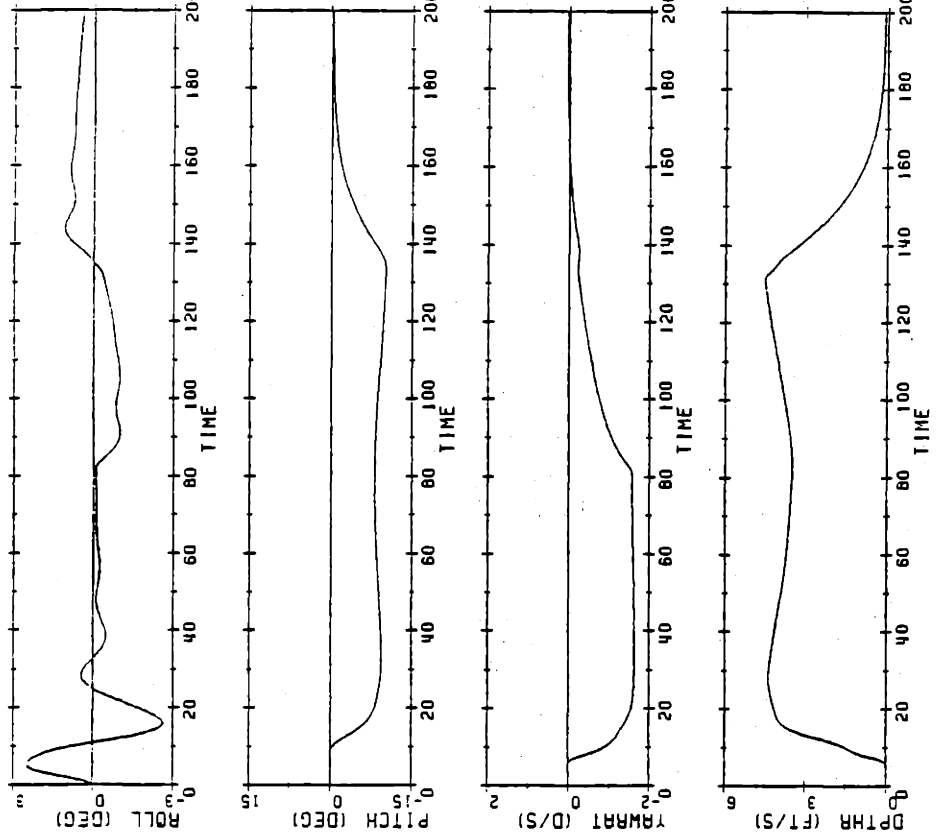


Figure 5.7 Comparison of 15 Knot and 30 Knot Compensators for Simultaneous Turn and Dive (30 to 15 Knots)

OUTPUTS

NONLINEAR INTEGRATION FOR 4.5 FT/SEC, -10 DEG 4 -2 DEG/SEC



OUTPUTS

NONLINEAR INTEGRATION FOR 4.5 FT/SEC, -10 DEG 4 -2 DEG/SEC (ANIMATE)

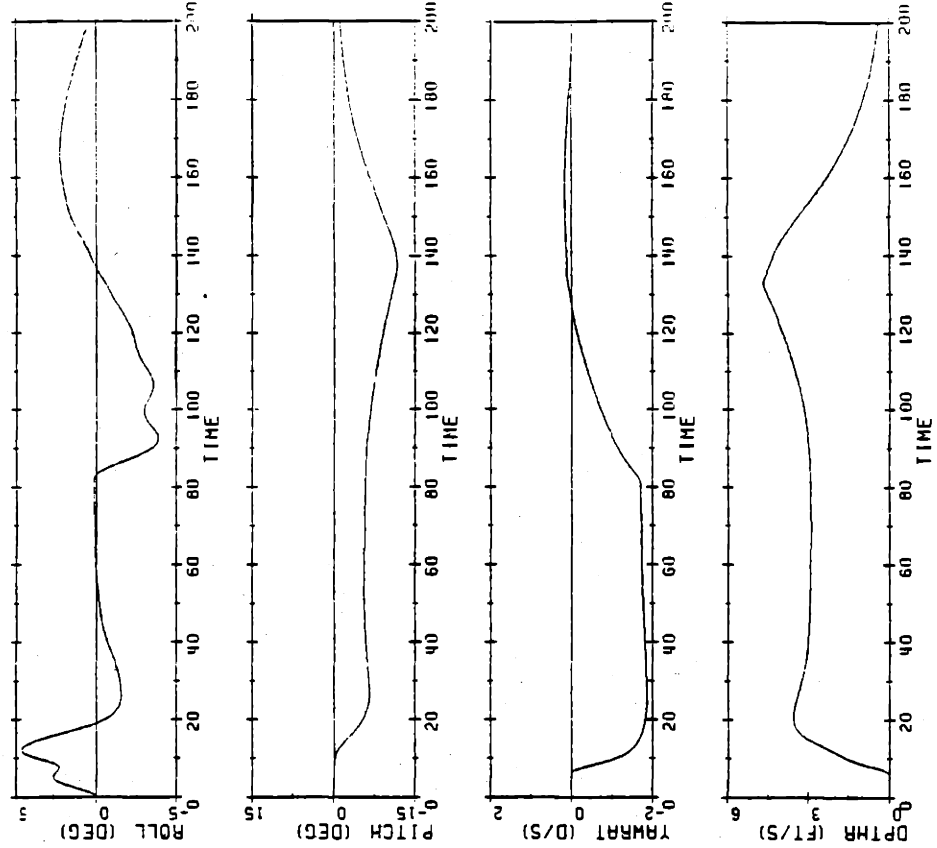


Figure 5.7 Comparison of 15 Knot and 30 Knot Compensators for Simultaneous Turn and Dive (30 to 15 Knots)

commands are removed. The results of the roll and dive maneuver provided similar results and are therefore not presented.

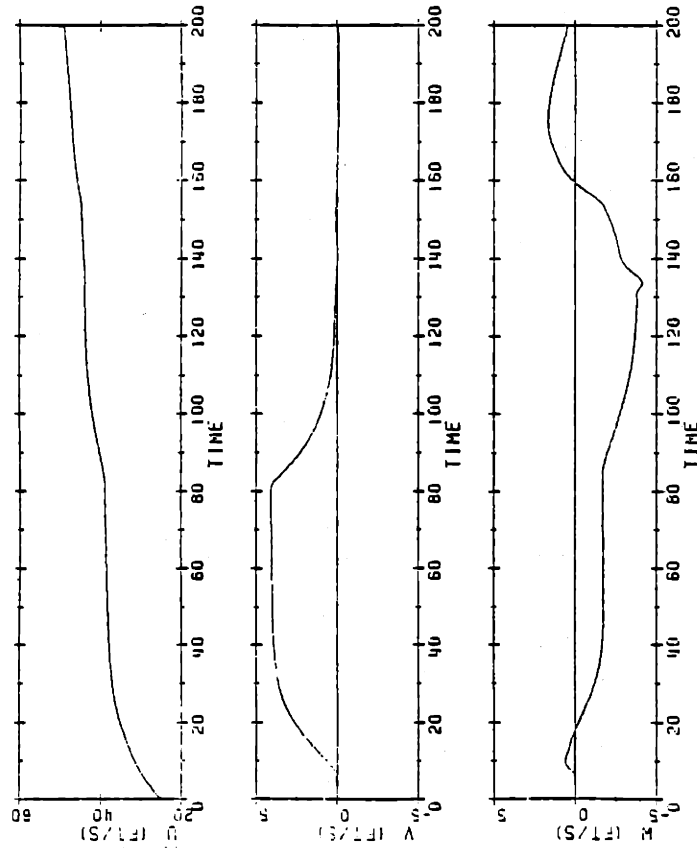
As shown in Figure 5.8, very interesting results were obtained when the simulation was repeated for 15 to 30 knots. The results are similar until the yawrate command is removed. At that time, the system with the 30 knot compensator experiences a large snap roll, almost twice that of the 15 knot compensator. At $t = 110$ seconds, the fairwater planes of the 30 knot compensator saturate which the system also handles but with a larger error in pitch and depthrate. At $t = 130$ however, the pitch and depthrate commands are zeroed and the system goes unstable in the vertical plane as evidenced by the growing depthrates and pitch angles and repeated saturation of the fairwater planes and the oncoming saturation of the sternplanes.

As shown by Martin, the 30 knot compensator performs well for large yawrates. It appears then that the problem arises only for motion in the vertical plane. The reason or reasons why the system with the 30 knot compensator goes unstable and the system with the 15 knot compensator does not are unknown but the following is offered as a possible explanation.

- (1) The higher crossover frequency for the 30 knot compensator causes the control surfaces to move faster. These quick movements result in quicker control surface saturations resulting in large integrated errors.
- (2) Since we are operating away from the nominal design point, the model is no longer accurate for motion in the vertical plane.
- (3) The drag terms associated with the 15 knot compensator simulation are actually 4 times larger at 30 knots than at

VELOCITIES

NONLINEAR INTEGRATION FOR 4.5 FT/SEC, -10 DEG & -2 DEG/SEC



VELOCITIES

NONLINEAR INTEGRATION FOR 4.5 FT/SEC, -10 DEG & -2 DEG/SEC YAHARATE

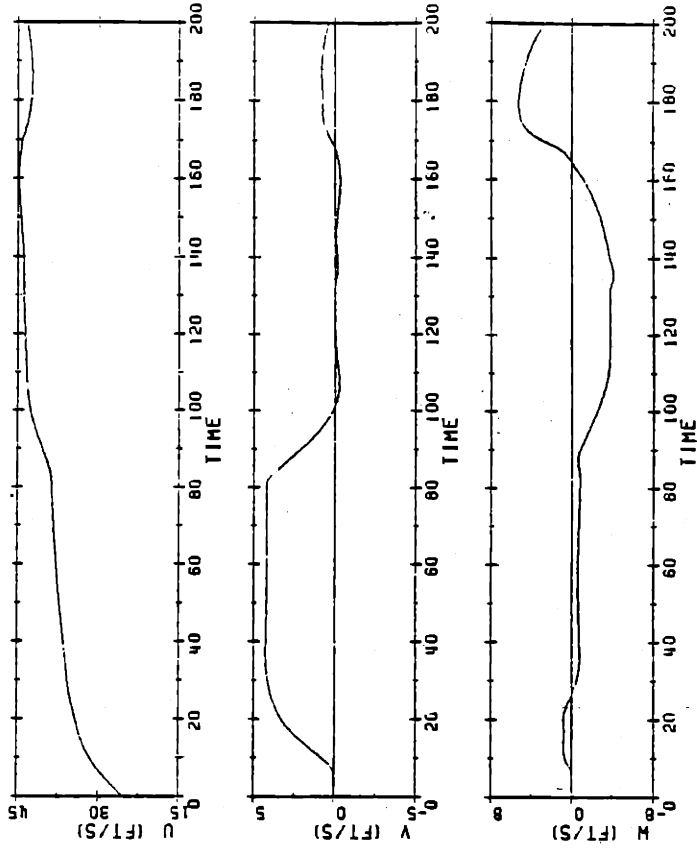
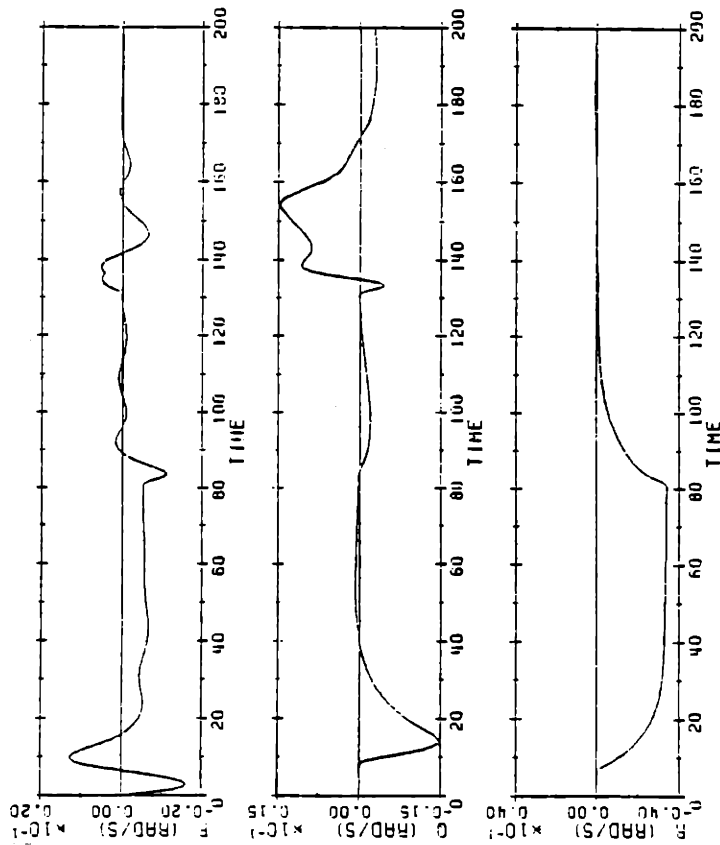


Figure 5.8 Comparison of 15 Knot and 30 Knot Compensators for Simultaneous Turn and Dive (15 to 30 Knots)

ANGULAR VELOCITIES

NONLINEAR INTEGRATION FOR 4.5 FT/SEC. -10 DEG & -2 DEG/SEC



ANGULAR VELOCITIES

NONLINEAR INTEGRATION FOR 4.5 FT/SEC. -10 DEG & -2 DEG/SEC TAARATE

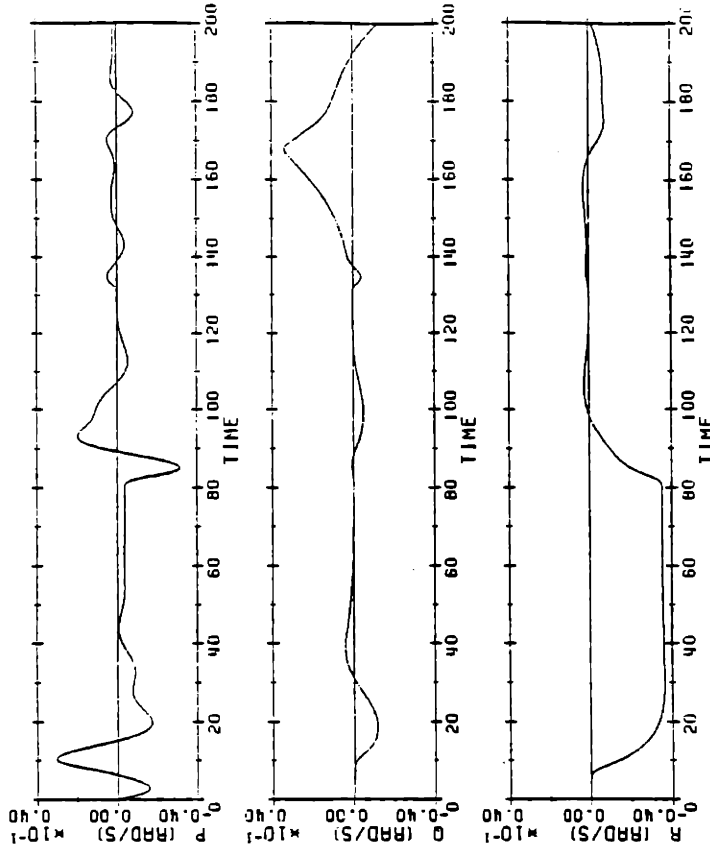
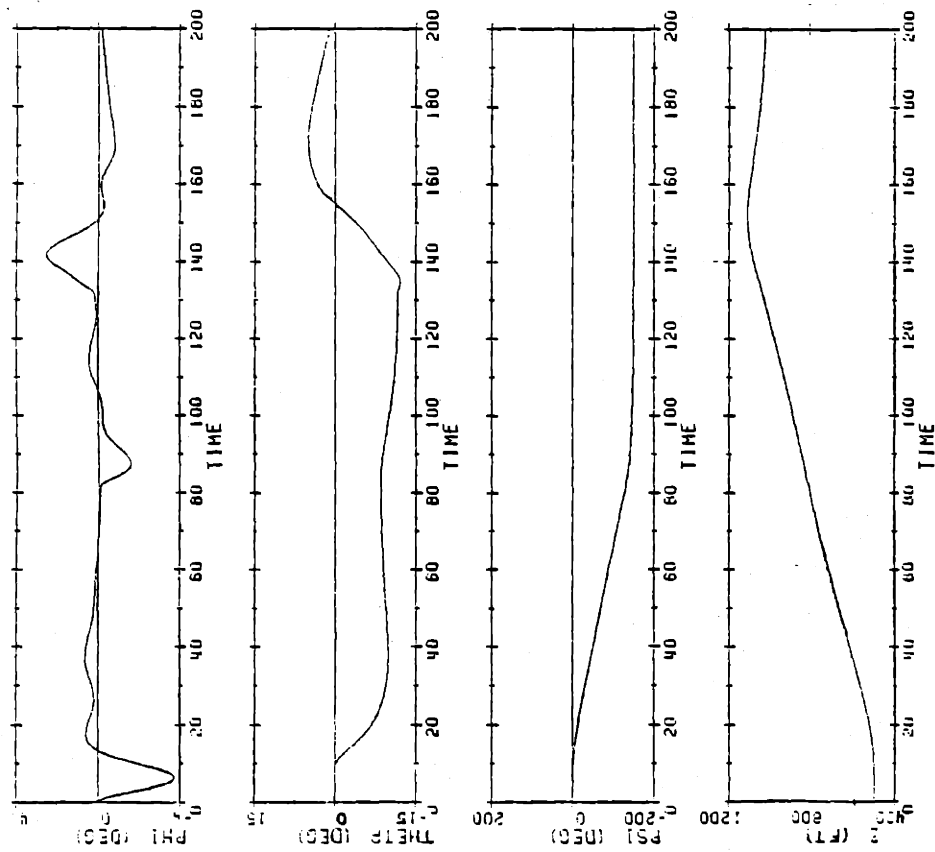


Figure 5.8 Comparison of 15 Knot and 30 Knot Compensators for Simultaneous Turn and Dive (15 to 30 Knots)

ATTITUDE AND DEPTH

NONLINEAR INTEGRATION FOR 4.5 FT/SEC, -10 DEG & -2 DEG/SEC



ATTITUDE AND DEPTH

NONLINEAR INTEGRATION FOR 4.5 FT/SEC, -10 DEG & -2 DEG/SEC YAHARAIE

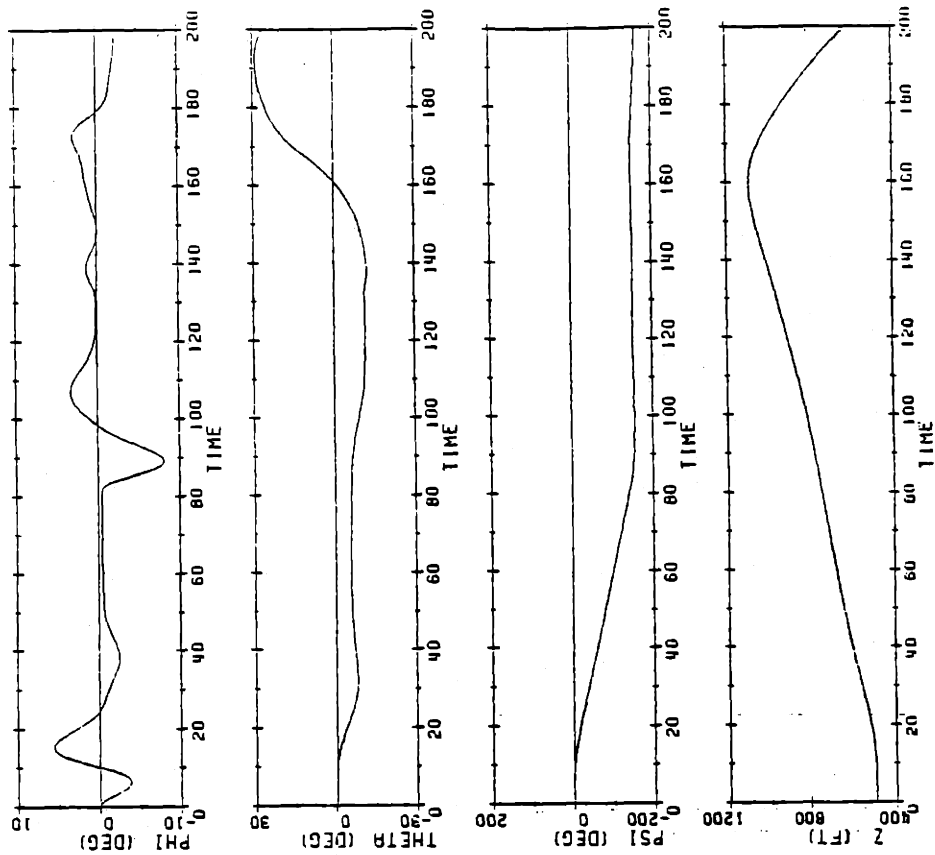
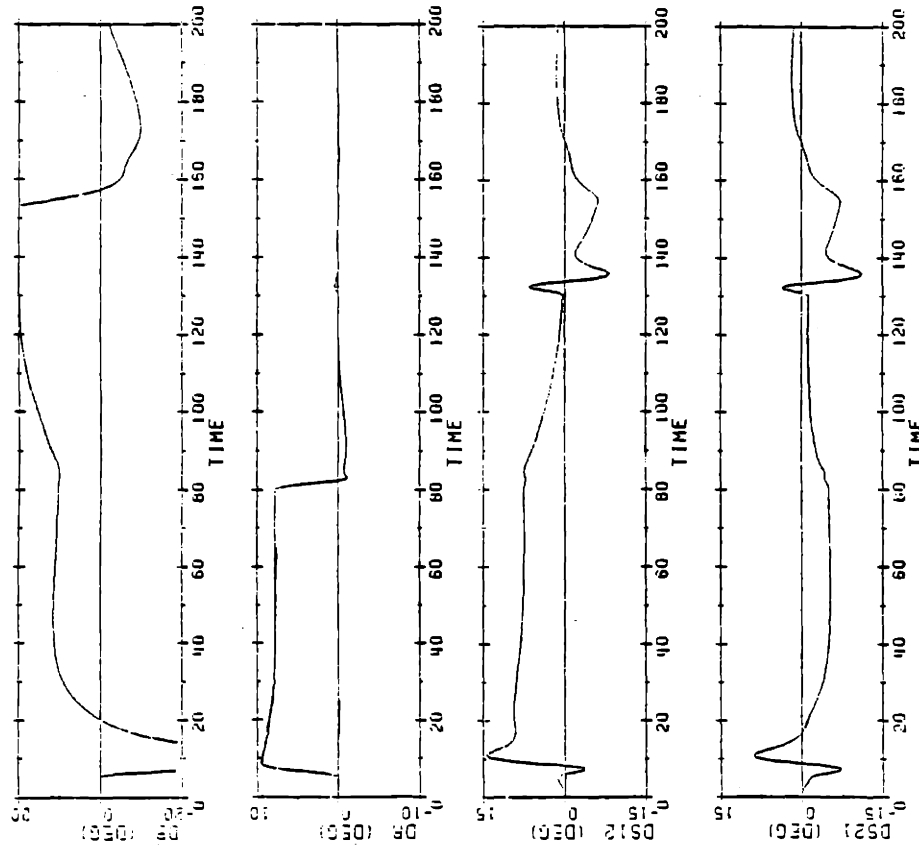


Figure 5.8 Comparison of 15 Knot and 30 Knot Compensators for Simultaneous Turn and Dive (15 to 30 Knots)

CONTROL INPUTS

NONLINEAR INTEGRATION FOR 4.5 FT/SEC, -10 DEG & -2 DEG/SEC



CONTROL INPUTS

NONLINEAR INTEGRATION FOR 4.5 FT/SEC, -10 DEG & -2 DEG/SEC TURNRATE

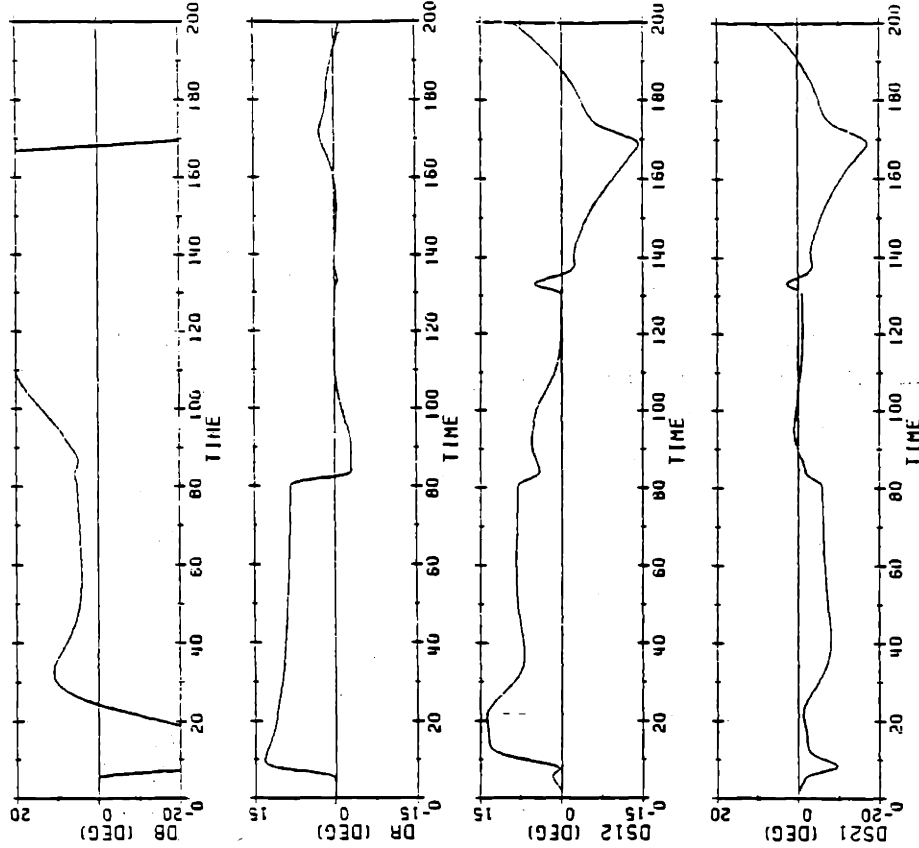
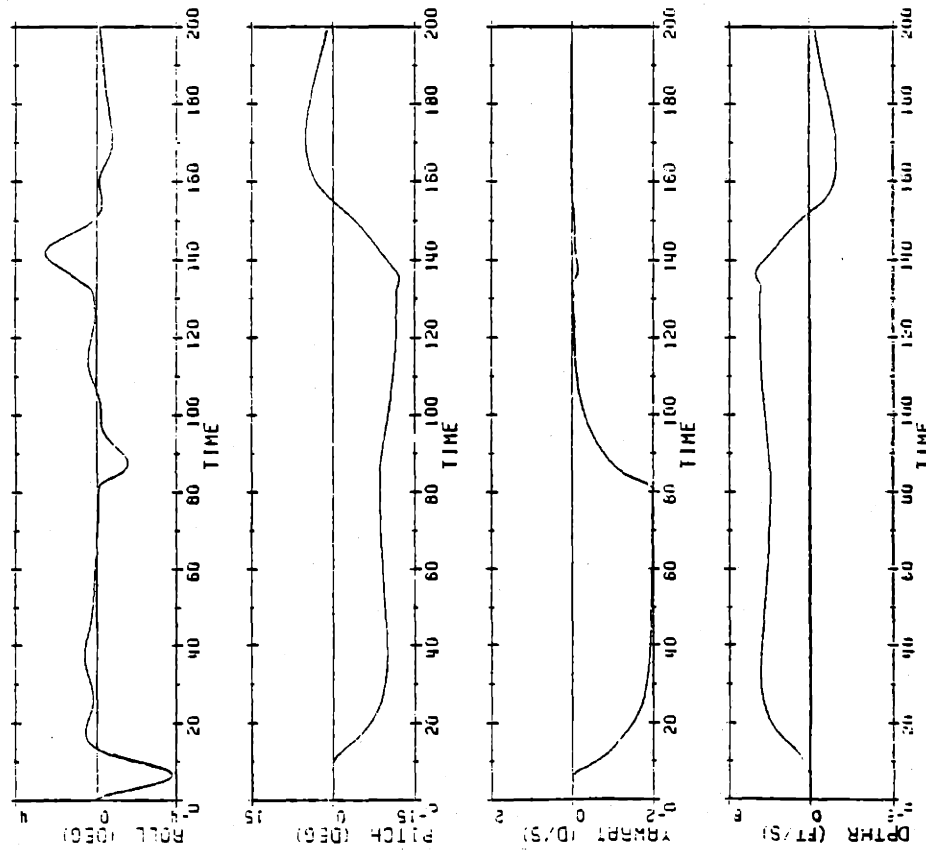


Figure 5.8 Comparison of 15 Knot and 30 Knot Compensators for Simultaneous Turn and Dive (15 to 30 Knots)

OUTPUTS

NONLINEAR INTEGRATION FOR 4.5 FT/SEC, -10 DEG & -2 DEG/SEC



OUTPUTS

NONLINEAR INTEGRATION FOR 4.5 FT/SEC, -10 DEG & -2 DEG/SEC YAWRATE

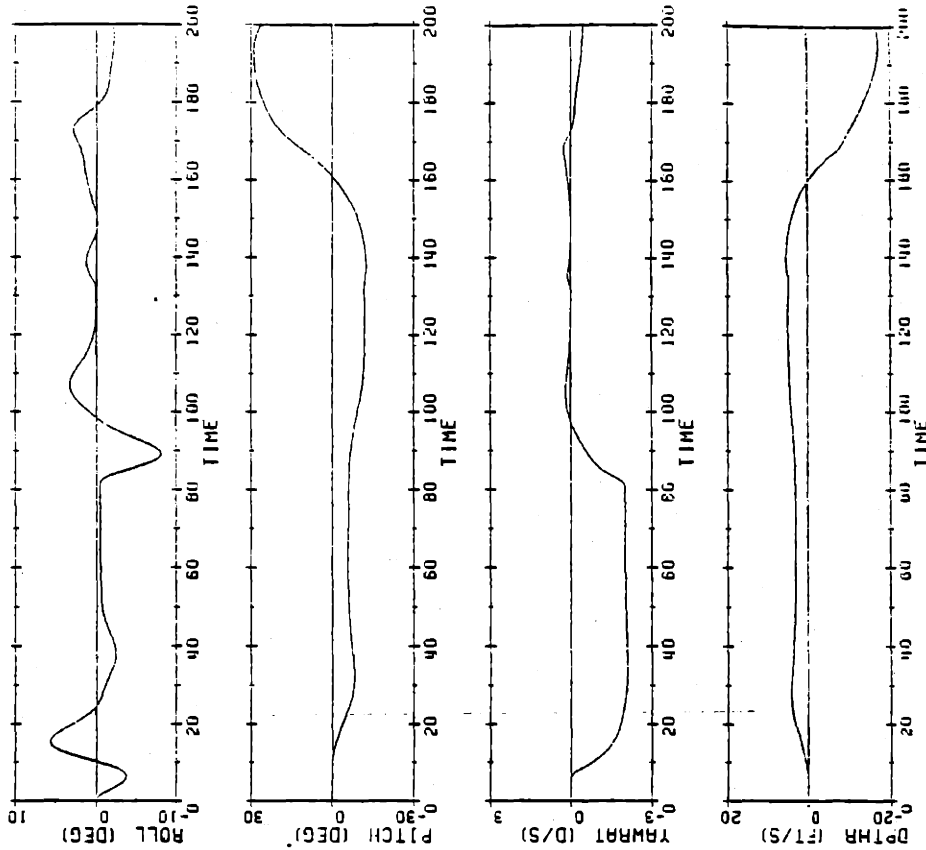


Figure 5.8 Comparison of 15 Knot and 30 Knot Compensators for Simultaneous Turn and Dive (15 to 30 Knots)

15 knots (drag is proportional to velocity squared) where the compensator was designed. This has sufficiently slowed the system response at 30 knots, particularly in the directions related to motion in the vertical plane.

Determination of the exact cause is a subject which requires further research. In any case, the 30 knot does exhibit better performance in mild maneuvers so to implement a global control system for the submarine at various speed and for various maneuvers, there may be some merit to using a quick controller for mild maneuvers and a slower controller for more radical maneuvers.

As a result of this analysis, it was determined that implementing a gain scheduling algorithm would not be feasible without either redesigning the 30 knot compensator for a lower crossover frequency or limiting the maneuvers at higher speeds. As shown by Lively [7], implementing a gain scheduling scheme is rather straightforward and in this case, it was felt that nothing new would be learned from the exercise.

5.4 Summary

This chapter has covered some of the more stressful maneuvers which the 15 knot compensator performed. The 30 knot compensator exhibited better behavior for less stressful maneuvers and at lower speeds where the quick control surface movements did not excite any instabilities like it did at higher speeds. As a result of this comparison, gain scheduling was not used as it was felt that more could be learned from investigating the effect of control surface saturation. The use of an Antireset Windup (ARW) feedback loop is investigated in Chapter 6.

CHAPTER 6

IMPLEMENTATION OF ANTI-RESET WINDUP FEEDBACK

6.1 Introduction

In Chapter 5, it became apparent that as the submarine is ordered to do more difficult maneuvers, control surface saturation enters into the picture. While the 15 knot compensator remained stable throughout the testing, the 30 knot compensator did not. As was evident in the simulations presented in Chapter 5, control surface saturation of the fairwater planes occurred frequently and in some cases for long periods of time. To decrease the time required for a control surface to come out of saturation, an Anti-Reset Windup (ARW) feedback loop is installed. The chapter begins with a discussion of the ARW feedback loop. This is followed by an analysis of the impact of the ARW loop on the open loop and closed loop systems. Finally, several simulations which demonstrate the use of ARW are presented.

6.2 ARW Feedback Loop

As a result of prolonged control surface saturation, the system experiences a phenomena known as integrator windup or reset windup. The delay in the control surface or surfaces coming out of saturation after the saturating condition is no longer in effect is caused by the integration of the error between the ordered deflection and the saturation level. If the

error is large and/or the period of saturation is long, the integrated error may also become large and quite significant delays can be encountered. To counter this problem, a nonlinear feedback loop is employed whose effect is to "turn off" the integrator for the saturating actuator.

The use of ARW strategy in a MIMO control system is not fully developed and the method employed here is based on [27] and personal interactions with its authors, Kpasouris and Athans. Figure 6.1 shows the closed loop system with the ARW feedback loop installed around the

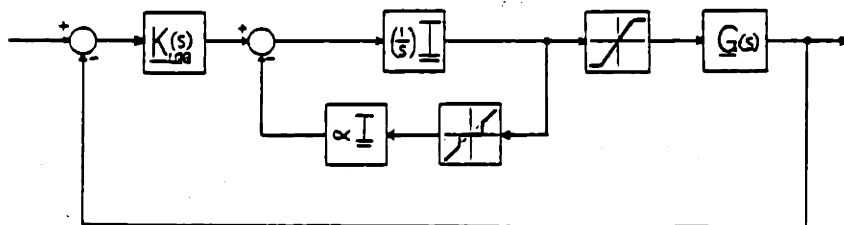


Figure 6.1 Structure of the Closed Loop System With ARW

integrators. The nonlinearity prior to the plant represents the saturating control surfaces of the submarine, with the saturation limits as listed in Table 3.1. When the control surfaces are not in saturation, the feedback loop is "deenergized" through the "dead-zone" as shown. As a control surface saturates, the feedback loop for that control channel energizes. As a result of this feedback, the integrator is replaced by a lag network as shown by (6.1). The amount of feedback used is a function of the

$$\begin{aligned}
 \underline{u}(s) &= (\underline{I}/s) [\underline{I} + \alpha(\underline{I}/s)]^{-1} \underline{K}(s) \underline{e}(s) \\
 &= \underline{K}(s) [\underline{I}/(s + \alpha)] \underline{e}(s)
 \end{aligned}
 \tag{6.1}$$

variable α in the loop but the net effect of the feedback is to reduce the gain at low frequency. Figure 6.2 shows the effect of the parameter α on the Bode plot of a lag network. As α is decreased, the behavior of the

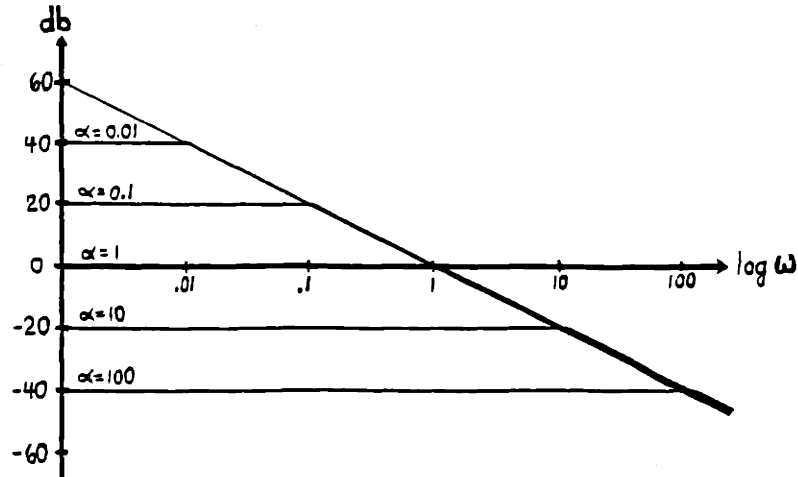


Figure 6.2 Bode Plot of Simple Lag for Varying α

loop approaches that for the integrator. As α is increased, the gain at low frequency decreases. At present, there is no known straightforward method for selecting α , especially for the MIMO case. To gain some insight on a method of selection, several areas were examined.

Figure 6.3 shows the effect the ARW method has on the singular values of the loop transfer matrix $\underline{G}(s)\underline{K}(s)$ where $\underline{G}(s)$ now contains the dynamics of the ARW feedback loop instead of the integrators as presented in Section 3.5. At low frequencies, the singular values have spread with two showing slight increases, one a slight decrease and the one associated with the saturated control surface a drastic decrease. When α was decreased by a factor of 1/2 from 0.1 to 0.05, the minimum singular value increased by a factor of 2 or 6 dB. There was little or no effect on the transfer function relating reference commands to control inputs (4.30) or its singular value decomposition. Finally, the effect on the singular values

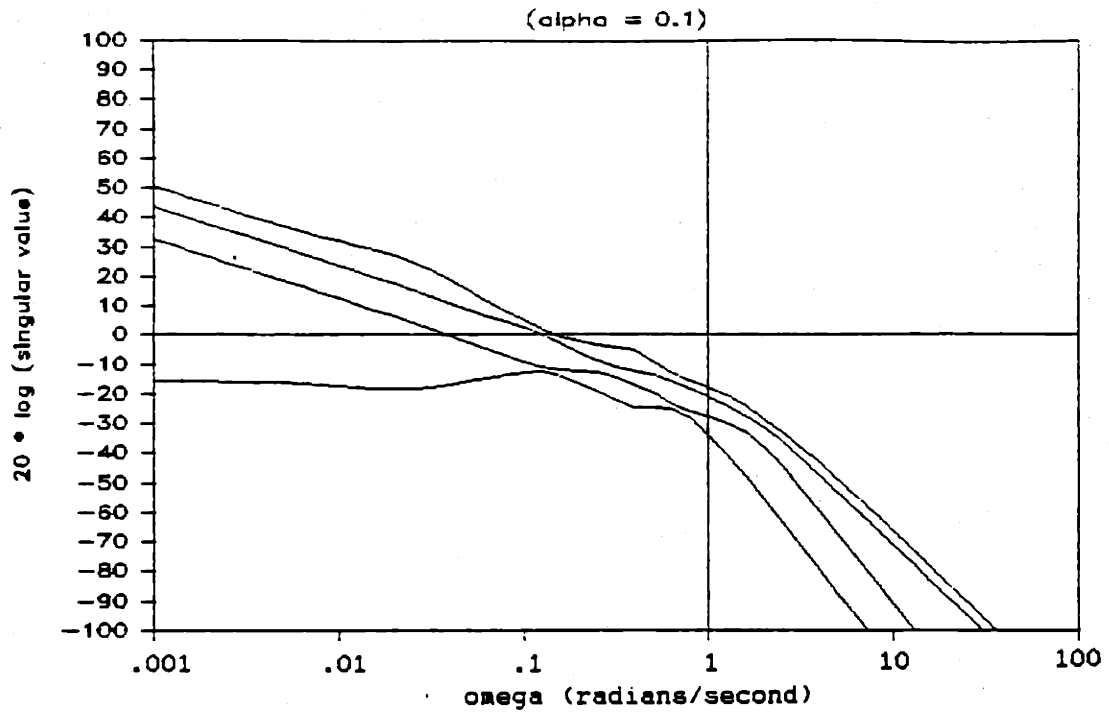


Figure 6.3a Singular Values of $G(s)K(s)$ for $\alpha = 0.1$

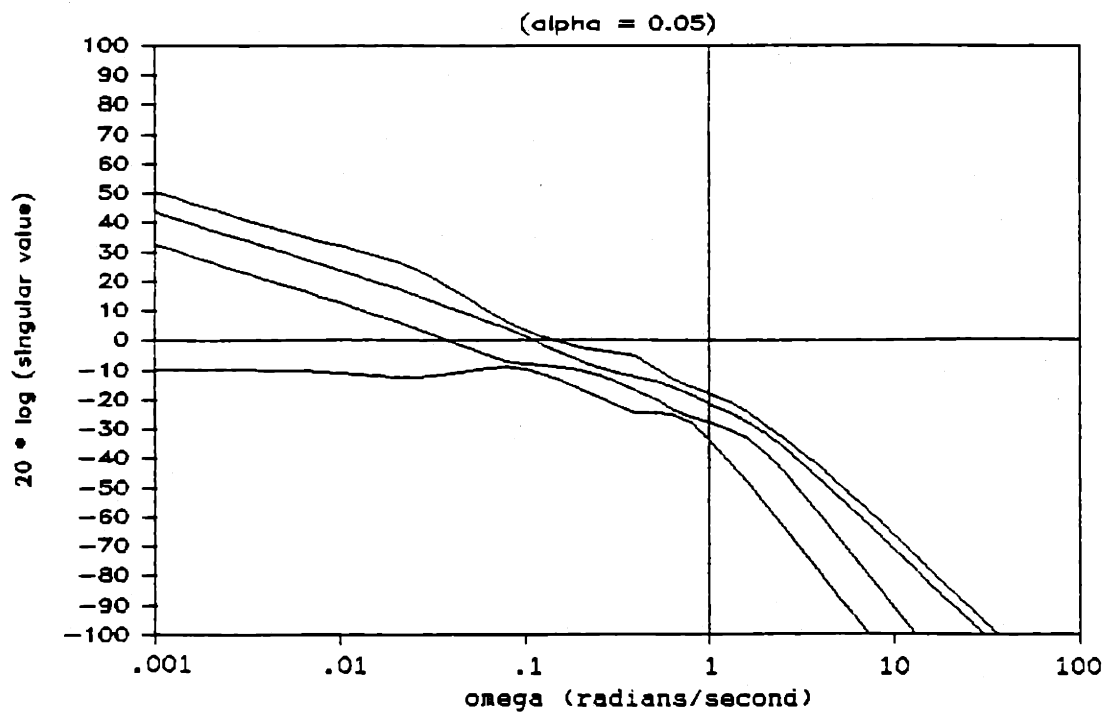


Figure 6.3b Singular Values of $G(s)K(s)$ for $\alpha = 0.05$

of the closed loop system for $\alpha = 0.05$ is shown in Figure 6.4. Again, spreading of the singular values occurs at low frequency and one would expect problems in the channel with the -10 dB minimum singular value. For this design then, the only noticeable effect is on the singular values and not the singular vectors. Therefore, selection of the parameter α appears to be based on how much the minimum singular value of the unaugmented system needs to be increased at low frequency to assure acceptable command performance. In the next section, several simulations which show the merit of using an ARW feedback loop are presented.

6.3 Simulations for System With ARW Feedback

Using the ARW feedback loop as described in Section 6.2, several simulations were made for various values of α . Because the minimum singular value of $\underline{G}(s)\underline{K}(s)$ exhibits such a large dependence on α , it was thought that to have adequate performance and robustness, α would have to be selected such that the value of the minimum singular value was at least 20 dB at low frequency, consistent with the low frequency barrier in Figure 3.6. This proved not to be the case as an α of 0.05 seemed to provide adequate command following. This may only be sufficient for the series of tests performed by the author. Additional testing may indeed indicate that command following is not satisfactory for some combination of command inputs. But that is a subject for further research.

Since saturation of the fairwater planes occurs most frequently, the first two simulations deal with an ordered depthrate with zero commanded pitch as this would easily cause saturation. A comparison of the closed loop system response for a 2 feet/second commanded depthrate with and

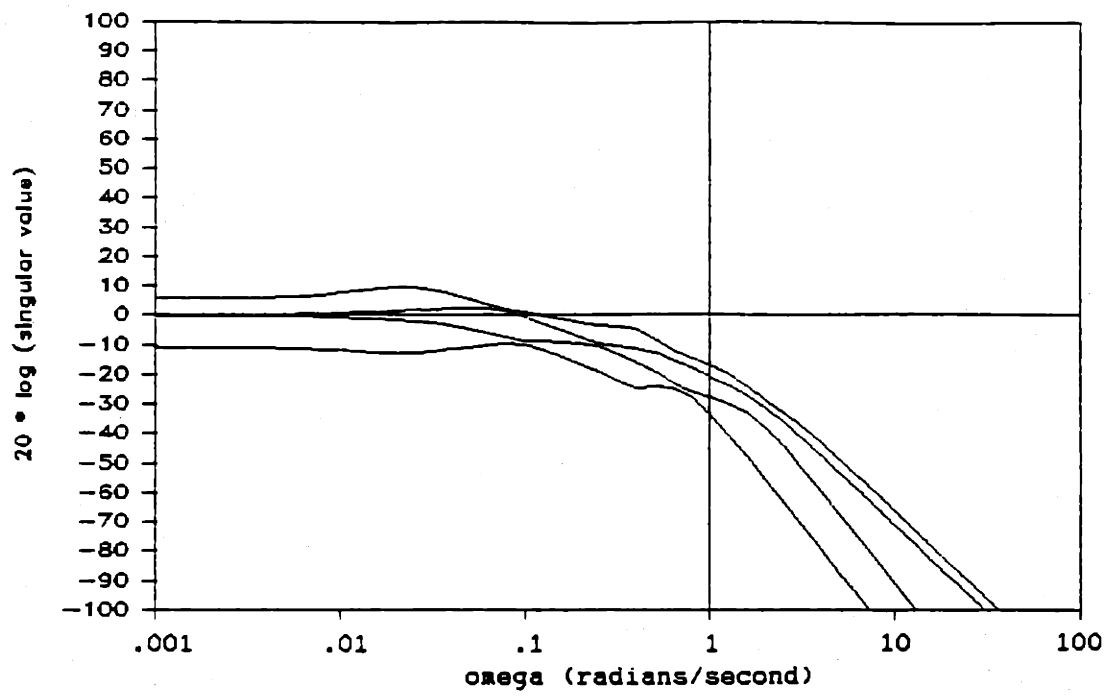


Figure 6.4 Singular Values of the Closed Loop for $\alpha = 0.05$

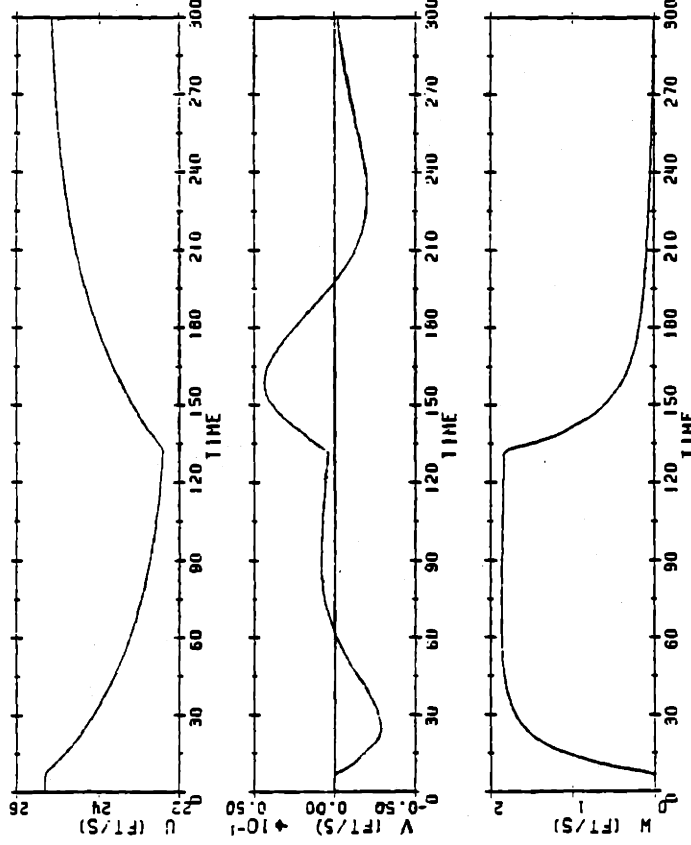
without ARW feedback is shown in Figure 6.5. A "mild" saturation is created by application of the reference command at $t = 5$ seconds. Noting the change in scale on the graphs, we see that the responses remain identical until $t = 130$ seconds when the reference command is zeroed. At that time, sternplane and rudder deflections are the same but a slight difference in the fairwater plane deflection occurs with the ARW simulation displaying a slight overshoot. Review of the outputs show that the oscillations have been effectively decreased and the output errors slightly reduced in magnitude.

To demonstrate the effects of a prolonged "hard" saturation, another simulation was made with a 4 feet/second commanded depthrate as shown in Figure 6.6. There is a slight difference in the rudder and sternplane deflections but an obvious improvement in fairwater plane response is noted. At $t = 130$ seconds when the reference command is zeroed, the fairwater planes for the system with ARW immediately deflect to reduce the depthrate to zero while the fairwater planes for the system without ARW do not come out of saturation for another 110 seconds! A comparison of output variables again shows that the ARW feedback loop has decreased oscillations and more importantly, decreased the error by as much as a factor of 2 in the case of depthrate and yawrate.

These simulations have shown that for a system which experiences prolonged control surface saturation, the use of an ARW feedback loop will decrease oscillations in the outputs and sometimes significantly decrease the magnitude of the maximum error. Additionally, the use of the fairwater planes as an effective dynamic control input is regained almost immediately instead of waiting until the integrated error is nulled.

VELOCITIES

NONLINEAR INTEGRATION FOR 2.0 FT/SEC WITHOUT ANTI-RESET HINDUP



VELOCITIES

NONLINEAR INTEGRATION FOR 2.0 FT/SECOND ANTI-RESET HINDUP

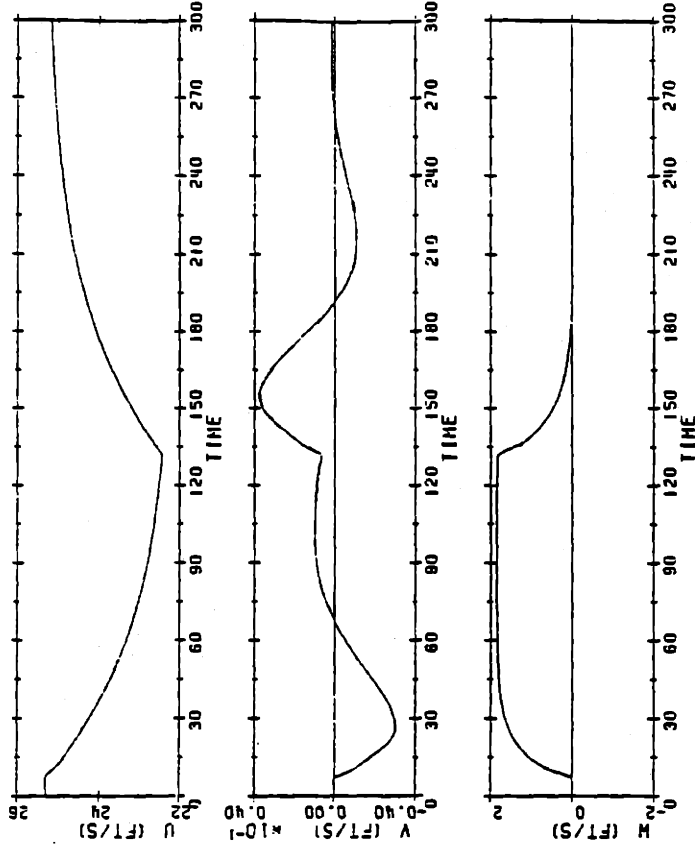
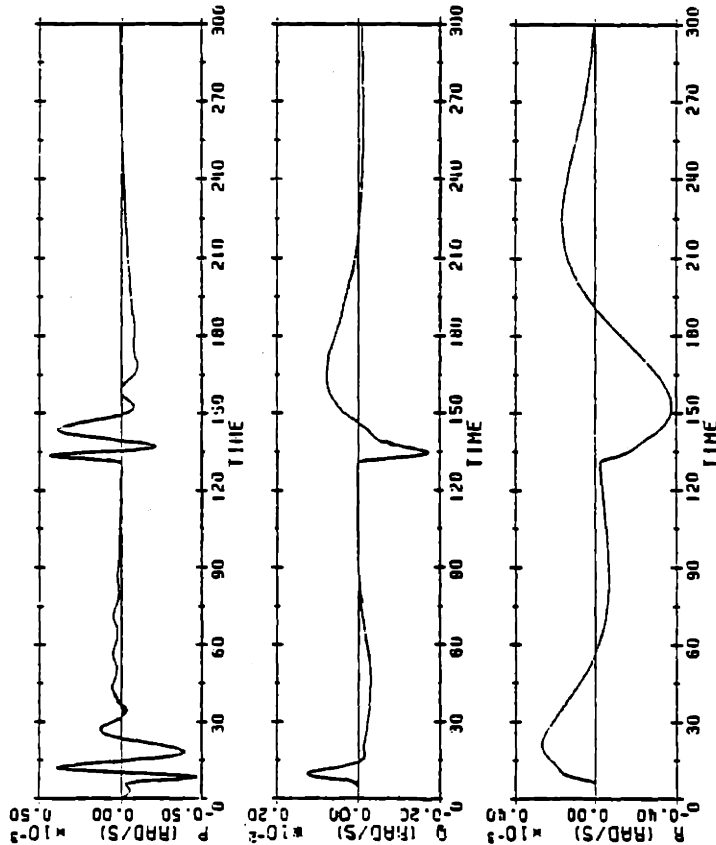


Figure 6.5 Comparison of Systems Without and With ARW ($\alpha = 0.05$) for 2 Feet/Second Depthrate

ANGULAR VELOCITIES

NONLINEAR INTEGRATION FOR 2.0 FT/SEC WITHOUT ANTI-RESET WINDUP



ANGULAR VELOCITIES

NONLINEAR INTEGRATION FOR 2.0 FT/SEC AND ANTI-RESET WINDUP

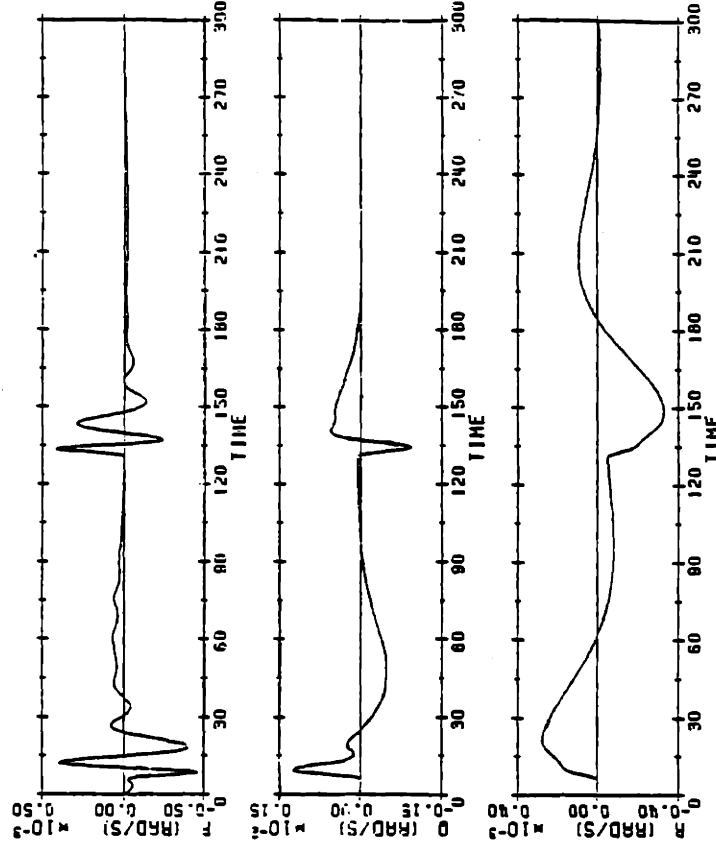
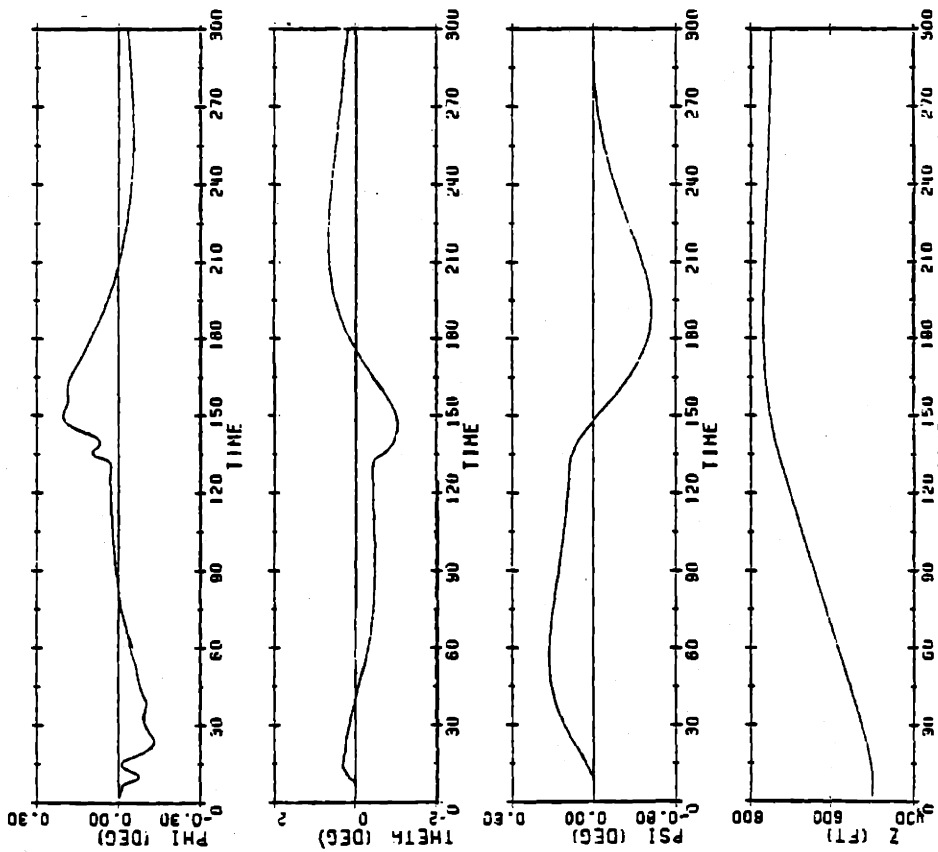


Figure 6.5 Comparison of Systems Without and With ARW ($\alpha = 0.05$) for 2 Feet/Second Depthrate

ATTITUDE AND DEPTH

NONLINEAR INTEGRATION FOR 2.0 FT/SEC WITHOUT ANTI-RESET HINDUP



ATTITUDE AND DEPTH

NONLINEAR INTEGRATION FOR 2.0 FT/SECOND ANTI-RESET HINDUP

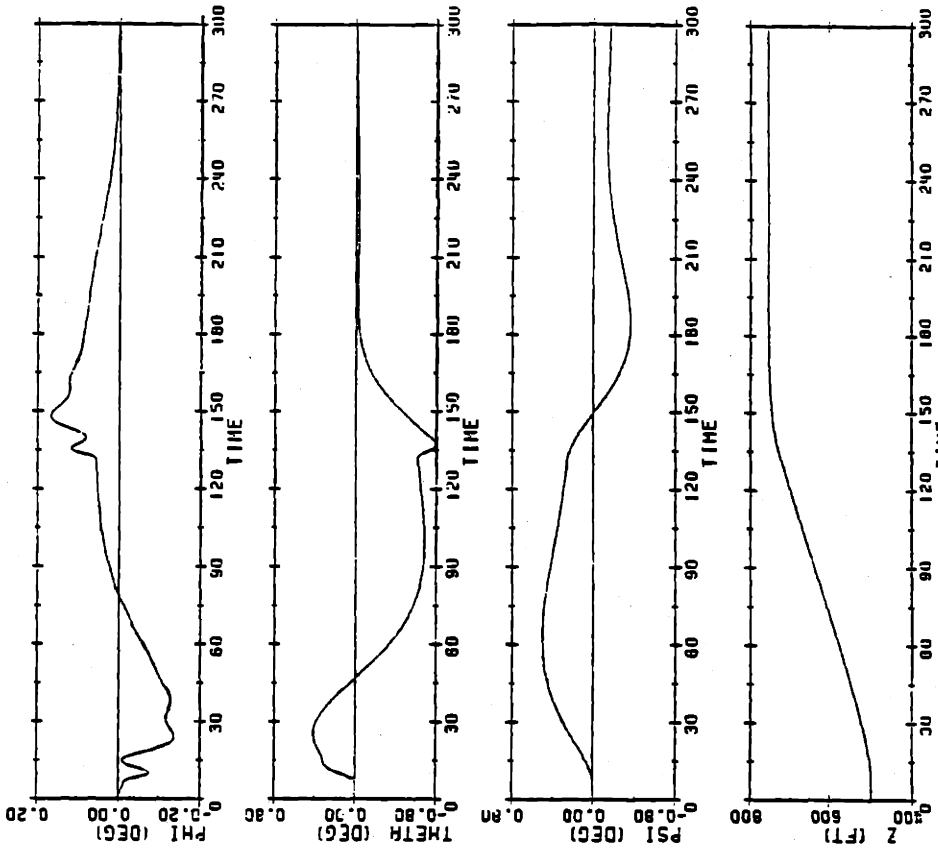
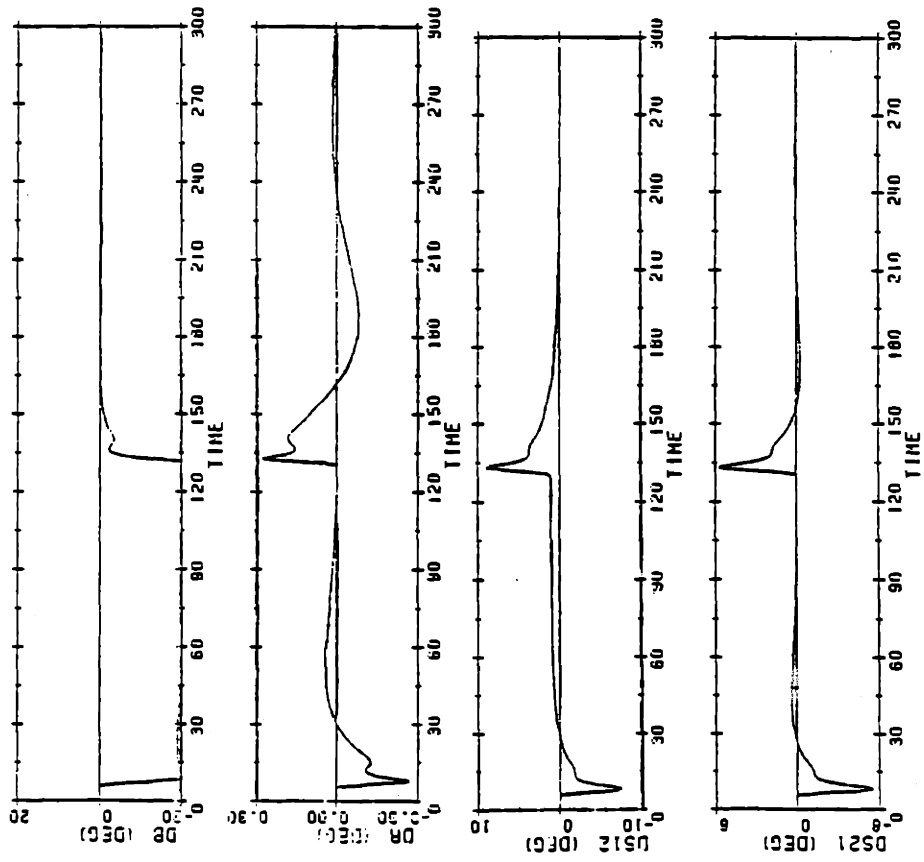


Figure 6.5 Comparison of Systems Without and With ARW ($\alpha = 0.05$) for 2 Feet/Second Depthrate

CONTROL INPUTS

NONLINEAR INTEGRATION FOR 2.0 FT/SEC WITHOUT ANTI-RESET HINDUP



CONTROL INPUTS

NONLINEAR INTEGRATION FOR 2.0 FT/SECOND ANTI-RESET HINDUP

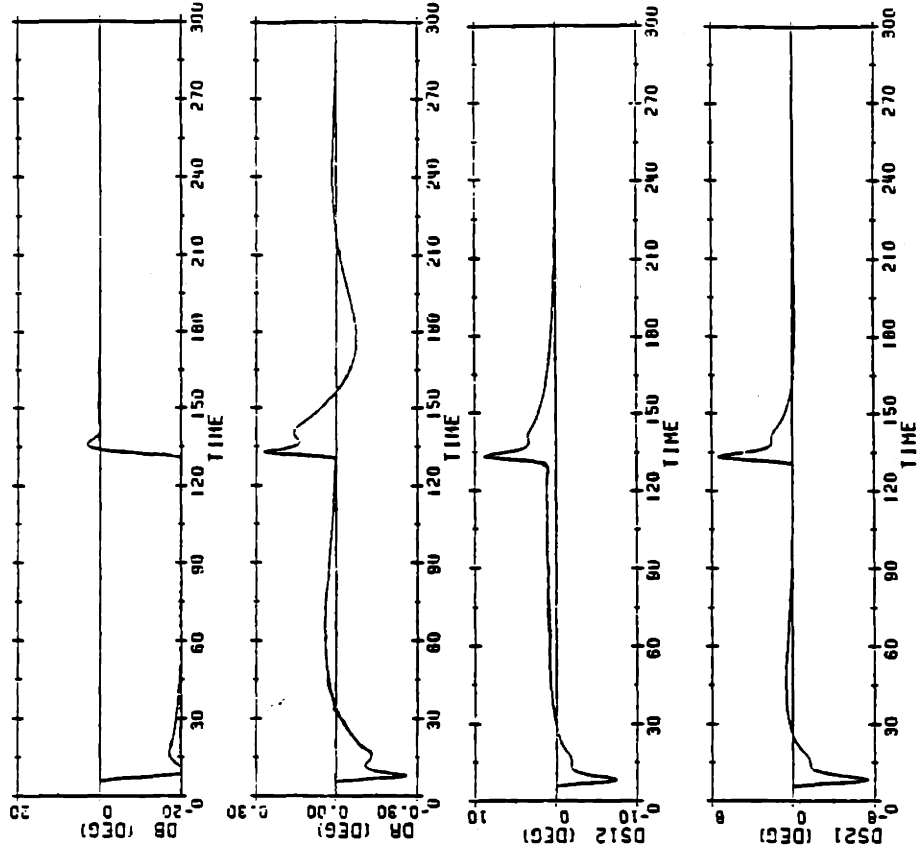
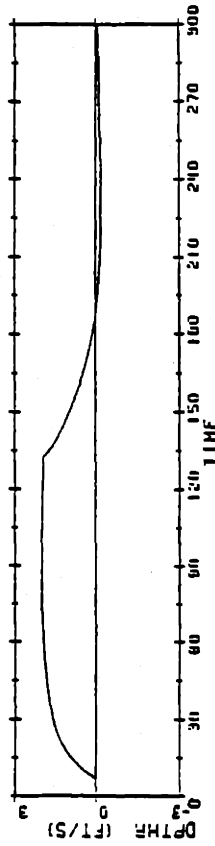
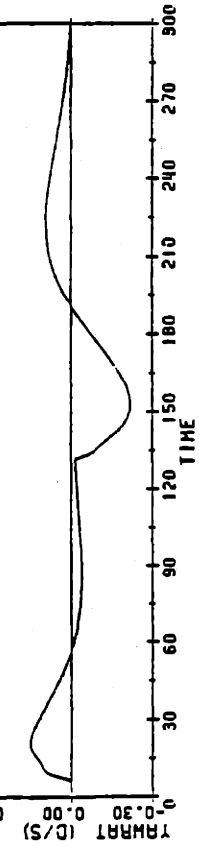
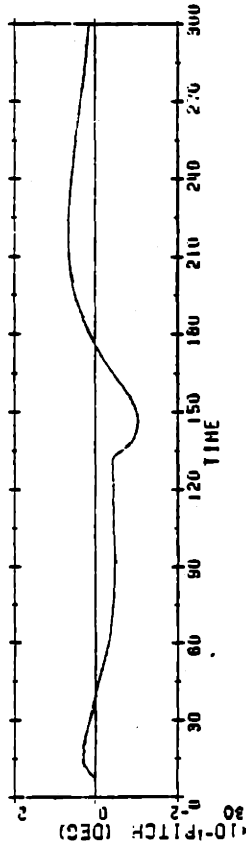
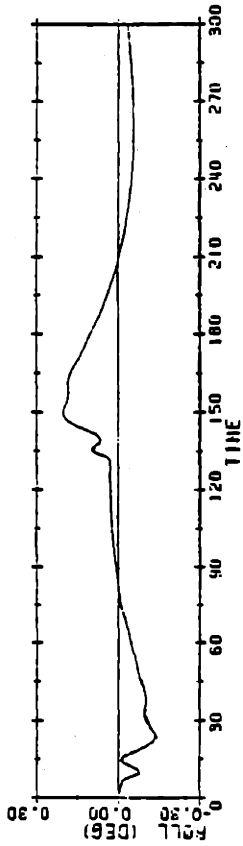


Figure 6.5 Comparison of Systems Without and With ARW ($\alpha = 0.05$) for 2 Feet/Second Depthrate

OUTPUTS

NONLINEAR INTEGRATION FOR 2.0 FT/SEC WITHOUT ANTI-RESET HINDUP



OUTPUTS

NONLINEAR INTEGRATION FOR 2.0 FT/SEC AND ANTI-RESET HINDUP

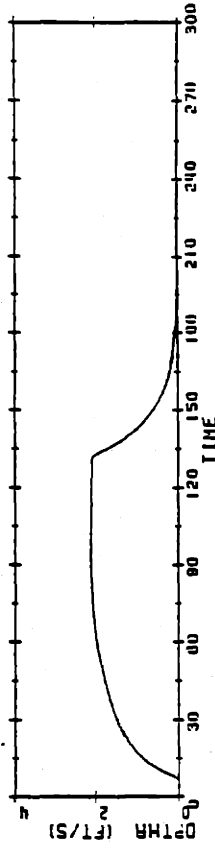
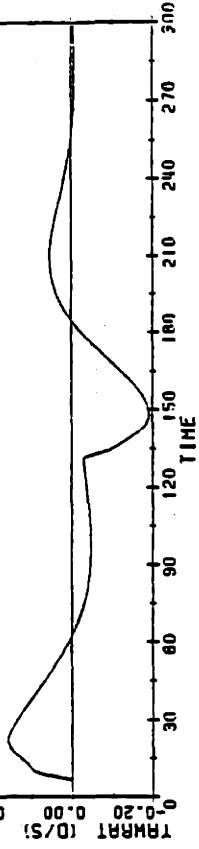
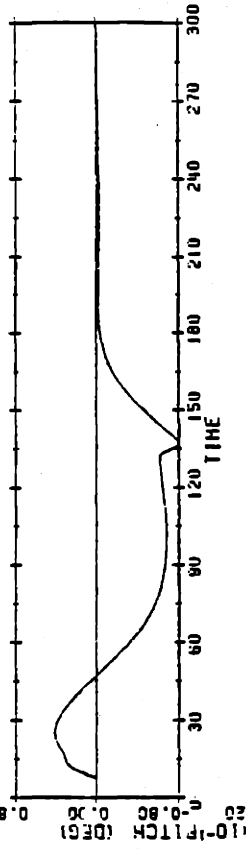
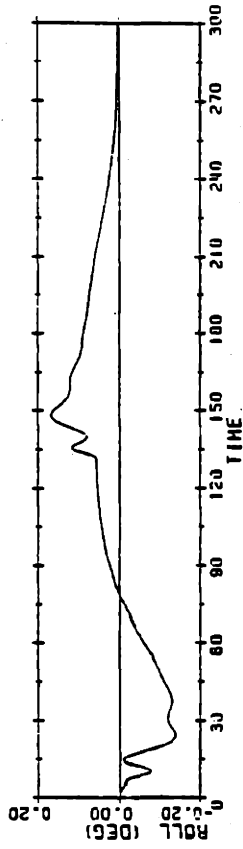
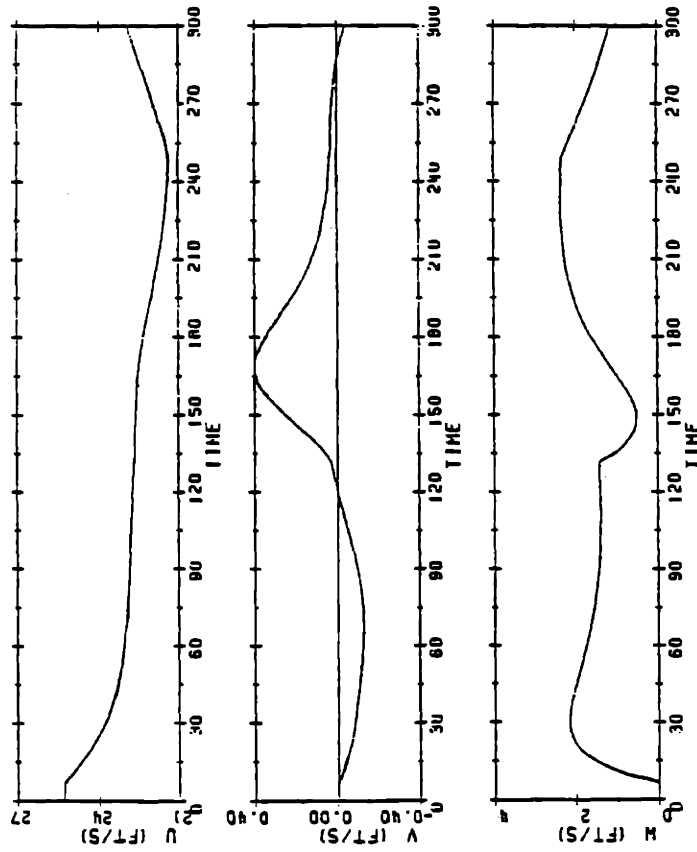


Figure 6.5 Comparison of Systems Without and With ARW ($\alpha = 0.05$) for 2 Feet/Second Depthrate

VELOCITIES

NONLINEAR INTEGRATION FOR 4.0 FT/SEC WITHOUT ANTI-RESET HINDUP



VELOCITIES

NONLINEAR INTEGRATION FOR 4.0 FT/SEC AND ANTI-RESET HINDUP

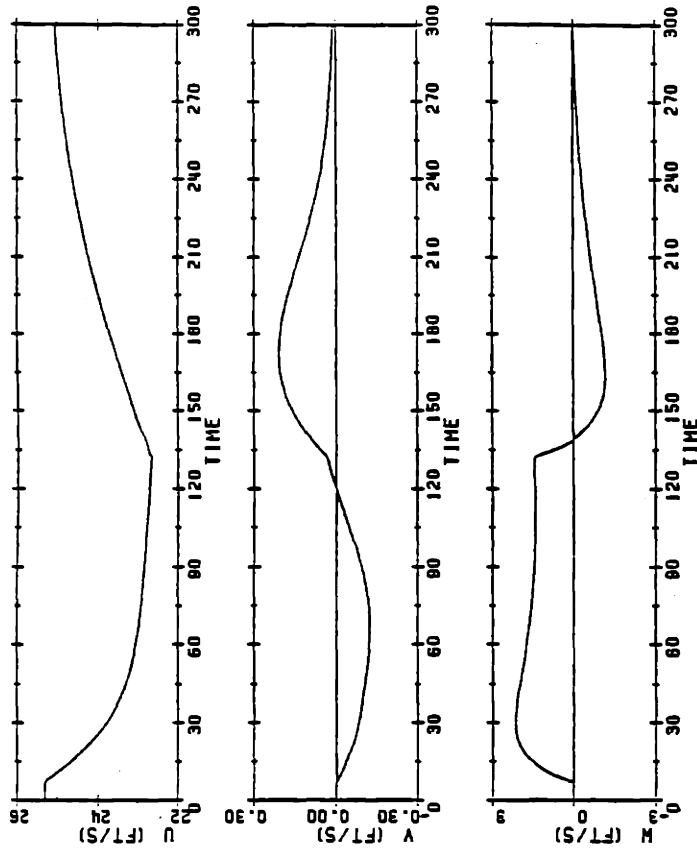
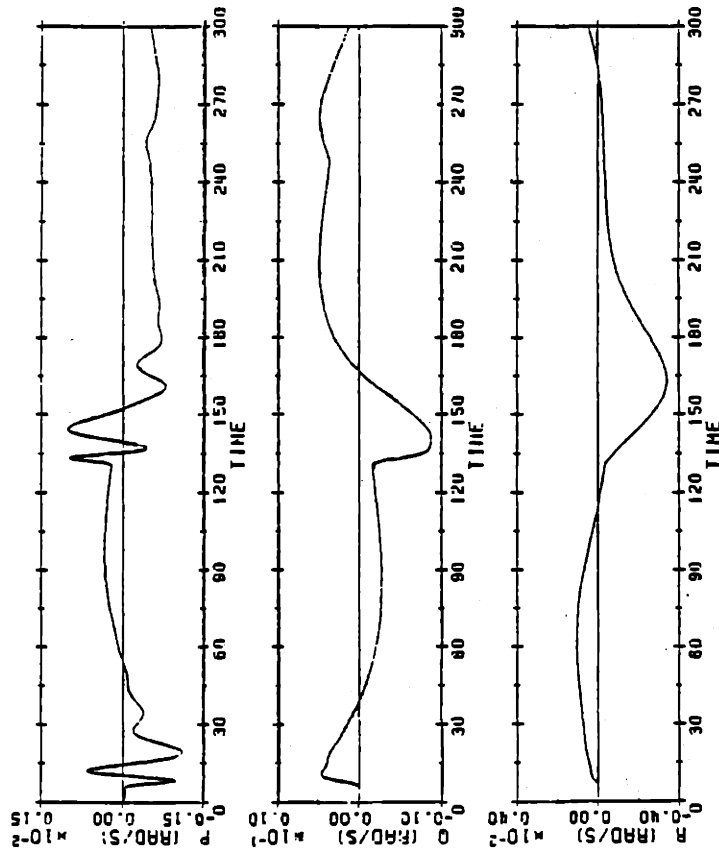


Figure 6.6 Comparison of Systems Without and With ARW ($\alpha = 0.05$) for 4 Feet/Second Depthrate

ANGULAR VELOCITIES

NONLINEAR INTEGRATION FOR 4.0 FT/SEC WITHOUT ANTI-RESET WINDUP



ANGULAR VELOCITIES

NONLINEAR INTEGRATION FOR 4.0 FT/SECOND ANTI-RESET WINDUP

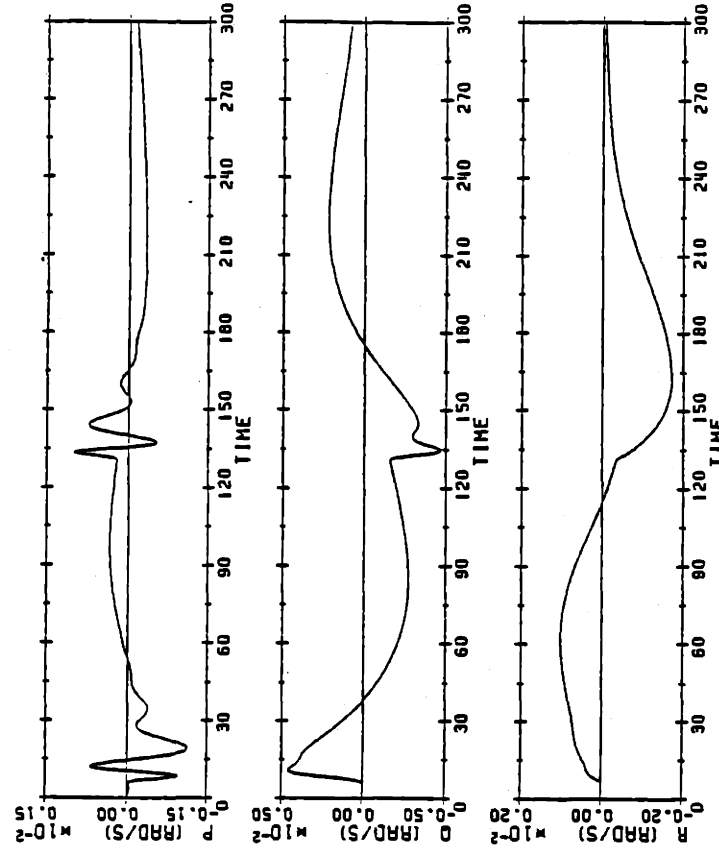
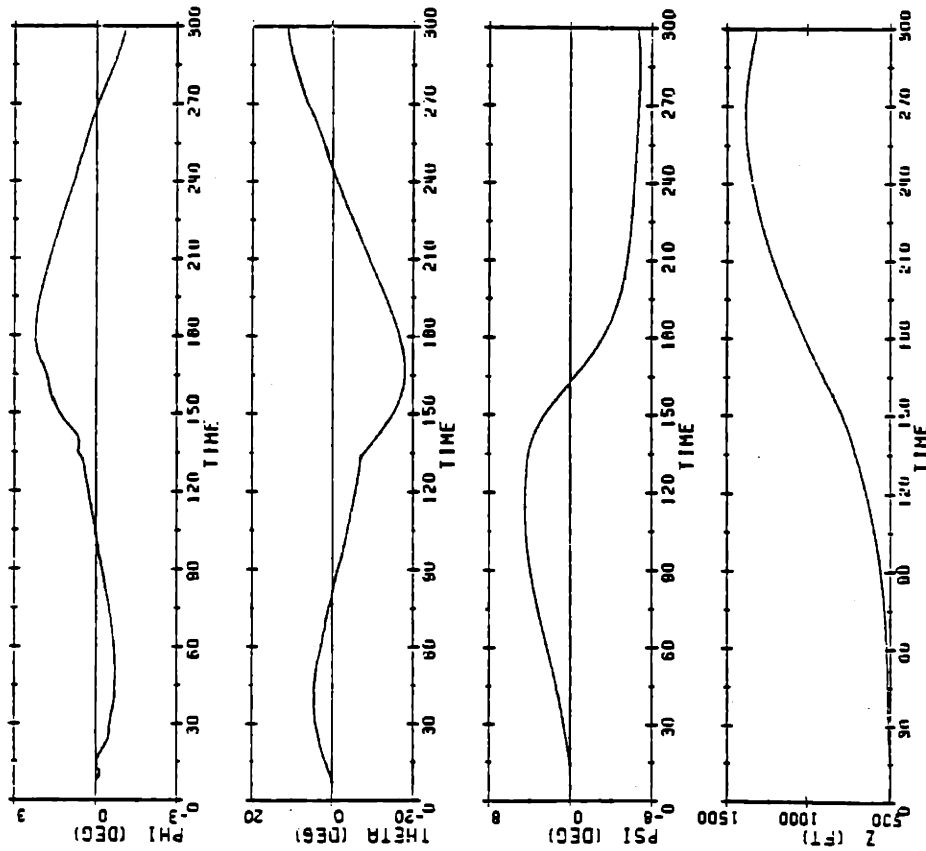


Figure 6.6 Comparison of Systems Without and With ARW ($\alpha = 0.05$) for 4 Feet/Second Depthrate

ATTITUDE AND DEPTH

NONLINEAR INTEGRATION FOR 4.0 FT/SEC WITHOUT ANTI-RESET WINDUP



ATTITUDE AND DEPTH

NONLINEAR INTEGRATION FOR 4.0 FT/SEC AND ANTI-RESET WINDUP

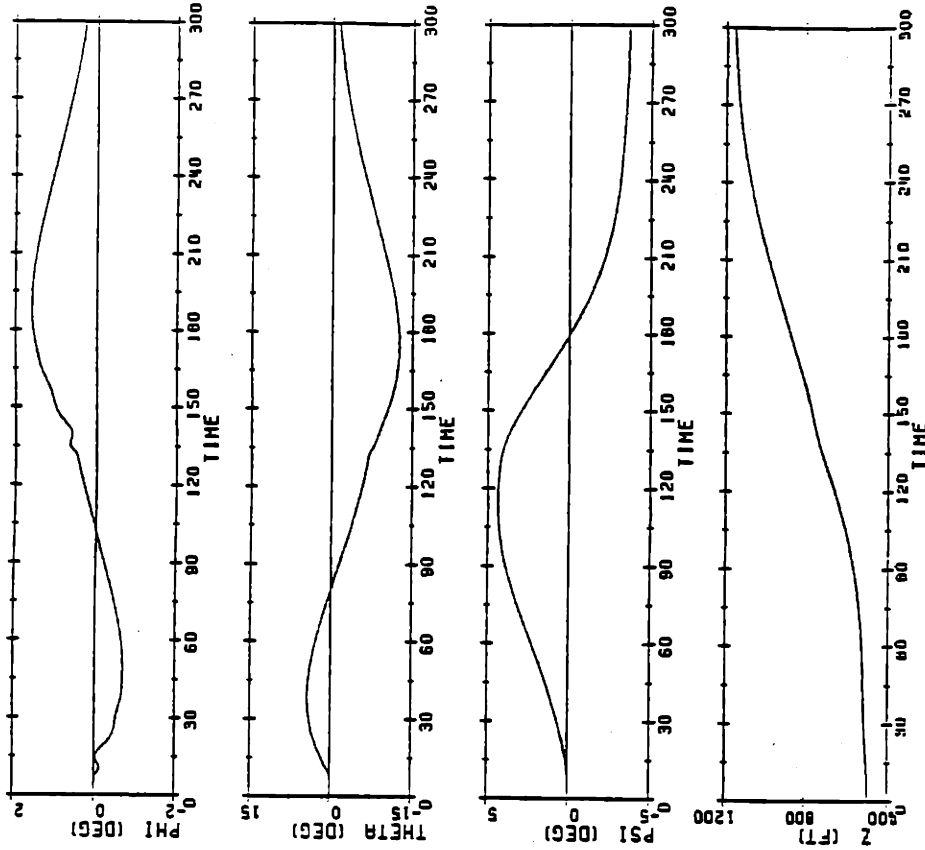
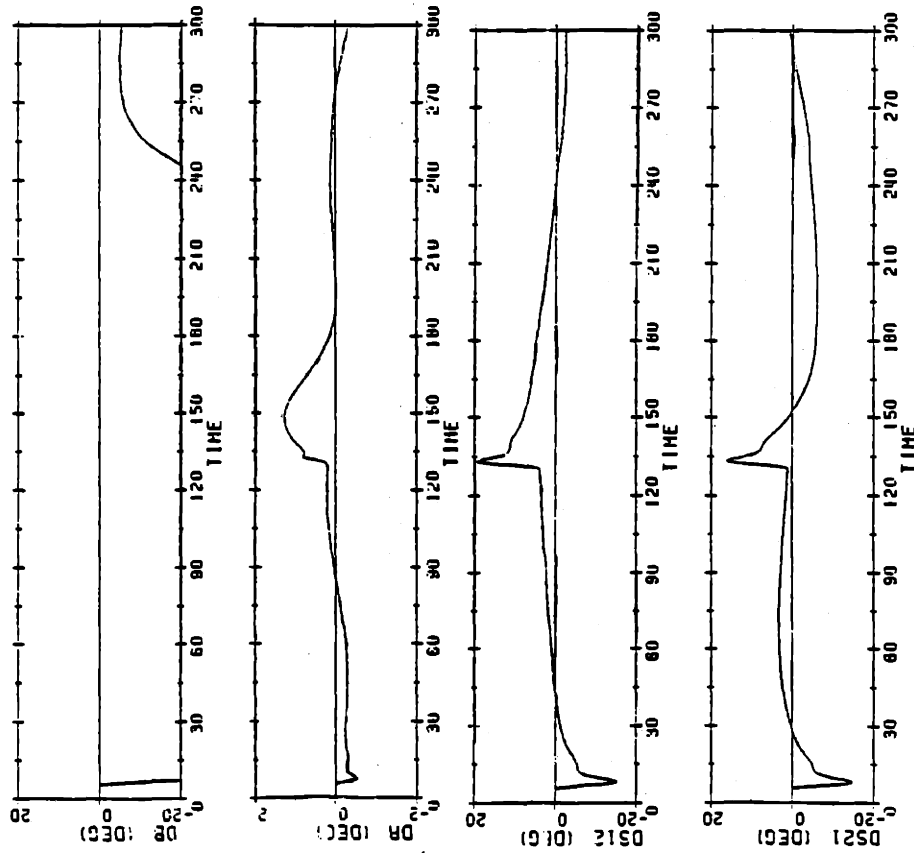


Figure 6.6 Comparison of Systems Without and With ARW ($\alpha = 0.05$) for 4 Feet/Second Depthrate

CONTROL INPUTS

NONLINEAR INTEGRATION FOR 4.0 FT/SEC WITHOUT ANTI-RESET WINDUP



CONTROL INPUTS

NONLINEAR INTEGRATION FOR 4.0 FT/SECOND ANTI-RESET WINDUP

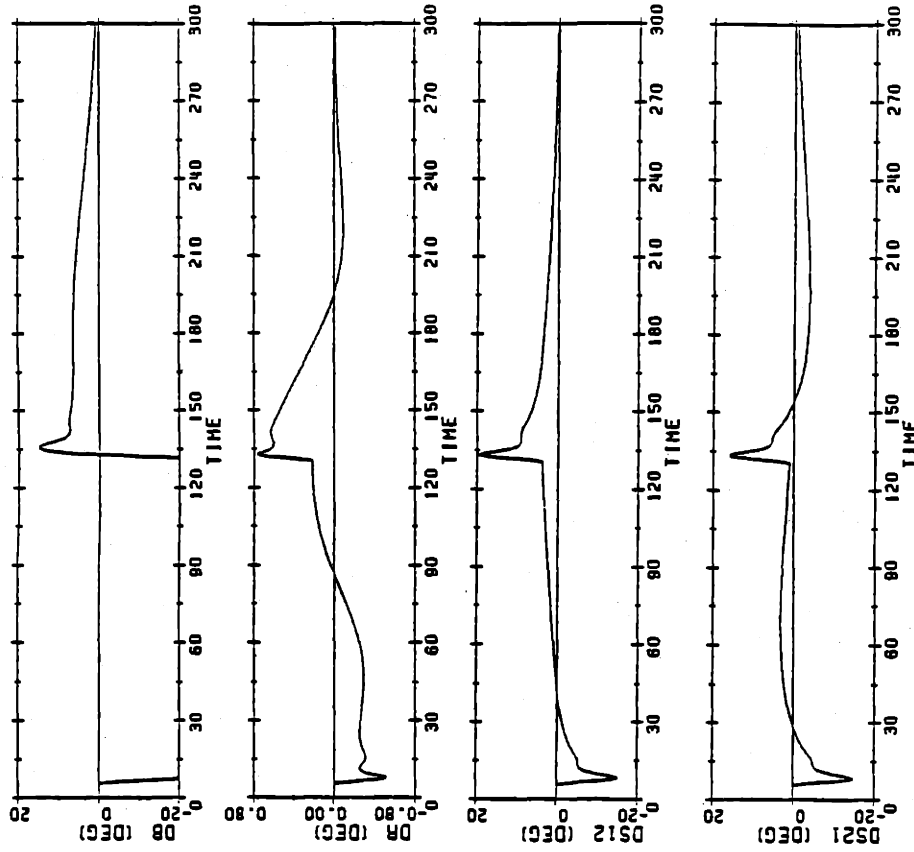
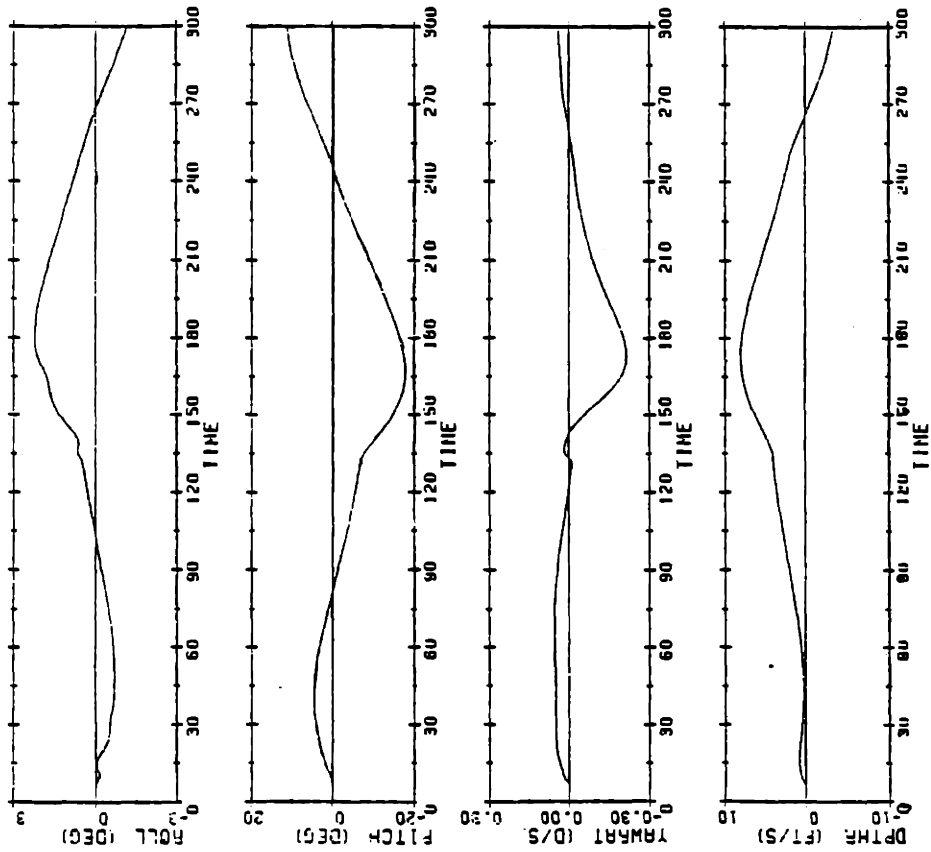


Figure 6.6 Comparison of Systems Without and With ARW ($\alpha = 0.05$) for 4 Feet/Second Depthrate

OUTPUTS

NONLINEAR INTEGRATION FOR 4.0 FT/SEC WITHOUT ANTI-RESET WINDUP



OUTPUTS

NONLINEAR INTEGRATION FOR 4.0 FT/SEC ANTI-RESET WINDUP

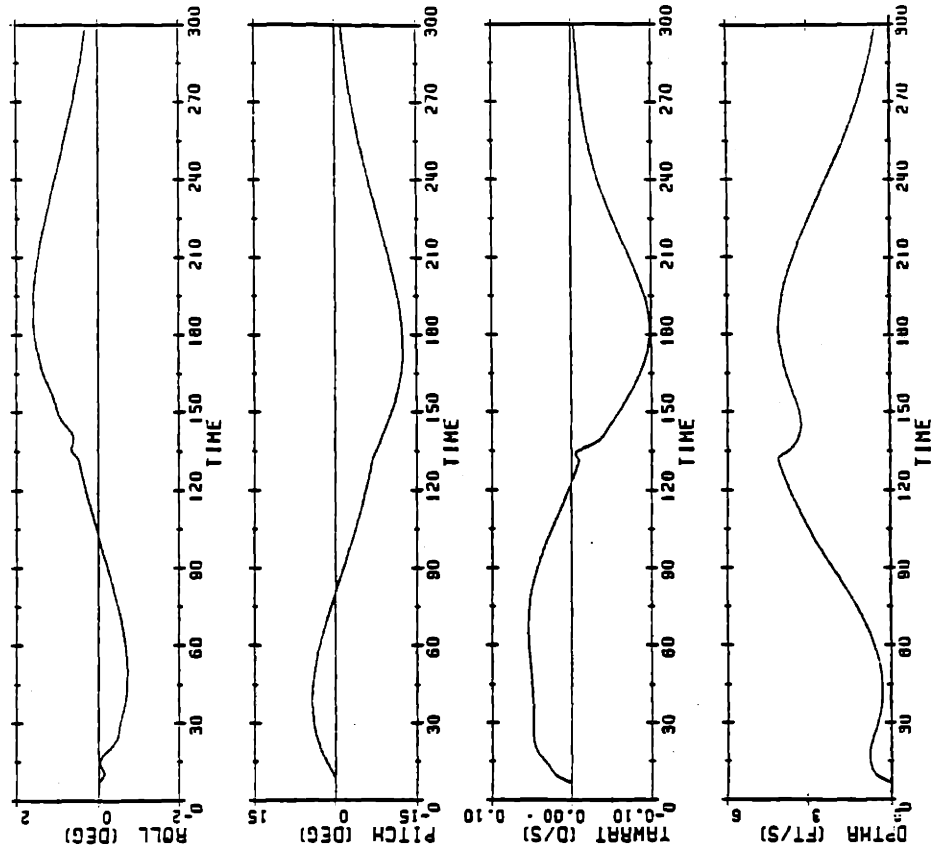


Figure 6.6 Comparison of Systems Without and With ARW ($\alpha = 0.05$) for 4 Feet/Second Depthrate

6.4 Summary

This chapter has covered the use of an Anti Reset Windup feedback loop to improve performance of the submarine in the presence of saturating control surfaces. In particular, the effect on fairwater plane saturation was demonstrated with notable improvements by reduction in the oscillation and maximum error of the output variables and the time lag until dynamic control of the saturating surface is regained.

CHAPTER 7

SUMMARY AND DIRECTIONS FOR FURTHER RESEARCH

7.1 Summary

This thesis has presented the design of a multivariable control system for a submarine using the Linear Quadratic Gaussian with Loop Transfer Recovery (LQG/LTR) methodology. The submarine model was based on the NSRDC 2510 equations of motion modified to include the crossflow terms of the updated equations, differential control of the sternplanes and a constant RPS constraint on the propeller.

The 10th order linear model based on a nominal point of 15 knots forward speed and 1 degree rudder deflection was reduced to an 8th order system and then scaled for units and input/output weightings. Using LQG/LTR, a Model Based Compensator was designed for a crossover frequency of 0.1 radians/second for the plant augmented with integrators to reduce steady state error to step inputs. The design was extensively tested at speeds from 15 to 30 knots and then compared to the compensator design by Martin [8]. That design is based on a 30 knot model of the same submarine but has a crossover frequency of 0.5 radians/second.

Subsequently, an Anti-Reset Windup (ARW) feedback loop was incorporated to reduce the effects of saturating control surfaces on the dynamic response of the submarine. This is accomplished by replacing the integrator in the input channel with a simple lag when that channel issues a command above the saturation level of the control surface.

7.2 Conclusions and Directions for Further Research

The LQG/LTR multivariable control system design methodology has been used to design a controller which considers rather than neglects the cross coupling present in the dynamics of a submarine. This provides for better control over a wider variety of maneuvers since the model is valid for larger perturbations than one which is based on decoupled vertical and horizontal planes of motion. Active roll control through the differential deflection of the sternplanes also helps by limiting perturbations in roll angle during maneuvers, thereby limiting cross-coupling.

The use of modal analysis and singular value decomposition have proven to be an excellent means of providing the designer with insight on the states and control inputs which dominate the response of the submarine. Additionally, the singular value decomposition of the transfer function relating the reference commands to the control inputs $K_r(s)$, provides important information on their coupling, i.e. what control inputs are generated in the controller for a given reference command.

Comparisons of the 15 knot compensator designed in this thesis and the 30 knot compensator designed by Martin [8] indicate that a higher crossover frequency is desirable for improved performance during mild maneuvers of the submarine, but a lower crossover design is preferable for more radical maneuvers. This was evident by the instability experienced during the turn and dive maneuver by the system using the 30 knot compensator.

The effectiveness of an ARW feedback loop was demonstrated in a system that experienced control surface saturation. It was determined that the feedback parameter alpha must be selected such that the gain of $G(s)K(s)$ remains high enough to guarantee adequate command following. There was no

effect on the singular value decomposition of $K_r(s)$ and only a slight effect on its singular values.

This thesis has provided an avenue for advancement in the area of submarine control system design but prior to any actual system being built and put to sea, much more research must be performed. This thesis and Martin's have demonstrated the advantage of using differential deflection of the sternplanes to provide active roll control for the submarine. Additional research is required however, in the area of casualty control in the event of a sternplane or other control surface failure. In Chapter 5, it was shown that the 15 knot and 30 knot compensators could be operated at speeds and operating points far away from nominal but that the severity of the maneuver had to be restricted for the 30 knot compensator due to instabilities. The reason for this unstable condition is mostly attributed to the higher crossover frequency, but the effect of the higher nominal speed must be investigated. The use of gain scheduling will obviously be required for an actual controller design which effectively controls the submarine at all speeds.

The singular value decomposition of the plant and the reference to command input transfer function $K_r(s)$, provided useful information about the coupling of the system at low frequency, but the singular values and singular vectors change as a function of frequency. Additional research in this area will provide insight into how the coupling of the system changes as a function of frequency.

The last area which requires further research is the use of Anti-Reset Windup feedback. The improvement in the submarine's performance was evident, but the method of selecting the feedback parameter α needs further development. Additionally, the effect of prolonged multiple

saturations while using as ARW feedbackloop and the effect of the ARW loop
 on closed loop stability must be addressed.

REFERENCES

1. Kapsouris, P., "Gain-Scheduled Multivariable Control for the GE-21 Turbofan Engine Using the LQR and LQG/LTR Methodologies", Master's Thesis, MIT, Cambridge, MA, May 1984.
2. Kappos, P., "Robust Multivariable Control for the F100 Engine", Master's Thesis, MIT, Cambridge, MA, September 1983.
3. Pfeil, W., "Multivariable Control for the GE T700 Engine Using the LQG/LTR Design Methodology", Master's Thesis, MIT, Cambridge, MA, August 1984.
4. Harris, K., "Automatic Control of a Submersible", Masters' Thesis, MIT, Cambridge, Ma, May 1984.
5. Milliken, L., "Multivariable Control of an Underwater Vehicle", Engineer's Thesis, MIT, Cambridge, MA, May 1984.
6. Dreher, L., "Robust Rate Control System Designs for a Submersible", Engineer's Thesis, MIT, Cambridge, MA, May 1984.
7. Lively, K., "Multivariable Control System Design for a Submarine", Engineer's Thesis, MIT, Cambridge, MA, May 1984.
8. Martin, R., "Multivariable Control System Design for a Submarine Using Active Roll Control", Engineer's Thesis, MIT, Cambridge, MA, May 1985.
9. Abkowitz, M., Stability and Motion Control of Ocean Vehicles, MIT Press, Cambridge, MA, 1969.
10. Gertler, M. and Hagen, G., "Standard Equations of Motion for Submarine Simulation", NSRDC Report 2510, Washington, DC, June 1967.
11. Feldman, J., "DTNSRDC Revised Standard Submarine Equations of Motion", DTNSRDC/SPD-0393-09, Bethesda, MD, June 1979.
12. Bonnice, W. and Valavani, L., "Submarine Configuration and Control", Charles S. Draper Laboratory Memo SUB 1-1083, October 1983.
13. Bonnice, W. and Valavani, L., "Submarine Configuration and Control", Charles S. Draper Laboratory Memo SUB 2-1183, November 1983.
14. Bonnice, W., "Propulsion and Drag Models for the Submodel Submarine Simulation", Charles S. Draper Laboratory Memo SUB 3-984, September 1984.
15. Bonnice, W., CONSTRPS Fortran and Command List Computer Programs, Charles S. Draper Laboratory, May 1984.

16. Athans, M., Class Notes for Course 6.232, MIT, Cambridge, MA, Spring 1984.
17. Boettcher, K., "Analysis of Multivariable Control Systems with Structural Uncertainty", Doctoral Dissertation, MIT, Cambridge, MA, 1983.
18. Lehtomaki, N., "Practical Robustness Measures in Multivariable Control System Analysis", Doctoral Thesis, MIT, Cambridge, MA, May 1981.
19. Lehtomaki, N., Sandell, N. and Athans, M., "Robustness Results in Linear-Quadratic-Gaussian Based Multivariable Control Designs", IEEE Transactions on Automatic Control, Vol.AC-26, No.1, February 1981.
20. Safanov, M., "Robustness and Stability Aspects of Stochastic Multivariable Feedback System Design", Doctoral Thesis, MIT, Cambridge, MA, 1979.
21. Lehtomaki, N., et al, "Robustness Tests Utilizing the Structure of Modelling Error", LIDS Report P-1151, MIT, Cambridge, Ma, October 1981.
22. Lehtomaki, N., et al, "Robustness and Modelling Error Characterization", LIDS Report P-1311, MIT, Cambridge, MA, June 1983.
23. Doyle, J. and Stein, G., "Multivariable Feedback Design: Concepts for a Classical/Modern Synthesis", IEEE Transactions on Automatic Control, Vol. AC-26, No.1, February 1981.
24. Stein, G., "LQG-Based Multivariable Design: Frequency Domain Interpretation", AGARD-LS-117, 1981.
25. Stein, G. and Athans, M., "The LQG/LTR Procedure for Multivariable Feedback Control Design", LIDS Report P-1384, MIT, Cambridge, MA, May 1984.
26. Kwakernaak, H. and Sivan, R., Linear Optimal Control Systems, Wiley, New York, NY, 1972.
27. Kapsouris, P., and Athans, M., "Multivariable Control Systems with Saturating Actuators Antireset Windup Strategies", Draft of Paper for American Control Conference, Boston, MA, June 1985.

APPENDIX A

MATRICES OF THE SISR1 LINEAR MODEL

APPENDIX A1

ORIGINAL PLANT MATRICES PRIOR TO SCALING AND MODEL REDUCTION

A MATRIX (10 x 10)

-1.9012E-02	-1.1096E-02	-4.2241E-04	-9.5941E-03	-1.6035E-02	1.5933E+00	0.0000E+00	2.9550E-04	0.0000E+00	0.0000E+00
5.8364E-04	-8.0771E-02	3.4469E-04	-6.4682E-01	9.4882E-02	-7.8164E+00	1.3176E-01	-3.4021E-05	0.0000E+00	0.0000E+00
7.2953E-06	-7.8932E-05	-5.3862E-02	-8.0323E-01	6.1384E+00	9.7422E-03	0.0000E+00	7.6175E-03	0.0000E+00	0.0000E+00
1.1097E-04	-5.8726E-03	-7.1679E-04	-2.2072E-01	-1.2851E-01	-1.4504E-02	-1.6206E-01	4.1845E-05	0.0000E+00	0.0000E+00
-6.5774E-07	-2.2004E-06	6.7287E-04	-5.7594E-03	-2.0682E-01	1.4001E-04	0.0000E+00	-2.5124E-03	0.0000E+00	0.0000E+00
-1.3843E-05	-1.0317E-03	3.7870E-06	-3.5813E-03	4.7420E-04	-1.9379E-01	2.6177E-04	-6.7592E-08	0.0000E+00	0.0000E+00
0.0000E+00	0.0000E+00	0.0000E+00	1.0000E+00	2.5811E-04	-9.1543E-03	-1.3327E-12	-6.2735E-03	0.0000E+00	0.0000E+00
0.0000E+00	0.0000E+00	0.0000E+00	0.0000E+00	9.9960E-01	2.8184E-02	6.2730E-03	0.0000E+00	0.0000E+00	0.0000E+00
0.0000E+00	0.0000E+00	0.0000E+00	0.0000E+00	-2.8186E-02	9.9965E-01	1.4553E-10	5.7451E-05	0.0000E+00	0.0000E+00
9.1576E-03	-2.8183E-02	9.9956E-01	0.0000E+00	0.0000E+00	0.0000E+00	7.9107E-01	-2.4818E+01	0.0000E+00	0.0000E+00

B MATRIX (4 x 10)

-4.2090E-04	-1.5065E-02	7.2244E-04	7.2244E-04
0.0000E+00	5.9604E-01	-4.3727E-02	4.3727E-02
-3.7257E-01	-3.8218E-07	-2.5391E-01	-2.5391E-01
0.0000E+00	1.0988E-02	5.3783E-02	-5.3783E-02
3.5786E-03	1.2605E-07	-6.1424E-03	-6.1424E-03
0.0000E+00	-1.5105E-02	-8.6874E-05	8.6874E-05
0.0000E+00	0.0000E+00	0.0000E+00	0.0000E+00
0.0000E+00	0.0000E+00	0.0000E+00	0.0000E+00
0.0000E+00	0.0000E+00	0.0000E+00	0.0000E+00
0.0000E+00	0.0000E+00	0.0000E+00	0.0000E+00

APPENDIX A2

Matrix used to postmultiply the B matrix:

1.7452E-02	0.0000E+00	0.0000E+00	0.0000E+00
0.0000E+00	1.7452E-02	0.0000E+00	0.0000E+00
0.0000E+00	0.0000E+00	1.7452E-02	0.0000E+00
0.0000E+00	0.0000E+00	0.0000E+00	1.7452E-02

Matrix used to premultiply the C matrix:

5.7300E+01	0.0000E+00	0.0000E+00	0.0000E+00
0.0000E+00	5.7300E+01	0.0000E+00	0.0000E+00
0.0000E+00	0.0000E+00	5.7300E+01	0.0000E+00
0.0000E+00	0.0000E+00	0.0000E+00	1.0000E+00

Matrix used to postmultiply the C matrix:

1.0000E+00	0.0000E+00	0.0000E+00	0.0000E+00	0.0000E+00	0.0000E+00	0.0000E+00	0.0000E+00	0.0000E+00	0.0000E+00
0.0000E+00	1.0000E+00	0.0000E+00	0.0000E+00	0.0000E+00	0.0000E+00	0.0000E+00	0.0000E+00	0.0000E+00	0.0000E+00
0.0000E+00	0.0000E+00	1.0000E+00	0.0000E+00	0.0000E+00	0.0000E+00	0.0000E+00	0.0000E+00	0.0000E+00	0.0000E+00
0.0000E+00	0.0000E+00	0.0000E+00	1.7452E-02	0.0000E+00	0.0000E+00	0.0000E+00	0.0000E+00	0.0000E+00	0.0000E+00
0.0000E+00	0.0000E+00	0.0000E+00	0.0000E+00	1.7452E-02	0.0000E+00	0.0000E+00	0.0000E+00	0.0000E+00	0.0000E+00
0.0000E+00	0.0000E+00	0.0000E+00	0.0000E+00	0.0000E+00	1.7452E-02	0.0000E+00	0.0000E+00	0.0000E+00	0.0000E+00
0.0000E+00	0.0000E+00	0.0000E+00	0.0000E+00	0.0000E+00	0.0000E+00	1.7452E-02	0.0000E+00	0.0000E+00	0.0000E+00
0.0000E+00	0.0000E+00	0.0000E+00	0.0000E+00	0.0000E+00	0.0000E+00	0.0000E+00	1.7452E-02	0.0000E+00	0.0000E+00
0.0000E+00	0.0000E+00	0.0000E+00	0.0000E+00	0.0000E+00	0.0000E+00	0.0000E+00	0.0000E+00	1.7452E-02	0.0000E+00
0.0000E+00	0.0000E+00	0.0000E+00	0.0000E+00	0.0000E+00	0.0000E+00	0.0000E+00	0.0000E+00	0.0000E+00	1.0000E+00

APPENDIX A2

PLANT MATRICES SCALED FOR UNIT TRANSFORMATION ONLY

A MATRIX (8 x 8)

-1.9012E-02	-1.1096E-02	-4.2241E-04	-1.6744E-04	-2.7984E-04	2.7806E-02	0.0000E+00	5.1570E-06
5.8364E-04	-8.0771E-02	3.4469E-04	-1.1288E-02	1.6559E-03	-1.3641E-01	2.2994E-03	-5.9374E-07
7.2953E-06	-7.8932E-05	-5.3862E-02	-1.4018E-02	1.0713E-01	1.7002E-04	0.0000E+00	1.3294E-04
6.3584E-03	-3.3650E-01	-4.1072E-02	-2.2072E-01	-1.2851E-01	-1.4504E-02	-1.6206E-01	4.1845E-05
-3.7689E-05	-1.2608E-04	3.8555E-02	-5.7594E-03	-2.0682E-01	1.4001E-04	0.0000E+00	-2.5124E-03
-7.9321E-04	-5.9116E-02	2.1699E-04	-3.5813E-03	4.7420E-04	-1.9379E-01	2.6177E-04	-6.7592E-08
0.0000E+00	0.0000E+00	0.0000E+00	1.0000E+00	2.5811E-04	-9.1543E-03	-1.3327E-12	-6.2735E-03
0.0000E+00	0.0000E+00	0.0000E+00	0.0000E+00	9.9960E-01	2.8184E-02	6.2730E-03	0.0000E+00

B MATRIX (8 x 4)

-7.3455E-06	-2.6291E-04	1.2608E-05	1.2608E-05
0.0000E+00	1.0402E-02	-7.6312E-04	7.6312E-04
-6.5021E-03	-6.6698E-09	-4.4313E-03	-4.4313E-03
0.0000E+00	1.0988E-02	5.3783E-02	-5.3783E-02
3.5786E-03	1.2605E-07	-6.1424E-03	-6.1424E-03
0.0000E+00	-1.5105E-02	-8.6874E-05	8.6874E-05
0.0000E+00	0.0000E+00	0.0000E+00	0.0000E+00
0.0000E+00	0.0000E+00	0.0000E+00	0.0000E+00

APPENDIX A2

C MATRIX (4 x 8)

0.0000E+00	0.0000E+00	0.0000E+00	0.0000E+00	0.0000E+00	0.0000E+00	1.0000E+00	0.0000E+00
0.0000E+00	0.0000E+00	0.0000E+00	0.0000E+00	0.0000E+00	0.0000E+00	0.0000E+00	1.0000E+00
0.0000E+00	0.0000E+00	0.0000E+00	0.0000E+00	-2.8185E-02	9.9964E-01	1.4552E-10	5.7450E-05
9.1576E-03	-2.8183E-02	9.9956E-01	0.0000E+00	0.0000E+00	0.0000E+00	1.3806E-02	-4.3313E-01

APPENDIX A3

PLANT MATRICES SCALED FOR UNIT TRANSFORMATION AND WEIGHTINGS
ON INPUTS AND OUTPUTS

A MATRIX (8 x 8)

-1.9012E-02	-1.1096E-02	-4.2241E-04	-1.6744E-04	-2.7984E-04	2.7806E-02	0.0000E+00	5.1570E-06
5.8364E-04	-8.0771E-02	3.4469E-04	-1.1288E-02	1.6559E-03	-1.3641E-01	2.2994E-03	-5.9374E-07
7.2953E-06	-7.8932E-05	-5.3862E-02	-1.4018E-02	1.0713E-01	1.7002E-04	0.0000E+00	1.3294E-04
6.3584E-03	-3.3650E-01	-4.1072E-02	-2.2072E-01	-1.2851E-01	-1.4504E-02	-1.6206E-01	4.1845E-05
-3.7689E-05	-1.2608E-04	3.8555E-02	-5.7594E-03	-2.0682E-01	1.4001E-04	0.0000E+00	-2.5124E-03
-7.9321E-04	-5.9116E-02	2.1699E-04	-3.5813E-03	4.7420E-04	-1.9379E-01	2.6177E-04	-6.7592E-08
0.0000E+00	0.0000E+00	0.0000E+00	1.0000E+00	2.5811E-04	-9.1543E-03	-1.3327E-12	-6.2735E-03
0.0000E+00	0.0000E+00	0.0000E+00	0.0000E+00	9.9960E-01	2.8184E-02	6.2730E-03	0.0000E+00

B MATRIX (8 x 4)

-7.3455E-06	-3.9417E-04	1.5760E-05	1.5760E-05
0.0000E+00	1.5595E-02	-9.5390E-04	9.5390E-04
-6.5021E-03	-9.9997E-09	-5.5391E-03	-5.5391E-03
0.0000E+00	1.6473E-02	6.7228E-02	-6.7228E-02
3.5786E-03	1.8898E-07	-7.6780E-03	-7.6780E-03
0.0000E+00	-2.2646E-02	-1.0859E-04	1.0859E-04
0.0000E+00	0.0000E+00	0.0000E+00	0.0000E+00
0.0000E+00	0.0000E+00	0.0000E+00	0.0000E+00

APPENDIX A3

C MATRIX (4 x 8)

0.0000E+00	0.0000E+00	0.0000E+00	0.0000E+00	0.0000E+00	0.0000E+00	1.0000E-01	0.0000E+00
0.0000E+00	0.0000E+00	0.0000E+00	0.0000E+00	0.0000E+00	0.0000E+00	0.0000E+00	1.0000E-01
0.0000E+00	0.0000E+00	0.0000E+00	0.0000E+00	-2.8185E-02	9.9964E-01	1.4552E-10	5.7450E-05
9.1576E-03	-2.8183E-02	9.9956E-01	0.0000E+00	0.0000E+00	0.0000E+00	1.3806E-02	-4.3313E-01

APPENDIX 3

MATRICES OF THE 15 KNOT PLANT AND COMPENSATOR

APPENDIX B1

POLES, ZEROS AND EIGENVECTORS

EIGENVALUES

-2.0413E-02 -2.0413E-02 -2.0618E-02 -3.3461E-02 -1.0603E-01 -1.0603E-01 -2.2040E-01 -2.4761E-01
1.4066E-02 -1.4066E-02 0.0000E+00 0.0000E+00 3.8084E-01 -3.8084E-01 0.0000E+00 0.0000E+00

TRANSMISSION ZEROS

3.1712E+08 3.3004E+06 5.8381E+03 -1.9007E-02 -1.2729E-01 -5.8321E+03 -1.2904E+07 -7.9657E+08

EIGENVECTORS (MODAL MATRIX)

5.4585E-03 5.4585E-03 9.7809E-01 5.2178E-01 -4.3995E-05 -4.3995E-05 -5.4014E-04 3.3478E-02
2.1218E-03 -2.1218E-03 0.0000E+00 0.0000E+00 2.9056E-04 -2.9056E-04 0.0000E+00 0.0000E+00

2.0006E-03 2.0006E-03 6.9651E-02 3.4612E-01 -7.5258E-04 -7.5258E-04 2.7841E-03 -3.7199E-01
-1.8330E-03 1.8330E-03 0.0000E+00 0.0000E+00 1.2856E-02 -1.2856E-02 0.0000E+00 0.0000E+00

-1.1406E-02 -1.1406E-02 1.4151E-02 6.0006E-02 7.7846E-03 7.7846E-03 1.3399E-01 -4.6995E-03
-7.1516E-02 7.1516E-02 0.0000E+00 0.0000E+00 1.1036E-02 -1.1036E-02 0.0000E+00 0.0000E+00

-5.2527E-03 -5.2527E-03 1.0682E-03 2.2280E-02 3.4260E-01 3.4260E-01 -2.2220E-02 -1.9978E-01
3.3729E-03 -3.3729E-03 0.0000E+00 0.0000E+00 -1.3309E-01 1.3309E-01 0.0000E+00 0.0000E+00

6.0737E-03 6.0737E-03 4.7564E-03 1.5018E-02 1.8075E-03 1.8075E-03 -2.1241E-01 -1.7366E-02
-2.4203E-02 2.4203E-02 0.0000E+00 0.0000E+00 4.8844E-03 -4.8844E-03 0.0000E+00 0.0000E+00

-5.5494E-04 -5.5494E-04 -2.8418E-02 -1.3178E-01 -1.9431E-03 -1.9431E-03 4.6092E-03 -4.2513E-01
4.9147E-04 -4.9147E-04 0.0000E+00 0.0000E+00 3.0331E-03 -3.0331E-03 0.0000E+00 0.0000E+00

7.7598E-04 7.7598E-04 -1.1242E-01 -7.3935E-01 -5.5690E-01 -5.5690E-01 1.2856E-01 7.9363E-01
3.7620E-02 -3.7620E-02 0.0000E+00 0.0000E+00 -7.4456E-01 7.4456E-01 0.0000E+00 0.0000E+00

-7.4935E-01 -7.4935E-01 -1.5755E-01 -1.9905E-01 1.9061E-03 1.9061E-03 9.5910E-01 9.8394E-02
6.5659E-01 -6.5659E-01 0.0000E+00 0.0000E+00 4.0419E-03 -4.0419E-03 0.0000E+00 0.0000E+00

APPENDIX B2

CONTROLLABILITY MATRIX

1.6552E-01	1.0504E-01	3.5334E-01	3.6637E-01
-5.7600E-01	-1.8233E-01	-2.9672E-01	-3.0245E-01
1.6552E-01	1.0504E-01	3.5334E-01	3.6637E-01
5.7600E-01	1.8233E-01	2.9672E-01	3.0245E-01
-6.8062E-03	-3.9264E-01	-5.6056E-03	-4.4330E-03
-2.0819E-10	-1.5146E-09	-3.3261E-09	3.2745E-09
4.0734E-03	7.1184E-01	1.7878E-03	-2.5278E-03
3.1612E-10	2.7899E-09	6.1340E-09	-6.1256E-09
-2.3352E-02	1.2539E-01	4.3242E-01	-3.9234E-01
3.4091E-03	2.8794E-01	2.9887E-01	-3.2909E-01
-2.3352E-02	1.2539E-01	4.3242E-01	-3.9234E-01
-3.4091E-03	-2.8794E-01	-2.9887E-01	3.2909E-01
-5.2958E-01	-2.3894E-02	1.4670E-01	1.5495E-01
-2.0413E-11	3.4676E-10	7.9478E-10	6.7265E-10
-5.4850E-03	2.2961E-01	-5.6294E-03	9.4034E-03
-9.9081E-12	2.1548E-11	4.4051E-11	-2.7408E-11

OBSERVABILITY MATRIX

7.7598E-04	7.7598E-04	-1.1242E-01	-7.3935E-01	-5.5690E-01	-5.5690E-01	1.2856E-01	7.9363E-01
3.7620E-02	-3.7620E-02	0.0000E+00	0.0000E+00	-7.4456E-01	7.4456E-01	0.0000E+00	0.0000E+00
-7.4935E-01	-7.4935E-01	-1.5755E-01	-1.9905E-01	1.9061E-03	1.9061E-03	9.5910E-01	9.8394E-02
6.5659E-01	-6.5659E-01	0.0000E+00	0.0000E+00	4.0419E-03	-4.0419E-03	0.0000E+00	0.0000E+00
-7.6899E-04	-7.6899E-04	-2.8551E-02	-1.3217E-01	-1.9932E-03	-1.9932E-03	1.0649E-02	-4.2448E-01
1.2112E-03	-1.2112E-03	0.0000E+00	0.0000E+00	2.8946E-03	-2.8946E-03	0.0000E+00	0.0000E+00
3.1317E-01	3.1317E-01	8.7825E-02	1.3101E-01	-7.1196E-04	-7.1196E-04	-2.7979E-01	-2.5567E-02
-3.5528E-01	3.5528E-01	0.0000E+00	0.0000E+00	-1.3587E-03	1.3587E-03	0.0000E+00	0.0000E+00

APPENDIX B3

MODEL BASED COMPENSATOR MATRICES

L MATRIX (12 x 4)

-5.2859E-01	-3.6891E+01	-1.9800E-02	-8.9967E+00
3.1664E-03	5.6612E-02	-3.0290E+00	1.0072E-02
1.2335E+01	2.0142E+00	-4.8602E+00	7.1824E-01
-1.1585E+01	-7.6681E-01	5.2128E+00	1.1306E-01
-1.2643E-03	3.9664E-02	-4.5390E-16	9.1576E-03
3.8909E-03	-1.2207E-01	1.3969E-15	-2.8183E-02
-1.3800E-01	4.3294E+00	-4.9544E-14	9.9956E-01
0.0000E+00	0.0000E+00	0.0000E+00	0.0000E+00
4.1013E-11	1.6191E-05	-2.8183E-02	2.8272E-14
-1.4546E-09	-5.7425E-04	9.9956E-01	-1.0027E-12
1.0000E+01	6.4753E-11	1.0100E-18	4.3422E-11
2.9472E-10	1.0000E+01	8.5822E-14	2.9325E-09

APPENDIX B3

MODEL BASED COMPENSATOR MATRICES

CONTROL GAIN MATRIX - G (4 x 12)

1.9075E+00	1.7309E-02	3.3175E-01	3.3927E-01	-2.2603E+00	6.3586E+00
-2.3374E+02	6.0251E-02	1.1518E+02	2.9814E+00	-2.4295E+00	1.2755E+02
1.7309E-02	3.6408E+00	2.7069E-02	-5.3234E-02	8.8669E-02	9.1610E+00
-4.3139E+00	1.4955E+00	7.0839E+00	-2.8537E+02	1.2667E+00	1.3071E+00
3.3175E-01	2.7069E-02	2.2008E+00	-4.1713E-01	-1.1099E+00	-3.4200E+00
-1.3371E+02	2.5322E+01	-1.5522E+01	1.1943E+01	1.7368E+01	4.0942E+01
3.3927E-01	-5.3234E-02	-4.1713E-01	2.1780E+00	-1.3532E+00	1.0440E+01
-1.3407E+02	-2.5060E+01	-1.0521E+01	-3.8677E+00	-2.1052E+01	4.1898E+01

FILTER GAIN MATRIX - H (12 x 4)

-5.9202E-02	-3.2113E+00	-3.8250E-02	-7.7983E-01
3.2510E-02	8.4010E-03	-2.6152E-01	-3.6334E-03
1.1180E+00	1.8450E-01	-2.8643E-01	1.6468E-02
-1.0548E+00	-7.6073E-02	3.2537E-01	5.3966E-02
9.5416E-04	2.0790E-03	3.5801E-02	7.4520E-04
1.9485E-03	-5.3268E-03	-8.6929E-02	-3.5640E-03
-1.0162E-02	3.7689E-01	1.0342E-03	8.7100E-02
5.2396E-03	6.0975E-03	-1.4220E-02	4.6202E-04
-3.9137E-03	-3.8591E-05	-1.9355E-03	8.6603E-05
-6.6970E-03	3.1629E-04	6.5711E-02	1.3147E-03
9.2545E-01	1.3114E-02	-6.5835E-02	-3.1072E-02
1.3114E-02	8.7089E-01	3.6730E-03	-1.2924E-03

APPENDIX B4

POLES AND ZEROS OF THE OPEN AND CLOSED LOOP SYSTEMS

OPEN LOOP POLES

(1 : 24)

REAL PART

7.1012E-09	1.3140E-09	8.0208E-10	8.0208E-10	-1.9007E-02	-2.0413E-02
-2.0413E-02	-2.0618E-02	-3.3461E-02	-1.0603E-01	-1.0603E-01	-1.2729E-01
-2.2040E-01	-2.4761E-01	-3.6083E-01	-3.6083E-01	-7.0970E-01	-7.0970E-01
-7.9225E-01	-1.3002E+00	-1.3002E+00	-1.5000E+00	-1.9273E+00	-1.9273E+00

IMAGINARY PART

0.0000E+00	0.0000E+00	3.6148E-09	-3.6148E-09	0.0000E+00	1.4066E-02
-1.4066E-02	0.0000E+00	0.0000E+00	3.3084E-01	-3.3084E-01	0.0000E+00
0.0000E+00	0.0000E+00	6.0017E-01	-6.0017E-01	1.3235E+00	-1.3235E+00
0.0000E+00	1.3200E+00	-1.3200E+00	0.0000E+00	1.9220E+00	-1.9220E+00

OPEN LOOP ZEROS

(1 : 24)

REAL PART

9.2849E+02	9.2849E+02	1.2343E+02	1.2343E+02	1.5137E+00	1.5099E+00
-1.9007E-02	-1.9161E-02	-2.0404E-02	-2.0404E-02	-5.7143E-02	-1.0619E-01
-1.0619E-01	-1.2729E-01	-2.0323E-01	-2.2075E-01	-1.2357E+02	-1.2357E+02
-1.4663E+03	-1.4663E+03	-2.0371E+03	-4.9196E+03	-4.9196E+03	-7.2851E+04

IMAGINARY PART

1.7100E+03	-1.7100E+03	1.2349E+02	-1.2349E+02	7.6191E+04	-7.6191E+04
0.0000E+00	0.0000E+00	1.4044E-02	-1.4044E-02	0.0000E+00	3.7490E-01
-3.7490E-01	0.0000E+00	0.0000E+00	0.0000E+00	1.2349E+02	-1.2349E+02
2.3463E+03	-2.3463E+03	0.0000E+00	1.6495E+04	-1.6495E+04	0.0000E+00

APPENDIX B4

POLES AND ZEROS OF THE OPEN AND CLOSED LOOP SYSTEMS

CLOSED LOOP POLES

(1 x 24)

REAL PART

-1.8917E-02 -1.9007E-02 -2.0299E-02 -2.0299E-02 -4.2237E-02 -4.2237E-02
-8.5722E-02 -8.7075E-02 -9.3104E-02 -1.0740E-01 -1.0740E-01 -1.2729E-01
-2.2005E-01 -2.6290E-01 -3.5428E-01 -3.5428E-01 -7.0714E-01 -7.0714E-01
-7.1471E-01 -1.2584E+00 -1.2584E+00 -1.4126E+00 -1.8944E+00 -1.8944E+00

IMAGINARY PART

0.0000E+00 0.0000E+00 1.4076E-02 -1.4076E-02 3.2491E-02 -3.2491E-02
0.0000E+00 0.0000E+00 0.0000E+00 3.8202E-01 -3.8202E-01 0.0000E+00
0.0000E+00 0.0000E+00 5.5033E-01 -5.5033E-01 1.2751E+00 -1.2751E+00
0.0000E+00 1.2795E+00 -1.2795E+00 0.0000E+00 1.8898E+00 -1.8898E+00

CLOSED LOOP ZEROS

(1 x 24)

REAL PART

1.9711E+03 9.7852E+01 9.7852E+01 -1.9007E-02 -1.9161E-02 -2.0403E-02
-2.0403E-02 -5.7143E-02 -1.0619E-01 -1.0619E-01 -1.2729E-01 -2.0323E-01
-2.2075E-01 -3.1904E+01 -3.1904E+01 -9.9733E+01 -9.9733E+01 -1.1079E+02
-1.1079E+02 -1.7998E+03 -1.7998E+03 -1.2192E+04 -1.2192E+04 -8.6288E+04

IMAGINARY PART

-9.9187E+02 9.8791E+01 -9.8791E+01 0.0000E+00 0.0000E+00 1.4043E-02
-1.4043E-02 0.0000E+00 3.7490E-01 -3.7490E-01 0.0000E+00 0.0000E+00
0.0000E+00 2.1984E+03 -2.1984E+03 9.8791E+01 -9.8791E+01 2.7447E+04
-2.7447E+04 1.1325E+03 -1.1325E+03 2.3498E+04 -2.3498E+04 0.0000E+00

APPENDIX C

MATRICES OF THE 30 KNOT PLANT AND COMPENSATOR

APPENDIX C1

STATE SPACE MATRICES OF THE S30R1 LINEAR MODEL

ORIGINAL MATRICES PRIOR TO SCALING

A MATRIX

-3.8245E-02	-2.1911E-02	-2.7720E-03	-1.8964E-02	-2.9363E-01	3.1674E+00	0.0000E+00	2.9326E-04	0.0000E+00	0.0000E+00
1.1461E-03	-1.5919E-01	-1.9338E-03	-1.1464E+00	1.1276E-01	-1.5397E+01	1.3004E-01	-1.7564E-03	0.0000E+00	0.0000E+00
2.4225E-05	4.6499E-04	-1.0631E-01	-1.5984E+00	1.2070E+01	8.0194E-02	0.0000E+00	7.5397E-03	0.0000E+00	0.0000E+00
2.4614E-04	-1.1680E-02	-1.3226E-03	-4.3445E-01	-2.3879E-01	-7.1773E-03	-1.5995E-01	2.1603E-03	0.0000E+00	0.0000E+00
-5.3732E-06	-1.8585E-05	1.3207E-03	-1.1380E-02	-4.0755E-01	1.0074E-04	0.0000E+00	-2.4934E-03	0.0000E+00	0.0000E+00
-2.7564E-05	-2.0277E-03	2.4063E-05	-8.1034E-03	3.6042E-03	-3.8180E-01	2.5836E-04	-3.4895E-06	0.0000E+00	0.0000E+00
0.0000E+00	0.0000E+00	0.0000E+00	1.0000E+00	1.3427E-02	-1.2348E-01	-2.0244E-10	-1.2660E-02	0.0000E+00	0.0000E+00
0.0000E+00	0.0000E+00	0.0000E+00	0.0000E+00	9.9414E-01	1.0810E-01	1.2467E-02	0.0000E+00	0.0000E+00	0.0000E+00
0.0000E+00	0.0000E+00	0.0000E+00	0.0000E+00	-1.0893E-01	1.0018E+00	1.6423E-09	1.5605E-03	0.0000E+00	0.0000E+00
1.2326E-01	-1.0728E-01	9.8656E-01	0.0000E+00	0.0000E+00	0.0000E+00	1.5702E+00	-4.8493E+01	0.0000E+00	0.0000E+00

B MATRIX

-1.6315E-03	-5.8396E-02	2.8022E-03	2.8022E-03
0.0000E+00	2.3119E+00	-1.6950E-01	1.6950E-01
-1.4442E+00	-1.4815E-06	-9.8476E-01	-9.8476E-01
0.0000E+00	4.2586E-02	2.0848E-01	-2.0848E-01
1.3872E-02	4.8862E-07	-2.3825E-02	-2.3825E-02
0.0000E+00	-5.8593E-02	-3.3676E-04	3.3676E-04
0.0000E+00	0.0000E+00	0.0000E+00	0.0000E+00
0.0000E+00	0.0000E+00	0.0000E+00	0.0000E+00
0.0000E+00	0.0000E+00	0.0000E+00	0.0000E+00
0.0000E+00	0.0000E+00	0.0000E+00	0.0000E+00

APPENDIX C1

STATE SPACE MATRICES OF THE SBOR1 LINEAR MODEL

REDUCED AND SCALED PLANT MATRICES WITH APPROPRIATE C MATRIX

A MATRIX

-3.8269E-02	-2.1964E-02	-2.7533E-03	-3.3173E-04	2.0734E-03	5.5394E-02	0.0000E+00	5.1285E-06
1.1417E-03	-1.5939E-01	-3.3786E-05	-2.3578E-02	2.8353E-03	-2.6860E-01	2.2745E-03	-2.5914E-05
-4.7476E-04	1.3910E-03	-9.6526E-02	-2.7949E-02	2.1163E-01	7.6140E-04	0.0000E+00	1.3221E-04
1.3945E-02	-6.6430E-01	-8.0931E-02	-4.3452E-01	-2.5262E-01	-2.1920E-02	-1.6030E-01	1.8264E-03
7.1418E-05	-2.5929E-04	7.8117E-02	-1.1406E-02	-4.0815E-01	-7.7327E-04	0.0000E+00	-2.4985E-03
-1.5782E-03	-1.1622E-01	3.4035E-04	-8.0011E-03	2.2809E-03	-3.8201E-01	2.5893E-04	-2.9501E-06
0.0000E+00	0.0000E+00	0.0000E+00	1.0000E+00	1.1328E-02	-1.0538E-01	-4.9352E-10	-1.2635E-02
0.0000E+00	0.0000E+00	0.0000E+00	0.0000E+00	9.9427E-01	1.0689E-01	1.2494E-02	0.0000E+00

B MATRIX

-1.2666E-03	-1.5279E-03	9.8625E-05	9.8625E-05
0.0000E+00	6.0491E-02	-3.6976E-03	3.6976E-03
-2.5204E-02	-3.8763E-08	-2.1483E-02	-2.1483E-02
0.0000E+00	6.3847E-02	2.6060E-01	-2.6060E-01
1.3873E-02	7.3256E-07	-2.9781E-02	-2.9781E-02
0.0000E+00	-8.7846E-02	-4.2094E-04	4.2094E-04
0.0000E+00	0.0000E+00	0.0000E+00	0.0000E+00
0.0000E+00	0.0000E+00	0.0000E+00	0.0000E+00

APPENDIX C1

STATE SPACE MATRICES OF THE SSOR1 LINEAR MODEL

C MATRIX

0.0000E+00	0.0000E+00	0.0000E+00	0.0000E+00	0.0000E+00	0.0000E+00	1.0000E-01	0.0000E+00
0.0000E+00	0.0000E+00	0.0000E+00	0.0000E+00	0.0000E+00	0.0000E+00	0.0000E+00	1.0000E-01
0.0000E+00	0.0000E+00	0.0000E+00	0.0000E+00	-1.0749E-01	9.9984E-01	4.6827E-09	1.3316E-03
1.0539E-01	-1.0629E-01	9.8873E-01	0.0000E+00	0.0000E+00	0.0000E+00	2.7119E-02	-8.4843E-01

APPENDIX C2

MATRICES OF THE 30 KNOT COMPENSATOR

FILTER GAIN MATRIX

-1.0282E+00	-1.8198E+01	-8.1019E-01	-2.1680E+00
1.1923E-01	7.9327E-02	-7.5141E-01	2.8994E-02
1.9031E+00	1.7664E+00	-8.6529E-01	1.5857E-01
-1.4904E+00	4.2619E-01	1.2014E+00	1.1415E-01
9.3005E-03	4.4870E-01	9.2495E-02	5.4981E-02
6.8777E-03	-3.4783E-01	-2.6354E-01	-3.8983E-02
2.4814E-02	4.1892E+00	2.1197E-01	4.9849E-01
1.8704E-01	2.4765E-01	-3.5220E-01	4.9200E-02
-3.0473E-02	-4.2343E-03	-3.1907E-02	3.5337E-04
-4.2073E-02	2.1331E-02	3.8510E-01	-4.2349E-03
5.3431E+00	2.1792E-01	-3.8501E-01	-1.5210E-01
2.1792E-01	4.9887E+00	2.8426E-01	-4.8414E-03

CONTROL GAIN MATRIX

1.3487E+00	1.4722E-03	-1.8437E-03	3.2330E-03	-2.8933E+00	2.1865E+00
-2.3081E+01	4.6679E-02	2.3366E+01	2.0238E+00	-2.3789E-01	2.5951E+01
1.4722E-03	2.0983E+00	-1.1733E-02	-4.2671E-02	-4.7100E-02	2.5212E+00
-7.6947E-01	1.9053E-01	1.7016E+00	-2.3196E+01	8.8982E-02	3.6430E-01
-1.8437E-03	-1.1733E-02	1.3132E+00	-3.5292E-01	-7.9515E-01	-1.3192E+00
-8.6155E+00	2.5982E+00	-1.9569E+00	1.4596E+00	1.4934E+00	4.8954E+00
3.2330E-03	-4.2671E-02	-3.5292E-01	1.2833E+00	-9.4105E-01	2.7612E+00
-8.7112E+00	-2.5781E+00	-5.8551E-01	6.8046E-01	-1.9771E+00	5.4309E+00

APPENDIX C2

MATRICES OF THE 30 KNOT COMPENSATOR

L MATRIX

-6.0839E-01	-3.6479E+01	5.6633E-01	-4.3555E+00
1.5610E-02	8.7114E-02	-1.5284E+00	6.4870E-03
3.3627E+00	3.5327E+00	-2.4355E+00	4.4871E-01
-2.6540E+00	8.8502E-01	2.7545E+00	1.5325E-01
-2.8582E-02	8.9419E-01	8.1547E-14	1.0539E-01
2.8826E-02	-9.0182E-01	-8.2242E-14	-1.0629E-01
-2.6814E-01	8.3888E+00	7.6502E-13	9.8873E-01
0.0000E+00	0.0000E+00	0.0000E+00	0.0000E+00
4.9774E-09	1.4154E-03	-1.0629E-01	-4.4369E-13
-4.6300E-08	-1.3166E-02	9.8873E-01	4.1272E-12
1.0000E+01	-1.4691E-09	-3.8444E-17	1.2488E-11
-1.3286E-10	1.0000E+01	6.9211E-12	-5.5841E-09

OPEN LOOP EIGENVALUES

9.5843E-09	0.0000E+00	0.0000E+00	0.0000E+00	-1.4176E-02	-3.8412E-02
-4.4084E-01	-4.4084E-01	-4.5114E-01	-5.0486E-01	-5.8965E-01	-5.8965E-01
-4.0661E-02	-4.2886E-02	-7.1364E-02	-1.9689E-01	-1.9689E-01	-2.5114E-01
-9.5148E-01	-9.5148E-01	-1.0104E+00	-1.3887E+00	-1.3887E+00	-1.4462E+00
0.0000E+00	0.0000E+00	0.0000E+00	0.0000E+00	0.0000E+00	0.0000E+00
4.7901E-01	-4.7901E-01	0.0000E+00	0.0000E+00	1.1366E+00	-1.1366E+00
0.0000E+00	0.0000E+00	0.0000E+00	3.1300E-01	-3.1300E-01	0.0000E+00
1.0148E+00	-1.0148E+00	0.0000E+00	1.3186E+00	-1.3186E+00	0.0000E+00

APPENDIX C2

MATRICES OF THE 30 KNOT COMPENSATOR

OPEN LOOP TRANSMISSION ZEROS

1.0000E+30	1.0000E+30	1.0000E+30	1.0000E+30	1.1625E+08	1.0192E+08
-3.9767E-02	-3.9767E-02	-1.9869E-01	-2.0469E-01	-2.0469E-01	-2.5097E-01
1.2816E+05	1.4260E+04	1.2133E+00	1.2202E+00	-1.4256E-02	-3.8414E-02
-2.8357E-01	-4.5944E-01	-1.4263E+04	-1.2816E+05	-8.6484E+07	-5.8038E+09
0.0000E+00	0.0000E+00	0.0000E+00	0.0000E+00	0.0000E+00	0.0000E+00
1.6540E-03	-1.6540E-03	0.0000E+00	2.8343E-01	-2.8343E-01	0.0000E+00
0.0000E+00	0.0000E+00	1.0851E+04	-1.0851E+04	0.0000E+00	0.0000E+00
0.0000E+00	0.0000E+00	0.0000E+00	0.0000E+00	0.0000E+00	0.0000E+00

CLOSED LOOP EIGENVALUES

-1.4220E-02	-3.8414E-02	-3.8479E-02	-4.1399E-02	-1.0317E-01	-1.0317E-01
-5.1064E-01	-5.1064E-01	-5.1516E-01	-5.2355E-01	-5.2355E-01	-7.1513E-01
-2.3970E-01	-2.3970E-01	-2.5106E-01	-2.7292E-01	-2.7292E-01	-4.1228E-01
-7.4533E-01	-7.5232E-01	-7.5232E-01	-1.0388E+00	-1.1957E+00	-1.1957E+00
0.0000E+00	0.0000E+00	0.0000E+00	0.0000E+00	1.0659E-01	-1.0659E-01
7.0401E-02	-7.0401E-02	0.0000E+00	9.2146E-01	-9.2146E-01	0.0000E+00
3.3649E-01	-3.3649E-01	0.0000E+00	2.7737E-01	-2.7737E-01	0.0000E+00
0.0000E+00	8.5953E-01	-8.5953E-01	0.0000E+00	1.1639E+00	-1.1639E+00

CLOSED LOOP TRANSMISSION ZEROS

7.5203E+10	1.1350E+04	8.6830E+03	6.7422E+03	2.5300E+02	2.5300E+02
-3.9768E-02	-3.9768E-02	-1.9869E-01	-2.0469E-01	-2.0469E-01	-2.5097E-01
1.5900E+00	1.4499E+00	2.5446E-01	7.5307E-01	-1.4253E-02	-3.8414E-02
-2.8357E-01	-4.5944E-01	-5.0698E+02	-6.7412E+03	-8.6823E+03	-1.1349E+04
0.0000E+00	0.0000E+00	0.0000E+00	0.0000E+00	4.3878E+02	-4.3878E+02
1.6527E-03	-1.6527E-03	0.0000E+00	2.8343E-01	-2.8343E-01	0.0000E+00
2.4470E+05	-2.4470E+05	1.5450E+04	-1.5450E+04	0.0000E+00	0.0000E+00
0.0000E+00	0.0000E+00	0.0000E+00	0.0000E+00	0.0000E+00	0.0000E+00